Iakov Benediktovich Ulanovskiy – Doctor of Engineering Science, Professor, Member of the European Academy of Natural Science.

The graduate of the Physical Chemistry Department of the Moscow Institute of Steel and Alloys, headed at that times by Professor, honored worker of science and technology Alexander Abramovich Zhuhovitskiy.

For many years he had worked at the All-Union Institute of Light Alloys (VILS).

The area of expertise – material engineering, physical chemistry.

Today he is the Head of the R&D and manufacturing group of companies “Scienmet”, working on development and implementation of innovation technologies in ecology, power engineering and medicine.

Professor Ulanovskiy has been awarded with the honorary title “Engineer of Russia”, awarded with the Grand Prix and three gold medals of the “EUREKA”, Innovation Exhibition in Brussels, awarded with a medal of the International Academy of Sciences of Nature and Society “For the contribution into the revival of science and economy of Russia”, awarded with a gold medal of the International Science-Innovation Organization “Nikola Tesla”.

He is the author of more than 100 scientific research papers and inventions, including 4 monographs in Russian and English and one scientific discovery.

MISIS

I.B. Ulanovskiy

THEORY AND PRACTICE OF MAKING FOILS BY VACUUM DEPOSITION

MINISTRY OF EDUCATION
AND SCIENCE OF RUSSIAN FEDERATION
NATIONAL UNIVERSITY OF SCIENCE AND TECHNOLOGY “MISIS”

I.B. Ulanovskiy

THEORY AND PRACTICE OF MAKING FOILS BY VACUUM DEPOSITION

MISIS

Moscow 2016

УДК 544.3
У47

Ulanovskiy I.B.

У47 Theory and practice of making foils by vacuum deposition / I.B. Ulanovskiy. – M. : Izdatelskiy Dom “MISIS”, 2016. – 232 c.

ISBN 978-5-87623-975-4

This book is the first attempt ever to offer a consistent review of the main stages of a new way to produce foil from metals and alloys through vacuum deposition; the author has created physical models adequately describing this process and enabling engineering calculations of its basic parameters. The results of this study have laid a scientific foundation for the development of commercial scale process of making ultrathin foils, including those from difficult-to-form titanium alloys, as well as for the development of vacuum engineering devices working something of semiconductors.

This book aims to draw the attention of materials science experts, students and postgraduate students of technical universities.

УДК 544.3

ISBN 978-5-87623-975-4

CONTENT

This work is a tribute to Academician Alexander F. Belov − an architect of the Soviet aviation metallurgy, the founder of the National Institute of Light Alloys

Foreword

This monograph is based on the author's thesis "The study of principles of formation of the structure of vacuum condensates of titanium-based alloys and the development of the process of titanium foil production" submitted for the Doctor of Science in Process degree and successfully defended in 1991. The study was made in 1973−1990 at the National Institute of Light Alloys (VILS) − one of major research and process centers of the Soviet aviation industry at the time.

Due to the secrecy policies enforced at the time, this work was classified "For Official Use Only", which greatly impeded the possibility to publish its findings. Today such formal barriers have become obsolete, but it is the author's belief that its consistently structured solutions to all the problems involved may be still useful for a broad scientific community. This is the monograph's mission.

Academician Alexander F. Belov, the founder of the National Institute of Light Alloys under the auspices of the Ministry of Aviation Industry of the USSR, was enthusiastic concerning about all kinds of new manufacturing processes, materials and equipment. In early 1970s, at the International Conference on Vacuum Metallurgy, he learned from a report of American experts about allegedly successful development of a breakthrough process of making foil from titanium alloys through vacuum evaporation and deposition.

This method works as follows. A titanium alloy ingot, from which a foil shall be made, is put into a vacuum chamber. The surface of the ingot is heated by an electron beam gun. It causes the alloy to evaporate and deposit on the surface of substrate strip continuously moving over the vaporizer. Once the coating is formed, it is separated from the substrate strip as finished foil. Before the start of the process, the surface of the substrate strip is coated with a special separating/antiadhesive material to provide separation of the condensate from the substrate strip.

Leading experts from VILS were quite skeptical concerning this idea as the development of such process obviously involved a number of brand new challenges.

It was not without good reason that skeptics would argue that even the traditional process of crystallization of alloys from the liquid phase has not been thoroughly studied over many decades of researches. The processes related to foil structure formation during subsequent thermomechanical processing also were not clear in detail. Moreover, the process of titanium alloy crystallization from vapor phase was not studied at all, to say nothing of the absence of any information on the resulting structure and physical and mechanical properties of the foil obtained.

Another challenge was making the foil of a given chemical composition with the even distribution of alloying elements along width, thickness and length of the foil. The thing is that titanium alloys contain alloying elements characterized by respective vapor pressures varying hundredfold or thousandfold. Agents with a higher vapor pressure evaporate from the molten metal before other agents. Therefore it was necessary to study kinetics and thermodynamics of the evaporation process for alloys containing components having different vapor pressures.

Besides, the foil should have a given thickness with minimum deviations throughout its width and length. It is known that the thickest part of the foil forms directly over the center of the vaporizer while away from the center it becomes thinner. Therefore, the challenge was to ensure proper spatial distribution of the vapor flow during highly intensive electron beam evaporation.

It was difficult to select a proper antiadhesive agent and adjust the parameters of its application on the substrate strip. In fact, if the condensate would be peeled off the substrate strip over the vaporizer too early a part of the foil will melt down due to the lack of heat removal through the substrate strip. Besides, the condensate must not peel off the coiled substrate strip in the process of coiling since the foil peeled too early will be damaged. The condensate must peel off the substrate strip free in the form of finished foil once the process is over.

However, despite any understandable difficulties, the suggested process looked very promising, because it allowed to produce the finished product – a thin foil in one run, while the traditional rolling process of making foil from hard alloys required many processes, not to say that thin and wide strip of foil cannot be made from titanium alloys is virtually impossible. Therefore, Academician A.F. Belov decided to develop at VILS the process of making titanium foil from hard titanium alloys through metal evaporation and deposition in a vacuum.

At the time of the Cold War, we were still unaware that the development of new production processes by our counterparts overseas hinged on their proprietary organizational and economic know-how. A successful invention would be no longer mentioned in any scientific, technical literature and international conference reports. However, a failed invention would be widely publicized in scientific and technical literature and highlighted in reports made at international conferences alleging a success of a new production process.

What was the reason for this? As the money put into the development of such "dead-end" process was gone, they tried to lure their counterparts into the development of such process thus causing them substantial financial losses as well.

This monograph was inspired by this know-how. We did succeed in developing a new production process.

In 1972, the author of this book, a graduate of the Department of Physical Chemistry, Moscow Institute of Steel and Alloys, quite young employee at VILS, successfully defended his PhD thesis on "Hydrogen diffusion and development of porosity in aluminum." The thesis addressed the most topical scientific issues and offered solutions to a number of practical problems in VILS' major field of research. Previously, VILS would organize annual conferences on the interaction of hydrogen with aluminum causing porosity in aluminum semi-products. The author's PhD thesis virtually exhausted this subject, having addressed its main issues, thus making any further conferences on this topic unnecessary.

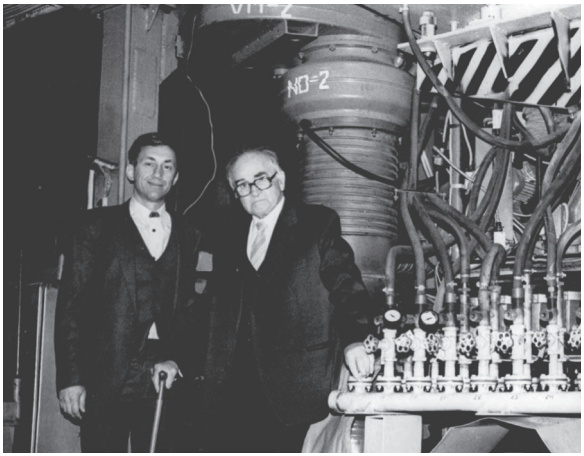

Academician A. F. Belov and I. B. Ulanovskiy

A good knowledge of physical chemistry, obtaining fundamentally important scientific results and their successful application to industries, apparently, prompted Academician A.F. Belov to appoint the author as

research manager and administrator of a new unit in VILS aiming to solve the above problem.

The first specimens of titanium alloy foil were obtained just a few months after the appointment, despite overwhelming skeptical attitude. But that was only the beginning, only the foretaste of the actual complexity of future problems.

Our main experiments and invention of new production processes aimed to make a foil from titanium alloys. However, process patterns and solutions to technological problems discovered during this work are rather general and can be applied to processes of foil making by vacuum evaporation and deposiyion of other metals and alloys.

Along with the development of scientific platform of the process, we developed technological parameters of the foil production and created all necessary equipment for its manufacture.

This monograph also shows a practical application of the resulting foil for making heavy-duty products. Based on our theory of gas-permeable screens consisting of multi-layered titanic foil with a preset through-thickness porosity pattern, we developed a vacuum device resembling electronic semiconductors.

Such screening device is gas-permeable at a moderate temperature and it ensures the pumping of all remaining gases through pores in the layers of foil, while at a higher temperature it becomes selectively impermeable for gases and prevents the access of “harmful” components of remaining gases to the product placed under the screens.

It is noteworthy that during this work the author met outstanding scientists and specialists who greatly contributed to successful implementation of this project. First of all, I would like to acknowledge the input from the Head of SKB “Vacuum Coatings” unit (currently Sidrabe company, Riga), a prominent scientist and designer, PhD in Technical Sciences, Edgar V. Yadin; Director of the E. O. Paton Institute of Electric Welding (Kiev), Academician Boris Paton and Head of the Department of E. O. Paton Institute of Electric Welding, Academician Boris A. Movchan; Chief Engineer of Vekshinsky Research Institute (Moscow) Vladimir Vladimirovich Ivanov; Head of Laboratory of E. O. Paton Institute of Electric Welding Mikhail Ivanovich Vinogradov and Leading Specialist Vladimir Fedorovich Ulyanov; Director of Kharkov Institute of Physics and Process, Academician Viktor Vladimirovich Ivanov; specialists of

ANTK Tupolev: Head of Department of New Equipment Implementation (one of the main units of the complex) a successful Design Engineer Oleg Nikolayevich Sankov, Chief Technologist Vladimir Vasilyevich Sadkov, Head of Laboratory, Phd in Technical Sciences, Yury Viktorovich Gorshkov, Chief Specialist of the Ministry of Aviation Industry Lev Isidorovich Karseladze, and VILS employees – Deputy Director of the Institute, Prof. Nikolai Fedorovich Anoshkin, Head of Unit, Phd in Technical Sciences, Vyacheslav Petrovich Mitin, Head of Research and Production Complex, Phd in Technical Sciences, Vladimir Mikhailovich Lovtsov, Scientific Secretary, Phd in Technical Sciences, Lev Khaskelevich Roytberg, Senior Fellow, Phd in Technical Sciences, Boris Abramovich Kopeliovich.

My special acknowledgements go to the specialists who worked under my direct supervision: Evgeny Stepanovich Zhiltsov, Alexander Vladimirovich Bushuev, Valentin Fedorovich Eliseev, Georgy Isaakovich Dubnik, Alexander Fedorovich Sorokin, Alexander Dmitrievich Dolmatov, Viktor Stepanovich Zhukovsky, Tikhon Sergeyevich Tretyakov to name but a few.

I am especially grateful to my teacher − Head of Department of Physical Chemistry of MISiS, Honored Scientist of the RSFSR, Professor, Doctor of Chemistry, Alexander Abramovich Zhukhovitsky.

I would also like to thank Mikhail Soloveitchik, PhD, and Vladimir Soloveitchik, PhD, for help in fulfilling this work.

Finally, I would like to thank Irina Vladimirovna Apykhtina for her comprehensive assistance in preparing this monograph, as well as the Head of the Department of Physical Chemistry of NITU “MISiS”, Doctor of Chemistry, Professor Mikhail Vasilyevich Astakhov, Doctor of Sciences in Physics and Mathematics Yuri Rakhmilyevich Nemirovskiy for their kind attention towards this work.

Introduction

The development of new material and processes is an integral part of scientific and technological processes. The evolution of aviation and space engineering, modern acceleration devices, vacuum process and a number of other industries needs unique foil materials, including ultra thin ones made from difficult-to-deform metals, alloys of complex chemical composition, as well as multilayer foil, a foil with high strength, ductility, heat resistance, and preset through-thickness porosity, etc.

The traditional method of producing foil by rolling the original billet has a number of significant limitations.

The principal limitation of the chemical composition of the foil made by this technique is due to solubility of alloying elements in the initial molten metal. It is virtually impossible to produce a wide ultrathin foil from difficult-to-deform alloys by this method. Fabrication of multilayered foils is only possible within a limited range of the layers thickness ratio and a limited combination of different materials. Furthermore, manufacturing foils from difficult-to-form alloys by gradually reducing the thickness of initial ingot through several steps is a rather time-consuming process.

Foil production by vacuum deposition is free of such constraints. The process involves evaporation of alloy in a vacuum and vapor deposition onto the surface of a substrate continuously moving over vaporizer followed by the separation of the condensate from the substrate in the form of finished foil. To ensure the separation of the condensate the substrate is pre-coated with a special separating material, i.e. antiadhesive.

Rolling technique begins with making a thick ingot followed by gradual reduction of its thickness, while the new process allows to make foil consistently increasing its thickness to the preset parameters.

Potential advantages of this process are obvious because it allows to make a wide ultra-thin foil from various alloys, as deformability limits do not apply in this case. It makes possible to produce multilayer foils by stepwise deposition of various metals and alloys, while freely varying physical and mechanical properties of the foil due to unlimited solubility of the different elements in the vapor phase and the rapid crystallization effect.

Its other advantages include zero environment pollution as the process takes place in a sealed equipment; the possibility to combine most production stages within one apparatus and the streamlined process, plus no oil traces on the foil surface, unlike in the rolling method.

In addition, this process provides a unique opportunity to study and develop new alloys. Typically, the study and development of new alloys involves much work to melt ingots with different concentrations of selected alloying elements, fabrication of deformable semi-finished products from the ingots with subsequent heat treatment thereof, production of specimens for mechanical tests; a labor-intensive manufacturing of thin specimens for electronic microscopy and other types of research, etc.

The new process allows to make, in one run the foil specimens with a smoothly varying content of alloying elements ready for research of the

foil structure and properties. By varying the substrate temperature, one can study the influence of crystallization rate on the structure and properties of resulting alloys in a wide range of parameters. These specimens also can be used to study the impact of heat treatment regimes on the structure and properties of new alloys made by this process.

Finally, thanks to unlimited solubility of various materials in a vapor phase it is possible to make and study the specimens of brand new alloys that can not be produced by crystallization from a liquid state due to limited solubility of its components.

These advantages demonstrate not only the unique potential of the new process, but also its advisability in a wider range of metallurgical and materials science applications. However, a wider use of the new process is largely impeded by a number of unsolved scientific problems that are crucial for the development of basic process parameters.

To ensure the reqoired thickness of the foil, its minimal deviations and the optimal temperature of the substrate it was necessary to solve the task of mass and heat transfer during a high-speed evaporation and vapor deposition on the moving substrate

In order to obtain appropriate chemical composition of the foil it is necessary to know the basic patterns of the multi-component alloys evaporation process.

To make sure that the foil separates from the substrate it is necessary to determine the principles for the selection of materials of the substrate and antiadhesive.

General rules of crystallization from the gas phase, as well as the main features of the formation of structure and phase composition of vacuum condensates of alloys were studied in order to produce the foil with appropriate working properties.

Significant attention is paid to the problems of the formation of foil through-thickness porosity by vacuum deposition and the application of the process features for making foil with freely adjustable open porosity and the practical use of this foil in vacuum technologies, resembling the role of semiconductors in electronics.

There are various methods of vacuum evaporation of materials, however, for industrial foil production it is expedient to use the most efficient high-speed electron beam evaporation technique for industrial production of the foil. Therefore, this book considers this particular evaporation method.

Technical literature has some information on the above issues but without any physical models adequately describing this process and allowing for engineering calculations in order to determine and optimize its key parameters.

We have pioneered a consistent study of the main stages of the high-rate evaporation process and deposition of metals and alloys on a moving substrate in a vacuum and also we thoroughly described physical processes during the manufacture of foil by vacuum deposition. Therefore the resulting principles and practical advice may generally apply to the manufacture of foil from various metals and alloys.

This monograph is based on the findings obtained by successful addressing of scientific, industrial and technological challenges involved in foil production from titanium and its alloys by vacuum deposition, as well as a description of some solutions to the problems of practical use of the unique properties of such foil.

However, the complex nature of the specific problem facing us along with peculiar physical and chemical processes and the conditions of their controlled implementation – all have created objective conditions and incentives for the examination of scientific and technological tasks in a rather general way.

This monograph presents a comprehensive summary of all issues related to the use of vacuum deposition technique for successful and cost-effective fabrication of a thin foil, and the author believes that these findings are undoubtedly of scientific and practical value. These include:

− description, based on literature data, of general physical and chemical patterns of the process of metals vacuum deposition and, specifically, of the results of our titanium alloys studies (Chapter 1);

− description of all the equipment crea during our work in order to ensure consistent foil quality (Chapter 2);

− general theoretical solution of the problem of heat and mass transfer during a vacuum vapor deposition onto a moving substrate (Chapter 3) and the problem of electron beam evaporation of multi-component alloys at a continuous feed of molten metal (Chapter 4);

− development of principles for the selection of the substrate and anti-adhesive materials (Chapter 5);

− formation and use of the through-thickness porosity of foil (Chapter 6).

The results of our research of the structure and properties of foil made by vacuum deposition of titanium alloys are presentedin Chapter 7, while Chapter 8 gives an example of using titanium foil with adjustable through-thickness porosity.

Chapter 1. GENERAL REGULARITIES OF VACUUM CONDENSATE STRUCTURE FORMATION AND BASIC REQUIREMENTS TO INDUSTRIAL THIN FOIL PRODUCTION THROUGH VACUUM DEPOSITION

To reveal the peculiarities of foil production through vacuum deposition along with the influence of main technological parameters on the structure and properties of foil we have to study first of all the general patterns of foil structure formation and its correlation with properties of vacuum condensates materials.

The structure of the thin foil made through vacuum deposition results from:

− vapor condensation on the substrate;

− thermally-activated structural and/or phase changes during the build-up of a condensate layer up to required thickness;

− special heat treatment of the foil.

Therefore, the structure-sensitive mechanical properties depend more or less upon parameters of all these processes.

Systematic presentation and analysis of the results of numerous theoretical and experimental researches of vacuum deposition processes are found, in particular, in monographs [1−4]. This chapter briefly describes the existing general ideas concerning the formation of vacuum condensates together with the results of our studies of the influence of vacuum deposition and heat treatment parameters on the structure of the condensate of various metals and alloys obtained in the course of simulation experiments.

A method used for the production of a condensate can significantly influence its structure. For instance, an electric field accelerating the ions of sputtered material substantially alters the energy balance of the process and the adherence of the condensate to the substrate that are paramount factors for the formation of the foil structure. However, among the three major methods (cathode sputtering, thermal spraying, and ion deposition) only thermal spraying is highly productive, which is critical for industrial production of thin and wide foil [5]. The results given below mainly refer to this process of making vacuum condensates.

1.1. Mechanisms of condensation from a gas phase and "original" structure of the condensate

The first studies of vacuum deposition processes refer to early 20th century [6–8].

Condensation from a vapor phase can be conventionally divided into several successive stages:

- metallic gas atoms hitting the surface;
- the atoms migrating over the surface;
- condensate forming and growing.

As an atom hits the surface it becomes physically adsorbed (adatom state). Subsequently, depending on the energy of the colliding atom, the temperature of the condensation surface, the density of the molecular beam, and the nature of the condensate and substrate, there occurs either re-evaporation or formation of a stronger bond of the adsorbed atom with the surface.

Condensation coefficient is understood as the probability of an atom hitting the surface being captured thereby; it is measured as the ratio of the number of atoms actually condensed on the surface to the total number of atoms hitting the surface during the same lapse of time. According to [9–11], if the masses of condensate atoms and the substrate atoms are similar and the kinetic energy of an incident atom is not more than 25 times of that of desorption, then the atom will be captured by the substrate If a condensate atom is much lighter than an atom of the substrate or if its kinetic energy is great, then the condensation coefficient is significantly below 1.

If the masses of colliding atoms are comparable, then a trapped atom loses almost all of its kinetic energy already within the first three periods of the lattice vibrations [9]. Such adatom moves over the surface and its average life on the surface until its desorption τ_s is written as [12].

$$\tau_s = \nu^{-1} \exp\left(\frac{\Theta_{\text{дес}}}{kT}\right) \tag{1.1}$$

where ν is oscillation frequency of adsorbed atom; $\Theta_{\text{дес}}$ is desorption activation energy.

Average relaxation time τ_R, which is necessary for setting up a thermodynamic equilibrium between the trapped atoms and the substrate, is $\tau_R \approx 2/\nu$ and, therefore,

$$\tau_R \approx 2\tau_s \exp\left(-\frac{\Theta_{\text{дес}}}{kT}\right). \qquad (1.2)$$

At high bound energy, when $\Theta_{\text{дес}} >> kT$, the time τ_s is great, while τ_R is small. In this case, thermodynamic equilibrium is established quickly; atoms are regarded as localized and diffusing over the surface. At $\Theta_{\text{дес}} \approx kT$ equilibrium of atoms relative to the substrate is not established instantly. Adatoms remain "hot" and their condensation coefficient is below 1.

Having analyzed theoretical works on the formation of condensates published in 1960−1970, Komnik [3] pointed out that moving atoms located on the surface and being in adsorbed state, are regarded as "two-dimensional vapor", where complexes (nuclei) are formed resulting from collisions of atoms, and the growth of these nuclei causes the formation of a condensate film (average temperature of this vapor does not necessarily match the temperature of the substrate). According to [3], these nucleation theories have led to conclude that "at the initial time, condensation is incomplete, i.e. condensation coefficient is below 1, but this time interval is relatively small. An increase in the number and size of the nuclei means lesser likelihood of their dissociation and ensures the overlapping of capture fields of adsorbed atoms resulting in virtually complete condensation of the molecular beam. An increase in temperature causes an increase in the time interval at the initial stage of partial condensation".

It is also noted that "the nucleation mechanism of condensate formation is not all-inclusive and does not reflect some extreme cases. Thus, at a very low temperature, the coefficient of surface diffusion is small while the lifetime of atoms in the adsorbed state is long, so condensation is a process of accumulation of adsorbed atoms retained near the point of their collision with the surface of the substrate. Another example is the case of strong interaction of condensable atoms with the substrate, for instance, when metal vapor is deposited onto a clean surface of allied metal. In this case, the adsorbed atoms enable the formation and growth of the layer, which is crystallographically conjugated with the substrate (i.e. the case of "strong" epitaxy). This process does not require a formation of stable complexes of adsorbed atoms".

However, according to [3], "nucleation" mechanism corresponds to the most common cases of condensation on a neutral or alien, slightly orienting, substrate (in case of "weak" epitaxy), where the initial stage of con-

densate formation is a process of nuclei generation and growth. It is obvious that "the structure of the resulting condensed layer will be determined to a large extent by the number of the nuclei, their mutual orientation and interaction in the process of growth" − these, by themselves, depending on "the substrate temperature, the density of the incident molecular beam, which determines the concentration of adsorbed atoms; the nature of interaction of deposited atoms with the substrate, etc.".

The substrate temperature is one of the most influential factors impacting the process of vacuum condensation. Numerous researches have found out characteristic temperatures, at which qualitative changes of the condensation process take place being manifested in rather drastic (clearly identified in the experiment) changes in the structure and properties of resulting condensates.

1.1.1. Critical temperature of condensation

Wood [6] and Knudsen [7] discovered a critical surface temperature, above which no condensation is possible thereon even in case of a supersaturated system. Knudsen believed that the existence of critical temperature (T_{cr}) was caused by the type of interaction of condensing particle with the substrate: below T_{cr} vapor atoms suffer inelastic collision with the surface and "stick" thereto, and above T_{cr} there is an elastic collision and bouncing of the particles that hit the surface. Elaborating on the idea of "sticking" of condensing atoms to the surface, Langmuir [8] noted that at low vapor pressure the likelihood of condensation of the second atom near the first atom is negligible and it increases as the pressure becomes higher. If two atoms are located near each other on the surface, then the evaporation of one of them requires an increased energy in order to overcome the attraction between this atom and the substrate and between the condensed atoms as well. Therefore, the rate of evaporation of such twin atoms is considerably less than that of single atoms and the groups of a greater number of atoms will be even more stable.

Khariton and Semenov [13] have demonstrated experimentally the dependence of T_{cr} on the density of molecular beam. This dependence is explained through initial condensation theories suggested by Frenkel [14] and Semenov [15].

Frenkel based his theory on two main ideas:

− molecular beam particles after the collision with the surface of the substrate remain thereon for a mean time τ forming a two-dimensional (2D) vapor;

− collisions of atoms result in the formation of longer living complexes on the surface compared to a life span of a single adsorbed atom, however, only two-atom complexes were considered for simplicity sake.

By this model, the condensation mechanism implies a direct transfer of atoms from vapor phase to crystal phase (V→C), and the bond T_{cr} with the critical density of the molecular beam m_{cr} has the following form:

$$m_{\text{cr}} = A\exp\left(-\frac{\left(U_0 + \Delta U_0\right)}{kT_{\text{cr}}}\right) \tag{1.3}$$

where A is constant; $(U_0 + \Delta U_0)$ is the sum total of adsorption energies of a single atom and the dissociation energy of twin atoms.

According to Semenov's model, the atoms hitting the substrate and migrating over it are regarded as a bidimensional (2D) gas, which transforms at "saturation" into a 2D liquid, which subsequently is crystallized, i.e. condensation mechanism Vapor→ Liquid → Crystal (V → L → C) is at work. In addition, there is critical pressure P_{cr} (and the corresponding density of molecular beam), below which there is only 2D rarefied gas on the surface and above which − a 2D liquid covering the surface with a continuous monomolecular layer. This pressure is linked to the temperature by exponential dependence similar to that found by Frenkel:

$$P_{\text{cr}} = D\exp\left(-\frac{\left(U_0 + \Delta U_0\right)}{kT_{\text{cr}}}\right) \tag{1.4}$$

Subsequent theoretical and experimental studies have shown, firstly, that nucleation requires something more than two-atomic complexes (because they are not stable enough), and, secondly, mainly 3D nuclei are formed and, starting with the smallest thicknesses, the deposited layer has discrete rather than solid structure suggested in Semenov's theory concerning the implementation of the mechanism V→L [12, 16−19]. However, according to [3], the dependence between the flow density and T_{cr}, obtained through established modern ideas of the mechanism of condensation process implying condensate nuclei formation from 2D vapor, has the same exponential form as in the theories of Frenkel or Semenov. Moreover, the condition for reaching saturation of 2D vapor determines the threshold nucleation rate.

In [3] it is further noted that according to available experimental data, "the effect of critical condensation temperature becomes clearly seen only on neutral, highly pure surfaces free of any foreign particles and impurities that may become centers of 2D vapor condensation" and that condensation heat is close to the metal vaporization heat and that T_{cr} is significantly influenced by physical and chemical properties of the substrate: "T_{cr} values for a given substance and selected flow density can vary by several tens or hundreds of degrees when changing the type of the substrate".

1.1.2. Influence of the substrate temperature on the condensation mechanism

A detailed experimental study of the mechanism of condensation in a vacuum can be found in works of Palatnik and Komnik et al al. These studies, along with analysis of the results of the study of condensation mechanisms by other authors, are given in the monographs [2, 3].

Based on the study of the structure of condensates, as well as direct electron microscopic observation of the condensation process of various metals, it was found out that depending on the temperature of the substrate $T_{substrate}$ ($T_{substrate} < T_{cr}$) both crystalline and liquid condensate nuclei can occur i.e. mechanisms V → C or V → L, respectively. It was found that each metal had a characteristic boundary temperature of the substrate $T_{cryst/liquid}$, at which the mechanism is changed: at $T_{substrate} < T_{cryst/liquid}$ mechanism V → C is at work replaced by the mechanism V → L at $T_{substrate} > T_{cryst/liquid}$. The higher the temperature of the substrate and the smaller the thickness of the condensed metal, the longer the liquid phase, occurring at $T_{substrate} > T_{cryst/liquid}$, is maintained (not crystallized).

Experiments found out that for many metals, when using neutral substrates the temperature $T_{cryst/liquid}$ depends on the melting temperature of compact material T_s according to the ratio $T_{cryst/liquid} \approx 2/3\ T_s$. However, condensation conditions can significantly influence the temperature $T_{cryst/liquid}$. For instance, the increase of $T_{cryst/liquid}$ and, respectively, the ratio $T_{cryst/liquid}/T_s$ is achieved by the reduction of a corner of wetting of the substrate surface by a liquid metal (in particular, the transition from neutral amorphous substrates to crystal ones), pollution of metal with oxides, which depends on the pressure of residual gases in the chamber and the condensation rate, etc. However "in all cases the temperature range where initial stage of condensate formation occurs in liquid phase is lower than the melting temperature by tens and hundreds of degrees" [3].

Existing concepts of the physical nature of the effect $T_{cryst/liquid}$ are discussed in [3].

The initial interpretation of the phenomenon of condensation of metals in a liquid phase at $T_{substrate} < T_s$ was based on the assumption that condensation process has a 2D nature thus requiring energy consumption ~ 2/3 of the melting heat of a bulky crystal [20].

Later it was suggested that the liquid phase in the case of condensation in the temperature range $T_{cryst/liquid} < T_{substrate} < T_s$ occurs due to a lower melting temperature as radiuses of small particles decrease [21].

In this case, temperature $T_{cryst/liquid}$ corresponds to the intersection point of the two temperature/dimensional dependencies (dependence of the melting temperature on a particle size and the dependence of a nucleus critical size on the temperature during condensation), and the physical nature of the effect of $T_{cryst/liquid}$ acquires, according to [3], a very definite interpretation, i.e. it occurs because at $T_{substrate} > T_{cryst/liquid}$, the equilibrium state of critical size particles is a liquid rather than crystalline one. The estimates given in [3] evidence that this model, apparently, explains similar values of $T_{cryst/liquid}/\ T_s \approx 2/3$ calculated for various metals on neutral substrates but, according to the author, "it failed to explain definitely the fact of increasing temperature $T_{cryst/liquid}$ in the case of transition from amorphous to crystalline substrates and in the case of deterioration of vacuum conditions". Yet it is noted that "macroscopic manifestation of temperature $T_{cryst/liquid}$ is ensured by a long-term retention of liquid phase without crystallization and that particles in liquid phase at $T > T_{cryst/liquid}$ reach sizes exceeding both the critical and equilibrium size (for crystallization) ... as a result of the propensity of liquid metals to significant supercooling (especially in small droplets under high-purity conditions)".

The latter fact obviously is taken into account by one of the interpretations of the effect of $T_{cryst/liquid}$ considered in [8], i.e. the assumptions made in works of Gladkikh et al ia [22−24] that the temperature 2/3 T_s is the lowest temperature at which it is possible to preserve a supercooled liquid state (experimentally the correspondence of temperature $T_{cryst/liquid}$ to the temperature of crystallization of very thin layers of several metals was obtained [2]). It follows from these assumptions, in particular, that the observed specific manifestations of the mechanism of condensation of V→L at $T_{substrate} > T_{cryst/liquid}$ are due to a more or less long-term preservation and growth of resulting supercooled liquid particles. Accordingly, the influence of condensation conditions on the experimental temperature

$T_{\text{cryst/liquid}}$ will depend on a greater or lesser impact of catalytic activity of the substrate surface, oxides, etc. on the crystallization process of the initial liquid phase, which can change $T_{\text{cryst/liquid}}$ in the temperature range ~ 2/3 $T_s < T < T_s$. Thus, this interpretation provides a qualitatively plausible explanation for the observed differences in the results of experimental determination of temperature $T_{\text{cryst/liquid}}$ and ratio $T_{\text{cryst/liquid}}/T_s$. However even this interpretation, according to [3], is somewhat problematic regarding quantitative assessments of possible effects and correlation of its consequences with earlier results of determination of interphase surface energy.

Works of Palatnik et al [25, 26] at temperatures ~1/3 T_s (i.e. much below $T_{\text{cryst/liquid}}$) have demonstrated the existence of critical substrate temperature (marked as Q_2 by the author and as T_1 by us hereinafter), close to which in a certain temperature range ΔT_1 a significant change in the structure and structure-sensitive properties of condensates of many materials occurred. It was interpreted as another temperature at which condensation mechanism has changed. It was assumed that at $T_1 < T_{\text{substrate}} < T_{\text{cryst/liquid}}$ mechanism V→C is activated, while at $T_{\text{substrate}} < T_1$ it is replaced by the mechanism V→L, with some specifics due to a relatively low condensation temperature. The existence of a low-temperature mechanism V→L was, in particular, experimentally proved by domed structures forming on the surface of condensates of some metals at $T_{\text{substrate}} < T_1$ [25, 26], and the presence of globular particles in the insular (before the formation of a continuous layer) condensates [20, 27, 28]. Respective experimental results and conclusions thereon are given in [2].

Alternative interpretation of "T_1-effect" is offered in Komnik's works [3, 21]. Existence of special temperature $T_1 \approx 1/3\ T_s$ for many metals and the fact of changes observed in transition through T_1 were explained by temperature dependence of structurization processes of structurization in a crystalline condensate (see below).

The inapplicability of ideas of a low-temperature transition V→L to actual structure of thick condensates formed at $T_{\text{substrate}} < T_1$ is noted in [4].

1.1.3. Primary structure formation in thin films

Processes eventually leading to the formation of thin films due to vapor condensation on the substrate have been extensively researched, the results of these studies being presented, for example, in the monographs [2, 3, 17, 19].

Even the first electron microscopic studies of the initial stage of thin films formation found out that films of small thickness consist of insular

condensate including individual particles, and further on a detailed picture of dynamics of morphological transformations of the structure of insular films condensated onto neutral and crystalline substrates was given by condensation experiments conducted directly inside electron microscope, the results of which were consistent with electron microscopic data on the condensates made in autonomous vacuum chambers and corresponding to sequential but discrete stages of the process of the film formation [3, 19].

According to [3, 19], characteristic features of the formation of thin films in the initial stage of condensation under conditions of adequate thermal activation of diffusion of condensate atoms are as follows.

At the initial time, many 3D randomly distributed nuclei particles emerge; they are formed instantly and virtually simultaneously followed by the growth of nuclei without a significant change in the surface density of the particles.

As particles increase in size during the formation of contacts between them (or in the case of sufficient approaching of the particles' walls) an interaction between the insulas particles occurs causing their merging. The process of merging of interacting particles is known as coalescence [3]. The coalescence leads to the reduction of the surface density of particles on the substrate and typically causes an increasing gap between them.

Crystal particles intergrowth in a condensate can also occur without coalescence, while maintaining the interface between the particles and replicating the outline as particles increase in size. This process is typical for metals with a high vapor elasticity, which produce well faceted crystalline particles even on non-orienting substrates (Mg, Zn, Cd, Be) [2].

Further increasing of condensed metal amount over a certain critical value causes a rapid formation of a common net from the coalesced particles. This stage is characterized by a "maze" structure. The "channels" of equal width forming an extensive system of gaps are retained between the particles. At this stage, the film already possesses electrical conductivity of metallic type.

Heating or annealing of films corresponding by their thickness to the stage of channels may be accompanied by rupture of bridges between the particles due to there tend to acquire thermodynamical equilibrium shape determined by forces of surface tension. This process is known as self-coalescing [2, 29].

If due to the coalescence a rather large portion of the substrate surface is exposed, then a secondary nucleation occurs and new nuclei usually grow very slowly.

The “channels” incrustation at the last stage of film formation is greatly delayed in time, due to, firstly, the continuation of the process of coalescence and recrystallization as the film grows thicker, and, secondly, a weaker inflow of atoms from 2D vapor to the borders of the “channels” due to decreasing effective supply area (the alignment of the channels’ width is the result from the fact that the narrower the duct, the slower its incrustation rate is).

It is also noted that “at a low temperature, significantly below the threshold of recrystallization ($T < 1/3\ T_s$), the absence of a pronounced coalescence process is natural and it must be the case for almost all metals” [3].

A thorough discussion of details and mechanisms of coalescence (bridges between insular particles, migration of not only liquid, but also crystal particles in general, the phenomenon of “liquid-like” coalescence of insular crystals, etc.) is given in the monograph [29].

Obviously, specific parameters of “primary” structures of the resulting film depend on many factors. For instance, the surface density of nuclei and hence the size of the primary condensate grain is largely determined by the temperature of the substrate, but it can be significantly influenced also by the condensation rate, the nature and condition of the substrate surface, the level and purity of vacuum etc. The presence or absence of “primary” texture effects etc. depends on the temperature and interaction of condensate atoms with the substrate. The role of some of these factors will be further considered when analyzing the influence of condensation conditions on the final structure of “thick” condensates.

1.2. The structure of “thick” condensates

The classification of condensates by their thickness is mostly conventional. Thus, the experimental data presented in [2] show that the notion of critical thickness, which is useful in certain applications and is determined by an abrupt change in a physical characteristic or a structural state of condensate as it becomes thicker, can not be comprehensive, because the influence of scaling factor on various properties of materials is not all-inclusive. The thickness alteration due to variance of different parameters of condensation process is often accompanied by gradual changes in the structure and properties of condensates, which also makes it impossible to draw a strict distinction between “thin” and “thick” films.

Previous section covered the existing ideas concerning the formation of primary condensate film on the substrate plate. Further condensation pro-

cesses occur on a primary film without direct interaction of atoms and/or condensation nuclei with the substrate.

Hereinafter, "thick" condensates are understood as those in which processes of structure formation are associated primarily with the building of their thickness to the required level and with simultaneous secondary processes of structural and/or phase changes, which does not exclude, of course, the possibility of more or less significant influence of the substrate and/or structural features of primary film structure on the structure of "thick" condensates (e.g., on the grain size, internal stresses in the condensate, etc.).

The factors that have the most significant influence on the structure of "thick" condensates include substrate temperature, condensation rate, vacuum rarefaction and esidual gas composition in the condensation chamber, deposited layer thickness, relative orientation of vapor flow and the substrate, chemical composition of the condensate and its interaction with the substrate. The following are some general regularities and specific data concerning the influence of these factors on the condensate structure according to recent researches.

1.2.1. The influence of substrate temperature on the condensate structure

The role of the temperature of the substrate has been thoroughly studied with a focus on the analysis of temperature dependence of characteristics of the grain structure and substructure of condensates, e.g, [2, 3, 5, 30, 31].

At low substrate temperatures ($T_{substrate} < T_1 \approx 1/3\ T_s$) condensates typically demonstrate high density of defects of crystal structure (effective dislocation density can reach 10^{13} cm^{-2}, the concentration of vacancies $–10^{-3}$). The flaw rate of condensates is largely caused by the growth of crystallites from a large number of centers. They can inherit twin boundaries and stacking faults from the stage of nucleation and dislocation walls along the boundaries of coalesced particles − from the stage of coalescence. The increase of $T_{substrate}$ reduces the concentration of all types of defects and induces heterogeneity of their distribution over the thickness of the condensate, because in the process (during) of the increase of the thickness, a more or less complete annealing of defects occurs [2, 3].

Results obtained by Movchan and Demchishin et al are the main ones to be considered in the study of the grain structure, and these results allowed systematizing various experimental data on the shape and size of

crystallites at the substrate temperatures that are most usable for protective coating and thin foil making [4, 32, 33]. Researches of the structure of condensates of several metals (Ti, Ni, Cu, Fe, W) and refractory oxides obtained by electron-beam evaporation allowed the authors to suggest a three-zone model of temperature dependence of the structure of thick condensates with boundary temperatures $T_1 \approx 1/3\ T_s$ and $T_2 \approx (0{,}45\ldots0{,}5)\ T_s$.

The first zone is a low-temperature one (ranging from a temperature below room temperature to T_1) and characterized by domed structure of condensate surface, while in a cross-section it displays conic crystallites expanding in the direction from the substrate towards the condensate surface. Inter-crystallite boundaries are blurred and they are characterized by the presence of micropores (it is obvious that the temperature T_1 in this model is identical to the temperature Q_2 in the works [25, 26]).

The second zone, for which $T_1 < T_{\text{substrate}} < T_2$, is characterized by a smooth matte surface of condensate and a distinct columnar crystallite structure in a cross section. Grain boundaries are clearly identified by metallography while micro-porosity is virtually absent.

In the third, high-temperature, zone ($T_{\text{substrate}} > T_2$) the form of crystallites is virtually equiaxial.

According to [4], the rise of the substrate temperature within each of the three zones causes a gradual increase in characteristic crystallite sizes (diameters of domes on the surface of the condensate, the width of columnar crystals, diameters of equiaxial grains). Temperature dependence of crystallite size D in each zone of condensates of pure metals has the following form

$$D^2 = A\exp\left(-\frac{U}{RT}\right), \tag{1.5}$$

where U is the effective activation energy of the processes that control the formation of crystallites, the value of which for the first zone corresponds to transitions of atoms between two neighboring equilibrium positions on the surface; for the second zone it corresponds to the surface diffusion, and for the third zone – to the volume self-diffusion.

It is suggested that the first zone the domed nuclei are generated, which grow into conical crystallites; in the second zone the processes of "surface" recrystallization occur, and in the third zone the processes of volume recrystallization and grain growth take place.

According to heterogeneous nucleation theory, an increase in mean crystallite size in the film caused by rising temperature may be due to a decrease in the surface density of nuclei [17]. Indeed, the experiment allowed to obtain a clear linear relationship $\ln N$ from $1/T_{substrate}$, where N is the surface density of grains, proportional to the nucleation rate [30]. The temperature dependence of coalescence and recrystallization processes also results in a bigger size of crystallites with increasing $T_{substrate}$.

Based on their own data and literature, the authors [4] have come to the conclusion that the above three-zone model is relevant for thick condensates of pure metals, solid solutions and mono-phase refractory compounds. In addition it is noted that if the condensable material undergoes a polymorphic transformation at a certain temperature $T_{polymorphic\ transformation}$, there is one more substrate temperature $T_{substrate} \approx T_{polymorphic\ transformation}$, the transition of which may lead to significant change in the condensate structure.

The dependence of the structure of the condensate on the substrate temperature can vary greatly under the influence of other parameters of the condensation process and/or the nature of the condensate. Thus, the complication of phase composition of the condensate will have a significant influence on the recrystallization processes by changing to a greater or lesser extent the temperatures T_1 and T_2 (T_1, T_2/T_s), even making the three-zone model inapplicable. In multi-component condensates, already at the stage of their formation, some chemical heterogeneity may occur which may result in respective structural features (see, for example [34]).

Obviously, the three-zone model also does not explain cases of "strong" epitaxy and low-temperature condensation followed by the formation of amorphous or pseudo-amorphous condensates, which are usually considered in connection with making thin films.

We researched a low-temperature condensation on a neutral substrate while studying the effect of alloying on the possibility of obtaining amorphous state in condensates of the system Ti–Al–V [35, 36]. At the substrate temperature –150±5°C thin films were made from pure titanium (BT1-00) and alloys: % mass.[1] Ti–6Al–4V (BT6), Ti–18Al–12V, Ti–36Al–12V. In conventional (bulk) state these materials have a phase-based a structure on the base of α, (α+β), α_2– (~Ti_3Al) and γ-(~TiAl) phases of the Ti–Al system, respectively (Fig. 1.1).

The given film thickness (≤100 nm) allows electron microscopic study of their structure "in transmission" without additional preparation of the objects. Results of the study are shown in Fig. 1.2.

[1] Hereinafter in alloys – % mass.

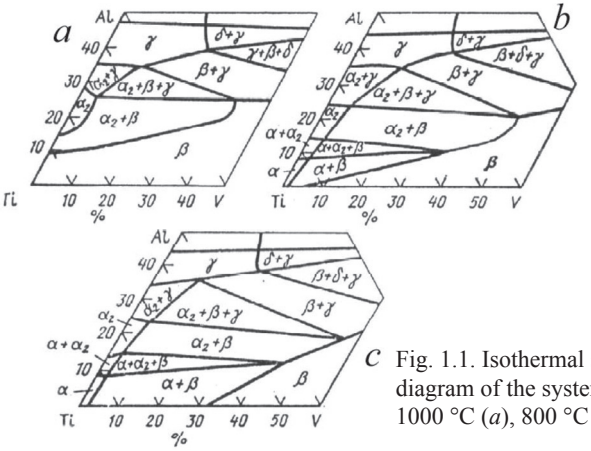

Fig. 1.1. Isothermal sections of the diagram of the system state Ti–Al–V at 1000 °C (*a*), 800 °C (*b*) и 550 °C (*c*) [37]

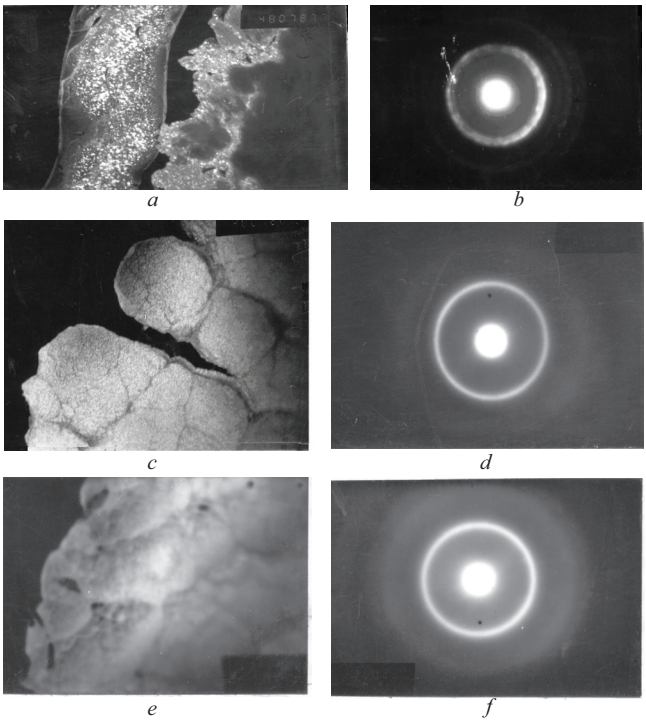

Fig. 1.2. Microstructure of low-temperature condensates ($T_{substrate} \approx -150$ °C) of alloys BT1-00 (*a, b*), Ti–18Al–12V (*c*, *d*) и Ti–36Al–12V (*e, f*): *a, c, e* – dark-field images (× 80000); *b, d, f* – microdiffractions

In all cases considered, the films structure was uniform and did not contain any extended boundaries of structural and/or phase-specific components.

Bright-field images of pure titanium demonstrated a heterogenic contrast; the first diffraction ring "halo" was formed by a cluster of reflexes, while dark-field images obtained in the "light" of "halo" spots revealed the presence of crystallites in the film with crystallites size ~ 1 nm, which indicates its "pseudo-amorphous" state (Fig. 1.2, *a, b*).

In bright-field images of alloy films BT6 and Ti–18Al–12V no fields of heterogeneous contrast are found; in the first "halo" ring no individual reflexes are resolved, but on dark-field images in the "light" of "halo" spots we observed a fine pattern of decay, indicating the existence of ultrafine crystal structure, with crystallite size of not more than 0.5 nm (Fig. 1.2, *c, d*).

The Ti−36Al−12V alloy with the maximum total alloying had absolutely no heterogeneous contrast on images (bright-field and dark-field) and on micro-diffraction pattern (Fig. 1.2, *e, f*) indicating that in this case an amorphous film was obtained.

The presented results confirm the possibility of obtaining both pseudo-amorphous and fully amorphous state by vacuum condensation of metallic materials at sufficiently low temperatures of the substrate; the fixing of amorphous state is facilitated by increasing the content of alloying elements.

In alloys of the Ti−Al−V system the obtaining of amorphous state is not impeded by a rather high reactivity of the components, which is proved by the existence of equilibrium ordered Ti_3Al- and TiAl-based phases. At a low-temperature vacuum condensation even in this case it is possible to obtain a homogeneous solid solution with the total content of Al and V up to ~ 50 %.

Deviation of the phase composition from the equilibrium one is the general feature of the vacuum condensate structure obtained at low temperatures of the substrate. This allows, in particular, to extend significantly the concentration area of homogeneous solid solutions compared with the area shown in equilibrium phase diagrams. So, for example, at condensation of the Fe–Cu alloy vapor onto a non-heated substrate, the copper content in solid solution up to 50 % was reached whereas the equilibrium concentration was ~2 % [38]; in the system Cu–Al up to 11 % of Al was fixed up, which is ~3 % more than the equilibrium content [39], etc. According to available literature data, in vacuum condensates can occur phases not existing on the equilibrium phase diagrams of respective alloying systems (see e.g. [2]).

1.2.2. Textural effects in the structure of vacuum condensates

In the general case the structure of vacuum condensates can be characterized by the presence (or absence) of three types of texture: crystallographic, morphological and substructural one. In the first case it concerns the presence of preferential orientation (or several orientations) of the crystal lattice of condensate grains; in the second case it has to do with the anisotropy of the grains shape and in the third case it refers to preferential orientation of elements of the substructure relative to the substrate and/or the direction of the molecular beam hitting it.

When analyzing the structure of condensates, the substructure texture is typically not considered, but the possibility of its existence is demonstrated, for example, by the significant heterogeneity of microdeformations which is obviously associated with the normal to the substrate surface and the molecular beam direction, and which is observed in thick films obtained under high supercooling conditions [2, 3].

A good example of morphological structure is columnar crystal structure observed in condensates of different metals and alloys, that are typical for the second zone in the structural model of Movchan (see e.g, [4]). The emergence of the morphological texture of condensates is accompanied by crystallographic texture, but no regular link between these two types of textures exists: there is a crystallographic texture in condensates with almost equiaxed polyhedral grains, while for a qualitatively identical morphological texture different crystallographic textures are possible.

The subject of formation of crystallographic and morphological textures of vacuum condensates has been extensively studied, and the main findings are summarized, for example, in the monographs [1, 3, 40].

The analysis of conditions of emergence and transformation of *crystallographic texture* of condensates distinguishes between the texture of nucleation, growth texture and recrystallization texture (as earlier, we do not consider epitaxial growth of condensate).

According to [3], "at a very early stage of condensate formation, at the minimal thickness suitable for registration by microdiffraction or electron diffraction, no texture is present".

The term *nucleation texture* is referred to the thin film texture found in many cases of condensation on amorphous (neutral) substrates even before the formation of a continuous layer, the occurrence of which is associat-

ed with the formation of particles in the insular film. In the cases when the growth of condensate particles is connected with the process of coalescence, and the origin of texture (almost) coincides with the development of the process of coalescence in insular condensates, it is possible to use the term "coalescence texture" [2].

The direction of the axis of the nucleation (coalescence) texture does not depend on the tilt of the molecular beam: the texture axis is always perpendicular to the substrate. If epitaxy is absent, the azimuthal orientation of crystallites is spontaneous. In the case of the oblique incidence of the beam after the formation of a continuous layer, the texture axis in a certain thickness range is retained perpendicular to the substrate. However, if molecular beam is perpendicular to the substrate, then the degree of perfection of the texture augments as the layer thickness increases, which is not the case at oblique incidence. The higher the density of the molecular flow (condensation rate), the lower the degree of the texture perfection. No texture is formed at a low substrate temperature (typically, at $T_{\text{substrate}} < T_1$).

The fact that the nucleation texture is formed as condensate particles grow to a certain size, allowed to assume that the reason for the formation of this texture is the tendency of surface energy minimization causing atoms of the condensate to be placed on the substrate so as to predominantly form a face with a high reticular density. This ensures the positioning of respective crystal plane parallel to the substrate surface in the condensate of "subcritical" thickness. Similarly, during the formation of the coalescence texture the predominant orientation ensures the lowest surface energy of combined particles.

For thick condensates the growth texture and recrystallization texture are most important.

Growth texture is formed after the formation of a continuous layer of condensate in the process of increasing its thickness. As in the case of nucleation texture, the predominant crystallographic orientation of the crystallites in the plane parallel to the substrate surface is absent if no epitaxy takes place. Accordingly, both the texture and its perfection are characterized by the presence and the scattering angle of the preferred orientation of the crystallographic direction of the condensate crystal lattice relative to the normal to the substrate surface and/or the direction of the molecular beam.

According to available information, the type and perfection of growth texture depend on the substrate temperature. From the foregoing general understanding of the structure formation of during condensation, it

follows that the formation of growth textures requires $T_{substrate} > T_1$, i.e. $T_{substrate} > 1/3\ T_s$. As $T_{substrate}$ increased the following change of growth textures was observed: the first one to form is the texture, in which the highest reticular density is parallel to the substrate plane, and at higher temperature less densely packed planes emerge in parallel to the substrate. For example, for silver at $T_{substrate} \approx 420$, 480 and 700 °C we obtained textures (111), (100)+(111) and (100), respectively, were obtained; for gold at 450, 650 and 800 °C – textures (111), (100) and (110), respectively, etc. In addition, the actual values of $T_{substrate}$, that cause the origing of any growth texture, may substantially depend on other parameters of the condensation process [3, 40].

Having analyzed the impact of the substrate temperature on the growth texture type, Dixit [41] obtained the $T_{substrate} = r_a T_s/d$ ratio, is interplane distance for the crystallographic planes parallel to the substrate; r_a is atomic radius. According to this ratio, increasing temperature enables the formation of the orientations corresponding to the planes with gradually decreasing reticular density, whose position is parallel to the substrate. The author's experimental data have matched well the calculated results.

Characteristic features of growth textures include the retention of preferred orientation in a wide range of thickness and increasing texture perfection caused by increasing thickness of condensate, as well as the sensitivity of the direction of the axis of the texture regarding the direction of the molecular beam. At the oblique incidence of the molecular beam both the retention and the deviation of the texture axis from the normal to the substrate were observed. In the latter case the ω angle between the normal to the substrate and the texture axis is typically smaller than the angle between the normal and molecular beam α, but for Zn, Cd, Mg, and Be with hexagonal lattices ω> α [3, 40].

When studying the texture of titanium condensates, it was found that for normal and oblique (α = 0 and 22°) molecular beams at $T_{substrate}$ = 200 °C for texture axis <0001> angle ω = 0 and ~ 30°, respectively [42]. In work [43] there was observed decreasing of inclination angle ω of the <0001> texture axis with increasing $T_{substrate}$, at a simultaneous decrease in the texture sharpness, and at $T_{substrate}$ = 500 °C, ω = 0 was obtained regardless of the incidence angle of the molecular beam. While condensing on a textured steel at $T_{substrate}$ = 200 °C, an epitaxial titanium texture with the angle ~30° of the basal plane (0001) to the substrate surface was obtained, which is

logically associated with the texture of the substrate. But by increasing the thickness of the condensate over 10 ... 15 μm, this texture was replaced by axial texture <0001> with $\omega = 0$ [44].

Systematization of various cases of texture axis orientation at the oblique incidence of the molecular beam as observed by different authors is given in the work [45]. For the texture axis of molybdenum condensate they always have got $\omega < \alpha$, and with increasing substrate temperature, decreasing condensation rate and lower residual gas pressure, researches have observed decreasing angle ω up to $\omega = 0$, which was indicative of the crucial role of the kinetics of growing crystallite faces formation in building up the texture.

According to [3], the formation of growth textures is the result of a competitive process: the crystallites that are favorably oriented relative to the molecular beam outgrow other crystallites that are oriented differently and thus gradually occupy the entire crystallization surface.

Experiments concerning the influence of vacuum rate and atmospherics composition on the type of condensate textures have led to the conclusion that one of the most probable causes of faster growth of specific orientations is a variance in the coefficient of adsorption of gas impurities on different faces of the crystallites, resulting in selective blocking of their growth. In this case the fact that the axes of the texture, as a rule, are low-index directions is explained by a lower adsorption of residual gases on high-density reticular planes.

A certain role in the formation of growth textures may also be played by a mechanism of spiral growth of crystals ensuring their rapid development along the axes of screw dislocations, to which low-index crystallographic directions correspond, as is the case with the axes of growth textures [46]. A significant influence can also be exercised by purely geometric effects of "shadowing" of faces of slowly growing crystals by rapidly growing crystallites.

Recrystallization texture may be result from a volume recrystallization process causing a change of the original structure and texture of the condensate at high substrate temperatures, due to the growth of $T_{substrate}$ during condensation and/or longer process for obtaining a preset film thickness, as well as in case of heat treatment of the condensate. The recrystallization may more or less completely eliminate the condensate texture created at the stage of the film formation.

A special case of recrystallization texture is a texture formed by heating an untextured condensate above a certain temperature. Thus, upon heating

an untextured silver film to 550 °C texture (111) is formed, and at 750 °C along with the (111)-component there is found the (100)-orientation, etc. (see., e.g., [3, 41]).

Morfological texture of condensates, as a rule, is the consequence of the above mechanisms of competitive growth of crystallites leading to creation of growth texture as well: it is the competitive growth that sets the trend of producing anisotropically shaped crystals elongated in the direction of the molecular beam, i.e., a more or less clear columnar structure. However, one may refer to the same type of texture the structure that is formed sometimes by recrystallization of condensates if the grain size becomes equal to the film thickness and, therefore, the grain boundaries get roughly perpendicular to the condensate surface, which may modify its working properties.

1.2.3. Specifics of structure formation in the case of condensation onto a moving substrate

It is obvious that textural effects described in pp.1.2.2 shall (may) result in specific features of the structure of condensates obtained by vapor deposition on a moving substrate. The existence of these specifics is caused by continuously varying angle between the direction of the molecular beam and the surface of the substrate for each specific point, as well as by changing the temperature of condensation surface during the entire time of building up the condensate thickness. More or less explicit manifestation of textural effects depends on specific parameters of the equipment and those of the end product, e.g. the distance from the surface of the melt to the substrate, the size and shape of screens limiting the condensation zone, the required thickness of the condensate, the velocity of movement of the substrate, etc.

While solving the problem of the industrial production of thin foil, we conducted experiments on the influence of angular ratios during vacuum condensation on the structure of a number of metals and alloys (Cu, Ni, Al, Ti, Ti−Al, Ti−V, Ti−Al−V). In our studies we used a substrate ensuring a continuous or discrete tilt of its surface in the range of ±45° from the normal to the axial direction of molecular beam and also a moving substrate with a spatially fixed plane. The temperature of the substrate in these experiments corresponded to the conditions for obtaining columnar crystals in a condensate, thus facilitating the detection and visualization of orientation effects.

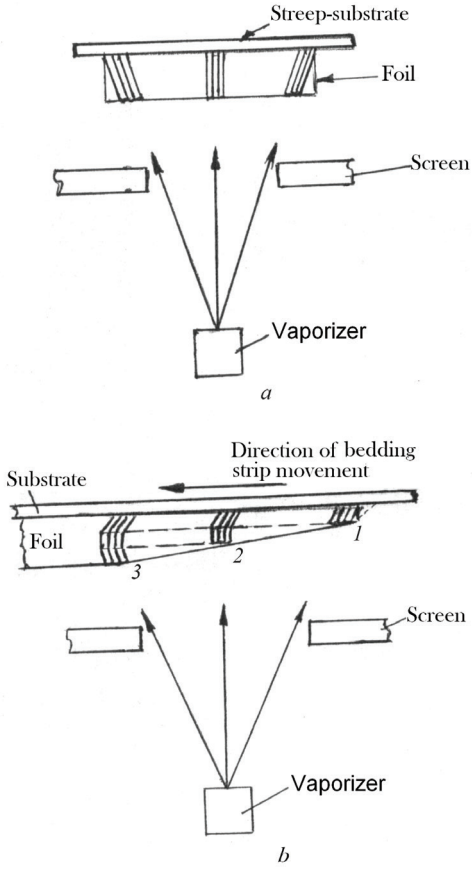

Fig. 1.3. Crystallites growth in the case of vapor deposition on a substrate strip:
a − cross-section of the strip;
b − longitudinal axial section

The figures, explaining the esssence and the origin of discovered structural specifics of the condensates obtained by deposition onto a moving substrate strip, are shown in Fig. 1.3 (cross-sections in the figure are perpendicular to the foil plane).

Fig. 1.3, *a* shows the pattern of columnar structure throughout the foil width, which can be obtained in its transverse (relative to the transporting direction) cross section at a fixed substrate if the vapor source is assumed to be of a point type and the direction of the most rapid growth of crystals (their longitudinal axis) coincides with the vapor flow direction. A similar picture is to be observed also on images (for example, metallographic) and in the case of using a moving substrate, because in this cross-section the tilt of detected boundaries of columnar crystals relative to the foil plane is retained.

Fig. 1.3, *b* illustrates sequential steps of changing the size and shape of crystals in the axial longitudinal section corresponding to the middle of the width of the foil. With increasing thickness of the foilduring the motion of some particular point from the beginning (*1*) to the middle (*2*) and to the end (*3*) of the condensation zone in the apparatus, one should expect sequential tilting of the axis of growing crystals relative to the plane of the foil (the figure shows three discrete stages of such process assuming a point source of vapor and exact alignment of the direction of the fastest growth of crystals with the direction of the vapor flow).

Since the condensation zone length was ~150 mm, the width ~110 mm and the distance from the melt surface to the substrate surface ~210 mm, then according to assumptions for Fig. 1.3 the maximum deflection of the axis of columnar crystals from the normal to the substrate could be ±14.5° in the transverse and ±19.5° in the longitudinal section of the condensate. The latter means that the rotation axis of the columnar crystal during its growth (its stay in the condensation zone of a moving substrate) can reach 39°. The use of rotational substrate allowed to extend the range of variation of geometric conditions, and also facilitated the simulation experiments aimed at assessing the effect of the substrate temperature and other factors on the structure formation process during condensation.

Our experiments confirmed that possible variants of columnar structures shown in Fig. 1.3 are actually formed in real condensates of all metals and alloys studied.

For the condensate from 2B alloy (Ti−2Al−1.5V) obtained on a moving substrate at $T_{substrate}$ = 600 °C this fact is illustrated in Fig. 1.4. In this case the entire thickness of the condensate film (~100 μm) depending on the specimen cutting spot and the orientation of its cross-section plane, longitudinal or transverse relative to the direction of the movement, was occupied by rectilinear columnar crystals that are perpendicular or inclined to the substrate plane (Fig. 1.4, *a*, *c*) or curved "falciform-shaped" crystals (Fig. 1.4, *b*).

Specific values of the angles of deviation of the axis of columnar crystals from the normal to the substrate depend both on geometrical (position of the spot on the substrate, the distance from the vapor source to the substrate) and technological factors. For instance, the crescent shape of crystals depends on the velocity of the substrate movement: as this velocity increases while other parameters of the process remain constant, this shape is smoothed due to reduced time allowed for the crystals reorientation. A similar effect is caused by increasing temperature of the substrate: higher mobility of the condensate atoms loosens the dependence between the direction of the crystals growth and the direction of the molecular beam (also reducing the efficiency of shielding of the vapor flow by growing crystals). It is also clear that in the general case of condensation onto a moving substrate, the direction of longitudinal axis of elongated crystals shall be represented in the form of a three-dimensional curve resulting from the combination of the "flat" falciform shape of crystals in the axial longitudinal section of the condensate and the tilt of the axis of peripheral crystals.

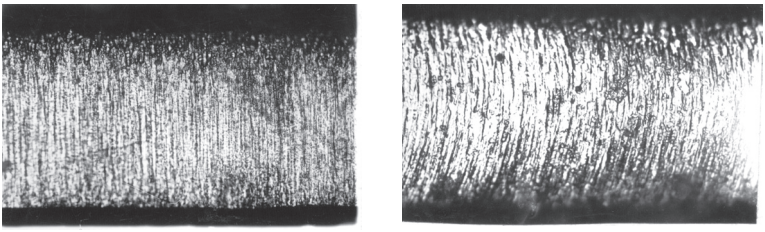

a *b*

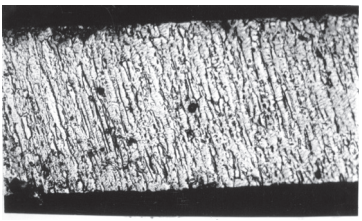

c

Fig. 1.4. Microstructure of the alloy condensate Ti–2Al–1.5V at $T_{substrate} \approx 600$ °C in cross sections perpendicular to the plane of the foil (×400): *a* – mid-width of the foil, transverse to the direction of the substrate movement; *b* – mid-width of the foil, along the direction of the substrate movement; *c* – edge of the foil, transverse to the direction of the strip movement

In the case of columnar crystallization the morphological texture is associated with crystallographic texture (longitudinal axis of the crystal approximately matches the crystallographic direction of the crystal lattice of the condensate). Therefore, the presence of a range of deviation angles of the crystal axes from the normal to the plane of the substrate should correspond to the presence of equivalent scattering of the crystallographic texture in the condensate and the possibility of a non-identical crystallographic texture in different areas of the thin foil depending, among others, on the width and on the conditions of vapor flow formation.

1.2.4. The influence of vacuum rarefaction, residual gas composition, condensation rate and the deposited layer thickness on condensate structure

Researches conducted at the initial stage of our work have shown that the influence of each factor, listed in the heading of this section, on the structure and, consequently, on the structure-dependent properties of vacuum condensates can be quite significant (see, for example, [9, 17, 47, 48]). Forecasting not only the magnitude but, sometimes, even the character of the influence (positive or negative) of these factors on the structure (properties) of condensates in general is difficult both due to variety of condensates and requirements and due to the dependence of the effect of varying

one factor from the absolute values of other parameters of the condensate production process. At the same time, the available information allows formulating a number of general statements and trends that can be used to solve specific practical tasks.

Vacuum rate and residual gas composition. Interaction of evaporated substance with residual gases may occur in the way of vapor flow from the surface of the melt to the substrate, on the surface of the condensate and inside it. High vacuum typically means the vacuum rate at which the interaction of vapor–gas on the way from the source to the substrate is negligible. In this case the role of residual gases is determined by their influence on:

− the formation of condensate nuclei: a poor vacuum results in a more or less abrupt decrease in size of the primary grains of the condensate;

− the formation of condensate texture (crystallographic, morphological), in particular – affecting the appearance of columnar crystallites; according to [3], the most influential factor modifying the change of textures is oxygen followed by hydrogen and nitrogen;

− the hardening of solid solutions, obtained by condensation, by interstitial impurities with a corresponding increase in strength properties and reduction in plasticity (these effects may be particularly significant for metals with body-centered cubic lattice);

− the formation of oxides along grain boundaries of the condensate, which, in particular, impedes grain growth and recrystallization processes;

− the occurrence of grain boundary porosity in the condensate: a lower vacuum causes higher porosity (e.g., the key role of oxygen in creating porosity in titanium condensates has been demonstrated in [49]).

Obviously, when assessing a possible influence of the composition of residual atmosphere on structure formation processes and phase composition of condensates, it is also necessary to take into account available information on the effect of oxygen, nitrogen, hydrogen and also carbon, which may be contained in the atmosphere when using diffusion pumps, on the structure and properties of solid metals. For example, chromium condensates may be greatly influenced not only by oxygen but also nitrogen (nitride formations) for condensates of titanium – by hydrogen, etc.

The progress of secondary processes of structural and phase changes associated with the influence of residual atmosphere on the primary structure of the condensate (recrystallization, dispersion hardening, evolution of porosity, etc.) − all these certainly depend on the substrate temperature and/or thermal treatment of the condensate.

Condensation rate. An increasing condensation rate results in higher concentration of adsorbed atoms and, consequently, to greater supersaturation on the surface of the substrate (condensate). Qualitatively, a similar effect of supersaturation can be obtained at a constant condensation rate by lowering the temperature of the substrate. Accordingly, the effects of changes (up or down) in condensation rate and substrate temperature when forming the condensate structure may be opposite.

Literature data prove this conclusion, but only for a limited range of condensation rates. For example, in the case of nickel films ~70 nm thick it has been demonstrated that decreasing condensation rate from 30 to 0.1 nm/s leads to grain size growth [30], i.e. to the effect otherwise obtainable by increasing $T_{substrate}$. However, this is not the case for lower and higher condensation rates.

Lower rates resulted in smaller grain size with decreasing condensation rate, which was explained by a growing influence of impurities on the growth of condensation nuclei. Higher condensation rates resulted in bigger grains, that was attributed to a higher temperature of the substrate during evaporation processes at higher condensation rates.

An increase in actual temperatures of both the condensate surface and volume at higher condensation rates, that are necessary for efficient processing of thin foil production, is one of the major factors determining the structure and related properties of the end product. Specific results of this effect depend primarily on the energy of the molecular beam hitting the substrate, heat removal conditions, nominal relative temperature $T_{substrate}/T_s$ (which affects, in particular, the progress of recrystallization processes) and the condensate nature, which determines the possibility of phase transformations and related structural changes in the condensate at higher temperature of the process.

In studying titanium coatings BT1-00 in the range of condensation rates 0.003 ... 0.2 μm/s it was found out that up to 0.01 μm/s the condensate structure remains virtually unchanged, while its further increase causes a bigger transverse size of columnar grains being most likely associated with a higher condensate temperature. Condensates obtained at $T_{substrate}$ = 400 ... 550 °C and rates 0.003 ... 0.02 μm/s have a porosity along grain boundaries, while increasing condensation rate up to 0.03 ... 0.07 μm/s allowed to eliminate porosity starting from $T_{substrate}$ > 530 °C [43]. Higher film density caused by higher condensation rate was observed in case of other condensates as well (see, e.g. [18, 50]).

In [32] it is shown that at a high condensation rate (0.1 ... 0.3 μm/s), a decrease in oxygen content in condensates of titanium and a number of other materials compared to its amount in the initial ingot takes place (from 0.07 to 0.03 %), demonstrating a possible getter and protective action of the intense vapor flow resulting in a reduced partial pressure of gases in central zones of the molecular beam.

Condensate thickness. Significant influence of thickness on the structure and various properties of condensates are observed, primarily, for small thicknesses (in the range of fractions of a micrometer) and/or low temperatures of the substrate, when, on the one hand, the role of condensate interaction with the substrate is great, and, on the other hand, heat-activated relaxation processes are slowed down (see, e.g. [2]).

The effect of changing thickness on the structure and structural-sensitive properties of "thick" condensates at $T_{\text{substrate}} > 1/3\ T_s$ often can be reasonably regarded as indirect resulting, in particular, from the different time of the temperature influence on primary structure of the condensate, thus determining the final grain structure thereof. At the same time, the absolute film thickness determines such an important structural feature as the extreme diameter condensate grains, because when grain boundaries emerge on the surface of the condensate, the grains are likely to cease growing in size in the foil plane.

The ratio of thickness to grain size and shape anisotropy of the condensate may be important. This ratio influences, in particular, such important characteristics crucial for specific applications, as gas permeability of the foil and the anisotropy of its mechanical properties.

1.3. Main requirements to the development of foil production process by vacuum deposition

From a brief review of the existing information on the characteristics and results of processes of vacuum condensation of molecular beams onto a solid substrate, given in pp. 1.1 and 1.2, it follows that by using the method of vacuum condensation on the surface of the substrate it is possible to obtain films of various metallic and nonmetallic materials in quite a wide range of thicknesses (from nanometrical to ~100 μm and more). Moreover, the structure, texture, phase composition and other characteristics of these films are determined and can be adjusted by varying the parameters of applied production process. The variety of materials and characteristics of resulting films provides a rather wide range of possible applications of vacuum condensates.

For “thick” vacuum condensates in all the variety of their applications two main fields reserve special attention. The first and arguably foremost one is to produce coatings on various products including safety items (e.g, heat-resistant and erosion-resistant coatings on blades of turbines and compressors in aviation industry), decorative or any other special applications. The second field is the production of thin foils.

The main and in many respects fundamental difference between these two fields is that coatings must have, as a basic requirement, a strong bond of the condensate with the substrate, whereas for the foil an opposite and equally important requirement holds, that is an easy separation of the condensate from the substrate.

In addition to respective specific requirements to the prosessing technologies, this also means that the production of coatings and foils needs substantially different conditions of the condensate interaction with the substrate, that define, in particular, the conditions of the origination and growth of condensate nuclei, heat removal during condensation, the level of residual stresses in the end product etc.

The second difference is that given a qualitative identity of the requirements concerning equal-thickness of the condensate, coatings are applied usually to objects of complex (not flat) shape and limited in size, which may be done using more or less sophisticated, but cyclic movements of coated objects in a vacuum chamber. On the contrary, industrial manufacturing of thin foil requires a foil coil as the final product, therefore only unidirectional plane-parallel movement of the substrate can be applied.

Moreover, there are also noteworthy differences in the criteria used to choose the condensate material and to determine the feasibility of using the vacuum deposition technique for coatings and foil production. The coating material is selected aiming mainly on obtaining the maximum level of one of applied properties of the coated product (scaling resistance, appearance, etc.), while other applicable properties are ensured by the “substrate” which, in general, creates favorable conditions for choosing the right material and making the coatings applications cost-effective. Unlike coatings, the foil, made by vacuum deposition, should have full spectrum of working properties. Furthermore, it has to be either competitive compared to a thin foil of analogous chemical composition and/or application made by traditional deformation and heat treatment techniques, or have unique properties inherent in the nature of vacuum condensates and impossible to achieve by deformational thinning of massive billets.

We would like to list briefly the specifics of thin foil obtained by vacuum deposition, as well as the requirements to production processes and the criteria for selecting the material (chemical composition, product range), which can provide the feasibility of using vacuum deposition process for industrial production of thin foil.

Specific structural features of thin metal foils, made by vacuum deposition, compared to the foil produced by volumetric plastic deformation define both the possibility (expediency) and limitations of using this technique for practical applications of foil materials. Such features include:

− actual possibility of obtaining, throughout the volume of the condensate, an axial texture with the axis being approximately perpendicular to the surface of the foil thus providing an isotropy of mechanical properties in the plane of the foil, while crystallographic and morphological textures, as well as oriented location of phase components of multiphase alloys and extraneous impurities, resulting from deformation (and especially – from cold rolling), are likely to create a significant anisotropy of foil properties along and across the rolling direction (apparently, existing possibilities of reducing anisotropy by transverse-longitudinal rolling are not of practical importance for industrial foil production);

− fundamental possibility of positioning along the normal to the foil surface of the crystallographic direction (axis of axial texture of the condensate) which is not typical for textures of rolled foil, which may cause a regular divergence of the properties of vacuum condensate from those of volumetrically deformed material of the same chemical composition (examples of this type include condensates of titanium as well as titanium-based α- and pseudo α- alloys with axial texture <0001>);

− feasibility of obtaining a fine-grained structure directly in the condensate, whereas additional heat treatment is required after cold deformation in order to form a grain structure;

− possibility of forming, in a sufficiently wide range of parameters of condensation process, a columnar grain structure with crystallites, elongated in the direction normal to the surface of the foil, which is not possible in the foil made by deformation and heat treatment;

− higher condensate porosity adjustable (within certain limits) by varying the process parameters, which is not the case with rolled material;

− possibility of a specific defect in the condensate, i.e. more or less large crystallized drops, mainly caused by spraying molten metal by the impact of gases contained in the pores of initial billet or in the pores of

the wire put into the molten metal (reducing the probability of this defect requires appropriate technological solutions);

− in the general case, a more developed and less smooth surface of the foil produced by vacuum deposition, which is due, firstly, to the formation of this surface by numerous condensate grain boundaries at reaching it, and secondly − by a number of factors ensuring preferential growth in a direction close to the direction of the vapor flow just for some of near-surface grains.

The production process must ensure:

− production of a thin foil with thickness variations as well as the structure and its derivative structure-sensitive properties in the longitudinal and transverse directions within specified tolerances, which, in particular, requires certain conditions concerning the type, number, and location of crucibles with vaporized material and vaporizers relative to the substrate;

− possibility of separating the foil from the substrate intact, which can be achieved by choosing an effective antiadhesive agent and the substrate material matching an appropriate chemical composition and temperature conditions for producing the required condensate;

− sufficiently high output and cost-effectiveness of the process, which is crucial for competitive production and which, in particular, requires:

a) continuous (semi-continuous) process, i.e. using condensation onto a moving substrate and eventually obtaining a final or intermediate product in the form of a coil of material having a high enough level of ductility and strength;

b) using molecular beams (evaporation) of high intensity and, therefore, big (for alloys with elevated melting temperature) thermal load onto the substrate material, the loud varying as the condensate thickness grows;

c) reusability of the substrate and, preferably, of antiadhesive agent;

− obtaining a predetermined chemical composition and sufficiently uniform distribution of alloying elements of multi-component alloys through the condensate volume, which can be achieved either by continuous feeding of molten metal pool with vaporized material in the form of ingot or wire of the same composition, or by evaporation of separate alloy components from independent sources. It should be noted that for the alloys with substantially different partial pressures of components the latter variant is considered as the only one feasible [4, 51].

In view of the above-stated, *the criteria for the choice of material and product mix* when using vacuum deposition process for manufacturing a thin foil can include the following:

− difficulties in obtaining a thin foil by cold rolling due to specific physical and mechanical properties of the material of required chemical composition, which to a greater or lesser extent increase as the final foil thickness decreases and in case of the necessity of intermediate annealing to remove work-hardening and improve foil ductility;

− technical complexity (impossibility) of obtaining a thin foil by cold rolling using standard rolling equipment, which becomes even more difficult in case of decreasing the required thickness and increasing a preset width of the foil;

− need to improve certain properties of the foil due to the specifics of the process of vacuum deposition (for example, reducing the anisotropy of mechanical properties in the plane of the foil by changing the type of texture, increasing the sorption capacity of the foil due to a more extended surface compared to analogous foil made by cold rolling, etc.);

− need to obtain the properties of the foil caused by the specifics of the vacuum deposition process that are incompatible with the specifics of the processes of deformation thinning of bulk materials (for example, regulated through porosity of the foil);

− actual (considering technical and economic factors) possibility of selecting the substrate material and antiadhesive agent for their repeated use under conditions of condensation onto a moving substrate strip at process parameters that provide desired physical, mechanical and dimensional characteristics of the end product;

– desirability of minimal alloying and, if possible, avoidance of alloying with elements whose partial pressure is significantly different from that of the base metal, in order not to use separate evaporation of components and to prevent corresponding complications of the production process to obtain the needed chemical composition of the condensate.

Our academic and applied researches combined with available literature data have revealed that most of the listed criteria for selection of material and product range for expedient implementation of thin foil production by vacuum condensation onto a moving substrate are matched by titanium and titanium-based alloys with moderate alloying (α- and pseudo α- alloys), if the foil thickness is less than 30 μm and its width is more than 150 ... 200 mm. Some findings of these researches illustrating the influence of the main factors of the process on the properties of condensates of titanium and its alloys are shown below (see Chapter 7).

Chapter 2. DEVELOPING A SPECIALIZED EQUIPMENT COMPLEX AND MASTERING THE FOIL PRODUCTION PROSESS

In this country, first attempts of making an apparatus for manufacturing metal foil through vapor condensation onto a substrate date to the 1960s [52].

In 1973, the «Giprotsvetmetobrabotka» Institute together with the Vacuum Coating Special Design Bureau (СКБ ВП), Riga, and the Technological Design Institute of Food Industpy (ОТИПП), Odessa, conducted exploratory researches on the production of pure copper foil and started to build a laboratory drum-type plant УВ55Ма for producing specimens of coiled copper foil.

Literature on this topic included several patents, which did not reveal any details of the respective design and process [53−57]. In addition, there was information [58] on a laboratory plant for making specimens of foil through vapor condensation on a substrate 203 × 760 mm. The variants described in these patents can be divided into two groups for convenience sake. These are, firstly, the plants with a flexible substrate [53−55] made of metal or polymer, and, secondly, the plants where metal is deposited onto a rigid substrate shaped as a cooled drum [56, 57]. The patent [59] suggests vapor deposition directly onto the drum surface or onto a flexible band moving along the surface of the cooled drum.

The development of new techniques is still going on. Over the past two decades, several patents have been registered in various countries, for example, [60−63].

The advantages of plants applying condensate onto a flexible substrate are as follows:

− a relative ease of transportation in vacuum and the optional output of the foil along with the substrate via linking devices;

− possibility to pass the substrate sequentially over a large number of evaporative devices to achieve high output in one plant;

− a relative ease of foil separation from the substrate outside the vacuum chamber, in the open air.

The disadvantages of this foil production method include:

− difficulties with cooling the substrate during the condensation of metal vapors;

− difficulties with obtaining desirable substrate surface finish and cleanliness.

When using a cooled (or thermally stabilized) hard drum as the substrate, it is quite easy to achieve a high class of surface finish and heat removal from the condensation surface. However, the condensation area is limited, thereby reducing the output of the plant. In our opinion, the design of the plant where vapor is condensed directly onto the surface of the drum, has two crucial disadvantages preventing it from being recommended as a base model, such as accumulation of defects on the drum surface and difficult separation of the condensate from the substrate in the vacuum deposition process.

Therefore, the preferred option is vapor deposition onto the substrate strip surface moving over the vaporizer followed by separation of the condensate from the substrate outside the vacuum chamber.

2.1. Development of УВФ -75-1, УВФ -78-1 plants and a foil heat treatment plant

In 1974−1975, together with the S.A. Vekshinsky Research Institute, we built a specialized laboratory plant УВФ-75-1 for producing the specimen foil coils of 100 mm wide. This plant was a trendsetter in national production of foil strip from titanium alloys. The layout and general view of the plant are shown in Fig. 2.1 and Fig.2.2.

The alloy was evaporated from a copper water-cooled crucible (*1*) 90 mm in diameter by using electron beam gun (*3*) with the beam rotation 270°. The highest power of the gun was 20 kw. The vacuum rate

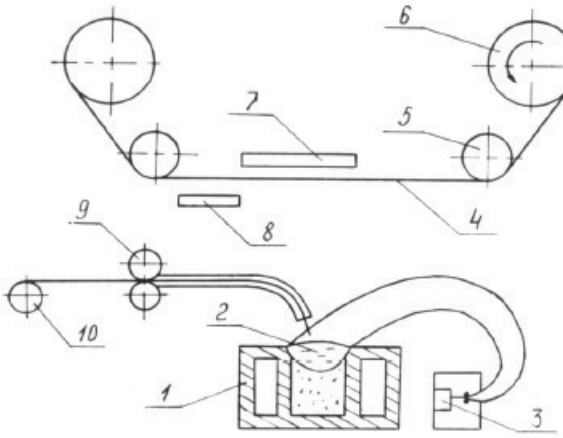

Fig. 2.1. Layout of plant УВФ-75-1:
1 − water-cooled copper crucible; *2* − evaporated metal; *3* − electron-beam gun; *4* – strip substrate; *5* – guide rollers; *6* − water-cooled roller; *7* – substrate heater; *8* −antiadhesive vaporizer; *9* − wire feeder; *10* − coil of wire made from evaporated material

in the evaporation chamber due to an additional cryogenic pump was $2 \cdot 10^{-5}$ ... $5 \cdot 10^{-6}$ mm Hg ($2{,}67 \cdot 10^{-3} \ldots 6{,}67 \cdot 10^{-4}$ Pa). While the alloy was taken from the crucible, the molten metal pool was continuously fed with a wire at the rate equal to the alloy evaporation rate. Metal vapor was condensed onto substrate strip (*4*) 0.2 mm thick, up to 100 mm wide and up to 10 m long, moving over the vaporizer.

After degreasing, the substrate strip was annealed in vacuum with resistive heater (*7*), and then, without depressurizing the vacuum chamber, the antiadhesive vapor from resistive vaporizer (*8*) and the alloy vapor were successively deposited during back-rewinding of the strip. The substrate temperature was altered with resistive heater (*7*) to control the alloy deposition conditions.

Having completed the process, the vacuum chamber was depressurized and the foil was separated from the substrate out of the vacuum chamber.

УВФ-78-1 plant is based on the pumping system and vacuum chamber of a vacuum sputtering/ionic-plasma deposition plant УВН-72-П1 and its design is the same as that of УВФ-75-1 plant except for the ingot feeder of the molten metal pool (УВФ-75-1 feeds the molten metal pool with wire). General view of the plant is shown in Fig. 2.3.

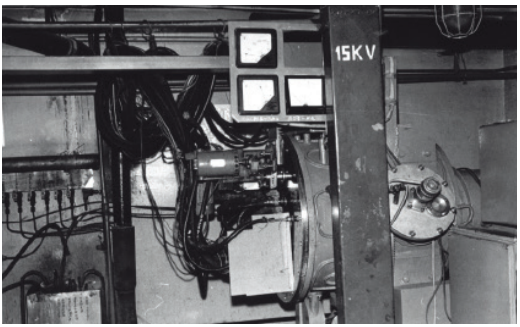

Fig. 2.2. General view of the plant УВФ-75-1

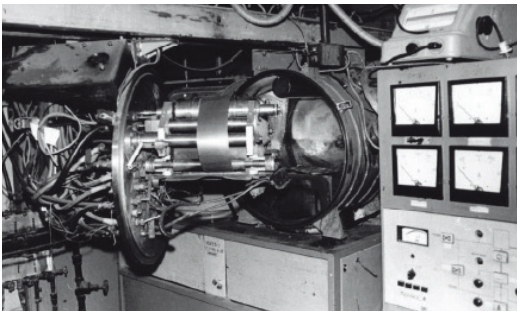

Fig. 2.3. General view of the plant УВФ-78-1

To carry out heat treatment of foil in vacuum we have modernized vacuum sputtering plant УВН-71-П3. Two axially mounted cylindrical heaters of molybdenum wire were installed inside the vacuum chamber to place coiled foil specimens between them. In addition, a system of molybdenum screens which prevents from overheating the walls

of the vacuum chamber, an additional cryogenic pump cooled with liquid nitrogen, and thermocouple for temperature control were installed.

Working vacuum of $1 \cdot 10^{-5}$ Hg ($1.33 \cdot 10^{-3}$ Pa), the maximum temperature of the foil heating − 950 °C, the maximum length of the annealed foil coils is 20 m.

General view of the installation is shown in Fig. 2.4.

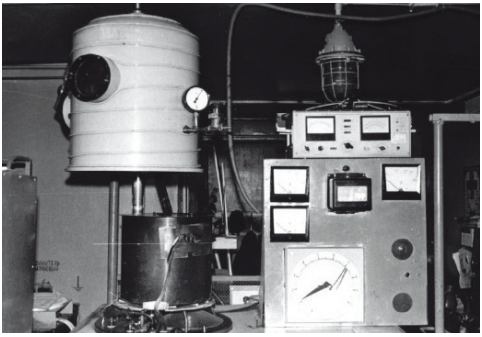

Fig. 2.4. General view of the foil heat treatment plant

Plants УВФ-75-1 and УВФ-78-1 were used as a research tool and as production equipment for manufacturing batches of foil 100 mm wide on a customer demand.

2.2. Development of the first national pilot plant УВ68Л for foil production by vacuum deposition

Batch-operated plant УВ68Л designed to manufacture foil from hard-to-deform alloys 5... 20 μm thick, 400 mm wide, through vacuum deposition. Development of the УВ68Л plant began in 1974 by VILS together with SKB of Vacuum Coatings (currently − Sidrabe company) in Riga under the supervision of E.V. Yadin, PhD, and the E.O. Paton Institute, Kyiv, in accordance with the technical design specification based on the research results presented in this book [64−67].

The foil manufacturing process involves sequential deposition of anti-adhesive and alloy vapors onto a substrate, coiling the substrate together with the condensed material, the plant depressurization followed by separation of the foil from the substrate by peeling it off while uncoiling the substrate strip [65].

A specific design feature of УВ68Л is the absence of any contact between the substrate surface facing the vaporizer and the intermediate rollers along the entire length of the substrate strip.

The layout of the plant is shown in Fig. 2.5, and its general view is given in Fig. 2.6.

The substrate strip made from rolled polished stainless steel is loaded into unwinding camera (*3*) (see Fig. 2.5), and inserted into a recoiler. Dur-

ing the process cycle, the substrate is rewound from the uncoiler shaft onto recoiling shaft (*17*) through all vacuum chambers. Operating pressure in the chambers was $5 \cdot 10^{-3}$ Pa. Evaporation chambers (*4*), (*5*) and (*6*) have compartments for electron beam guns to heat the strip and electron-beam evaporation guns (*7*) and (*8*).

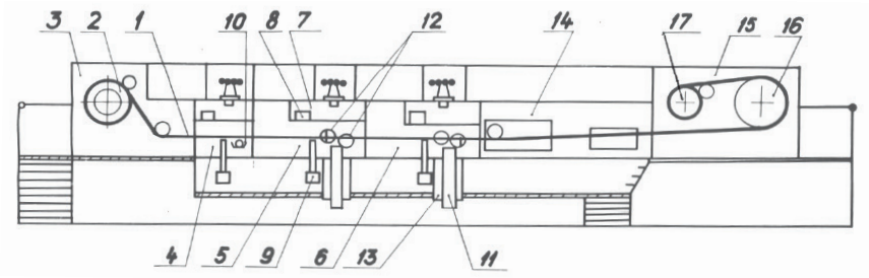

Fig. 2.5. Layout of УВ68Л installation:
1 – substrate; *2* − uncoiler; *3* – unwinding chamber; *4* – antiadhesive evaporation chamber; *5* – alloy evaporation chamber (AEC-1); *6* – alloy evaporation chamber (AEC-2); *7* − compartment of electron-beam heating device; *8* – electron-beam heating; *9* – substrate temperature monitoring; *10* – antiadhesive vaporizer; *11* – vaporized ingot; *12* – electron-beam vaporizer device; *13* – water-cooled crucible; *14* – intermediate chamber; *15* – winding chamber; *16* – cooled drum; *17* – coiler

A layer of magnesium fluoride 0.5 μm thick is put onto the substrate inside the antiadhesive chamber. The evaporation source is the resistive vaporizer made of a 25×1 mm molybdenum tube heated by direct current.

Magnesium fluoride in the form of sintered pellets is loaded into tubular evaporating element (EE) to get ready for operation. Evaporation occurs at the EE temperature of 1400...1460 °C; EE is positioned horizontally across the direction of the movement and has a number of lunules facing the substrate. The plant has two successively placed titanium alloy deposition chambers.

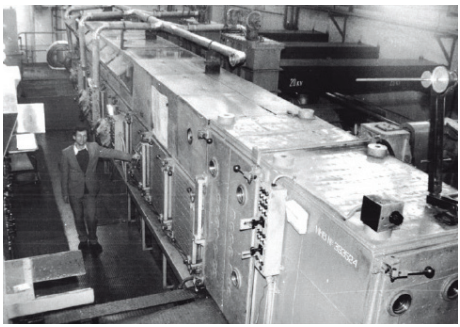

Fig. 2.6. General view of УВ68Л

Each titanium alloy evaporation device consists of two electron beam guns (EBG) (*12*) (see Fig. 2.5) up to 100 kw and

acceleration voltage of 18 ... 20 kV, with a band-type cathode and two crucibles (*13*). Evaporation in each chamber is effected from two water-cooled copper crucibles, 100 mm in diameter, located across the width of the substrate. Each crucible is fed with an ingot of the evaporated alloy. To ensure the required chemical composition, the ingot is continuously fed into the crucible for maintaining a constant level of molten metal pool. Both electron beam guns are located in the one compartment inside evaporation chamber.

After deposition of the second layer of metal (alloy), the substrate passes through intermediate cooling chamber (*14*) and winding chamber (*15*), where it is cooled on drum (*16*) before being coiled onto coiler (*17*).

The plant has twelve manually opened doors for servicing it prior to operation.

Observation windows, dustless viewport devices, temperature sensors after heaters and vaporizers are used to monitor the production process.

A reversible rewinder is used. It is possible to center the substrate when rewinding and aligning the foil coil ends on the uncoiler and the coiler. The rewinder has a multi-motor, automated drive. The coil is tightened by a pneumatic drive with a pressure roller.

Due to unilateral arrangement of the electron beam guns relative to the substrate, the electron beam enters the crucibles at a different angle. This is why,

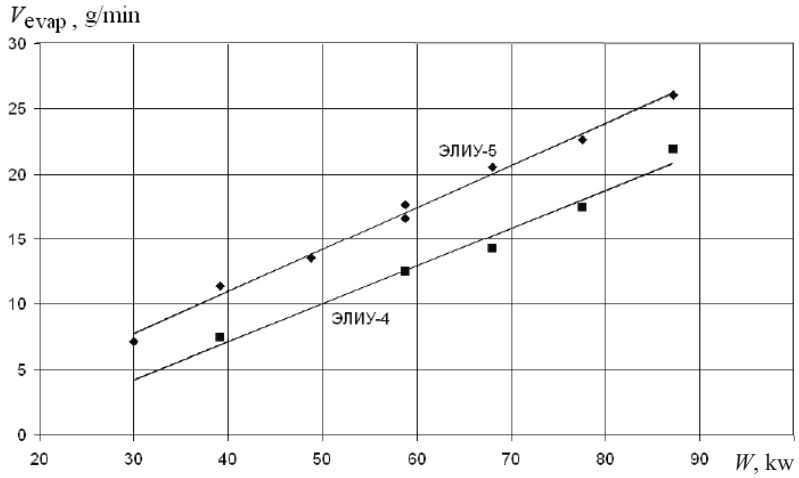

Fig. 2.7. The correlation between titanium evaporation rate from the power of electron beam gun No. 4 and No. 5 in УВ68Л plant

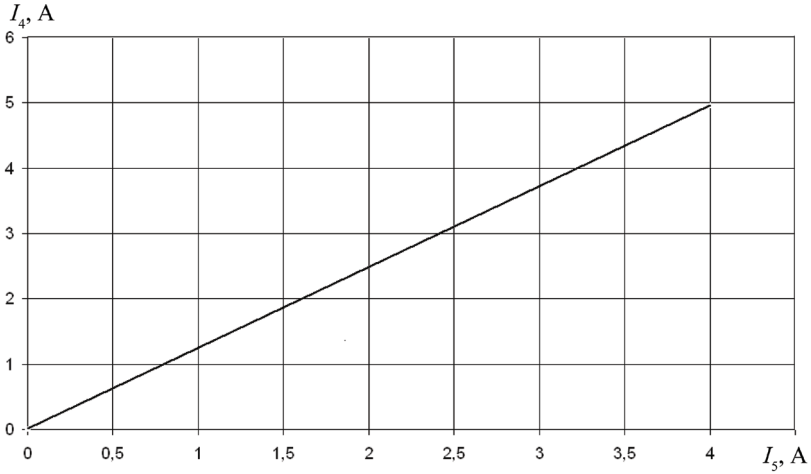

Fig. 2.8. The ratio of the electron beam currents
in EBGs No. 4 and No. 5 equalizing their evaporation rate

given the same input power, the metal evaporation rate from the crucibles is different depending on their distance from the guns (i.e. closer or farther).

Fig. 2.7 shows the correlation between the evaporation rate and the input power for the near and distant crucible.

The desired equal evaporation rate on both crucibles, according to the data presented in Fig. 2.8, is based on the corresponding power ratio of the electron beam guns.

Vapor utilization factor was determined as the tangent of the gradient of the correlation between condensation and evaporation rate.

For УВ68Л , vapor utilization factor is 40 %.

The study of the energy balance of vaporizer found out that vaporizer efficiency increases along with higher power of electron beam gun. At the power of 70 ... 90 kw, the percentage of the energy used for evaporation is 8...11 % corresponding to global standards for similar systems.

УВ68Л was initially developed as experimental one, but due to thorough improvement of its design including its main parts, it was successfully operated, since 1981, for a trial production as well.

Having developed the УВ68Л project, we learned about foil manufacturing plant made by AJRCO TEMESCAL [68].

This plant operated as follows: A polished substrate 0.8 mm thick and 300 mm wide was covered with Antiadhesive layer in a vacuum chamber,

then the substrate is heated by an electron beam and further on passes over the vaporizer, which is a water-cooled copper crucible fed from the bottom with alloy ingot.

The ingot surface in the crucible is heated with a 80 kw electron beam gun. Two vaporizers are placed across the substrate The foil is separated from the substrate outside the vacuum chamber. Reportedly, after a while, this plant was disassembled due to unreliable operation of its electron beam guns and low productivity.

We believe that the attempt of AJRCO TEMESCAL to use vacuum deposition process to produce the foil types that were already manufactured by rolling was not quite reasonable.

In 1983, УВ68Л began to make ultra-thin (5...15 μm) foil 400 mm wide from alloy ВТ6 with preset through porosity. Manufacturing such a foil by rolling was impossible.

2.3. Development of high-capacity plant УВФ-2,0 for making foil from hard-to-deform alloys and auxiliary facilities. Launching foil production process

The increasing industry demand for ultra-thin foil prompted the development of a high-capacity plant and a set of auxiliary equipment to boost output and launch the production of new foil types.

The successful experience of development and operation of the first domestic plant УВ68Л for the manufacture of the foil by vacuum deposition allowed to design high-efficiency unit УВФ-2.0 [69].

Analysis of the УВ68Л operation has demonstrated that its efficiency is mainly limited by insufficiently effective heat removal from the substrate in the alloy condensation zone.

Increasing input power applied to the crucibles causes overheating and severe warping of the substrate. In addition, the location of electron beam guns at the rear wall of the vacuum chamber of УВ68Л and, therefore, the resulting significant difference in the distance from the guns to the crucibles caused different metal evaporation rates in the crucibles at the same input power.

Since there is no electromagnetic deflection system in the evaporation chamber, it causes electron beam to enter the crucible at a small angle, thus also reducing the efficiency of evaporation device and the plant productivity.

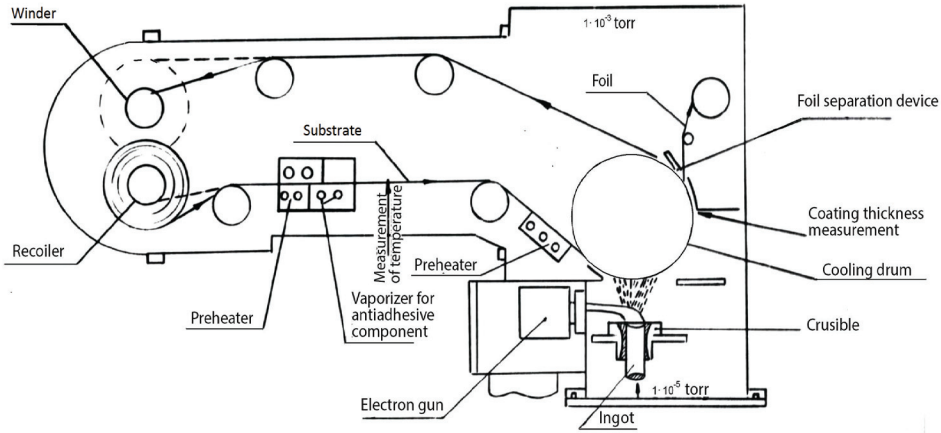

Fig 2.9 Layout of УВФ-2.0 process unit

These factors were taken into account while designing УВФ-2.0 plant the layout of which is shown in Fig. 2.9, and its general view − in Fig. 2.10.

According to this process, the alloy ingot is fed from the bottom into a water-cooled copper crucible. The ingot surface is heated by an electron beam gun. The alloy vapor is deposited as a coating onto the substrate surface moving over the vaporizer and then this coating is separated off the substrate as finished foil.

To ensure separation of the foil, the surface of the heated substrate is pre-coated with a layer of magnesium fluoride used as Antiadhesive, a release agent.

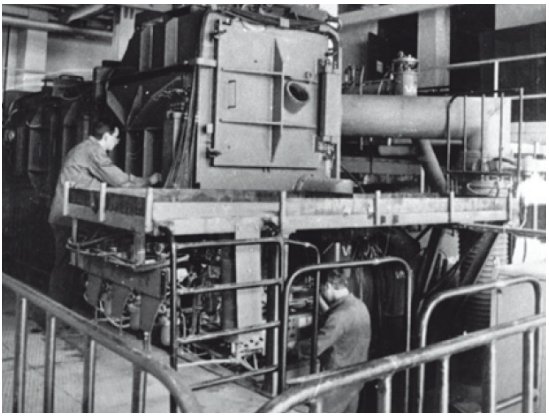

Fig. 2.10. General view of УВФ-2,0

The plant output was increased primarily by increasing heat removal from the substrate in the alloy condensation zone. This was achieved by placing the water-cooled drum, around which the substrate moves, over the condensation zone. Due to insignificant contact heat removal in vacuum,

a neutral gas pressure of 3...7 mm Hg ($4 \cdot 10^2$...$9.3 \cdot 10^2$ Pa) is built up between the substrate and the drum.

To prevent the neutral gas penetration into the alloy vaporization chamber, shutter devices separating the evaporation chamber and rewinding chamber are used.

The winder is placed directly over the uncoiler, thus allowing to reduce the full length of the vacuum chamber and the plant itself, plus significantly increase the angle of coverage of the water-cooled drum by the substrate.

Two electron beam guns 100 kw each are placed in the compartment of the alloy evaporation chamber, opposite the respective crucible. The electromagnetic deflection system located inside the alloy evaporation chamber significantly increases the angle at which the electron beam enters the crucible. It also helped increase the plant capacity.

The 0.2...0.3 mm thick substrate is heated with straight-duct molybdenum tubular heaters. The same heaters located under the substrate strip and having openings at the top are used as antiadhesive vaporizers. Separation of the resulting foil from the substrate occurs directly in the vacuum chamber during deposition with a special device.

Organizing of the foil production based on УВФ-2.0 required to develop auxiliary equipment including:

− substrate preparation and foil separation line;
− furnaces for remelting antiadhesive agent;
− foil quality control station.

The substrate preparation line (Fig. 2.11) is designed to rewind the substrate strip from the coil, supplied by manufacturer, to the uncoiler shaft of УВФ-2.0. Simultaneously, a special mechanism separates and unwinds the paper protector and a special device degreases the substrate surface. Subsequently, the coiler shaft with the prepared substrate is placed into УВФ-2.0.

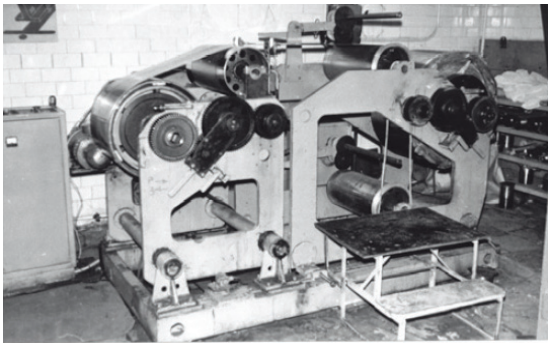

Fig. 2.11. General view of the UPP line for substrate preparation and foil separation

Having completed the vacuum deposition process in УВФ-2.0 and de-

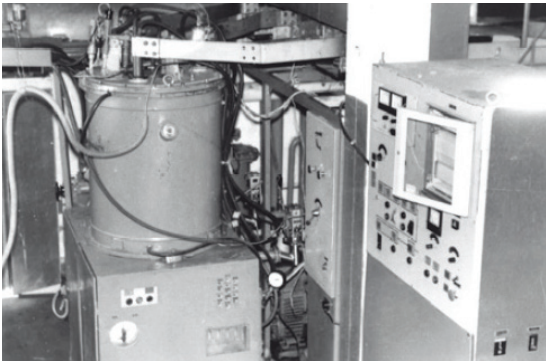

Fig. 2.12. General view of a vacuum furnace for melting antiadhesive agent

pressurized the vacuum chamber, the coiler shaft with the substrate coil covered with the alloy condensate is placed in the substrate preparation line and the foil is separated from the substrate with a special mechanism.

Antiadhesive agent was melted in the ОКБ 8086 furnace (Fig. 2.12). We developed process of remelting Antiadhesive agent in an inert atmosphere (argon) and making evaporative billets to be placed in direct-duct molybdenum vaporizers of УВФ-2.0.

The foil quality control station included devices for determining geometric dimensions of the foil, foil visual inspection, measurement of through porosity characteristics, preparation of specimens for mechanical testing, and rejection of defective foil.

While launching the foil production we experimentally improved the design of certain components and developed foil production process, published relevant technical documentation − ТИ ОПУ-06.08.88, ТЭК No. 015-0002.

Chapter 3. HEAT AND MASS TRANSFER AT A HIGH-SPEED ELECTRON BEAM EVAPORATION OF METALS, AND VACUUM VAPOR DEPOSITION ONTO A MOVING SUBSTRATE

One of the topical problems concerning the development of the process of electron beam metal evaporation and the vapor deposition onto a substrate strip, moving over the vaporizer [70–77], is to study not only the process of mass transfer, but also thermal processes occurring on the moving substrate, because its temperature largely controls the physical and chemical properties of vacuum condensates [2, 78].

The process of vacuum deposition followed by separation of the condensate from the substrate opens up new possibilities for making ultra-thin foil [67] whose properties depend substantially on the condensation mechanism largely determined by the substrate temperature. Unlike the process of foil making by vapor deposition onto the surface of a water-cooled drum [78], in this case the heat processes, accompanying the condensate formation, occur in the condensation zone area of a much greater extent.

So, what controls the substrate temperature change during vacuum deposition? The factors influencing this process are analyzed in [5]. The dependence of the total heat effect on the condensation rate of the evaporated substance is suggested to be divided into three sub-areas:

1) the area of low condensation rates ($< 5 \cdot 10^{-4}$ μm/s), where the substrate is heated mainly by the vaporizer heat radiation;

2) the area of intermediate condensation rates (from $5 \cdot 10^{-4}$ to $1 \cdot 10^{-2}$ μm/s), where the heat effect of condensation is comparable to the radiation energy;

3) the area of high condensation rates ($> 1 \cdot 10^{-2}$ μm/s), where the heat of condensation of the evaporated material is the main factor affecting the substrate heating.

It is the latter case that corresponds to modern high-intensity industrial coaters.

Some works on this topic use simplifications to arrive at an analytical solution, the acceptance of which cannot ensure a veracious description of the substrate temperature field. Thus, in works [5, 79, 80] the calculation is made without taking into account the movement of the substrate and

the heat transfer along its plane. In most of the works, the radiation and the evaporation geometry is described not quite correctly, which can cause significant errors while describing the heat and mass transfer in the workspace of the vacuum deposition plant. Work [5] is focused on the optimization of geometrical parameters of the plant to obtain a uniform coating across the width of the substrate surface, but the evaporation surface is considered to be flat. The same assumption is usually shared by other authors [81]. However, experimental studies have demonstrated that the directivity pattern of the vapor flow density is more narrow-beamed than it should be in the case of a flat evaporation surface. To account for this phenomenon, empirical equations are typically used [74, 82, 83]. Yet, using empirical equations requires to obtain necessary setting parameters actually for each specific plant design or its operation mode, which essentially decreases the value of the mathematical models used.

Thus, the task of creating a mathematical simulation, correctly describing heat and mass transfer processes in a vacuum deposition plant as a substrate strip passes through it, is impending. Such a model must meet a number of requirements, namely:

– describe properly the processes of heat and mass transfer of evaporated substance in the working space of a vacuum deposition plant;

– take as the initial data those parameters that are known for the existing plant operation;

– allow calculating the characteristics of the vacuum deposition process that are relevant to determine the structure and properties of the resulting coating, such as the temperature field of the substrate strip within the condensation and the cooling areas, temperature conditions of condensation in different parts of the substrate, the thickness profile of the resulting coating.

Physical models suggested by the author allowed him, in collaboration with M.R. Soloveitchik, V.R. Soloveicthik, S.A. Krupennikov and I.A. Levitsky to give theoretical description of the basic processes of mass and heat transfer [84−87].

Our theoretical model [67, 84] is based on the assumption that the main factor, determining the spatial distribution of vapor and heat flows, is the curvature of the evaporation surface under the recoil momentum of evaporating atoms. This approach allowed us to obtain analytical expressions for evaporation and radiation directivity pattern, however, it still requires some adjustments.

The solution to this problem, briefly summarized in [85, 86], is given in the subsequent sections of this chapter and contains:

– description of the geometry of radiation and evaporation processes (sequential implementation of the analogy of these processes, presentation of the calculation method for angular radiation coefficients, development of the expressions for heat and vapor flow densities in different zones of the substrate strip movement);

– consideration of various formulations of the heat conduction problem for a moving substrate strip, the description of their numerical implementation (general 3D and simplified 2D equations of the problem, their finite-difference analogs and numerical solution algorithms);

– verification of the agreement of the developed mathematical simulation with by comparing calculated dependencies with industrial experiment results;

– applications of this model to the analysis of the influence ot the most significant technological and structural parameters on the heat and mass transfer characteristics of the vacuum deposition process.

3.1. Calculation of heat and mass transfer between vaporizer and substrate

Theoretical calculations of heat and mass transfer between the vaporizer and the substrate provide favorable conditions to optimize the implemented processes of metals vacuum deposition onto a moving substrate.

3.1.1. Methods of description of spatial distribution of vapor and radiation flows

Angular densities of radiation and vapor flows

The description of the radiation energy distribution in different spatial directions, according to the theory of radiative heat transfer, uses the notion of the angular density of the radiation flow [88].

Let us consider an elementary area of the radiating surface with area dF and a certain spatial direction defined by observation angle θ measured from the normal to the dF spot. Let us denote as dω the elementary solid angle corresponding to the selected direction (Fig. 3.1). The angular density of radiation flow q_ω, w/(m^2 · sr), is the ratio of radiation flow density dq per elementary solid angle dω to the value of this elementary solid angle:

$$q_\omega = \mathrm{d}q/\mathrm{d}\omega. \qquad (3.1)$$

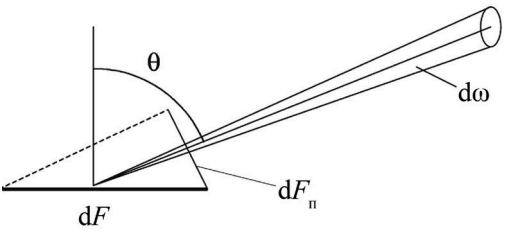

Fig. 3.1. To the definition of the angular density of a radiation flow

The integral (hemispherical) density of radiation flow q is related to angular density q_ω by the ratio

$$q = \int_{2\pi} q_\omega d\omega, \qquad (3.2)$$

where integration is made through the solid angle within the half-space.

According to researches, the angular density of the radiation flow of different bodies depends greatly on angle θ: its maximum value usually corresponds to the normal to the radiating section (θ = 0) while the angular density is zero by tangential directions (θ = π/2). For an absolute black body – according to the Lambert law – the angular density of a radiation flow is proportional to the cosine of the observation angle:

$$q_\omega = b\cos\theta, \qquad (3.3)$$

where the proportionality factor independent of the observation angle $b = q/\pi$, w/(m²·sr), is called brightness.

For real bodies, the dependence of the angular density of radiation flows on the observation angle may be conveniently represented in the form (3.3) where brightness *b,* describing individual characteristics of the body, may depend on the observation angle.

From Equations (3.1), (3.3) and the determination of radiation flow density, it follows that

$$b = \frac{q_\omega}{\cos\theta} = \frac{dq}{d\omega\cos\theta} = \frac{d^2Q}{d\omega dF\cos\theta} = \frac{d^2Q}{d\omega dF_n}$$

where $dF_n = dF\cos\theta$ – the projection of an elementary radiating pad onto the plane perpendicular to the direction of observation, or a visible (perceived by the observer) value of the radiating surface (see Fig. 3.1).

This implies that the brightness of radiation is the ratio of the radiation flow falling on the visible part of the elementary radiating pad and the elementary solid angle, to the values of these two elementary domains.

Typically, to describe the radiative heat transfer in vacuum deposition plants the vaporizer is regarded as a point source of radiation and vapor [74]. This assumption is true if the dimensions of the evaporation surface are small as compared to the distance from this surface to the substrate. For a point source, angular flow density Q_ω, w/sr and radiation brightness B, w/sr, can be introduced similarly to (3.1) and (3.2):

$$Q_\omega = \mathrm{d}Q/\mathrm{d}\omega; \tag{3.4}$$

$$Q_\omega = B\cos\theta. \tag{3.5}$$

It is noteworthy that the radiation brightness of an absolute black point source does not depend on the observation angle, $B = \mathrm{const}(\theta)$, only if this source replaces the flat radiating surface. Otherwise, there is some dependence of $B(\theta)$ determined by the shape of the radiating surface and a possible shading effect.

The spatial distribution of vapor flows is described similarly.

The angular density of vapor flow w_ω, kg/(s·m^2·sr) is the ratio of flow density dw per elementary solid angle dω to the value of this elementary solid angle

$$w_\omega = \mathrm{d}w/\mathrm{d}\omega. \tag{3.6}$$

According to Knudsen [89], the angular density of a vapor flow is proportional to the cosine of the observation angle

$$w_\omega = i\cos\theta, \tag{3.7}$$

at this, similarly to (3.2), the integral (hemispherical) vapor flow density is

$$w = \int_{2\pi} w_\omega \mathrm{d}\omega, \tag{3.8}$$

where the integration is carried out along the hemisphere within the half-space.

In Equation (3.7), the observation angle independent of proportionality factor $i = w/\pi$, kg/(s·m^2·sr) is called evaporation intensity.

For a point vapor source the notion of the angular density of vapor flow W_ω, kg/(s·sr) and evaporation intensity I, kg/(s·sr) can be introduced similarly to (3.6) and (3.7)

$$W_\omega = \mathrm{d}W/\mathrm{d}\omega; \tag{3.9}$$

$$W_\omega = I\cos\theta. \tag{3.10}$$

If the point source is replaced with a flat evaporation surface, the evaporation rate does not depend on the observation angle.

Otherwise, there are deviations from the cosine law expressed as a certain dependence of evaporation intensity $I(\theta)$ on the observation angle called the *directivity pattern* of a vapor flow and determined by the shape of the evaporation surface.

Calculation of the shape of isothermal lunule surface

Let us consider the methodology of calculating the directivity pattern as part of our «isothermal lunule» model based on the following assumptions [84]:

− evaporation occurs not on the whole surface of the molten metal but only on its part which interacts with the electron beam;

− the molten metal surface is curved, forming a lunule, due to the impact of the recoil momentum of evaporating atoms;

− the surface of the lunule can be regarded as isothermal.

Let us first consider the relations determining the dependence of the vapor pressure of the evaporated material and its evaporation rate on temperature [90−92].

According to the Boltzmann law, the number of vapor atoms per unit volume, having, at equilibrium, potential energy U, is equal to

$$n = n_0 e^{-\frac{U}{kT}}$$

where n_0 – density of the melt atoms whose potential energy is assumed to be zero; $k = 1.38 \cdot 10^{-23}$ J/K – Boltzmann constant; T – vapor temperature, K.

The average energy of atoms emitted from the molten metal mass, differs from the energy of the atoms inside the molten metal mass by value L/N_A, where L – molar heat of the evaporation, J/mol; N_A – Avogadro's number. Without taking into account the work against external pressure $U = L/N_A$

$$n = n_0 e^{-\frac{L}{RT}},$$

where $R = N_A k = 8.314$ J/(mole·K) – molar gas constant.

Vapor pressure is

$$p = nkT = n_0 kTe^{-\frac{L}{RT}}$$

or

$$\ln p = -\frac{L}{RT} + B + \ln T.$$

The following dependence is used for processing experimental data [91]

$$\lg p = -\frac{A}{T} + B - C \lg T. \tag{3.11}$$

The values of coefficients *A, B* and *C* for Ti, Ni and Cu [91] (when measuring pressure in Pa and temperature in K) are shown in Table. 3.1.

Table 3.1

Values of coefficients A, B and C for Ti, Ni and Cu

Metal	A	B	C
Ti	23 200	13.86	0.66
Ni	22 400	19.07	2.01
Cu	17 650	15.51	1.27

Knowing [92] that the number of atoms hitting unit area (of the wall) per unit time is equal to

$$\nu = \frac{1}{4} n\bar{v},$$

where the arithmetic mean value of atom speeds

$$\bar{v} = \frac{2}{\sqrt{\pi}} \left(\frac{2kT}{m} \right)^{1/2}, \tag{3.12}$$

and considering that $n = p/kT$, we'll find

$$\nu = \frac{p}{\sqrt{2\pi}} \left(\frac{1}{kTm} \right)^{1/2}$$

Assuming that evaporation rate w (mass flux density) is equal to the condensation rate, we'll have

$$w = m\nu = \frac{p}{\sqrt{2\pi}}\left(\frac{m}{kT}\right)^{1/2} = \frac{p}{\sqrt{2\pi}}\left(\frac{M}{RT}\right)^{1/2} \tag{3.13}$$

or

$$\lg w = \lg p - 0,5\lg T - D. \tag{3.14}$$

Values of coefficient D for Ti, Ni and Cu (when measuring the evaporation rate in kg/m^2·s), pressure in Pa, temperature − K) are shown in

Table. 3.2.

Values of coefficient *D* for Ti, Ni and Cu

Metal	D
Ti	1.5188
Ni	1.4747
Cu	1.4575

Excluding lg p from Equations (3.11) and (3.14), we shall have

$$\frac{A}{T} + \left(C + 0,5\right)\lg T + \lg w + D - B = 0, \tag{3.15}$$

having the solution which determines temperature T corresponding to preset evaporation rate w.

Having determined temperature T, the saturated vapor pressure is calculated by (3.11) or by the equation

$$\lg p = \lg w + 0,5\lg T + D, \tag{3.16}$$

derived from (3.14).

Let us consider the relation between the specific recoil momentum of evaporated atoms (momentum carried away from unit surface of evaporation per unit time) with vapor pressure.

As a first approximation, let us assume that specific recoil momentum P is half the value of saturated vapor pressure at the evaporation temperature [84]. To adjust this assessment we use the equation for the resulting specific recoil momentum directed along the normal to the elementary portion of the evaporation surface.

$$P = \int_{2\pi} w_\omega \overline{v} \cos\theta d\omega. \tag{3.17}$$

It should be noted that the latter ratio does not take into account the effect of increasing recoil impulse due to the collision of evaporated atoms with the concave evaporation surface, therefore it is applicable in the case of a shallow lunule, when the percentage of atoms evaporated from one part of its surface and colliding with the other part can be neglected.

Having transformed Equation (3.17) by taking into account Equations (3.12), (3.13) and the Knudsen law (3.7), we'll have

$$P = i\overline{v} \int_{2\pi} \cos^2\theta d\omega = \frac{2\pi}{3} i\overline{v} = \frac{2}{3} w\overline{v} = p\frac{2\sqrt{2}}{3\pi} \approx 0,3p. \tag{3.18}$$

Let us find the shape of the lunule surface assuming its constant temperature and its symmetry relative to the vertical axis (Fig. 3.2). Let us write the equation of static equilibrium in the vertical direction of the forces caused by recoil momentum of evaporating atoms, surface tension and buoyancy (Archimede's) for the surface limited by the horizontal section of the lunule at level z:

$$2\int_0^r P(\xi)\xi d\xi = 2\sigma r\cos(\alpha) + \rho g\left[r^2 h - 2\int_0^r z(\xi)\xi d\xi\right], \quad 0 < r < r_0, \tag{3.19}$$

where P – specific recoil momentum, σ – surface tension, ρ – molten metal density, g – acceleration of gravity, h –lunule depth, $z(r)$ – vertical section of the lunule surface profile, α – angle between the normal to the lunule surface and the horizontal plane, r – distance from the axis of the lunule, r_0 – lunule radius taken equal to the radius of the electron beam.

By differentiating Equation (3.19) with respect to r and having performed elementary transformations, we'll have

$$z'' = \frac{1}{\sigma}\left[P - \rho g(h - z)\right]\left(1 + z'^2\right)^{3/2} - \frac{z'}{r}\left(1 + z'^2\right), \quad 0 < r < r_0. \tag{3.20}$$

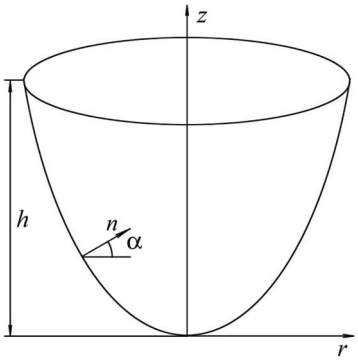

Fig. 3.2 Lunule formed on the evaporation surface

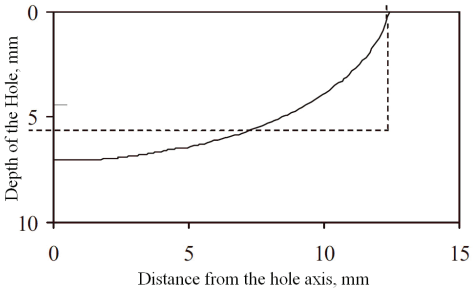

Fig. 3.3. The profile of the surface of the isothermal lunule during titanium evaporation in the УВ68Л plant

A numerical solution of Equation (3.20) with the boundary conditions

$$z(0)=0,\ z'(0)=0,\ z(r_0)=h$$

allows determining lunule depth h, its profile $z(r)$ and surface area S.

Fig. 3.3 shows dependence $z(r)$ drawn for the conditions of titanium evaporation in the УВ68Л plant [65] under the following values of critical parameters: electron beam radius r_0 = 12 mm; evaporation rate (assuming that the evaporation takes place only from the surface of a lunule with radius r_0) w = 0.75 kg/(m^2·s); evaporation temperature (found by solving Equation (3.15)) T = 2462 °C; vapor pressure (found by Equation (3.16)) p = 1288 Pa. The dependence of the density and the surface tension of molten metal on temperature was determined according to data [91].

The criterion of applicability of the isothermal lunule model

The above methodology for calculating the shape of the isothermal lunule surface is built on the assumption that metal does not evaporate from the entire surface of the molten mass, but only from its part which is hit with the electron beam. The following inequality may be considered as the condition for the validity of this assumption

$$\Delta r << r_0 \qquad (3.21)$$

where $\Delta r = r_{evap} - r_0$; r_{evap} – radius of the evaporation surface; r_0 – electron beam radius.

To assess the Δr value we use the following relations (Fig. 3.4)

$$\Delta r \approx -\frac{\overline{w}}{\left.\frac{\mathrm{d}w}{\mathrm{d}r}\right|_{r=r_0}} = -\frac{\overline{w}}{\left.\frac{\mathrm{d}w}{\mathrm{d}T}\right|_{T=\overline{T}} \left.\frac{\mathrm{d}T}{\mathrm{d}r}\right|_{r=r_0}} = \frac{\lambda q_{\text{evap}}}{\alpha_{\text{evap}} q_{\text{h}}}; \tag{3.22}$$

where T – temperature of the free surface of the molten metal; $\overline{T}$ – average temperature of the lunule surface; $\overline{w}$ – evaporation rate, corresponding to temperature $\overline{T}$; $q_{\text{evap}} = L\overline{w}$ – heat flow density consumed for evaporation (specific heat effect of evaporation); $q_h = -\left.\frac{\lambda \mathrm{d}T}{\mathrm{d}r}\right|_{r=r_0}$ – density of the heat flow removed from the lunule by heat conductivity; λ – heat conductivity coefficient of the molten metal; $\alpha_{\text{evap}} = L\frac{\mathrm{d}w}{\mathrm{d}T}$ – heat coefficient of evaporation, w/(m^2·K), characterizing the influence of temperature on the specific heat effect of evaporation.

Considering that $q_{\text{h}} \approx q_{\text{evap}}$, we'll have

$$\Delta r \approx \frac{\lambda}{\alpha_{\text{evap}}},$$

then condition (3.21) will be represented as follows:

$$K_{\text{evap}} = \frac{\alpha_{\text{evap}} r_0}{\lambda} >> 1, \tag{3.23}$$

where the dimensionless complex K_{evap} characterizes the rate of the decrease of evaporation intensity as the distance from the lunule in the radial direction increases.

The values of the heat coefficient of evaporation α_{evap} corresponding to preset temperatures on the lunule surface are found by solving Equation (3.15). Graphs of dependency α_{evap} from relative molten metal temperature T/T_s (T_s – melting point, K) for certain metals are shown in Fig. 3.5.

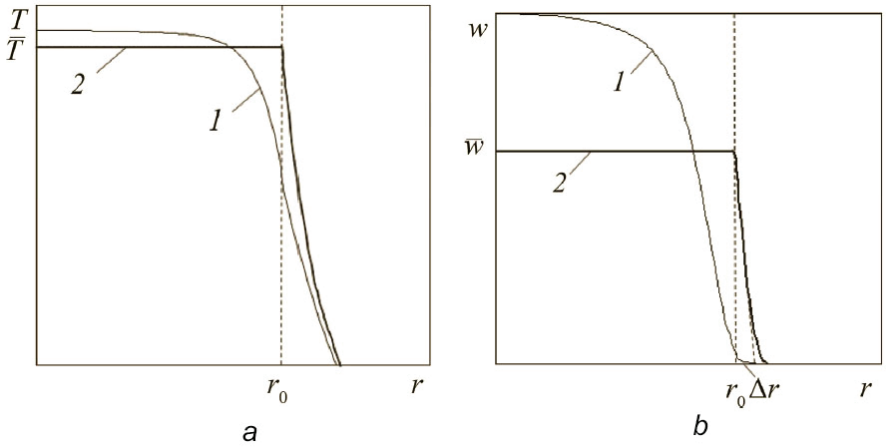

Figure. 3.4. Changes in the temperature of the molten metal surface (*a*) and evaporation rate (*b*) moving away from the axis of the electron beam: *1* − real molten mass; *2* – simulation of isothermic lunule

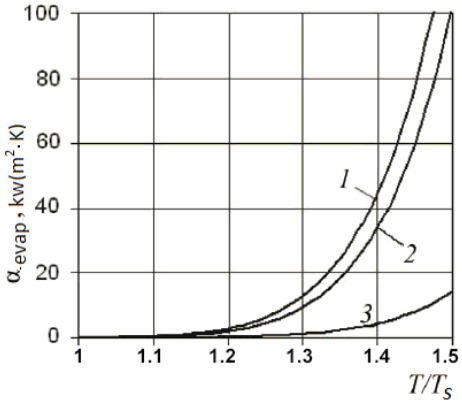

Figure 3.5. Dependence of evaporation heat coefficient α_{evap} on relative molten mass temperature $T/T_{s\ for}$ titanium (*1*), nickel (*2*) and copper (*3*)

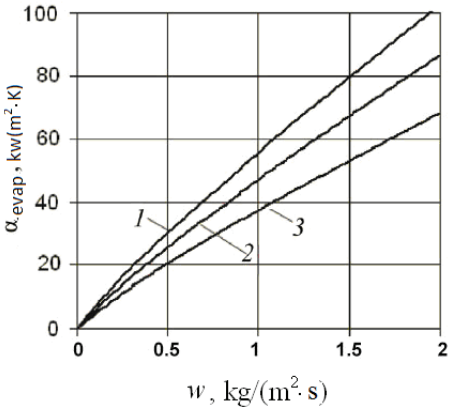

Fig. 3.6. Dependence of evaporation heat coefficient α_{evap} on evaporation rate *w* for titanium (*1*), nickel (*2*) and copper (*3*)

In practical calculations it is more convenient to use relations represented as $\alpha_{evap} = f(w)$ directly linking the heat coefficient of evaporation to evaporation rate. Graphs of such dependences are shown in Fig. 3.6.

As an example, let us define criterion value K_{evap} for the above conditions of titanium evaporation at r_0 = 12 mm and w = 0.75 kg/(m²·s). Using graph (*1*) in Fig. 3.6 we'll find $\alpha_{evap} \approx 43$ kw/(m²·K) and at the heat conductivity coefficient of titanium $\lambda \approx 20$ w/(m·K) we'll have $K_{evap} \approx 27 >> 1$.

This assessment suggests the possibility of using the isothermal lunule model to calculate the spatial distribution of titanium vapor flow in the УВ68Л plant.

Equivalent cylindrical lunule

To simplify the calculation of spatial distribution of vapor flow let us replace the abovementioned isothermal lunule with an *equivalent cylindrical lunule* of radius r_0, while its depth h_0 is determined based on the following ideas:

− metal evaporates only from the bottom of the equivalent lunule, so the vapor flow from this surface G must be equal to the actual vapor flow wS;

– vapor flow leaving the lunule, G_0, is equal to wS_0, where $S_0 = \pi r_0^2$ is surface area, confining the lunule cavity.

From the analogy of evaporation and radiation processes it follows that the ratio $G_0/G = S_0/S$ is the average angle coefficient of radiation from the bottom base of the equivalent lunule to the lunule top, equal to [88]

$$\varphi_{10} = 1 + 2H^2 - 2H\sqrt{1 + H^2}\ , \qquad (3.24)$$

where $H = h_0/(2r_0)$

Thus, the h_0 value is determined by solving the equation

$$1 + 2H^2 - 2H\sqrt{1 + H^2}\ = S_0 / S\ . \qquad (3.25)$$

The equivalent lunule depth h_0 = 5.1 mm under the conditions of the above-mentioned experiment is shown in Fig. 3.3 with a dotted line.

Simplified calculations of the directivity pattern of vapor flows

To calculate the directivity pattern of the vapor flow let us assume that the effect of shading the vapor flow with the walls of the equivalent lunule is determined by ratios that are typical for a cylindrical beam [84]. This approach results in the following expression for the directivity pattern:

$$I(\theta)=\begin{cases} I_0\dfrac{2\beta-\sin 2\beta}{\pi}, & \theta<\theta_0, \\ 0, & \theta\geq\theta_0 \end{cases} \tag{3.26}$$

where $\beta=\arccos\dfrac{h_0\,\mathrm{tg}\theta}{2r_0}$; $\theta_0=\mathrm{arctg}\dfrac{2r_0}{h_0}$ is the critical angle under which the bottom surface of the lunule stops being visible.

The evaporation rate in the direction normal to the bottom of the lunule I_0 in this case is expressed by experimentally determined vapor flow $G_{0,,}$ kg/s, equal to

$$G_0=\int_{\omega_0} J_\omega \mathrm{d}\omega=\int_{\omega_0} I(\theta)\cos\theta\mathrm{d}\omega=I_0\int_0^{\theta_0}(2\beta-\sin 2\beta)\sin 2\theta\mathrm{d}\theta, \tag{3.27}$$

where ω_0 is the solid angle corresponding to a cone with apex angle θ_0.

The calculations results based on the described approach match well the findings of experiments conducted at an industrial vacuum deposition plant. However, let us point out that the directivity pattern (3.26) as well as other similar expressions based on the replacement of the actual evaporation surface with a point vapor source are only applicable in the case of quite a long distance between the vaporizer and the substrate.

However, continuing the analogy of the processes of evaporation and heat radiation and applying the notion of local angle coefficient of radiation which is widely used in the radiation heat transfer theory, it is possible to obtain a more general solution valid for arbitrary geometrical characteristics of the system in question.

3.1.2. Determining local angle coefficients of radiation from the substrate onto the lunule

To describe quantitatively the process of radiation heat transfer between two surfaces – F_1 and F_2, we have to find angle coefficient of radiation $\varphi_{F_1-F_2}$ – a geometric characteristics showing the share of effective radiation of the first (radiating) surface F_1 reaching the second (i.e. radiant heat absorbing) surface F_2 [86]. However, if both surfaces are elementary, angle coefficient $\varphi_{\mathrm{d}F_1-\mathrm{d}F_2}$ is also called *elementary*, and if the radiant heat absorbing surface has a finite size, then angle coefficient $\varphi_{\mathrm{d}F_1-F_2}$ is called *local*.

The elementary angle coefficient of radiation is determined as

$$\varphi_{dF_1-dF_2} = \frac{1}{\pi}\cos\theta_1 d\omega = \frac{\cos\theta_1\cos\theta_2}{\pi r^2} dF_2, \tag{3.28}$$

where r – distance between elementary areas dF_1 and dF_2, θ_1 and θ_2 – angles between the normals to these areas and the direction of the line connecting them, $d\omega = dF_2\cos\theta_2/r^2$ – elementary solid angle at which the radiant heat absorbing surface is visible from the location point of the radiating area (Fig. 3.7).

To calculate local angle coefficient of radiation $\varphi_{dF_1-F_2}$ we should integrate Equation (3.28) over total lunule surface F_2:

$$\varphi_{dF_1-F_2} = \int_{F_2} \frac{\cos\theta_1\cos\theta_2}{\pi r^2} dF_2 . \tag{3.29}$$

In some cases, we can integrate this in elementary functions; however, in more complex cases, a numerical approach or other methods of finding angle coefficients shall be used [88].

Having defined local angle coefficient $_{F_1\ F_2}$ and regarding F_2 as the radiant surface, we can, based on the reciprocity property of angle coefficients, find the density of the radiation flow incident onto the surface F_1:

$$q_1^{\text{inc}} = \varphi_{dF_1-F_2} q_2^{\text{eff}} . \tag{3.30}$$

Thus, to describe the process of radiation (and evaporation) from the surface of the lunule, formed by an electron beam in the evaporated billet, onto the substrate surface facing the vaporizer it is necessary to find the local angle coefficient of radiation from an elementary area of the substrate surface onto the inner surface of the lunule .

This task is accomplished by introducing the coordinate system

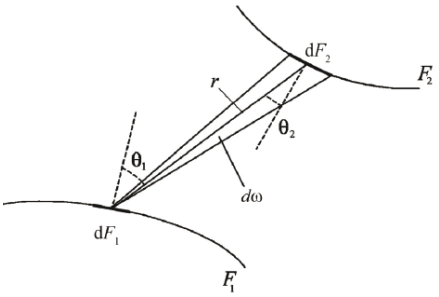

Fig. 3.7. To the calculation of the local angle coefficient of radiation

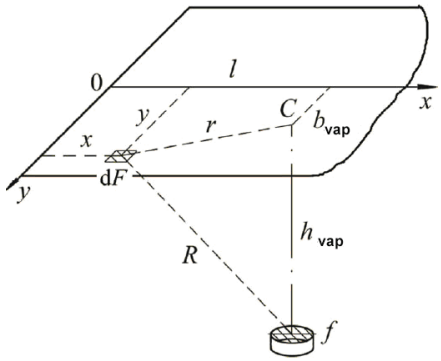

Fig. 3.8. To the calculation of local angle coefficient of radiation from the strip onto the lunule

0*xy* into the strip plane, directing axes *x* and *y* to the length and the width of the strip, respectively, and selecting the coordinate origin at a point in the middle of the lower surface of the strip, where the condensation zone starts (Fig. 3.8).

The location of the vaporizer relative to the strip is defined with three parameters *l,* b_{vap} and h_{vap}, where *l* is longitudinal distance from the condensation zone to the vaporizer, b_{vap} − transverse displacement of the vaporizer relative to the strip center line, h_{vap} − distance from the strip to the surface of the vaporized material. Then the distance from surface element d*F* with coordinates (*x, y*) to the surface center with the area of $f = \pi r_0^2$, closing the lunule cavity will be $R = \sqrt{r^2 + h_{vap}^2}$, where $r = \sqrt{\left(x - l\right)^2 + \left(y - b_{vap}\right)^2}$ – distance from the d*F* element to point *C* of the surface above the lunule .

Let us denote the local angle coefficients of radiation from the element d*F* onto the entire lunule surface, its bottom and its lateral surface as $\varphi_0(x,y)$, $\varphi_1(x,y)$ and $\varphi_2(x,y)$, respectively. Since the $\varphi_0(x,y)$ angle coefficient coincides with the local angle coefficient from the d*F* element onto surface *f*, Equation (3.29) leads to [88]:

$$\varphi_0\left(x,y\right) \equiv \varphi_0\left(x,y,h_{vap}\right) = \frac{1}{2}\cdot\left[1 - \frac{R^2 - r_0^2}{\sqrt{\left(R^2 + r_0^2\right)^2 - 4r^2 r_0^2}}\right]. \qquad (3.31)$$

The calculation of local angle coefficient $\varphi_1(x,y)$ from the strip onto the lunule bottom must take into account the shading effect:

$$\varphi_1(x, y) = \varphi_0\,(x, y, h_{vap} + h_0\,)\,D, \qquad (3.32)$$

where $\varphi_0(x, y, h_{vap}+h_0)$ – local angle coefficient of radiation from the strip onto the lunule bottom without any shading; D – visible part of the lunule bottom.

The shading effect occurs at $r > r_0$, i.e. for the points of the surface, whose distance from the C point exceeds the lunule radius (fig. 3.9). In fact, at $r \le r_0$ the entire lunule base is visible from the dF element and the D coefficient is 1. In the case of elements that are quite far away from the C point, at $r \ge r^*$, the lunule bottom is fully shaded and the D coefficient gets equal to 0. In geometrical terms, it is easy to demonstrate that $r^* = r_0(1+2h_{vap}/h_0)$.

Let us determine coefficient D at $r_0 < r < r^*$. As shown in Fig. 3.9, the size of the part of the lunule bottom visible from the location of the dF element is limited on one side by the arc of the top edge of the lunule with the angular measure of $2\gamma_1$, and on the other side – by the arc of the lower lunule edge with the angular measure of $2\gamma_2$. Values of angles γ_1 and γ_2 are calculated by the following equations

$$\gamma_1 = \arccos\left(\frac{h_0\left(r^2 + r_0^2\right) + 2h_{vap}r_0^2}{2\left(h_{vap} + h_0\right)r_0 r}\right);\ \gamma_2 = \arccos\left(\frac{h_0\left(r^2 - r_0^2\right) - 2h_{vap}r_0^2}{2h_{vap}r_0 r}\right). \quad (3.33)$$

By using dimensionless parameters $\eta = h_0/h_{vap}$ and $\rho = r/r_0$ we can simplify the relations (3.33):

$$\gamma_1 = \arccos\left(\frac{\eta\rho^2 + \eta + 2}{2(1+\eta)\rho}\right);$$
$$\gamma_2 = \arccos\left(\frac{\eta\rho^2 - \eta - 2}{2\rho}\right). \quad (3.34)$$

Having introduced an auxiliary function

$$\chi(\gamma) = \frac{2\gamma - \sin 2\gamma}{2\pi},$$

which determines the ratio of the area of a circular segment with the half-apex angle γ to the circle area, we'll have the following expression to describe the visible part of the lunule bottom:

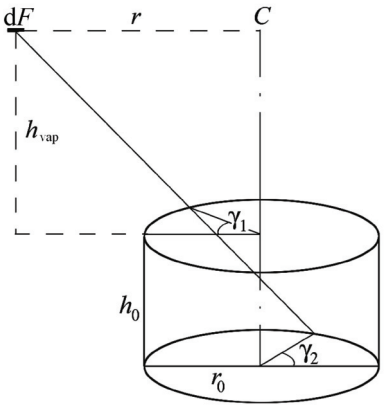

Fig. 3.9. To the determination of the visible part of the lunule bottom

$$D = \chi(\gamma_1) + \chi(\gamma_2)\,. \tag{3.35}$$

To define the local angle coefficient $\varphi_2(x, y)$ from the strip onto the lateral surface of the lunule the additive property of angle coefficient can be used, according to which

$$\varphi_2(x,y) = \varphi_0(x,y) - \varphi_1(x,y)\,. \tag{3.36}$$

It is useful to apply Equation (3.32) to evaluate the error of the simplified directivity pattern (3.26), suggested earlier in [84], using which is equivalent to setting a local angle coefficient of radiation from a strip element (visible at the angle of θ from the center of the lunule) onto the lunule according to the expression

$$\varphi(\theta) = \frac{(2\beta - \sin 2\beta)\cos^2\theta}{\int_0^{\alpha_0}(2\beta - \sin 2\beta)\sin 2\theta\, d\theta}\left(\frac{r_0}{r}\right)^2 \varphi_{10}\,. \tag{3.37}$$

This expression still has $\beta = \arccos\dfrac{h_0 \operatorname{tg}\theta}{2r_0}$ and the latter factor is the average angle coefficient of radiation from the bottom of the lunule onto its top section calculated by Equation (3.24). This factor ensures obtaining comparable results, because Equation (3.27) is the flow leaving the lunule, i.e. emitted not from the lunule bottom but by the surface closing its cavity.

Table 3.3

Local angle coefficients of radiation from the strip element located over the lunule center (θ = 0)

h_{vap}, mm	φ_1 by Equation (3.32)	φ_2 by Equation (3.36)	φ_1 by Equation (3.37)
320	0.001463	0.000037 (2.5%)*	0.001465 (0.15%)**
240	0.002576	0.000086 (3.4%)*	0.002583 (0.26%)**
120	0.009901	0.000664 (6.7%)*	0.010000 (1.00%)**
60	0.036181	0.004781 (13.2%)*	0.037539 (3.75%)**
20	0.210699	0.066966 (31.8%)*	0.266944 (26.7%)**
12	0.375244	0.141145 (37.6%)*	0.600625 (60.1%)**

*The number in brackets is the portion of the φ_1 value calculated by Equation (3.32).

** The number in brackets is the error relative to the calculation by Equation (3.32).

Comparing the calculation results obtained by Equations (3.37) and (3.32) were carried out for h_0 = 4 mm, r_0 = 12 mm and h_{vap} = 12…320 mm. These results are shown in Table 3.3 and Fig. 3.10.

As the results show, at small distances from the lunule to the strip ($h_{vap} < 20$ mm) the difference between values of the angle coefficient φ_1 obtained by different equations is quite substantial. In addition, the directivity pattern (3.37), used as a simplified approach [84], demonstrates considerably higher values, as opposed to strict calculations by Equation (3.32), of angle coefficient φ_1 in the axial zone and its sharper waning as the angle θ increases.

The directivity patterns (3.32) and (3.37) converge at a greater distance h_{vap}, and beginning from h_{vap} = 120 mm the divergence between the more exact description of the spatial distribution of heat and vapor flows and the approximated one [84] becomes virtually negligible.

The contribution of the lateral lunule surface into the radiation flow is significant only at quite small distances from the lunule to the strip: at $h_{vap} < 20$ mm, it exceeds 30 % in the axial zone and it increases even more when the angle θ becomes greater.

As the distance h_{vap} increases, the share of the axial zone radiation provided by the lateral lunule surface becomes less tangible: for h_{vap} = 120 mm it is less than 7 %, and for h_{vap} = 320 mm – less than 3 %. However, as the angle θ increases, this share grows reaching ~25 % at $\theta \approx 36^o$ due to the shift of the maximum local angle coefficient φ_2 away from the lunule axis as the distance h_{vap} increases.

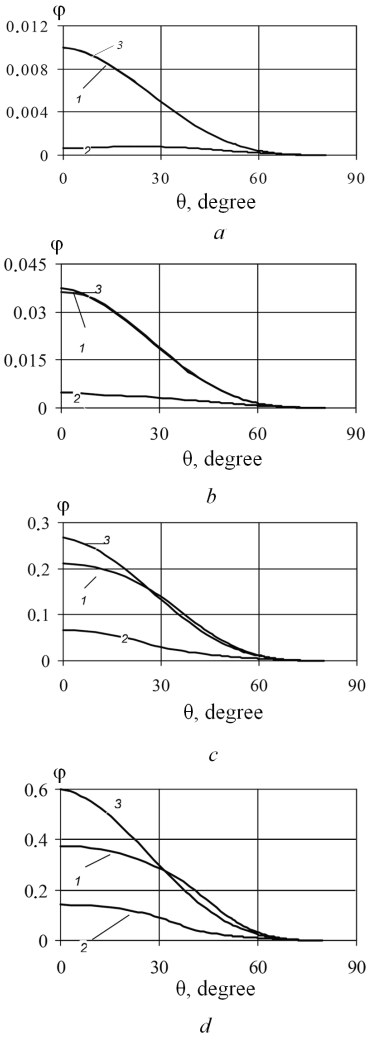

Fig. 3.10. Dependence of local angle coefficients of radiation φ on observation angles at h_{vap} = 120 mm (*a*); 60 mm (*b*); 20 mm (*c*); 12 mm (*d*): *1* – by Equation (3.32); *2* – φ_2 by Equation (3.36); *3* – φ_1 by Equation (3.37)

These results allow concluding that at quite big distances between the vaporizer and the strip it is possible to use the simplified method to calculate the spatial distribution of the vapor flow, however, for the calculation of the radiant heat exchange it is necessary to account for the radiation flow not only from the bottom but from the lateral surface of the lunule as well.

3.1.3. Calculations of vapor and heat flow densities on the strip surface

Taking into account the property of reciprocity of angle coefficients of radiation and assuming, as in [84], that the metal evaporates only from the lunule bottom, we have the following expression for the vapor flow on the surface $w(x, y)$

$$w(x, y) = \varphi_1(x, y)\, w_{\text{lun}}, \tag{3.38}$$

where $w_{\text{lun}} = \dfrac{G_0}{\varphi_{10} F_1}$ is the density of the vapor flow at the lunule bottom;

G_0 – the vapor flow leaving the lunule cavity (integral evaporation rate), kg/s; φ_{10} – the average angle coefficient of radiation (3.24) from the lunule bottom to the surface f; $F_1 = f$ – the lunule bottom area.

When determining the density of the heat flow incident onto the strip surface in the process of radiation heat exchange with the vaporizer, $q^{\text{inc}}(x, y)$, it should be taken into account that the source of heat radiation includes not only the bottom but the lateral surface of the lunule as well, hence

$$q^{\text{inc}}(x,y) = \varphi_1(x,y) q_1^{\text{eff}} + \varphi_2(x,y) q_2^{\text{eff}}, \tag{3.39}$$

where q_1^{eff} and q_2^{eff} – densities of the flows of effective radiation from the bottom and the lateral surface of the lunule, respectively.

The dependence of values q_1^{eff} and q_2^{eff} on the temperature of the lunule surface (evaporation temperature T_{evap}) is found by calculating the radiation heat transfer in the lunule cavity.

Let us put down the system of zonal equations relative to effective radiation flows Q_1^{eff} and Q_2^{eff} using the traditional zonal method [93] and neglecting the radiation incident to the lunule cavity externally:

$$Q_1^{\text{eff}} = \left(1-\varepsilon_{\text{lun}}\right)Q_2^{\text{eff}}\varphi_{21} + Q_1; \qquad (3.40\text{ a})$$

$$Q_2^{\text{eff}} = \left(1-\varepsilon_{\text{lun}}\right)\left(Q_1^{\text{eff}}\varphi_{12} + Q_2^{\text{eff}}\varphi_{22}\right) + Q_2; \qquad (3.40\text{ b})$$

where $Q_1 = qF_1$, $Q_2 = qF_2$ – flows of the intrinsic radiation from the bottom and lateral surfaces of the lunule; $q = \varepsilon_{\text{lun}}\sigma_0 T_{\text{evap}}^4$ – density of the flow of the intrinsic radiation from the lunule surface; ε_{lun} – emissivity coefficient of the lunule surface; $F_2 = 2\pi r_0 h_0$ – area of the lateral lunule surface; $\varphi_{12} = 1 - \varphi_{10,}$ $\varphi_{21} = \varphi_{12}F_1/F_2$ and $\varphi_{22} = 1 - 2\varphi_{21}$ – average angle coefficients of the radiation in the lunule cavity.

Solving the system of equations (3.40), we'll find

$$q_1^{\text{eff}} = q\frac{1-\varphi_{22}\left(1-\varepsilon_{\text{lun}}\right) + F_2\varphi_{21}\left(1-\varepsilon_{\text{lun}}\right)/F_1}{1-\left(1-\varepsilon_{\text{lun}}\right)\left[\varphi_{21}\left(1-\varepsilon_{\text{lun}}\right)\varphi_{12} + \varphi_{22}\right]}, \qquad (3.41\text{ a})$$

$$q_2^{\text{eff}} = q\frac{1 + F_1\varphi_{12}\left(1-\varepsilon_{\text{lun}}\right)/F_2}{1-\left(1-\varepsilon_{\text{lun}}\right)\left[\varphi_{21}\left(1-\varepsilon_{\text{lun}}\right)\varphi_{12} + \varphi_{22}\right]}. \qquad (3.41\text{ b})$$

The value q^{inc}, calculated by Equation (3.39), is the radiation flow density of the flow emitted by the vaporizer and directly reaching the strip surface – without any re-reflections of the radiation on the surfaces of the strip and the chamber walls. The value q^{inc} can be adjusted by adding to it part of the radiation flow density reflected by the strip, which returns to its surface due to such re-reflections. To this effect let us determine the overall angle coefficient [93] in the system formed by the lower surface of the strip (*a*) and the surface of the wall of the vacuum chamber facing it (*b*). Considering these surfaces as infinite parallel planes, we'll obtain the following system of equations to calculate the overall angle coefficients Φ_{aa} and Φ_{ba}:

$$\Phi_{aa} = \left(1-\varepsilon_{\text{ch}}\right)\Phi_{ba}, \quad \Phi_{ba} = 1 + \left(1-\varepsilon_{\text{cond}}\right)\Phi_{aa},$$

from where

$$\Phi_{aa} = \frac{1-\varepsilon_{ch}}{1-(1-\varepsilon_{cond})(1-\varepsilon_{ch})}\ ;\ \Phi_{ba} = \frac{1}{1-(1-\varepsilon_{cond})(1-\varepsilon_{ch})}, \quad (3.42)$$

where ε_{cond} and ε_{ch} – emissivity coefficients of the condensate and the chamber walls, respectively.

The density of the radiation flow emitted by the vaporizer and reflected by the strip is equal to $(1 - \varepsilon_{cond})\, q^{inc}$. Since the overall angle coefficient Φ_{aa} characterizes the part of this radiation, which returns to the surface due to the above-mentioned reflections, the value q^{inc} determined by Equation (3.39) should be increased by $(1 - \varepsilon_{cond})q^{inc}\Phi_{aa}$, replacing it with

$$q^{inc}* = q^{inc} + (-\varepsilon_{cond})q^{inc} \cdot \Phi_{aa} = \frac{nc}{1-(1-\varepsilon_{cond})(1-\varepsilon_{ch})} \quad (3.43)$$

It is to be noted that this problem is easy to summarize if we take several, for example, two vaporizers, by accounting for the input of each one into the densities of the vapor and heat radiation flows determined by Equations (3.38), (3.39) and (3.43). With this, the density of the vapor flow on the strip surface is

$$w(x,y) = \varphi_1^{(1)}(x,y)\, w_{lun}^{(1)} + \varphi_1^{(2)}(x,y)\, w_{lun}^{(2)},$$

while the density of the heat flow incident onto the strip surface in the process of radiation heat exchange with the vaporizers is

$$q^{inc}* = q^{inc\,(1)}* + q^{inc\,(2)}*,$$

where the upper indices correspond to the respective vaporizer number.

3.1.4. Determining the condensate depth, the vapor utilization coefficient and the grading screen shape

Having found the distribution of the vapor flow density *w(x,y)*, the current condensate depth can be defined using the following equation

$$\delta(x,y) = \frac{1}{\rho_{cond} u}\int_0^x w(\xi,y)\, d\xi, \quad (3.44)$$

where u – strip movement rate; ρ_{cond} – condensate density.

At the end of the condensation zone having the length L

$$\delta(L,y)=\frac{1}{\rho_{cond}u}\int_0^L w(\xi,y)\,d\xi\,. \tag{3.45}$$

Let us note that the relative coating profile at the end of the condensation zone $\Delta(y) \equiv \delta(L,y)/\delta(L,0)$ determined by the ratio

$$\Delta(y)=\frac{\int_0^L \varphi_1(\xi,y)\mathrm{d}\xi}{\int_0^L \varphi_1(\xi,0)\mathrm{d}\xi}\,, \tag{3.46}$$

depends only on the constructive parameters of the condensation zone (L, l, h_{vap}, b_{vap}) and the lunule dimensions (r_0 and h_0).

The coefficient of utilization K can be calculated by one of the following equations:

$$K=\frac{1}{G_0}\int_F w(x,y)\,\mathrm{d}F\,, \tag{3.47a}$$

where F – area of the strip surface facing the vaporizers within the condensation zone, or

$$K=\frac{\rho_{cond}u}{G_0}\int_{-b}^{b}\delta(L,y)\,\mathrm{d}y\,. \tag{3.47b}$$

A special screen is used for levelling the condensate depth across the strip width; it is installed in the condensation zone between the vaporizers and the substrate strip. If the distances from the vaporizers to the beginning and the end of the condensation zone are equal, i.e. $l = L/2$, then the shape of the two-sided symmetrical screen $x_{scr}(y)$ is determined by solving the equation

$$2\delta(x_{scr},y) = \delta(L, y) - \delta_{min} \tag{3.48}$$

where $\delta_{min}=\min_y \delta(L,y)$ – minimal value of the coating thickness at the end of the condensation zone without a screen.

If y is a fixed value, then Equation (3.48) can be solved by Newton's iterative method [94] as follows:

1. Setting the initial approximation x_{scr}.

2. Determining the residual of Equation (3.48)

$$d(x_{scr}) = 2\delta(x_{scr}, y) - \delta(L, y) + \delta_{min}, \tag{3.49}$$

where $\delta(x_{scr}, y)$ is calculated by Equation (3.44).

3. Determining the derivative of the residual (3.49)

$$d'(x_{scr}) = 2\frac{w(x_{scr}, y) - w(0, y)}{\rho_{cond} u}. \tag{3.50}$$

4. Finding an adjusted value $\tilde{x}_{scr}$ by Newton's equation

$$\tilde{x}_{scr} = x_{scr} - \frac{d(x_{scr})}{d'(x_{scr})}. \tag{3.51}$$

5. Assigning $x_{scr} = \tilde{x}_{scr}$ and returning to p. 2 if the current value $|\tilde{x}_{scr} - x_{scr}|$ exceeds the calculation error preset for given conditions.

When determining the coefficient of vapor utilization in the system with a levelling screen, the integration in Equation (3.47, a) extends over the unscreened part of the strip surface, while Equation (3.47, *b*) is simplified to $K = 2\rho_{cond} ub\delta_{min}/G_0$.

3.2. Mathematical description of heat transfer in a moving substrate

In the Cartesian coordinate system (the axis x coincides with the direction of the strip movement, the axis y goes along the strip width and the axis z goes along its thickness), the differential problem of steady heat conduction for a strip moving at a constant velocity u is described by a system of equations comprising:

− 3D steady heat conduction equation

$$A_{xyz}T = 0, \quad 0 < x < L_0, \ 0 < y < b, \ 0 < z < d, \tag{3.52}$$

where

$$A_{xyz}T = \frac{1}{c\rho}\left[\frac{\partial}{\partial x}\left(\lambda\frac{\partial T}{\partial x}\right)+\frac{\partial}{\partial y}\left(\lambda\frac{\partial T}{\partial y}\right)+\frac{\partial}{\partial z}\left(\lambda\frac{\partial T}{\partial z}\right)\right]-u\frac{\partial T}{\partial x};$$

– boundary conditions for x (at $0 \le y \le b$, $0 \le z \le d$):

$$T\big|_{x=0} = T_0\ , \tag{3.53}$$

$$\left.\frac{\partial T}{\partial x}\right|_{x=L_0} = 0\ , \tag{3.54}$$

the condition (3.53) expresses the uniformity of the temperature field in the beginning of the condensation zone, and (3.54) – the immutability of the temperature field along the longitudinal coordinate at the end of the cooling zone;

– boundary conditions for y (at $0 \le x \le L_0$, $0 \le z \le d$):

$$\left.\frac{\partial T}{\partial y}\right|_{y=0} = 0, \tag{3.55}$$

$$\left.\frac{\partial T}{\partial y}\right|_{y=b} = 0, \tag{3.56}$$

where (3.55) corresponds to the condition of symmetry of the temperature field relative to the plane $y = 0$, and (3.56) – to the case when the heat transfer of the strip ends with surrounding bodies is neglected;

– boundary conditions for z (for $0 \le x \le L_0$, $0 \le y \le b$):

$$-\lambda\left.\frac{\partial T}{\partial z}\right|_{z=0} = \begin{cases} q^{\mathrm{r}}_{\mathrm{lower}} + q^{\mathrm{abs}} + q^{\mathrm{process}}, & 0 \le x \le L \\ q^{\mathrm{r}}_{\mathrm{lower}}, & L < x \le L_0 \end{cases} \tag{3.57}$$

$$\lambda\left.\frac{\partial T}{\partial z}\right|_{z=d} = q^{\mathrm{r}}_{\mathrm{upper}}\ , \tag{3.58}$$

where (3.57) describes the radiant heat exchange of the lower strip surface (at $z = 0$) with the vaporizer and the chamber wall, and the

heat emission at this surface during the condensation of the vaporized substance, and (3.58) is the radiant heat transfer of the upper strip surface (at $z = d$) with the chamber wall.

Equations (3.52) – (3.58) use the following symbols and calculation formulas: *T(x,y,z)* – strip temperature, K; u – speed of the strip, m/s; λ, c, ρ – coefficients of conductivity, w/(m·K), specific heat, J/(kg·K) and density of the strip material, kg/m^3, respectively; L – length of the condensation zone, m; L_0 – total length of the cooling and condensation zones, m; b – strip half-width, m; d – strip thickness, m; T_0 – temperature at the beginning of the condensation zone;

$$q^{\mathrm{r}}_{\mathrm{lower}} = \varepsilon_{\mathrm{lower\text{-}ch}}\sigma_0\left(T^4_{\mathrm{ch}} - T^4_{\mathrm{lower}}\right) \text{ and } q^{\mathrm{r}}_{\mathrm{upper}} = \varepsilon_{\mathrm{upper\text{-}ch}}\sigma_0\left(T^4_{\mathrm{ch}} - T^4_{\mathrm{upper}}\right) \qquad (3.59)$$

– densities of the resultant radiant flows during the radiation heat exchange between the lower and upper strip surfaces and the chamber walls, w/m^2; $\varepsilon_{\mathrm{lower-ch}} = 1/(1/\varepsilon_{\mathrm{cond}}+1/\varepsilon_{\mathrm{ch}}-1)$ and $\varepsilon_{\mathrm{upper-ch}} = 1/(1/\varepsilon_{\mathrm{strip}}+1/\varepsilon_{\mathrm{ch}}-1)$ – reduced emissivity of the systems formed by the lower and upper strip surfaces and the chamber walls, respectively, where $\varepsilon_{\mathrm{cond}}$, $\varepsilon_{\mathrm{strip}}$ and $\varepsilon_{\mathrm{ch}}$ – emissivity coefficients of the condensate, the substrate strip and the chamber walls, respectively; $\sigma_0 = 5.67\cdot10^{-8}$ – Stefan-Boltzmann constant, w/(m^2·K^4); $T_{\mathrm{lower}}(x,y) \equiv T(x,y,0)$ and $T_{\mathrm{upper}}(x,y) \equiv T(x,y,d)$ – temperatures of the upper and lower surfaces of the strip, respectively, K; T_{ch} – temperature of the chamber walls, K; $q^{\mathrm{abs}}(x,y) = \varepsilon_{\mathrm{cond}}q^{\mathrm{inc}}(x,y)$ – heat flow absorbed by the lower strip surface during the radiative heat exchange with the vaporizer, w/m^2; $q^{\mathrm{inc}}(x,y)$ – density of the heat flow incident on the lower surface of the strip during the radiative heat exchange with the vaporizer, w/m^2;

$$q^{\mathrm{proc}}(x,y) =$$
$$= w(x,y)\cdot\left[\Lambda_{\mathrm{cond}} + c_{\mathrm{liquid}}\cdot\left(T_{\mathrm{cond}} - T_{\mathrm{cryst}}\right) + \Lambda_{\mathrm{cryst}} + c_{\mathrm{solid}}\cdot\left(T_{\mathrm{cryst}} - T_{\mathrm{lower}}\right)\right] \qquad (3.60)$$

– density of the heat flow released on the lower surface of the strip during the processes of phase transformation and cooling, w/m^2; *w(x,y)* – condensation rate (the vapor flow density on the lower surface of the strip), kg/(m^2·s); c_{liquid} and c_{solid} – specific heat capacities of the condensate in the liquid and solid state, J/(kg·K); T_{cond} – condensation temperature related to the condensation rate w by Equation (3.15), K; T_{cryst} – condensate crystalli-

zation temperature, K; Λ_{cond} and Λ_{cryst} – latent heat of the condensation and crystallization, respectively, J/kg.

For the case of the operation with a levelling screen (see pp. 3.1.4) the original statement of the problem must be adjusted as follows:

− within the limits of the shielded part of the lower surface of the strip [at $x < x_{scr}(y)$ and $x > L - x_{scr}(y)$] the vapor density $w(x,y)$ should be assumed as zero and the radiation flow density $q^{inc}(x,y)$ should be multiplied by the radiation attenuation coefficient $\varepsilon_{scr}/2$, where ε_{scr} is the screen emissivity coefficient;

− reduced emissivity of the system "lower strip surface −chamber wall" should be determined by the equation $\varepsilon_{lower\text{-}ch} = \varepsilon_{lower\text{-}scr}\,\varepsilon_{scr\text{–}ch}/(\varepsilon_{lower\text{-}scr} + \varepsilon_{scr\text{-}ch})$, where $\varepsilon_{lower\text{-}scr} = 1/(1/\varepsilon_{cond} + 1/\varepsilon_{scr} - 1)$ and $\varepsilon_{scr\text{–}ch} = 1/(1/\varepsilon_{scr} + 1/\varepsilon_{ch} - 1)$.

The three-dimensional (3D) equation of the problem of heat conductivity (3.52) − (3.58), supplemented with Equations (3.59) and (3.60) for the calculation of thermal effects included into the boundary conditions, is the most complete one.

However, for many practical calculations it would be enough to use a 2D approximation of the problem by averaging the temperature distribution either over the width or over the depth of the strip.

In the first case, the temperature field averaged over the width of the strip,

$$T(x,z) = \frac{1}{b}\int_0^b T(x,y,z)\,\mathrm{d}y,$$

can be found by integrating Equations (3.52) – (3.54), (3.57) – (3.60) with respect to y.

Taking into account the boundary conditions (3.55) and (3.56), we'll have the following 2D heat conductivity problem:

$$A_{xz}T = 0\ ,\quad 0 < x < L_0\ ,\ 0 < z < d\ , \tag{3.61}$$

where $A_{xz}T = \frac{1}{c\rho}\left[\frac{\partial}{\partial x}\left(\lambda\frac{\partial T}{\partial x}\right) + \frac{\partial}{\partial z}\left(\lambda\frac{\partial T}{\partial z}\right)\right] - u\frac{\partial T}{\partial x}$;

$$T\big|_{x=0} = T_0\ ,\quad 0 \le z \le d\ ; \tag{3.62}$$

$$\left.\frac{\partial T}{\partial x}\right|_{x=L_0} = 0\ ,\quad 0 \le z \le d\ ; \tag{3.63}$$

$$-\lambda\left.\frac{\partial T}{\partial z}\right|_{z=0}=\begin{cases}q^{\mathrm{r}}_{\mathrm{lower}}+q^{\mathrm{abs}}+q^{\mathrm{proc}}, & 0\le x\le L\\ q^{\mathrm{r}}_{\mathrm{lower}}, & L<x\le L_0\end{cases} \tag{3.64}$$

$$\lambda\left.\frac{\partial T}{\partial z}\right|_{z=d}=q^{\mathrm{r}}_{\mathrm{upper}},\ 0\le x\le L_0; \tag{3.65}$$

where q means the densities of heat flows averaged over the width.

In the latter case, the temperature field averaged over the depth,

$$T(x,y)\quad -\int T(x,y,z)\ z,$$

can be found by integrating Equations (3.52) – (3.56) with respect to z.

Taking into account the boundary conditions (3.57) and (3.58), transformed into the source summand of the heat conductivity equation, we'll get another 2D problem:

$$A_{xy}T+\frac{q_\Sigma}{c\rho d}=0,\quad 0<x<L_0\ ,\quad 0<y<b\ , \tag{3.66}$$

where $A_{xy}T=\frac{1}{c\rho}\left[\frac{\partial}{\partial x}\left(\lambda\frac{\partial T}{\partial x}\right)+\frac{\partial}{\partial y}\left(\lambda\frac{\partial T}{\partial y}\right)\right]-u\frac{\partial T}{\partial x}$;

$$T\big|_{x=0}=T_0\ ,\quad 0\le y\le b\ ; \tag{3.67}$$

$$\left.\frac{\partial T}{\partial x}\right|_{x=L_0}=0,\quad 0\le y\le b\ ; \tag{3.68}$$

$$\left.\frac{\partial T}{\partial y}\right|_{y=0}=0\ ,\ 0\le x\le L_0\ ; \tag{3.69}$$

$$\left.\frac{\partial T}{\partial y}\right|_{y=b}=0\ ,\ 0\le x\le L_0\ ; \tag{3.70}$$

where $q_\Sigma(x,y)=\begin{cases} q^{\mathrm{r}}_{\mathrm{lower}}+q^{\mathrm{r}}_{\mathrm{upper}}+q^{\mathrm{abs}}+q^{\mathrm{proc}}, & 0\le x\le L,\ 0\le y\le b \\ q^{\mathrm{r}}_{\mathrm{lower}}+q^{\mathrm{p}}_{\mathrm{upper}}, & L\le x\le L_0,\ 0\le y\le b \end{cases}$ (3.71)

– cumulative effect of the thermal interaction of the strip with the vaporizer and the chamber walls, which is summed up of various components in the condensation and cooling areas.

For solving the stationary heat conductivity problems (3.61) – (3.65) and (3.66) – (3.71) the relaxation method [95, 96] was used, based on the solution of auxiliary non-stationary heat conductivity equations

$$\frac{\partial T}{\partial t}=A_{xz}T,\quad 0<x<L_0\ ,\quad 0<z<d\ , \tag{3.72}$$

$$\frac{\partial T}{\partial t}=A_{xy}T+\frac{q_\Sigma}{c\rho d},\quad 0<x<L_0,\quad 0<y<b, \tag{3.73}$$

until the time when the change in the temperature field becomes lower than the preset calculation error. The solution for the one-dimensional heat conduction problem was used in this case as the initial approximation:

$$A_xT+\frac{\overline{q}_\Sigma}{c\rho d}=0\ ,\ 0<x<L_0, \tag{3.74}$$

where $A_xT=\frac{1}{c\rho}\frac{\mathrm{d}}{\mathrm{d}x}\left(\lambda\frac{\mathrm{d}T}{\mathrm{d}x}\right)-u\frac{\mathrm{d}T}{\mathrm{d}x}$,

$$T(0)=T_0,\quad \left.\frac{\mathrm{d}T}{\mathrm{d}x}\right|_{x=L_0}=0, \tag{3.75}$$

resulted from the integration of the system of Equations (3.52) – (3.54) over the depth and the width of the strip and with taking into account the boundary conditions (3.55) – (3.58); here $\overline{q}_\Sigma(x)=\frac{1}{b}\int_0^b q_\Sigma(x,y)\mathrm{d}y$ – total thermal effect (3.71) averaged over the width of the strip.

The stationary problem (3.74) and (3.75) was also solved by the relaxation method using the auxiliary non-stationary heat conductivity equation

$$\frac{\partial T}{\partial t} = A_x T, \quad 0 < x < L_0, \tag{3.76}$$

under the initial condition $T(0) = T_0$.

3.3. Numerical solution of the problem

3.3.1. The algorithm for calculating the temperature field averaged over the strip width and thickness

To solve the one-dimensional heat conductivity problem (3.74)–(3.76) by the method of finite differences let us introduce a grid $x_i = i\Delta x$ ($i = 0,..,n_x$) with a step along the coordinate $\Delta x = L_0/n_x$ into the problem's domain $0 \le x \le L_0$ and build a system of difference equations relative to the grid function T_i.

The differential operator A_x for the internal nodes of the grid area can be approximated by the following difference expression:

$$A_x T \to \hat{A}_x T_i = \frac{1}{c\rho} \frac{\lambda_i^+ \left(T_{i+1} - T_i\right) - \lambda_i^- \left(T_i - T_{i-1}\right)}{\Delta x^2} - u \frac{T_{i+1} - T_{i-1}}{2\Delta x}, \tag{3.77}$$

where λ_i^- and λ_i^+ – values of the heat conductivity coefficient at temperatures $(T_{i-1} + T_i)/2$ and $(T_i + T_{i+1})/2$, respectively.

Let us introduce the discrete time $t_m = m\Delta t$, ($m = 1,2,\ldots$) with the step Δt and write a purely implicit difference scheme

$$\frac{T_i^m - T_i^{m-1}}{\Delta t} = \hat{A}_x T_i^m + \frac{\overline{q}_{\Sigma,i}}{c\rho d} \tag{3.78}$$

or

$$\left(1 + f_i^- + f_i^+\right) T_i^m =$$

$$= T_i^{m-1} + \left(f_i^- + U\right) T_{i-1}^m + \left(f_i^+ - U\right) T_{i+1}^m + \Delta T_i \ , \ i = 1,..,n_x - 1, \tag{3.79}$$

where T_i^{m-1} and T_i^m – grid temperature values at the beginning and at the end of the m-th time step, respectively; $f_i^- = \lambda_i^- \Delta t / (c\rho \Delta x^2)$

and $f_i^+ = \lambda_i^+ \Delta t / (c\rho \Delta x^2)$ are the grid Fourier numbers, where the coefficients of heat conductivity λ_i^- and λ_i^+ are determined by the temperatures at the beginning of the time step; $U = u\Delta t/\Delta x$ – grid velocity of the strip; $\Delta T_i \equiv \overline{q}_{\Sigma,i} \Delta t / (c\rho d)$.

It is to be noted that when writing the difference operator (3.77), the derivative $\partial T/\partial x$ is replaced by the central difference $(T_{i+1} - T_{i-1})/(2\Delta x)$, which provides a second-order approximation on the coordinate for the difference scheme (3.78). A disadvantage of this variant is the presence of the factor $\left(f_i^+ - U\right)$ in the right side of Equation (3.79). At $U > f_i^+$ this factor becomes a negative value causing a possible non-monotony of the difference scheme [95], which leads to physically implausible results.

To ensure the monotony of this difference scheme, one should approximate the derivative $\partial T/\partial x$ by the left-hand difference $(T_i - T_{i-1})/\Delta x$, while to preserve a second-order approximation on the coordinate one has to multiply the first summand in the operator (3.77) by the correction factor κ equal to $1/(1+U/2)$ [95]. In this case, instead of (3.77) and (3.79) we obtain

$$\hat{A}_x T_i = \frac{\kappa}{c\rho} \frac{\lambda_i^+ \left(T_{i+1} - T_i\right) - \lambda_i^- \left(T_i - T_{i-1}\right)}{\Delta x^2} - u \frac{T_i - T_{i-1}}{\Delta x}, \tag{3.80}$$

$$\left[1 + \kappa\left(f_i^- + f_i^+\right) + U\right] T_i^m =$$

$$= T_i^{m-1} + \left(\kappa f_i^- + U\right) T_{i-1}^m + \kappa f_i^+ T_{i+1}^m + \Delta T_i \ , \quad i = 1,\ldots,n_x - 1. \tag{3.81}$$

The difference analog of the boundary condition (3.74) at $x = 0$ has the usual form

$$T_{i=0}^m = T_0, \tag{3.82}$$

while at $x = L_0$ it is expressed as follows:

$$3T_{n_x}^m - 4T_{n_x-1}^m + T_{n_x-2}^m = 0. \tag{3.83}$$

When writing Equation (3.83), a three-point approximation of the first derivative was used, which ensures a second-order approximation of the boundary condition (3.75) for the stationary temperature field.

The system of difference equations (3.81) − (3.83) is solved at each time step (at the initial condition $T_i^0 = T_0$, $i = 0,...,n_x$) by the sweep method in the following sequence:

– calculation of the coefficients α_0 and β_0 for the leftmost node (at $i = 0$) by using the equations resulted from the boundary condition (3.82)

$$\alpha_0 = 0, \quad \beta_0 = T_0; \tag{3.84}$$

– calculation of the coefficients α_i and β_i for the internal nodes (at $i = 1,\ldots, n_x - 1$) by using the equations resulted from the system of difference equations (3.81)

$$\alpha_i = \frac{\kappa f_i^+}{1 + \kappa f_i^+ + \left(\kappa f_i^- + U\right)\left(1 - \alpha_{i-1}\right)}; \quad \beta_i = \frac{T_i^{m-1} + \Delta T_i + \left(\kappa f_i^- + U\right)\beta_{i-1}}{1 + \kappa f_i^+ + \left(\kappa f_i^- + U\right)\left(1 - \alpha_{i-1}\right)}; \tag{3.85}$$

– calculation of the boundary value of temperature $T_{n_x}^m$ by combining (3.83) with the difference equation (3.81) at $i = n_x - 1$:

$$T_{n_x}^m = \frac{T_{n_x-1}^{m-1} + \Delta T_{n_x-1} + \left[3\left(\kappa f_{n_x-1}^- + U\right) - \kappa f_{n_x-1}^+ - 1\right]\beta_{n_x-1}}{\alpha_{n_x-1} + \left[3\left(\kappa f_{n_x-1}^- + U\right) - \kappa f_{n_x-1}^+\right]\left(1 - \alpha_{n_x-1}\right)}; \tag{3.86}$$

– backward sweep at $i = n_x - 1,\ldots,0$ by the equation

$$T_i^m = \alpha_i T_{i+1}^m + \beta_i. \tag{3.87}$$

3.3.2. The algorithm for calculating the temperature field averaged over the strip width

For a numerical solution of the two-dimensional heat conduction problem (3.72), (3.61) – (3.65) let us introduce the grid $x_i = i\Delta x$, $z_k = k\Delta z$ ($i = 0,..,n_x$, $k = 0,..,n_z$) with steps along the coordinate $\Delta x = L_0/n_x$ and $\Delta z = d/n_z$ into the problem's domain $0 \le x \le L_0$, $0 \le z \le d$, thus presenting the differential operator (3.61) as

$$A_{xz} = A_x + A_z,$$

where $A_x T = \frac{1}{c\rho}\frac{\mathrm{d}}{\mathrm{d}x}\left(\lambda\frac{\mathrm{d}T}{\mathrm{d}x}\right) - u\frac{\mathrm{d}T}{\mathrm{d}x}$ and $A_z T = \frac{1}{c\rho}\frac{\partial}{\partial z}\left(\lambda\frac{\partial T}{\partial z}\right)$.

Let us approximate the resulting one-dimensional operators with the following difference equations:

$$A_x T \to \hat{A}_x T_{ik} = \frac{\kappa}{c\rho} \frac{\lambda_i^+ \left(T_{i+1,k} - T_{i,k}\right) - \lambda_i^- \left(T_{i,k} - T_{i-1,k}\right)}{\Delta x^2} - u \frac{T_{i,k} - T_{i-1,k}}{\Delta x}, \quad (3.88)$$

$$A_z T \to \hat{A}_z T_{ik} = \frac{1}{c\rho} \frac{\lambda_z^+ \left(T_{i,k+1} - T_{i,k}\right) - \lambda_k^- \left(T_{i,k} - T_{i,k-1}\right)}{\Delta z^2}; \quad (3.89)$$

where (similar to (3.80)) $\kappa = 1/(1+U/2)$; λ_i^-, λ_i^+, λ_k^- and λ_k^+ are the values of the heat conductivity coefficient at temperatures $\frac{T_{i-1,k}^{m-1} + T_{i,k}^{m-1}}{2}$, $\frac{T_{i,k}^{m-1} + T_{i+1,k}^{m-1}}{2}$, $\frac{T_{i,k-1}^{m-1} + T_{i,k}^{m-1}}{2}$ and $\frac{T_{i,k}^{m-1} + T_{i,k+1}^{m-1}}{2}$, respectively.

As a result, for the internal nodes of the problem's domain (at $i = 1,..,n_x - 1$, $k = 1,.., n_z - 1$) a difference analog of the heat conductivity equation (3.72) will be obtained, determining the change in grid temperatures T_{ik} during the time step Δt

$$\frac{T_{ik}^m - T_{ik}^{m-1}}{\Delta t} = \hat{A}_x T_{ik}^m + \hat{A}_z T_{ik}^m \ . \quad (3.90)$$

To solve the resulting system of difference equations we have to use the splitting method [95, 96] based on the reduction of the two-dimensional difference scheme (3.90) to the following set of one-dimensional difference schemes:

– for the heat transfer along the axis x (for $k = 0,..,n_z$)

$$\frac{T_{ik}^{'} - T_{ik}^{m-1}}{\Delta t} = \hat{A}_x T_{ik}^{'} \ , \quad i = 1,..,n_x - 1; \quad (3.91)$$

– for the heat transfer along the axis z (for $i = 0,..,n_x$)

$$\frac{T_{ik}^m - T_{ik}^{'}}{\Delta t} = \hat{A}_z T_{ik}^m, \quad k = 1,..,n_z - 1; \quad (3.92)$$

where T'_{ik} – intermediate temperature values at the end of a given time step for the heat transfer along the x axis, and in the beginning of this step for the heat transfer along the axis *z*. Under this locally represented one-dimensional approach, the calculation at each time step takes two stages: at the first stage, for each node (*i*, *k*) auxiliary values T'_{ik} are found at the preset initial temperature T_{ik}^{m-1} by taking into account heat transfer only along the axis *x*; at the second stage, the obtained values T'_{ik} are considered as the initial ones and the heat transfer along the axis z is accounted for.

Let us note that since intermediate temperatures T'_{ik} have no physical meaning, the heat conductivity coefficients included in Equation (3.91) and Equation (3.92) should be calculated according to the temperatures at the beginning of the time step T_{ik}^{m-1}.

Substituting Equation (3.88) for the difference operator $\hat{A}_x$ in Equation (3.91) and writing similarly to (3.82) and (3.83) the difference analogues of the boundary conditions (3.62) and (3.63), we'll get a comprehensive difference scheme describing the heat transfer along the axis *x*:

$$\begin{gathered}\left[1+\kappa\left(f_i^- + f_i^+\right)+U\right]T'_{i,k} = \\ = T_{i,k}^{m-1} + \left(\kappa f_i^- + U\right)T'_{i-1,k} + \kappa f_i^+ T'_{i+1,k}\ , \quad i = 1,...,n_x - 1\ ;\end{gathered} \tag{3.93}$$

$$T'_{0,k} = T_0, \tag{3.94}$$

$$3T'_{n_x,k} - 4T'_{n_x-1,k} + T'_{n_x-2,k} = 0. \tag{3.95}$$

The system of difference equations (3.93) – (3.95) for each $k = 0,..,n_z$ is solved by the sweep method, using equations analogous to (3.84) – (3.87):

$$\alpha_0 = 0, \quad \beta_0 = T_0; \tag{3.96}$$

$$\begin{gathered}\alpha_i = \frac{\kappa f_i^+}{1+\kappa f_i^+ + \left(\kappa f_i^- + U\right)\left(1-\alpha_{i-1}\right)}, \\ \beta_i = \frac{T_{i,k}^{m-1} + \left(\kappa f_i^- + U\right)\beta_{i-1}}{1+\kappa f_i^+ + \left(\kappa f_i^- + U\right)\left(1-\alpha_{i-1}\right)},\ i = 1,..,n_x - 1;\end{gathered} \tag{3.97}$$

$$T'_{n_x,k} = \frac{T^{m-1}_{n_x-1,k} + \left[3\left(\kappa f^-_{n_x-1} + U\right) - \kappa f^+_{n_x-1} - 1\right]\beta_{n_x-1}}{\alpha_{n_x-1} + \left[3\left(\kappa f^-_{n_x-1} + U\right) - \kappa f^+_{n_x-1}\right]\left(1-\alpha_{n_x-1}\right)}; \qquad (3.98)$$

$$T'_{i,k} = \alpha_i T'_{i+1,k} + \beta_i \ , \quad i = n_x - 1,..,0 \ . \qquad (3.99)$$

To calculate the heat transfer along the axis z let us rewrite the equations (3.92) as follows

$$\left(1 + f^-_k + f^+_k\right)T^m_{i,k} = T'_{i,k} + f^-_k T^m_{i,k-1} + f^+_k T^m_{i,k+1} \ , \quad k = 1,...,n_z - 1 \ , \qquad (3.100)$$

and add to them the difference analogs of the boundary conditions (3.64) and (3.65)

$$-\lambda_0 \frac{3T^m_{i,0} - 4T^m_{i,1} + T^m_{i,2}}{2\Delta z} = q_{i,0}; \qquad (3.101)$$

$$\lambda_{n_z} \frac{3T^m_{i,n_z} - 4T^m_{i,n_z-1} + T^m_{i,n_z-2}}{2\Delta z} = q_{i,n_z}; \qquad (3.102)$$

where (as well as when writing Equation (3.83)) the three-point approximation of the first derivative was used; λ_0, λ_{n_z} – values of the heat conductivity coefficient at the temperatures $T^{m-1}_{i,0}$ and T^{m-1}_{i,n_z}; $q_{i,0}$ and q_{i,n_z} – external heat flow density appearing in the boundary conditions (3.64) and (3.65), respectively.

The system of difference equations (3.100) − (3.102) for each $i = 1,..,n_x$ is solved by the sweep method in the following sequence:

– sweep coefficients α_0 and β_0 are calculated for the leftmost node (at $k = 0$) by the equations derived from the boundary condition (3.101) combined with the difference equation (3.100) at $k = 1$

$$\alpha_0 = \frac{3f^+_1 - f^-_1 - 1}{3f^+_1 - f^-_1}, \quad \beta_0 = \frac{T'_{i,1} + 2f^+_1 \Delta T_0}{3f^+_1 - f^-_1}; \qquad (3.103)$$

– sweep coefficients α_k and β_k for the internal nodes (at $k = 1,..,n_z - 1$) are calculated by the equations derived from the system of difference equations (3.100)

$$\alpha_k = \frac{f_k^+}{1 + f_k^+ + f_k^- \left(1 - \alpha_{k-1}\right)}, \quad \beta_k = \frac{T_{i,k}^{'} + f_k^- \beta_{k-1}}{1 + f_k^+ + f_k^- \left(1 - \alpha_{k-1}\right)}, \quad k = 1,..,n_z - 1; \quad (3.104)$$

– calculation of the boundary temperature $T_{n_x}^m$ based on Equation (3.102) combined with the difference equation (3.100) at $k = n_z - 1$

$$T_{i,n_z}^m = \frac{T_{i,n_z-1}^{'} + 2 f_{n_z-1}^- \Delta T_{n_z} + \left[3 f_{n_z-1}^- - f_{n_z-1}^+ - 1\right] \beta_{n_z-1}}{\alpha_{n_z-1} + \left(3 f_{n_z-1}^- - f_{n_z-1}^+\right)\left(1 - \alpha_{n_z-1}\right)}; \quad (3.105)$$

– backward sweep at $k = n_z - 1,\ldots,0$ by the equation

$$T_{i,k}^m = \alpha_k T_{i,k+1}^m + \beta_k. \quad (3.106)$$

3.3.3. The algorithm for calculating the temperature field averaged over the strip thickness

To solve the two-dimensional heat conduction problem (3.73), (3.66) – (3.71) numerically let us introduce into the problem's domain $0 \le x \le L_0$, $0 \le y \le b$ the grid $x_i = i\Delta x$, $y_j = j\Delta y$ ($i = 0,..,n_x$, $j = 0,..,n_y$) with steps along the coordinate $\Delta x = L_0/n_x$ и $\Delta y = b/n_y$, presenting the differential operator (3.66) as

$$A_{xy} = A_x + A_y,$$

where $A_x T = \frac{1}{c\rho}\frac{\mathrm{d}}{\mathrm{d}x}\left(\lambda \frac{\mathrm{d}T}{\mathrm{d}x}\right) - u\frac{\mathrm{d}T}{\mathrm{d}x}$ and $A_y T = \frac{1}{c\rho}\frac{\mathrm{d}}{\mathrm{d}y}\left(\lambda \frac{\mathrm{d}T}{\mathrm{d}y}\right)$.

Let us approximate the resulting one-dimensional operators with the following difference expressions:

$$A_x T \to \hat{A}_x T_{ij} = \frac{\kappa}{c\rho}\frac{\lambda_i^+ \left(T_{i+1,j} - T_{i,j}\right) - \lambda_i^- \left(T_{i,j} - T_{i-1,j}\right)}{\Delta x^2} - u\frac{T_{i,j} - T_{i-1,j}}{\Delta x}, \quad (3.107)$$

$$A_y T \to \hat{A}_y T_{ij} = \frac{1}{c\rho} \frac{\lambda_j^+ \left(T_{i,j+1} - T_{i,j}\right) - \lambda_j^- \left(T_{i,j} - T_{i,j-1}\right)}{\Delta y^2}; \qquad (3.108)$$

where (similar to (3.88)) $\kappa = 1/(1+U/2)$; λ_i^-, λ_i^+, λ_j^- and λ_j^+ – values of the heat conductivity coefficient at the temperatures $(T_{i-1,j}^{m-1} + T_{i,j}^{m-1})/2$, $(T_{i,j}^{m-1} + T_{i+1,j}^{m-1})/2$, $\left(T_{i,j-1}^{m-1} + T_{i,j}^{m-1}\right)/2$ and $\left(T_{i,j}^{m-1} + T_{i,j+1}^{m-1}\right)/2$, respectively.

As a result, the difference analog of the heat equation (3.73) for the internal nodes of the problem's domain (at $i = 1,..,n_x - 1$, $j = 1,..,n_y - 1$) is obtained, which determine the alteration of grid temperatures T_{ij} during the time step Δt

$$\frac{T_{ij}^m - T_{ij}^{m-1}}{\Delta t} = \hat{A}_x T_{ij}^m + \hat{A}_y T_{ij}^m + \frac{q_{\Sigma,ij}}{c\rho d} \ . \qquad (3.109)$$

Applying the splitting method let us write the following set of one-dimensional difference schemes:

– for the heat transfer along the axis x (for $j = 0,..,n_y$)

$$\frac{T_{ij}^{'} - T_{ij}^{m-1}}{\Delta t} = \hat{A}_x T_{ij}^{'} + \frac{q_{\Sigma,ij}}{c\rho d} \ , \quad i = 1,..,n_x - 1; \qquad (3.110)$$

– for the heat transfer along the axis y (for $i = 0,..,n_x$)

$$\frac{T_{ij}^m - T_{ij}^{'}}{\Delta t} = \hat{A}_y T_{ij}^m \ , \quad j = 1,..,n_y - 1 \ ; \qquad (3.111)$$

where $T_{ij}^{'}$ – intermediate temperature values at the end of a given time step for the heat transfer along the axis x and at the beginning of this step for the heat transfer along the axis y.

By substituting Equation (3.109) for the difference operator $\hat{A}_x$ in Equation (3.110) and writing similarly to (3.82) and (3.83) the difference analogues of the boundary conditions (3.67) and (3.68), we'll get a comprehensive difference scheme describing the heat transfer along the axis x

$$\left[1+\kappa\left(f_i^- + f_i^+\right)+U\right]T'_{i,j} = \\ = T_{i,j}^{m-1} + \left(\kappa f_i^- + U\right)T'_{i-1,j} + \kappa f_i^+ T'_{i+1,j} + \Delta T_{ij},\ i=1,...,n_x-1; \tag{3.112}$$

$$T'_{0,j} = T_0, \tag{3.113}$$

$$3T'_{n_x,j} - 4T'_{n_x-1,j} + T'_{n_x-2,j} = 0; \tag{3.114}$$

where $\Delta T_{i,j} \equiv q_{\Sigma,ij}\Delta t / \left(c\rho d\right)$.

The system of difference equations (3.112) – (3.114) for each $j = 0,..,n_y$ is solved by the sweep method using the equations similar to (3.84) – (3.87):

$$\alpha_0 = 0,\quad \beta_0 = T_0; \tag{3.115}$$

$$\alpha_i = \frac{\kappa f_i^+}{1+\kappa f_i^+ + \left(\kappa f_i^- + U\right)\left(1-\alpha_{i-1}\right)},$$

$$\beta_i = \frac{T_{i,j}^{m-1} + \Delta T_{i,j} + \left(\kappa f_i^- + U\right)\beta_{i-1}}{1+\kappa f_i^+ + \left(\kappa f_i^- + U\right)\left(1-\alpha_{i-1}\right)},\ i=1,..,n_x-1; \tag{3.116}$$

$$T'_{n_x,j} = \frac{T_{n_x-1,j}^{m-1} + \Delta T_{n_x-1,j} + \left[3\left(\kappa f_{n_x-1}^- + U\right) - \kappa f_{n_x-1}^+ - 1\right]\beta_{n_x-1}}{\alpha_{n_x-1} + \left[3\left(\kappa f_{n_x-1}^- + U\right) - \kappa f_{n_x-1}^+\right]\left(1-\alpha_{n_x-1}\right)}; \tag{3.117}$$

$$T'_{i,j} = \alpha_i T'_{i+1,j} + \beta_i,\quad i = n_x-1,..,0. \tag{3.118}$$

To calculate the heat transfer along the axis y let us rewrite Equation (3.111) as

$$\left(1+f_j^- + f_j^+\right)T_{i,j}^m = T'_{i,j} + f_j^- T_{i,j-1}^m + f_j^+ T_{i,j+1}^m,\ j=1,...,n_y-1 \tag{3.119}$$

and add to them the difference analogues of the boundary conditions (3.57) and (3.58)

$$3T_{i,0}^{m} - 4T_{i,1}^{m} + T_{i,2}^{m} = 0 \; ; \tag{3.120}$$

$$3T_{i,n_y}^{m} - 4T_{i,n_y-1}^{m} + T_{i,n_y-2}^{m} = 0 \; ; \tag{3.121}$$

here (like in the previous cases) we used a three-point approximation of the first derivative.

The system of difference equations (3.119) – (3.121) for each $i = 1,..,n_x$ is solved by the sweep method as follows:

– sweep coefficients α_0 and β_0 for the leftmost node (at $j = 0$) are calculated by the equations derived from the boundary condition (3.120) combined with the difference equation (3.119) at $j = 1$:

$$\alpha_0 = \frac{3f_1^+ - f_1^- - 1}{3f_1^+ - f_1^-}, \quad \beta_0 = \frac{T_{i,1}^{'} + 2f_1^+ \Delta T_{i,1}}{3f_1^+ - f_1^-}; \tag{3.122}$$

– sweep coefficients α_j и β_j for the internal nodes (at $j = 1,..,n_y - 1$) are calculated by the equations derived from the system of difference equations (3.119)

$$\alpha_j = \frac{f_j^+}{1 + f_j^+ + f_j^- \left(1 - \alpha_{j-1}\right)}, \quad \beta_j = \frac{T_{i,j}^{'} + f_j^- \beta_{j-1}}{1 + f_j^+ + f_j^- \left(1 - \alpha_{j-1}\right)}, \; j = 1,..,n_y - 1; \tag{3.123}$$

– calculation of the boundary temperature $T_{n_y}^{m}$ based on Equation (3.121) combined with difference equation (3.119) at $j = n_y - 1$:

$$T_{i,n_y}^{m} = \frac{T_{i,n_y-1}^{'} + \Delta T_{i,n_y-1} + \left[3f_{n_y-1}^- - f_{n_y-1}^+ - 1\right]\beta_{n_y-1}}{\alpha_{n_y-1} + \left(3f_{n_y-1}^- - f_{n_y-1}^+\right)\left(1 - \alpha_{n_y-1}\right)}; \tag{3.124}$$

– backward sweep at $j = n_y - 1,..,0$ by equation

$$T_{i,j}^{m} = \alpha_j T_{i,j+1}^{m} + \beta_j . \tag{3.125}$$

3.4. Testing the adequacy of the developed mathematical simulation

To test the adequacy of the developed mathematical simulation we conducted an experimental study of the process of titanium vacuum deposition in the УВ68Л plant designed to make hard-deformed alloy foils [35,

65]. The substrate was made of the strip 12C18Cr9Ni steel, $2b$ = 400 mm wide and d = 0.5 mm thick, having the initial temperature of T_0 = 300 °C and moving at the speed of 0.3 m/min in the condensation zone L = 400 mm long. Two vaporizers were installed in the middle of the condensation zone ($l = L/2$) at the distances of h_{vap} = 320 mm from the strip and of $2b_{vap}$ = 220 mm from each other. The capacity of the electron beam guns used to evaporate titanium was 80 kw with the corresponding total evaporation rate of $G_0 = 3.6 \cdot 10^{-4}$ kg/s. The following values and dependences were taken for the other simulation parameters [88, 97]: c_{strip} = 460 J/(kg·K); ρ_{strip} = =7900 – 0.4·T kg/m^3; λ_{strip} = 17 + 0.01·T, w/(m·K); $\varepsilon_{lun} = 0.15+0.12 \cdot 10^{-3} \cdot T$; ε_{ch} = 0.3; T_{ch} = 50 °C; T_{cryst} = 1670 °C ; Λ_{cryst} = 315 kJ/kg; Λ_{cond} = 8560 kJ/kg; c_{solid} = 640 J/(kg·K); c_{liquid} = 700 J/(kg·K); ρ_{cond} = 4500 kg/m^3; ε_{con} = = 0.13 + 0.25·10^{-3}·T; ε = 0.4 (in the equations defining the temperature dependence of the thermal characteristics T is expressed in °C). In using the model of cylindrical lunule we took its radius equal to the radius of the electron beam r_0 = 12 mm, while its depth h_0, calculated in p.p. 3.1.1, was taken equal to 5.1 mm. The calculated and experimentally found values of the dimensionless thickness of the condensate and the vapor utilization coefficient are compared in Fig. 3.11.

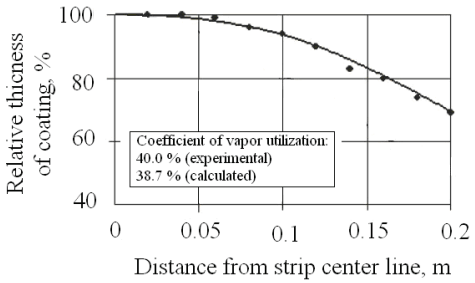

Fig. 3.11. Relative profile of the coating in the end of the condensation zone. The points correspond to the experimental data

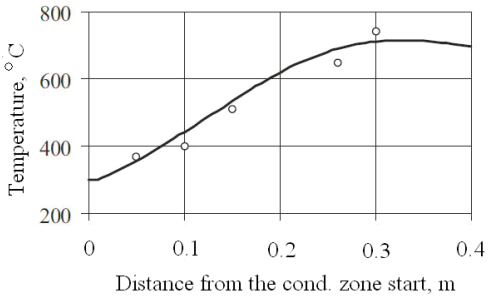

Fig. 3.12. Temperature change along the strip central line within the condensation zone. The points correspond to the experimental data

We also tested the adequacy of the developed mathematical simulation using the results of the experimental study of copper, nickel and titanium vacuum deposition in the УВФ-75-1 plant under the following conditions: $2b$ = 120…150 mm; L = 110…120 mm;

h_{vap} = 210 mm; r_0 = 3 mm [35]. As shown by the data in Table. 3.4, the calculated and experimentally found values of the vapor utilization coefficient match only in the case of titanium evaporation. This is another confirmation of the validity of the suggested method for calculating the spatial distribution of the vapor flow, because only in this particular case the condition of applicability of the isothermal lunule model is fulfilled (3.23).

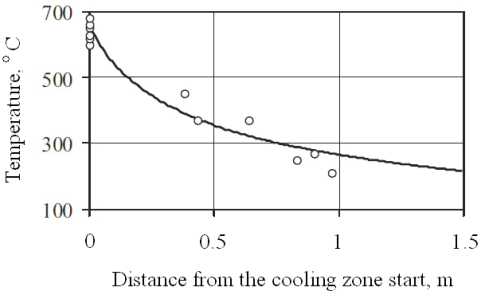

Fig. 3.13. Change of the strip average temperature within the cooling zone. The points correspond to the experimental data

Table 3.4

Comparison of calculated and experimental values of the vapor utilization coefficient in the УВФ-75-1 plant

Metal	Evaporation rate. kg/m² s	Evaporation temperature. °C	Excess evaporation temperature. °C	Evaporation heat coefficient. kW/ (m² · K)	Heat conductivity coefficient. W/(m² · K)	Criterion of applicability of the model of isothermal lunule	Estimated lunule depth. mm	Vapor utilization coefficient, %	
								Calculation	Experiment
Cu	7.08	2176	1093	128.7	300	1.3	11.8	71.3	17
Ni	2.83	2342	1183	118.3	70	5.1	3.6	21.9	13.7
Ti	1.80	2600	915	94.4	20	14.2	1.4	16.7	16.5

The experimental study of the temperature change along the substrate strip to test the adequacy of the calculational block, describing the processes of heat transfer, was carried out in the УВ68Л plant using one va-

porizer. As shown in Fig. 3.12 and Fig. 3.13, the calculated values of the strip temperature both within the condensation zone and the cooling zone match well the experimental data.

Note that under these conditions the maximum temperature spread over the strip thickness, found by solving the system of equations (3.61) − (3.65), is only 0.2 °C, thus confirming the possibility of using the two-dimensional heat conduction problem (3.66) − (3.71) for a sufficiently precise calculation of the temperature field of the strip.

Thus, this mathematical simulation of heat and mass transfer in the working space of the vacuum deposition chamber adequately describes both the temperature field of the strip during the deposition process and the parameters of the resulting condensate layer, which makes it possible to recommend the proposed method for predicting heat and mass transfer processes in vacuum deposition plants.

3.5. Application of the developed mathematical simulation to predict heat and mass transfer processes during vacuum deposition

As the analysis of the conditions ensuring the maximum uniformity of the condensate layer is of practical importance, the developed mathematical simulation was used to study the effect of the levelling screen on the condensate profile and on the substrate strip temperature field at vacuum deposition in the УВ68Л plant equipped with two vaporizers.

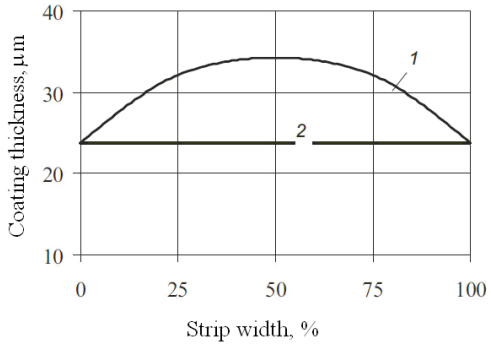

Fig. 3.14. Condensate profile at the end of the condensation zone: *1* – without the screen; *2* – with the screen

Figure 3.14 shows the results of calculating the condensate profile at the exit from the condensation zone without (*1*) and with (*2*) a two-sided symmetric levelling screen.

The shape of the screen, that ensures obtaining the condensate profile 2, was found by solving Equation (3.48) and is shown in Fig. 3.15. Here and on the next figures the letters *A, B* and *C* mark the condensation zone cross-sec-

tions corresponding to the end of the first half-screen, the beginning of the second half-screen and the end of the condensation zone, respectively. Figs. 3.16 − 3.18 show the results of calculating the temperature changes along the length and the width of the strip with and without the screen.

The results in Fig. 3.16 show that the temperature averaged over the width of the strip without the screen increases almost linearly within major part of the condensation zone (Curve *1*). The use of the levelling screen causes a slower rise in temperature only at the initial part of the zone (Curve *2*).

The rise in the strip temperature slows down at the end of the condensation zone, and then it stops and even reverses to negative, i.e. the strip begins to cool down, while still in the condensation zone. This is because the intensity of the heating factors, i.e. heat emission at condensation and heat radiation from the vaporizer, becomes lower than the intensity of radiation heat exchange with the chamber walls due to which the strip loses heat.

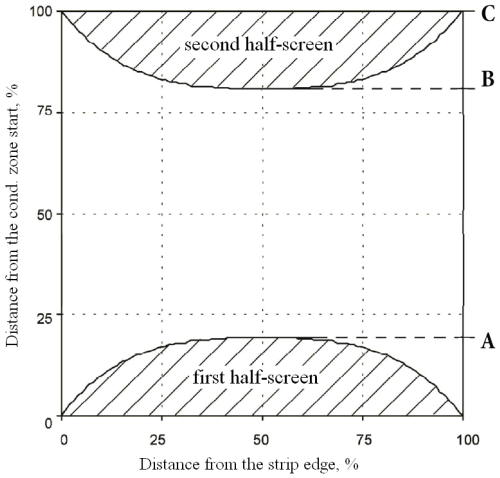

Fig. 3.15. The shape and position of the levelling screen within the condensation zone

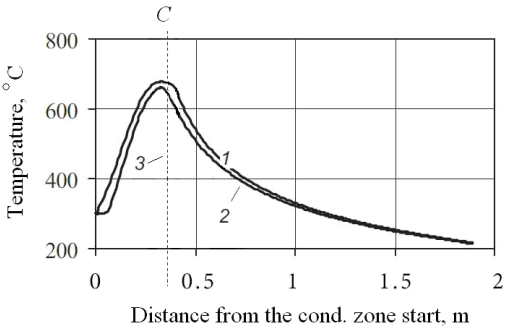

Fig. 3.16. Changes in the temperature averaged over the strip width within the condensation and cooling zones: *1* – without the screen; *2* – with the screen; *3* – end of the condensation zone

This change is mainly owing to the geometric factors and occurs more abruptly with the screen, as the screen retains the entire vapor flow and weak-

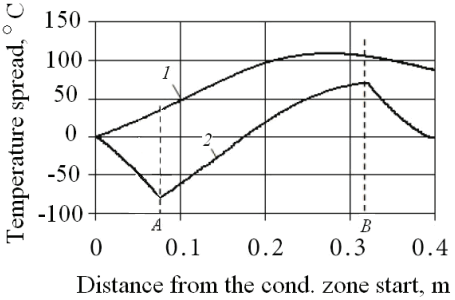

Fig. 3.17. Variations in the temperature spread across the width of the strip, $\Delta T(x)$, within the condensation zone: *1* – without the screen; *2* – with the screen

ens the heat radiation flow from the vaporizer, thus shifting the temperature maximum towards the beginning of the condensation zone. However, the strip temperature change caused by the screen is not very large, being not more than 85 °C at the end of the condensation zone, and, moreover, the range of the strip temperature change when using the screen is lower (by 30 °C) than without any screens.

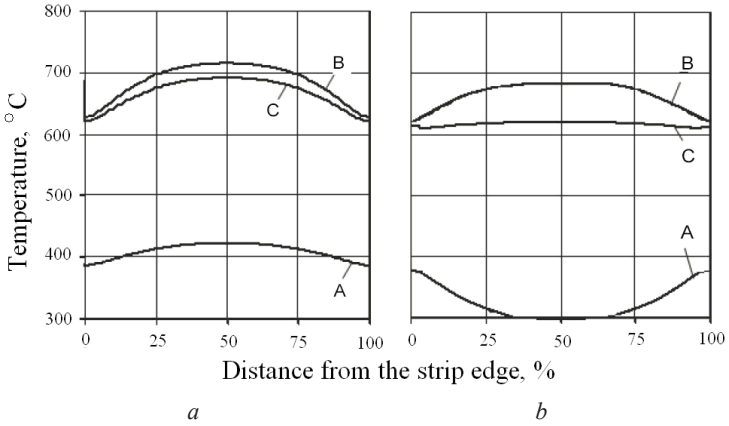

Fig. 3.18. The temperature change across the width of the strip in different sections of the condensation zone: *a* – without the screen; *b* – with the screen

A more detailed information on the temperature field of the strip is shown in Fig. 3.17 and Fig. 3.18, illustrating the temperature change across the width of the strip during its movement in the condensation zone. The strip temperature spread in the cross-section of the condensation zone ($x = 0$ at its beginning) means the difference $\Delta T(x) = T(x,0) - T(x,b)$ for the central and the edge strip points of a given cross-section x. Without screening the temperature heterogeneity across the strip width increases virtually through the entire zone of condensation (see Fig. 3.17, Curve *1*), while

with screening the first half-screen reverses the sign of the heterogeneity ΔT, which reaches its maximum (by the absolute value) in the cross-section *A* (see Fig. 3.17, Curve *2* and Fig. 3.18, *b*) and subsequently decreases up to $\Delta T = 0$ in the middle of the condensation zone. Then it increases till the cross-section *B,* when, with further *x* growth, the effect of the second half-screen leads to a substantial decreasing of ΔT up to almost zero at the exit from the condensation zone (cross-section *C*).

Thus, screening causes a significant change in the pattern of temperature distribution across the width of the substrate strip within a great part of the condensation zone.

When studying the conditions of foil formation, the information on the uniformity of temperature conditions in different cross-sections of the strip in the condensation zone at a given condensate thickness is of more significance than the above-mentioned results on the strip temperature spread. Fig. 3.19 shows mathematical simulation results of temperature conditions for the formation of condensate layers of a given thickness. The comparison of Fig. 3.19, *a* and Fig. 3.19, *b* indicates that the presence of the screen has no significant effect on the homogeneity of these conditions.

To facilitate the comparison of the results of the structural analysis of a condensate layer with the temperature conditions of its formation, the data shown in Fig. 3.19 can be presented in a tabular form. Thus, Tables 3.5 and 3.6 show absolute (T, °C) and relative (T/T_s, K; T_s – melting point) temper-

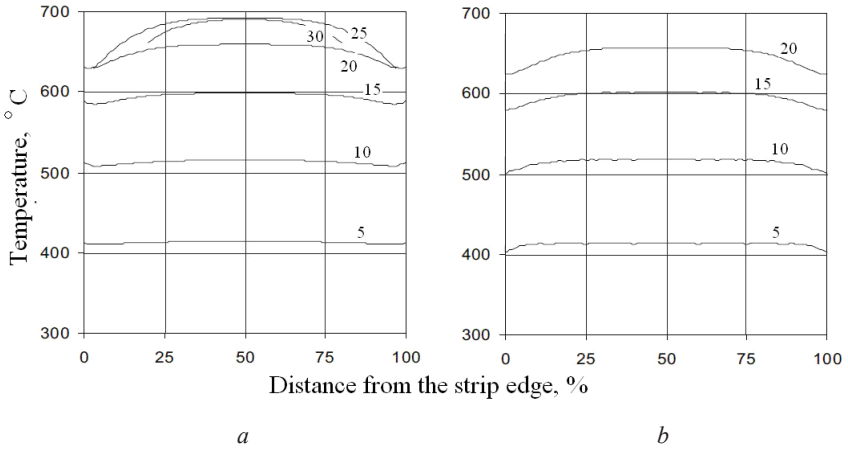

Fig. 3.19. Temperatures at which a condensate layer of preset thickness is formed: *a* – with no screen; *b* – with the screen (numbers at the curves – condensate layer thickness, μm)

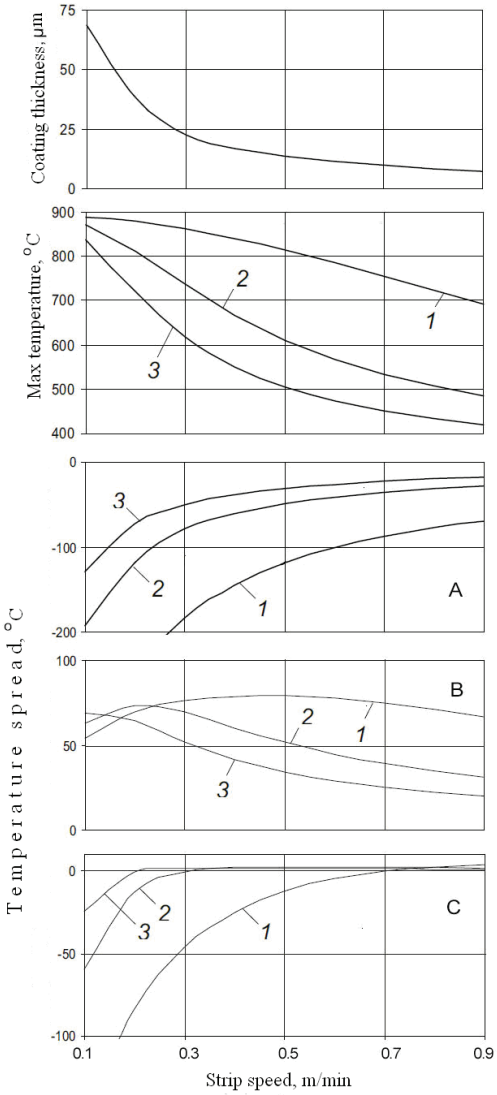

Fig. 3.20. The effect of strip speed on condensate thickness and thermal characteristics of the vacuum deposition process at strip thickness of 0.2 mm (*1*), 0.5 mm (*2*) and 0.8 mm (*3*)

atures, corresponding to the formation of condensates of preset thickness, at various distances from the central line of the substrate strip when using the screen.

The developed mathematical simulation can be used also for studying the dependence of different factors that may concern the researcher (condensate thickness, maximum temperature, heterogeneity of the temperature field) on the technological (integral evaporation rate, strip speed) and structural (strip thickness, the number of vaporizers and their position in the condensation zone) parameters. Some of these dependencies are shown in Fig. 3.20.

The present data show that the condensate thickness increases as the strip speed decreases and when the speed falls below 0.3 m/min this dependence becomes stronger than at a higher speed; the maximum strip temperature decreases as its speed increases, but the type of this dependence is significantly influenced by the strip thickness: this dependence is stronger for thin strips and, on the contrary, weaker for thick strips at a higher speed of the strip movement.

Table 3.5

Temperatures (°C) in condensate layers of preset thickness δ

δ, μm	The distance from the central line of the strip, mm										
	0	20	40	60	80	100	120	140	160	180	200
1	320.0	320.0	319.2	320.5	319.9	319.6	320.8	320.9	321.9	323.2	317.7
2	344.2	344.2	343.4	344.7	344.1	343.7	344.8	344.7	345.3	345.7	338.6
3	367.9	368.0	367.1	368.5	367.8	367.4	368.4	368.0	368.3	367.9	359.9
4	391.2	391.3	390.4	391.8	391.0	390.5	391.4	390.8	390.7	389.6	381.2
5	414.0	414.0	413.2	414.5	413.7	413.2	413.9	413.1	412.6	410.8	402.4
6	436.2	436.2	435.4	436.6	435.8	435.3	435.9	434.7	433.9	431.5	4233
7	457.7	457.8	457.0	458.2	4573	456.7	457.1	455.8	454.5	451.6	443.7
S	478.6	478.7	477.9	479.0	478.2	477.5	477.8	476.2	474.5	471.1	463.6
9	498.8	498.9	498.1	499.2	4983	497.6	497.7	495.8	493.8	489.9	482.9
10	518.2	518.3	517.5	518.5	517.7	516.9	516.8	514.7	512.3	507.9	501.4
11	536.8	536.9	536.1	537.1	536.2	535.4	535.1	532.8	529.9	525.1	519.2
12	554.5	554.6	553.8	554.7	553.8	553.0	552.6	550.0	546.7	541.5	536.0
13	571.2	571.3	570.6	571.4	570.5	569.6	569.1	566.2	562.4	556.8	551.9
14	586.9	587.0	586.3	587.1	586.2	585.3	584.5	581.3	577.1	571.1	566.6
15	601.6	601.7	601.0	601.7	600.8	599.8	598.7	595.3	590.7	5843	580.1
16	615.2	615.3	614.6	615.2	6143	613.1	611.7	608.0	603.0	596.1	592.2
17	627.6	627.7	627.1	627.5	626.5	625.2	623.5	619.5	613.9	606.7	602.8
18	638.8	638.8	638.2	638.5	637.5	636.0	633.9	629.5	623.5	615.8	611.8
19	648.6	648.7	648.1	648.2	647.1	645.4	643.0	638.2	631.5	6233	619.0
20	657.2	657.2	656.6	656.6	655.4	653.4	650.5	645.2	638.0	629.1	624.2
21	664.3	664.2	663.7	663.5	662.1	659.9	656.5	650.7	642.7	633.0	6273
22	669.9	669.8	669.3	668.8	6673	664.8	660.8	654.4	645.6	634.9	628.0

The temperature spread across the strip width substantially depends on the strip speed and thickness. As both parameters increase, the temperature differences in the cross-section *A* are reduced, while in the *B* section the temperature profile is close to a uniform one, but, in qualitative terms, the type of such dependence on the strip speed varies due to different strip thickness. The second half-screen generates a reverse thermal heterogeneity (negative spread) at the exit from the condensation zone, the value of which also depends on the strip thickness and speed. For example, the strip thickness of more than 0.5 mm and its speed higher than 0.3 m/min ensures a virtually uniform temperature field across the width of the strip at the exit from the condensation zone, while at the strip thickness of 0.2 mm and its speed of 0.3 m/min the temperature difference across the strip width at the exit from the condensation zone is ~50 °C,

demonstrating small values only at the strip speed of around 0.7 m/min. At low speeds (< 0.2 m/min) of thin strips (d < 0.2 mm) the temperature gradient across the strip width at the exit from the condensation zone can exceed 100 °C.

Table 3.6

Relative temperatures, T/T_s, in condensate layers of preset thickness δ

δ, μm	Distance from the center line of the strip, mm										
	0	20	40	60	80	100	120	140	160	180	200
1	0.303	0.303	0.302	0.303	0.303	0.303	0.303	0.303	0.304	0.304	0.302
2	0.315	0.315	0.315	0.315	0.315	0.315	0.316	0.315	0.316	0.316	0.312
3	0.327	0.327	0.327	0.328	0.327	0.327	0.328	0.327	0.328	0.327	0.323
4	0.339	0.339	0.339	0.340	0.339	0.339	0.339	0.339	0.339	0.338	0.334
5	0.351	0.351	0.350	0.351	0.351	0.350	0.351	0.350	0.350	0.349	0.345
6	0.362	0.362	0.362	0.362	0.362	0.362	0.362	0.361	0.361	0.360	0.356
7	0.373	0.373	0.373	0.373	0.373	0.373	0.373	0.372	0.372	0.370	0.366
8	0.384	0.384	0.383	0.384	0.384	0.383	0.383	0.383	0.382	0.380	0.376
9	0.394	0.394	0.394	0.394	0.394	0.394	0.394	0.393	0.392	0.390	0.386
10	0.404	0.404	0.404	0.404	0.404	0.403	0.403	0.402	0.401	0.399	0.396
11	0.414	0.414	0.413	0.414	0.413	0.413	0.413	0.412	0.410	0.408	0.405
12	0.423	0.423	0.422	0.423	0.422	0.422	0.422	0.420	0.419	0.416	0.413
13	0.431	0.431	0.431	0.431	0.431	0.430	0.430	0.429	0.427	0.424	0.421
14	0.439	0.439	0.439	0.439	0.439	0.438	0.438	0.436	0.434	0.431	0.429
15	0.447	0.447	0.446	0.447	0.446	0.446	0.445	0.443	0.441	0.438	0.436
16	0.454	0.454	0.453	0.454	0.453	0.453	0.452	0.450	0.447	0.444	0.442
17	0.460	0.460	0.460	0.460	0.459	0.459	0.458	0.456	0.453	0.449	0.447
18	0.466	0.466	0.465	0.466	0.465	0.464	0.463	0.461	0.458	0.454	0.452
19	0.471	0.471	0.470	0.471	0.470	0.469	0.468	0.465	0.462	0.458	0.456
20	0.475	0.475	0.475	0.475	0.474	0.473	0.472	0.469	0.465	0.461	0.458
21	0.479	0.479	0.478	0.478	0.478	0.476	0.475	0.472	0.468	0.463	0.460
22	0.482	0.482	0.481	0.481	0.480	0.479	0.477	0.474	0.469	0.464	0.460

Calculations made for different values of the integral evaporation rate lead to the conclusion about a significant impact of this factor both on the temperatures reached by different parts of the strip and on the temperature spread across the width of the strip. Table 3.7 shows the data for the strip speed of 0.3 m/s and the two values of strip thicknesses, 0.2 mm and 0.8 mm (the values referring to the strip thickness of 0.8 mm are given in brackets).

Table 3.7

The effect of evaporation rate and substrate thickness on the temperature characteristics of the vacuum deposition process

Evaporation rate, g/s	Temperature spread, °C		Maximum temperature, °C
	Cross-section A	Cross-section B	
0.2	–106 (–28)	67 (32)	706 (484)
0.3	–155 (–42)	73 (45)	811 (570)
0.4	–202 (–56)	77 (56)	892(651)

The calculation method developed for heat and mass transfer processes in the chamber for vacuum deposition of metals onto a moving substrate strip, taking into account the influence of structural and technological parameters of the vacuum deposition plant as well as thermal characteristics of the strip and the condensate, can be pivotal for the analysis of the influence of the temperature field of the substrate strip on the structure and the properties of foils produced by the vacuum deposition method.

CHAPTER 4. MAIN LAWS OF THE EVAPORATION PROCESS OF MULTI-COMPONENT ALLOYS OUT OF A CONTINUOUSLY FED MOLTEN POOL

To ensure the required chemical composition of the foil, made by the metal evaporation and deposition onto a substrate, it is necessary to know the kinetics of the changes in the metal pool composition during evaporation and the resulting stationary concentrations of the alloying components.

The problem of the formation of the chemical composition of vacuum condensates made of alloys is dealt with in [98−110]. They suggest various calculation methods of the equilibrium pool composition, descriptions of the evaporation kinetics for binary alloys, calculation methods of the changes in the compositions of both the melt and its condensate depending on the evaporation time; consider the case of binary alloy evaporation from one source, offer a numerical method of solving the problem of the changes in the binary melt and its condensate compositions under the steady conditions for pool volume, melt surface temperature and melt feeding rate.

In [98] they studied binary alloys evaporation from one source without feeding. A numerical method to calculate the condensate compositional changes in dependence on the deposition time was suggested. However, the results of this work are of limited importance as far as a long process of intense evaporation is concerned, as it requires feeding the molten pool as the melt is evaporated.

The evaporation of binary alloys from one source with the melt feeding was studied in [99]. An expression for the equilibrium composition of the molten metal pool was obtained, but no analytical results for the time dependence of the compositional changes in the pool were given. An approximate estimation of the time needed for the binary alloy pool to reach the steady state can be found in [100], though without taking into account the pool feeding.

In [101−103] the problem of analytical description for the kinetics of binary alloy evaporation was solved, however, it does not take into account that, in a general case, evaporation rates are proportional to the mole fraction but not to the mass fraction. It significantly affects the form of the main equation. Another limitation of the analytical description in [101−103] is the necessity of a preliminary experimental determination of the stationary state parameters (evaporation rate and equilibrium

concentration of the components). In a number of cases, in particular, if an alloy comprises refractory components with low vapor pressure, it may be quite a difficult task.

An approximate numerical calculation method suggested in [104] accounts for the changes in the melt and its condensate compositions depending on the evaporation time.

In [105, 106] the case of binary alloy evaporation from one source was considered, however, the process in [105] does not include the feeding of the molten metal pool during evaporation. The numerical method proposed in [106] permits solving the problem of the changes in the binary melt and its condensate compositions under the constant conditions of molten metal pool volume, melt surface temperature and melt feeding rate.

Analytical solutions for two- and three-component alloys were obtained in [107], and it was proved that all the eigenvalues of the solutions were valid. However, there is an inaccurate point in this article. The equation given is true not for the constant volume of the molten metal, as indicated by the authors, but for the constant total number of molecules in the molten metal pool.

The above mentioned works have some strong and weak points. The general shortcoming of the works in question was the lack of analytical solutions for the case of the evaporation from one source with feeding the molten metal and an arbitrary number of alloy components.

Further analytical solutions for the problems of determining the composition of the equilibrium pool and changing the composition of the molten metal during the evaporation process for multi-component alloys with an arbitrary number of alloying elements will be proposed. The calculation results will be compared with the experimental data on titanium alloy evaporation.

4.1. The composition of the equilibrium pool of molten metal with an arbitrary number of alloy components

The component vapor pressure over the molten metal P_i is proportional to the component activity in the molten metal pool a_i:

$$P_i = a_i \cdot P_i^{st} = \gamma_i N_i P_i^{st} \tag{4.1}$$

where P_i^{st} – vapor pressure in standard state; γ_i – activity ratio; N_i – mole fraction of the i-th component.

Evaporation rate of the *i*-th component Q_i is proportional to the vapor pressure over the molten metal pool

$$Q_i = K_i P_i \tag{4.2}$$

or

$$Q_i = \alpha_i N_i, \tag{4.3}$$

where

$$\alpha_i = kS\left(\frac{M_i}{T}\right)^{1/2} \gamma_i P^{\text{st}} \quad ; \tag{4.4}$$

K – a constant dependent on Q_i and P_i dimensions; S – evaporation surface area; T – evaporation surface temperature.

The pure component is taken as the standard state for the components of the melts close to ideal solutions and for the solvent in the melts close to dilute solutions, and in this case

$$P_i^{\text{st}} = P_i^0,$$

where P_i^0 – the vapor pressure of a pure *i*-th component.

For substances dissolved in molten metal pools close to dilute melts, the vapor pressure in the standard state is numerically equal to the reciprocal of the Henry coefficient, h_i [111].

$$P_i^{\text{st}} = h_i^{-1}$$

In most works, dedicated to the problem of alloy evaporation, this feature is not taken into account, and the vapor pressure of a melt component is taken proportional to the vapor pressure of the pure component, which is not always correct.

The concentration ratio of the components in vapor phase X_i equals to the ratio of the evaporation rates of these components:

$$\frac{X_i}{X_j} = \frac{Q_i}{Q_j}. \tag{4.5}$$

The stationary state is achieved when the equality of the concentrations of the components in the vapor phase and the feeding alloy is reached:

$$X_i = C_i, \tag{4.6}$$

where C_i – mass fraction of *i*-th component in the feeding alloy.

Thus,

$$N_i = N_j \frac{C_i}{C_j} \frac{M_j^{1/2} \gamma_j P_j^{st}}{M_i^{1/2} \gamma_i P_i^{st}} \tag{4.7}$$

Having summed up the left-hand and right-hand sides of the equation (4.7) and taking into account that $\sum_{i=1}^{n} N_i = 1$ we'll have

$$N_j = \frac{C_j}{M_j^{1/2} \gamma_j P_j^{st} \sum_{i=1}^{n} C_i \left(M_i^{1/2} \gamma_i P_i^{st} \right)^{-1}} \tag{4.8}$$

Mole fraction and mass fraction are related as follows

$$W_j = \frac{N_j M_j}{\sum_{i=1}^{n} N_i M_i}. \tag{4.9}$$

Substituting (4.8) to (4.9) we'll have

$$W_j = \frac{C_j M_j^{1/2}}{\gamma_j P_j^{st} \sum_{i=1}^{n} M_i^{1/2} C_i \left(\gamma_i P_i^{st} \right)^{-1}} \tag{4.10}$$

Equation (4.10) establishes a relationship between the component mass parts in the equilibrium molten metal pool W_j and feeding alloy C_j with an arbitrary number of the alloying elements.

It is obvious that for binary alloys, the equation (4.10) is similar to the existing expression

$$W_2 = \frac{C_2}{C_2 + (1 - C_2)\dfrac{P_2^0 \gamma_2}{P_1^0 \gamma_1}\left(\dfrac{M_1}{M_2}\right)^{1/2}}, \tag{4.11}$$

obtained earlier in the works [100, 101], the only difference being that in this equation one has to substitute h_i^{-1} for P_i^0 for the dissolved substance.

Therefore, it is expedient to calculate the equilibrium composition of a molten metal pool in two stages.

At the first stage it is necessary to find out what type of solutions – close to ideal or close to dilute – the equilibrium melt belongs to, and, if dilute, which component will be the solvent. It can be done by using an approximate estimate of the component concentrations in the equilibrium molten metal pool W'_j by applying Raoult's law to all the components, without taking into account their activity, using (4.10):

$$W_j^{'} = \frac{C_j M_j^{1/2}}{P_j^0 \sum\limits_{i=1}^{n} C_i M_i^{1/2} \left(P_i^0\right)^{-1}}. \tag{4.12}$$

Based on the above, at the second stage the composition of the equilibrium molten metal pool can be determined through Equation (4.10).

In practice, the calculation of equilibrium concentrations may be complicated due to the lack of tabulated values of the activity and Henry coefficients. In this case the following experiment-calculation method can be suggested.

Firstly, the «initial» composition of the molten metal pool is calculated according to Eq. (4.12). Then, after the thermal state of the melt gets steady, a brief metal evaporation with continuous feeding of the pool is carried out. When this part of the experiment is over, the component mass fractions, W_i^* and C_i^*, in the crystallized melt pool and in the resulting condensate, respectively, may be determined.

Then we have to calculate the equilibrium pool composition through the following equation

$$W_j = \frac{C_j W_j^*}{C_j^* \sum\limits_{i=1}^{n} C_i W_i^* \left(C_j^*\right)^{-1}}, \tag{4.13}$$

resulted from (4.7) and (4.8), taking into account

$$N_j = \frac{W_j}{M_j \sum_{i=1}^{n} W_i / M_i}. \qquad (4.14)$$

To determine the equilibrium concentrations more precisely, the above procedure may be repeated.

The proposed experiment-calculation method is most efficient for alloys taking a long time to stabilize their chemical composition during evaporation, for example, for alloys doped with refractory components.

Table 4.1 shows the results of determining the equilibrium pool for the alloy BT20 obtained by using the above method.

Table 4.1

The calculated and experimental results of alloy BT20 foil making

Composition	Sampling place	Concentration of the components, %				
		Al	V	Mo	Zr	Ti
Calculated, approximate estimation of liquid pool	Pool	0.04	0.3	38.5	53.6	7.56
Intermediate, experimental	Pool	0.2	5.1	35.8	28	30.9
	Foil	1.9	1.9	0.3	0.6	95.3
Calculated, equilibrium liquid pool	Pool	0.8	1.6	48.8	38.5	10.3
Resulting foil	Foil	4.7	1.3	0.6	1.9	91.5
Fed ingot	Ingot	5.6	1.5	1.0	2.0	89.9

Experimental data and results of calculation through Equation (4.10) are compared in P. 4.4.

4.2. The evaporation kinetics for multicomponent alloys

The mole number of the substance contained in the molten metal pool is taken as the process invariant.

It should be noted that the selection of any extensive, physically meaningful value such as the volume of the molten metal pool or the molten metal mass is a certain idealization, approximately corresponding to the reality. Actually, the only invariant of the process is the input energy flow, and even the assumption of a constant temperature of the melt surface is not realized in reality.

Our choice allows simplifying greatly the mathematical simulation of the process. Its validity can be confirmed or refuted experimentally thus enabling to set the limits of applicability of the proposed mathematical simulation [112].

The considered process can be described by the system of equations

$$\frac{\mathrm{d}}{\mathrm{d}t}\left(N_i\right)M_i N = -\alpha_i N_i + \omega_i, \tag{4.15}$$

where N – the total number of moles of the molten metal taken as constant throughout the entire evaporation process; ω_i – the rate of the i-th component input due to melt feeding; α_i – is calculated through equation (4.4).

As

$$\omega_i = \lambda_i M_i \sum_{\mathrm{j}=1}^{n} \alpha_j \chi_j, \tag{4.16}$$

where λ_i – mole fraction of the i-th component in the feeding alloy, then Equation (4.15) can be written as

$$\frac{\mathrm{d}}{\mathrm{d}t}\left(N_i\right) = -\frac{\alpha_i}{M_i N} N_i + \frac{\lambda_i}{N}\left(\sum_{j=1}^{n} \frac{\alpha_i}{\mathrm{M}_i} N_i\right). \tag{4.17}$$

The system of differential equations (4.17) is the mathematical model of the researched process. Let us introduce the following designations:

$$\Theta_j = \frac{\alpha_j}{M_j}\frac{1}{N}, \tag{4.18a}$$

where $j = 1,2,\ldots..,n$; X – vector (column) composed of the set of concentrations

$$X = \begin{pmatrix} N_i \\ . \\ . \\ . \\ N_n \end{pmatrix}; \tag{4.18b}$$

A = $\{a_{ij}\}$ – matrix, having the $n \times n$ dimension,

$$a_{ij} = -\Theta_i \delta_{ij} + \lambda_i \Theta_j, \tag{4.18c}$$

where $\delta_{ij} = \begin{cases} 0, & \text{at } i \neq j \\ 1, & \text{at } i = j \end{cases}$

I – the identity matrix

$$I = \{\delta_{ij}\}. \tag{4.18d}$$

Then, Equation (4.17) in the matrix form will be

$$\frac{\mathrm{d}}{\mathrm{d}t}(X) = AX. \tag{4.19}$$

All the essential properties of the solutions of this equation depend on the coefficient of the matrix A, which is generally not symmetrical: $a_{ij} \neq a_{ji}$. To bring matrix A to a symmetric form let us take that

$$G = \left\{ \delta_{ij} \sqrt{\frac{\Theta_i}{\lambda_i}} \right\}.$$

Let us consider the linear transformation of the coordinates given by matrix G:

$$y = G(X).$$

In the new coordinates, the operator corresponding to A will have the matrix

$$B = GAG^{-1}, \tag{4.20}$$

$$B_{ij} = \sqrt{\frac{\Theta_i}{\lambda_i}\left\{-\Theta_i \delta_{ij} + \lambda_i \Theta_j\right\}} \sqrt{\frac{\lambda_j}{\Theta_j}} =$$

$$= \left\{ -\Theta_i \sqrt{\frac{\Theta_i \lambda_j}{\lambda_i \Theta_j}} \delta_{ij} + \sqrt{\lambda_i \lambda_j} \cdot \sqrt{\Theta_i \Theta_j} \right\} = \left\{ -\Theta_i \delta_{ij} + \sqrt{\lambda_i \lambda_j} \cdot \sqrt{\Theta_i \Theta_j} \right\}.$$

Obviously, the matrix B is already symmetric: $B_{ij} = B_{ji}$. It is well known that many of the important characteristics of the matrices A and B are linked [113]. In particular, the eigenvalues of the matrices A and B are the same.

It is also known that if a matrix is symmetric, then there always exists a unique set of the eigenvalues $\{\nu^{(1)}, ..., \nu^{(n)}\}$, and, moreover, all $\nu^{(i)}$ are real numbers. Furthermore, there is a basis of the (orthonormal) eigenvectors:

$$e_1,\ldots,e_n, B(\mathrm{e}_j) = \nu^{(j)} e_j.$$

Equation (4.20) shows that the matrices A and B have the same eigenvalues.

Thus:

− all the eigenvalues of A are real;

− there is a basis of the eigenvectors of the matrix

$$\{e_1,...,e_n\}: A(e_j) = \nu^i e_j.$$

We can analyze the system by using Equation (4.20).

Let X, Y be two vectors. Let us introduce two types of scalar products of the vectors X and Y:

$$(X,Y) = \sum_{j=1}^{n} X_j Y_j - \text{standard scalar product,}$$

$$(X,Y)_G = \left[G(X), C(Y)\right] = \sum_{j=1}^{n} \left(\frac{\Theta_j}{\lambda_j} \right) X_i Y_i - G - \text{scalar product.}$$

Then the Equation (4.20) means that

$$[A(x), y)_G = (x, A(y)]_G.$$

This property of A is called self-adjointness regarding the form (scalar product) – $(\,.\,,\,.\,)_G$. Note that the self-adjointness regarding the standard scalar product is equivalent to the symmetry of A. Let us introduce the concept of the length of the vector associated with the scalar product

$$\left|X\right|^2 = \Sigma X_i^2 = \left(X,\ X\right),$$

$$\left|X\right|_G^2 = (x,x)_G = \Sigma x_j^2 \left(\frac{\Theta_j}{\lambda_j} \right).$$

Note that

$$|X|_G^2 \le \max\left(\frac{\Theta_j}{\lambda_j}\right)|x|^2, \tag{4.21}$$

$$|X|^2 \le \left(\min\left(\frac{\Theta_j}{\lambda_j}\right)\right)^{-1}|X|_G^2.$$

Thus, there is a linear differential equation with constant coefficients, having the coefficient matrix self-adjointed with respect to the scalar product $(\,.\,,\,.\,)_G$. In this case the basis of the eigenvectors of the matrix A can be selected orthonormal:

$$(e_i, e_j)_G = \delta_{ij};\ i,j = 1,\ldots,n.$$

And the general solution of (4.19) with the initial condition X^0 takes the form:

$$X(t) = \sum_{j=1}^{n} e_j \left(X^0, e_j\right)_G \exp\left(\nu^{(j)} t\right). \tag{4.22}$$

Thus, to solve the system (4.17) it is sufficient to find the eigenvectors e_j and eigenvalues $\nu^{(j)}$ of the matrix A. However, knowing only the eigenvalues is already sufficient to determine a number of important system parameters. Actually, as shown in (4.22), the eigenvalues determine the rate of growth or decay of the solutions of the system (4.19).

In particular, if among the eigenvalues $\nu^{(i)}$ there is at least one $\nu^{(k)} > 0$, the system is unstable, and it usually does not reach the stationary mode, since the general representation of the solution (4.22) includes exponential of a positive number. If $\nu^{(k)} = 0$, then e_k – stationary solution.

Further it will be shown that among the eigenvalues $\nu^{(j)}$ there exists $\nu^{(k)} = 0$. This implies the existence of a stationary mode.

In addition, it will be shown that all the other eigenvalues are strictly negative, i.e, the stationary mode is stable – every solution approaches the stationary one.

Let $\nu^{(1)}, \ldots, \nu^{(n-1)} < 0$, $\nu^{(n)}=0$.

Assume that $\nu^{+} = \max |\nu^{(j)}|$, j=1,2, ... , n,

$\nu^{-} = \min |\nu^{(j)}|$, j=1,2, ... , n–1.

Let *X(t)* be the solution, and $X_\infty = \lim_{t\to+\infty} X(t)$ be the stationary solution, attracting *X(t)*.

Note (without going into details) the following inequalities:

$$\left|X(0)-X_\infty\right|_G e^{-\nu^+ t} \le \left|X(t)-X_\infty\right|_G < e^{-\nu^- t}\left|X(0)-X_\infty\right|_G. \qquad (4.23)$$

As it can be seen, even the calculations of only the ν^+ and ν^- values give a good estimate of the process convergence rate to the stationary state, and, hence, of the time needed to reach the stationary mode.

The eigenvalues of *A* are the solutions of the equation

$$\det(A-\nu I) = 0,$$

i.e.

$$\det\left\{-\Theta_i\delta_{ij} + \lambda_i\Theta_j - \delta_{ij}\nu\right\} = 0$$

$$\det\left\{-\frac{(\Theta_i+\nu)}{\lambda_i\Theta_j}\delta_{ij}+1\right\}\Theta_1\ldots\Theta_n\lambda_1\ldots\lambda_n = 0$$

and

$$\det\left\{-\frac{(\Theta_i+\nu)}{\lambda_i\Theta_j}\delta_{ij}+1\right\} = 0.$$

Let us designated

$$P_i = \frac{1}{\lambda},\ q = \frac{1}{\lambda_i\Theta_i},$$

then

$$\det\left\{-\left(q_i\nu + P_i\right)\delta_{ij}+1\right\} = 0.$$

Let us subtract the first row of this matrix from all the other rows and calculate the determinant by the expansion of the elements of the first row

$$\left(I-\left(P_1+\nu q_1\right)\right)\prod_{i\neq1}\left(\nu q_i + P_i\right) + \prod_{i\neq2}\left(\nu q_i + P_i\right) + \ldots + \prod_{i\neq n}\left(\nu q_i + P_i\right) = 0$$

the result will be as follows

$$\sum_{j=1}^{n}\prod_{i\neq j}(\nu q_i + P_i) = \prod_{i=1}^{n}(\nu q_i + P_i). \tag{4.24}$$

Equation (4.24) is the expression for the eigenvalues of matrix A.

It is seen that $\nu = 0$ is the root of Equation (4.24). This is a simple consequence of the relation

$$\sum \frac{1}{P_j} = 1$$

Thus, there always exists an eigenvalue equal to zero. Hence, there also exists a stationary state.

If there are such components that

$$\Theta^{(S)} = \Theta_{i1} = \Theta_{i2} = \ldots = \Theta_{ir},\ r \geq 2,$$

then, as seen from (4.24), the value $\nu = -\Theta^{(S)}$ is the root of the characteristic equation of multiplicity r–1.

Let us now consider the roots of (4.24) such that

$$\nu \neq -\frac{P_i}{q_i};\ \ i = 1,\ldots,n. \tag{4.25}$$

Dividing (4.24) by its right-hand side, which is non-zero due to condition (4.25), we'll have

$$f(\nu) = \sum_{j=1}^{n}\frac{1}{q_j\nu + P_j} = 1. \tag{4.26}$$

The equation for a function describing the left-hand side of equation (4.26) is shown in Figure. 4.1.

Let us assume that

$$\eta_k = -\frac{P_j}{q_j} = \Theta_j;\quad \eta_1 \leq \ldots \leq \eta_n < 0.$$

It is seen that

$$\lim_{\nu\to\eta_m^-} f(\nu) = -\infty,\ \lim_{\nu\to\eta_m^+} f(\nu) = +\infty.$$

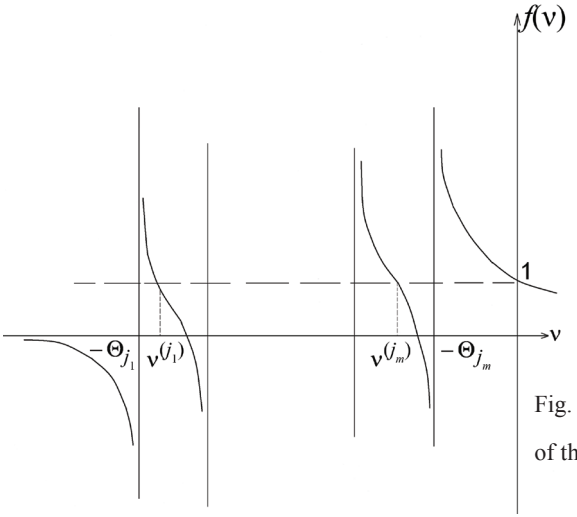

Fig. 4.1. The general form of the function $\sum_{j=1}^{n} = \frac{1}{q_j \nu + P_j}$

At the segment $[\eta_m, \eta_{m+1}]$, where $\eta_m < \eta_{m+1}$, function $f(\nu)$ is continuous and monotonic. Therefore, Equation (4.24) has in this segment exactly one root. It is easy to verify that the total number of found roots, taking into account the multiplicity, is exactly n. Finding the roots of (4.24), which are separated by values η_m, easy to achieve by numerical methods. In addition, the belonging of the roots to the segments $[\eta_m, \eta_{m+1}]$ offers a natural estimate of their value. In particular, if $\Theta_m = \max \Theta_i$, $\Theta_- = \min \Theta_i$, then

$$\Theta_- \le \nu_- \le \nu_+ \le \Theta_+.$$

Therefore, with (4.23) in mind we have

$$e^{-\Theta_+ t} \le \frac{\left|X(t) - x_\infty\right|_G}{\left|X(0) - x_\infty\right|_G} \le e^{-\Theta_- t}. \qquad (4.27)$$

Thus, the method of finding the roots of the characteristic equation (4.24) is the following: if there is a group of (exactly) $r \ge 2$ elements $\Theta_{i1} = \ldots = \Theta_{ir}$, then Θ_{i1} is a root of multiplicity $r-1$.

It is also the root of the value $\nu = 0$. Other roots have multiplicity 1 and are placed within the segments

$$[\eta_m, \eta_{m+1}], \eta_m < \eta_{m+1} \ (\eta_k = -\Theta_k).$$

Let us now consider the eigenvectors of the matrix A. The eigenvector e, corresponding to the eigenvalue ν, is found from the equation

$$Ae = \nu e$$

or in the coordinates $e = (e^1, \ldots, e^n)$

$$\sum_{j=1}^{n} \{-(\Theta_i + \nu)\delta_{ij} + \lambda_i \Theta_j\} e^j = 0. \tag{4.28}$$

Let us consider three cases:

1. The eigenvalue ν satisfies the condition (4.25). Let us divide each k-th equation in the system (4.28) by λ_k and subtract the first equation of the resulting system from all the other ones. Thus we'll have a system of equations from which it follows that

$$e^1 \left(\frac{\Theta_1 + \nu}{\lambda_1} \right) - e^k \left(\frac{\Theta_k + \nu}{\lambda_k} \right) = 0; \quad k = 2, \ldots, n,$$

$$e^k = e^1 \frac{\left(\dfrac{\Theta_1 + \nu}{\lambda_1} \right)}{\left(\dfrac{\Theta_k + \nu}{\lambda_k} \right)}.$$

If we take

$$e^1 = \frac{\lambda_1}{\Theta_1 + \nu},$$

we'll have

$$e^k = \frac{\lambda_k}{\Theta_k + \nu},$$

$$\hat{e} = \frac{e}{|e|_G}, \quad A(\hat{e}) = \nu(\hat{e}), \quad |\hat{e}|_G = 1. \tag{4.29}$$

Note that the condition (4.25) ensures the inequalities

$$\nu \neq -\Theta_k, \; k = 1, \ldots, n.$$

2. Let us point out the case of $\nu = 0$ (stationary state). As seen from (4.29)

$$e^k = \frac{\lambda_k}{\Theta_k} = \frac{\lambda_k}{\alpha_k} \cdot \frac{M_k}{N}.$$

The concentration vector at the stationary state is proportional to the vector e. Taking into account the normalization condition $\sum \hat{e}^k = 1$ we'll have

$$\hat{e}^k = \frac{\frac{\lambda_k M_k}{\alpha_k N}}{\sum \frac{\lambda_i M_i}{\alpha_i N}}.$$

3. Suppose, finally, that ν is an eigenvalue satisfying the equality

$$\nu = -\Theta_{i1} \ldots = -\Theta_{ir},\ r \geq 2.$$

In this case the eigenvector will be $\{e^k\}$:

$$e_{i1} = 1;\ \Theta_{i2} = -1;\ e_{ij} = 0.$$

Thus, we have completed the mathematical analysis of the system.

Let us estimate the time required to establish a stationary state. Suppose we set a certain accuracy $\varepsilon > 0$ and believe that the process reaches a stationary state if

$$\left| X(t) - X_\infty \right| < \varepsilon.$$

Minimum time t_c, after which this estimate is always true, is the time needed by the process to reach the stationary mode.

From (4.27)

$$\left| X(t) - X_\infty \right| < e^{-\Theta t} \left| X_0 - X_\infty \right|_G \left(\min \sqrt{\frac{\Theta_i}{\lambda_i}} \right)^{-1},$$

therefore, if

$$\varepsilon > e^{-\Theta t} \left| X(0) - X_\infty \right|_G \left(\min \sqrt{\frac{\Theta_i}{\lambda_i}} \right)^{-1},$$

then the process has reached the stationary mode, hence

$$t > \ln \frac{\left| X(0) - x_{\infty} \right|_G}{\varepsilon} \cdot \frac{1}{\Theta_-} - \frac{1}{\Theta_-} \ln \left(\min \sqrt{\frac{\Theta_i}{\lambda_i}} \right).$$

This means that

$$t_c \le \frac{1}{\Theta_-} \ln \frac{\left| X(0) - x_{\infty} \right|_G}{\varepsilon} - \frac{1}{\Theta_-} \ln \left(\min \sqrt{\frac{\theta_i}{\lambda_i}} \right).$$

Moreover, the vector X_{∞} coincides with the fixed set of concentrations

$$X_{\infty} = \frac{\dfrac{\lambda_k M_k}{\alpha_k N}}{\sum\limits_{j=1}^{n} \dfrac{\lambda_j M_j}{\alpha_j N}}.$$

Value Θ_- can be determined as follows:

$$\Theta_- = \min(\Theta_j) = \min \left(\frac{\alpha_j}{M_j N} \right).$$

Thus, Equation (4.27) provides an effective theoretical estimate of the time needed to reach the stationary state.

The most important qualitative conclusion is the conclusion about the stationary mode stability: the process reaches the stationary mode at any initial conditions. This follows from the negativity of all non-zero eigenvalues of matrix *A*.

Fig. 4.2 presents a comparison of experimental and calculated data for the alloy BT6.

The satisfactory agreement between the experimental and calculated data points to the validity of the proposed process model for the single-source evaporation of multi-component alloys with continuous feeding of the molten metal pool.

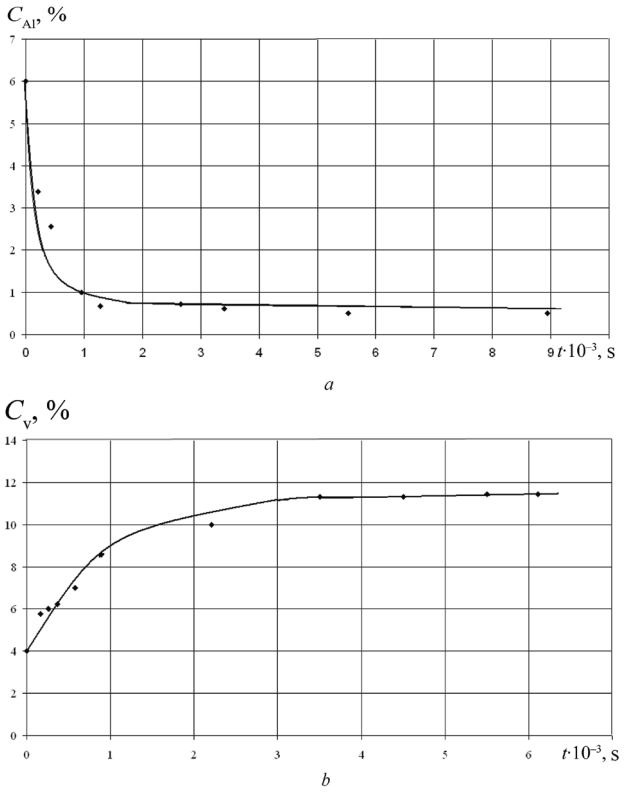

Figure 4.2. The dependence of aluminum (*a*) and vanadium (*b*) contents on the evaporation time for the BT6 melt. The solid lines are the calculated curves

4.3. The evaporation of the melts close to dilute solutions

It is noteworthy that if the conditions of the constant volume and the mole number in the molten metal pool are natural assumptions, the requirement of a constant melt surface temperature is not so universal.

Indeed, if the chemical composition of the molten metal pool is significantly changed during the process of evaporation at a constant input power, then the surface temperature must also change. For example, a significant enrichment of the pool with a refractory component will increase the surface temperature.

In the works on the kinetics of alloy evaporation, the condition of the constant melt surface temperature is widely used without any analysis of the limits of its admissibility. In fact, the condition of the constant surface temperature should be met only for the melts close to dilute solutions during the entire evaporation process.

In this section, the problem of evaporation kinetics is solved exactly for such melts [114].

It should also be noted that for such melts the requirement of the constant volume is identical to the condition of the constant total number of molecules in the molten metal pool.

Considering all this, the chemical composition of the pool can be described by the following equation:

$$\frac{\mathrm{d}C_i}{\mathrm{d}t} = -\frac{\alpha_i M_1}{\rho V M_i} C_i + \frac{\lambda_i M_1}{\rho V} \sum_{j=1}^{n} \frac{Q_1}{M_j}, \tag{4.30}$$

where index $i = 1$ denotes solvent, C_i – the mass fraction of the i-th component in the pool, ρ – the molten metal density, V – molten metal volume, λ_i – mass fraction of the i-th component in the feeding alloy, Q_j – the evaporation rate of the j-th component.

The value α_i is found by Equation (4.4). For the melts close to dilute solutions the following approximation can be used

$$\sum_{j=1}^{n} \frac{Q_j}{M_j} \cong \frac{Q_1}{M_1}.$$

Accordingly, Equation (4.30) will takes the form of

$$\frac{\mathrm{d}C_i}{\mathrm{d}t} = -\frac{kSM_1\gamma_i P_i^{st}}{\rho V \left(M_i T\right)^{1/2}} C_i + \frac{kS\left(\frac{M_1}{T}\right)^{1/2} \gamma_1 P_1^0 M_1}{\rho V} \lambda_i . \tag{4.31}$$

The solution of Equation (4.31) has the form of

$$C_i(t) = C_{i\infty} + \left(C_{i0} - C_{i\infty}\right) \exp\left[-\frac{kSM_1\gamma_i P_i^{\mathrm{st}}}{\rho V \left(M_i T\right)^{1/2}} \right], \tag{4.32}$$

where C_{i0} – mass fraction of the *i*-th component in the melt at the initial time

$$C_{i\infty} = \lambda_i \frac{\gamma_1 P_1^0}{\gamma_i P_i^{st}} \left(\frac{M_i}{M_1} \right)^{1/2}. \quad (4.33)$$

It is obvious that the Equation (4.33) is identical to (4.10), considering that the molten metal is close to a dilute solution.

The time needed for the *i*-th component to reach the stationary mode is determined by the expression

$$T_i = \frac{\rho V (M_i T)^{1/2}}{kSM_1 \gamma_i P_i^{st}} \ln \left| \frac{1 - \frac{C_{i0}}{C_{i\infty}}}{\varepsilon} \right|, \quad (4.34)$$

where ε – a permissible relative error of the equilibrium concentration of the *i*-th component.

It is apparent that the time needed for the entire pool to reach the stationary state takes the form of

$$T = \max_i T_i$$

For the melts close to the dilute solutions, the approximate ratio between the component concentration in the melt (C_i) and in the condensate (C_i^k) is represented as follows

$$C_i^k = \left(\frac{M_1}{M_i} \right)^{1/2} \left(\frac{\gamma_i P_i^{st}}{\gamma_1 P_1^0} \right) C_i. \quad (4.35)$$

Accordingly, the dependence of the condensate composition on the deposition time is identical to Equation (4.32)

$$C_i^k(t) = C_{i\infty}^k + \left(C_{i0}^k - C_{i\infty}^k \right) \exp \left[- \frac{kSM_1 \gamma_i P_i^{st}}{\rho V (M_i T)^{1/2}} \right], \quad (4.36)$$

where $C_{i\infty}^{k} = \lambda_i$;

$$C_{i0}^{k} = \left(\frac{M_1}{M_i}\right)^{1/2} \left(\frac{\gamma_i P_i^{st}}{\gamma_1 P_1^{0}}\right) C_{i0}\,.$$

As we determine experimentally the composition of the molten metal pool and the condensate, we can use Equation (4.35) to find the values $\left(\gamma_j P_i^{st}\right)$ that are necessary for practical calculations.

The accuracy of the resulting expressions (4.32) – (4.36) is the higher, the more diluted the molten metal is. The comparison of the theoretical and experimental data was carried out on the 2B alloy.

At certain time intervals, the evaporation process was interrupted and specimens for the chemical analysis were taken from the crystallized metal pool.

The kinetics of the melt alloying changes during the evaporation process is shown in Fig. 4.3. Experimental and calculated data match in satisfactory way.

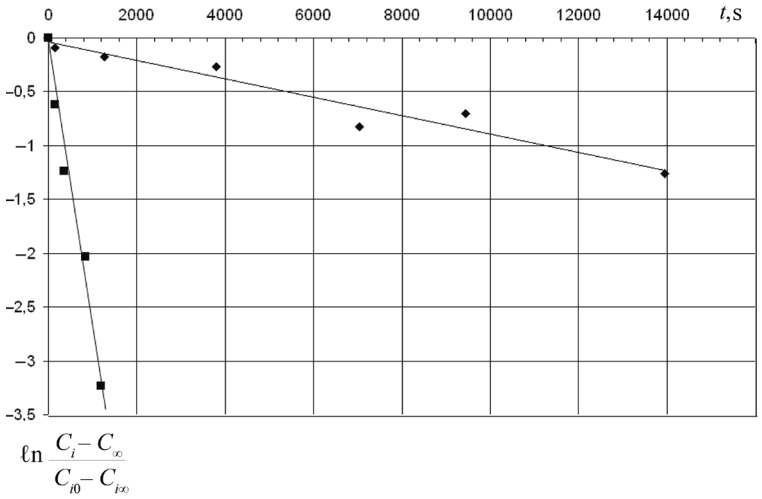

Fig. 4.3. The dependence of aluminum and vanadium contents in the pool on the evaporation time of alloy 2B. Solid lines – calculated data according to Equation (4.32)

4.4. Determination of the activity and Henry coefficients. Comparing the calculation methods of the equilibrium pool

There is a number of methods to determine the activity of the components in molten metal pools [111].

In particular, the determination of the activity can be based on the use of the process of evaporation and condensation in vacuum. In such a case it is necessary to determine the melt evaporation rate, as well as the concentrations of the alloying elements in the melt and in the condensate crystallized on the substrate located above the molten pool. The evaporation process can be periodically interrupted to take samples from the crystallized metal pool. The vapors of the molten metal can be condensed onto a fixed substrate, followed by the analysis of the distribution of the alloying elements through the cross-section of the condensate. Another variant of this method is the deposition of the melt vapor onto a substrate strip, continuously moving above the pool surface to form a coating, which is subsequently separated from the substrate strip as foil with a further assessment of the alloy concentrations in the foil.

The latter method was used in this work.

It is necessary to distinguish the methods of activity determination for the melts close to ideal ones and those close to dilute solutions.

The activity of the *i*-th component is

$$a_i = \frac{P_i}{P_i^{\text{st}}} \tag{4.37}$$

where P_i – vapor pressure of the *i*-th component; P_i^{st} – vapor pressure of the *i*-th component in standard state.

Activity coefficient is equal to

$$\gamma_i = \frac{\alpha_i}{N_i}, \tag{4.38}$$

where N_i – mole fraction of the *i*-th component in the melt.

For the components of close-to-ideal solutions, as well as for the solvent of close-to-dilute solutions, the vapor pressure in the standard state is equal to the vapor pressure of the pure *i*-th component – P_i^0 and

$$\alpha_i = \frac{P_i}{P_i^0}. \tag{4.39}$$

The evaporation rate of the *i*-th component Q_i is proportional to the vapor pressure of this component above the melt

$$Q_i = k_i P_i.$$

If Q_i – g/(cm^2·c) and P – torr, then

$$k_i = \frac{1}{17.14\sqrt{\frac{T}{M_i}}},$$

where T – the temperature of evaporation surface.

For pure *i*-th component

$$Q_i^0 = k_i P_i^0.$$

Taking into account (4.39) we'll have

$$\alpha_i = \frac{Q_i}{Q_i^0}. \tag{4.40}$$

If the condensation coefficient is equal to 1, then the mass fraction of the *i*-th component in the condensate is equal to

$$C_i^k = \frac{Q_i}{Q}, \tag{4.41}$$

where Q – the alloy evaporation rate.

Hence

$$\alpha_i = \frac{QC_i}{k_i P_i^0} \tag{4.42}$$

and the activity coefficient is equal to

$$\gamma_i = \frac{QC_i}{k_i P_i^0 N_i}. \tag{4.43}$$

For substances dissolved in molten metal pools close to diluted solutions, vapor pressure in standard state is equal to the value of the inverse Henry coefficient, h_i, i.e.

$$\alpha_i = P_i h_i = \frac{QC_i h_i}{k_i} \tag{4.44}$$

In this case

$$\gamma_i = \frac{\alpha_i}{N_i} = \frac{QC_i h_i}{k_i N_i} \tag{4.45}$$

The Henry coefficient can be determined by extrapolating the following ratio to the zero concentration

$$h_i = \lim_{N \to 0} \frac{N_i}{P_i} = \lim_{N \to 0} \frac{N_i k_i}{QC_i} \tag{4.46}$$

The value

$$\gamma_i P_i^{st} = \frac{QC_i}{k_i N_i} \tag{4.47}$$

is determined in a similar manner – both for the melts that are close to ideal and those close to dilute solutions. In the cases when calculations are based on this particular value, a separate determination of γ_i and P_i^{st} is unnecessary.

In this work, this method was used to determine the activity and Henry coefficients in the melts of the Ti–Al–V system. The process was performed in the УВФ-75-1 plant [51, 115], the layout of which is shown in Fig. 2.1.

The alloy was placed into a water-cooled copper crucible 90 mm in diameter. The pool surface was heated with an electron beam. The power of the electron beam gun was 20 kw, and the vacuum in the chamber was $2 \cdot 10^{-5}$ Hg ($2.67 \cdot 10^{-3}$ Pa).

A steel substrate strip coated with an anti-adhesive substance was moving above the molten metal pool surface. The anti-adhesive was used to facilitate the subsequent separation of the foil from the substrate strip.

The evaporation temperature was 2610 K.

The results of determining the composition of the pool (molten metal) and the condensate for the alloys of the Ti–Al, Ti–V and Ti–Al–V systems are shown in Table 4.2 – 4.4.

Table 4.2

The ratio of the vanadium concentration in the condensate and in the melt for the Ti–V system

Experiment No	Condensate, %	Molten metal, %
1	0.2	0.7
2	0.3	0.9
3	0.5	1.4
4	0.7	2.2
5	1.2	3.0
6	2.4	6.4
7	1.3	3.7
8	2.7	8.0
9	3.7	11.0

Table 4.3

The ratio of the aluminum concentration in the condensate and in the melt for the Ti–Al system

Experiment No	Condensate, %	Molten metal, %
1	1.7	0.2
2	1.9	0.2
3	3.7	0.3
4	5.4	0.5
5	4.5	0.5
6	6.1	0.6
7	7.0	0.7

Table 4.4

The ratio of the aluminum and vanadium concentrations in the condensate and in the melt for the Ti–Al–V system

Experiment No	Aluminum		Vanadium	
	Condensate, %	Molten metal, %	Condensate, %	Molten metal, %
1	11.0	1.0	2.3	5.6
2	8.7	0.7	2.5	5.8
3	7	0,7	0.7	6.0
4	6.8	0.5	2.9	6.2
5	4.9	0.4	3.4	9.8
6	4.1	0.3	8.1	13.6
7	2.6	0.3	7.0	19.0

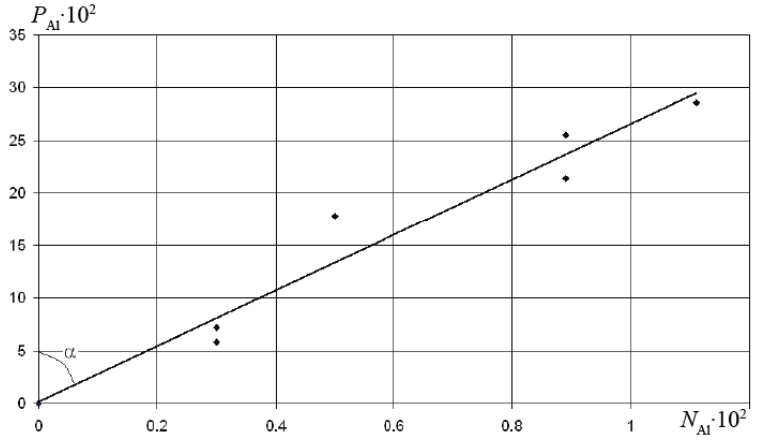

Fig. 4.4. The dependence of the vapor pressure on
the mole fraction of aluminum in the Ti–Al system

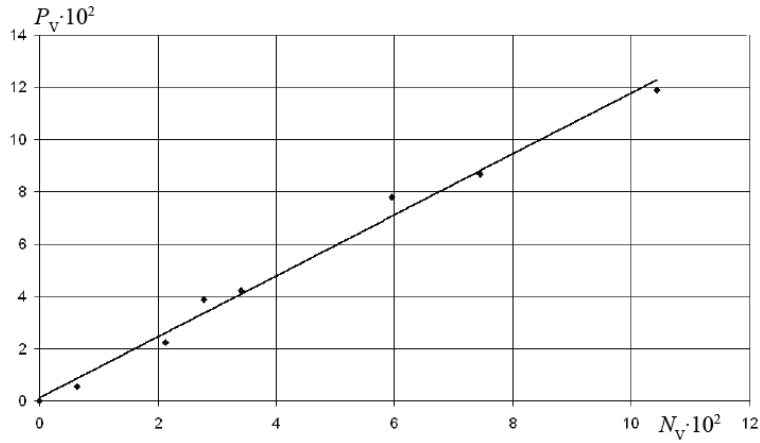

Fig. 4.5. The dependence of the vapor pressure on
the mole fraction of vanadium in the Ti–V system

The values of Henry coefficients for aluminum and vanadium were found from the dependence of the vapor pressure on the mole fractions of these elements (Fig. 4.4 and 4.5).

Henry coefficient for aluminum is $3.8 \cdot 10^{-2}$, for vanadium – 0.84.

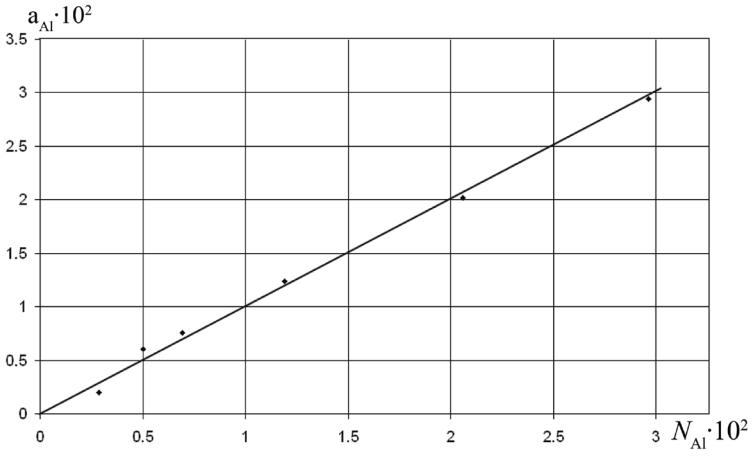

Fig. 4.6. The dependence of aluminum activity
on its mole fraction in the Ti–Al system

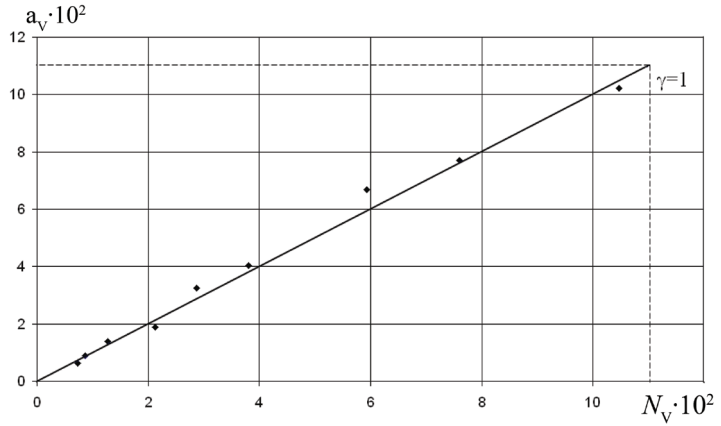

Fig. 4.7. The dependence of vanadium activity
on its mole fraction in the Ti–V system

Value ($\gamma_i \cdot P_i^{st}$) for aluminum is 29.4; for vanadium – 1.37; for titanium – 3.9.

The dependencies of the activities of aluminum and vanadium on their mole fraction are shown in Fig. 4.6 and 4.7.

In the range of aluminium concentrations up to 2 % and those of vanadium up to 10 %, the activity coefficients of aluminum and vanadium

in Ti–Al, Ti–V and Ti–Al–V systems at the temperature of evaporation 2610 K are equal to 1.

However, these data disagree with some literature data [116, 117], in which the activity coefficient of aluminum is (0.1...0.3) and $(0.6...1.4)\cdot 10^{-2}$, respectively. These discrepancies may be due to the fact that in these works the activity coefficients were calculated without taking into account the values of the Henry coefficient.

Thus, using our determination of the value $\gamma_{Al} \cdot P^0_{Al} = 29.4$ for the temperature of 2610 K, at which $P^0_{Al} = 365$ torr [91], the activity coefficient of aluminum of $8\cdot 10^{-2}$ would be found, which is close to the values given in [116, 117]. It confirms our assumption of Raoult's law being applied instead of Henry's law in [116, 117], the substitution which is not quite correct.

The resulting values of the activity and Henry coefficients made it possible to calculate the equilibrium composition of the molten metal pool during BT6 alloy evaporation through Equation (4.10).

Table 4.5 shows the experimental data on the equilibrium composition of the pool during the evaporation of alloy BT6, as well as calculated data which account for the activity and those based on the experiment-calculation method mentioned in P. 4.1.

Table 4.5

Melt and foil composition during evaporation of alloy BT6 (%)

Object	Successive approximations method				The equilibrium composition of the pool, calculation taking into account the activity according to the equation (4.10)	The composition of the equilibrium pool and the foil, experimental data
	"Initial" ingot, calculation through the equation (4.10)		The composition of the pool and foil after 10 minutes of evaporation	The equilibrium composition of the pool, calculation through the equation (4.13)		
Al	Ingot	0.03	0.42	0.7	0.6	0.5
	Foil	–	4,6	–	–	6.0
V	Ingot	42.7	41.4	15.6	12.8	13.5
	Foil	–	16.2	–	–	4.5

The comparison of the calculated and the experimental data (see Table 4.5) shows that accounting for the activities gives a better matching with the experimental data than the successive approximation method.

Chapter 5. DEVELOPING PRINCIPLES FOR SUBSTRATE STRIP AND ANTIADHESIVE MATERIAL SELECTION AND A TECHNOLOGY OF FOIL MANUFACTURING PROCESS

Taking into account the specifics of making foil by vacuum deposition, we defined the following requirements to the substrate strip material:

– no interaction between substrate material and foil at elevated temperatures;

– high quality of the strip surface;

– high mechanical properties at elevated temperatures;

– possibility of multiple use;

– being included into the domestic product range.

The analysis of Ti–Me system diagrams (Table 5.1) shows that the first requirement is met by some elements from the group of alkali and alkali-earth metals, i.e. Li, Na, K, Rb, Cs, Mg, Ca, Sr, Ba. However, these metals do not meet other requirements to the substrate strip material.

Table 5.1

Iinteraction of various metals with titanium

No interaction	Unlimited solid solutions		Limited solid solutions	Chemical compounds
	in α- and β-Ti	in β-Ti and limited solid solutions in α-Ti		
Li, Na, K, Rb, Cs, Mg, Ca, Sr, Ba	Zr, Hf	V, Nb, Ta, Mo	W, Co, Cu, Au, Mn, Fe, Ni, Pt, Al, Cr, Re	Cr, Mn, Fe, Co, Ni, Cu, Ag, Au, Sn, Rb

Therefore, a further research was conducted in two directions:

– exploring the possibility of foil production by titanium vapor deposition onto a substrate strip, which is subsequently pickled;

– selecting the substrate strip material, meeting all the above requirements except for the first one, and selecting the material of the separation layer-antiadhesive, which prevents the formation of strong coupling between the substrate strip and the condensate at a high temperature.

Literature sources describe a method of making the free condensate by vapor deposition onto a substrate strip, which is subsequently pickled [118, 119]. However, no data on titanium foils made through this technique are available.

In this work a copper tape, 120 mm wide and 50 μm thick, was used as a pickled substrate.

BT6 alloy condensates were obtained on the УВФ-75-1 plant. The alloy was evaporated using a 20 kw electron beam vaporizer, while continuously feeding the wire into the molten metal. The substrate strip was heated in the temperature range of 500...900 °C, the condensation rate being 2.8 μm/min, the condensate thickness – 40 μm. The foil was separated from the substrate strip by pickling copper with 15 % aqueous solution of nitric acid.

The dependence of the mechanical properties on the substrate strip temperature for the BT6 alloy foils obtained is shown in Fig. 5.1.

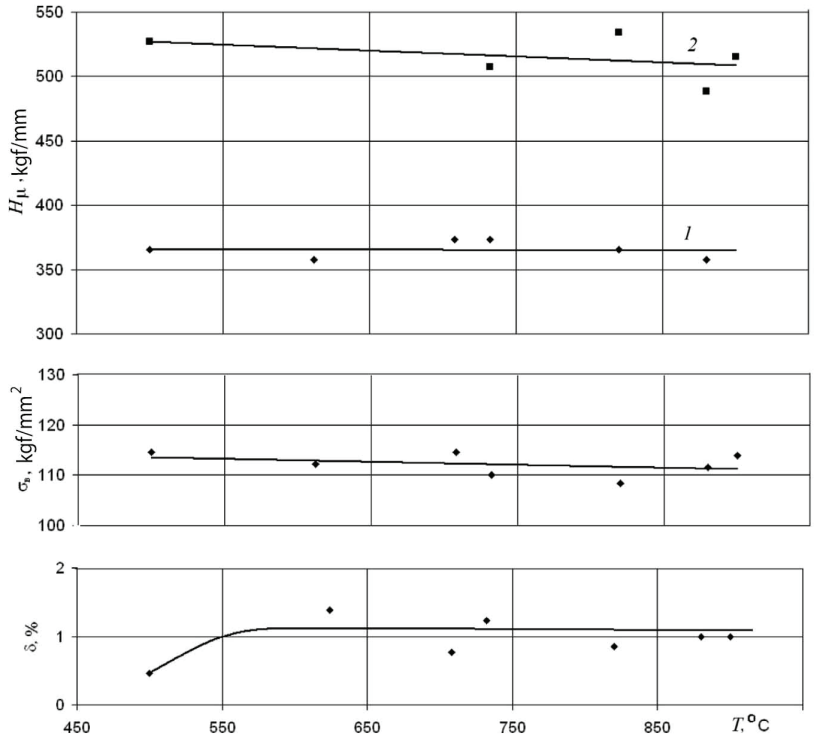

Fig. 5.1. The dependence of the mechanical properties of BT6 alloy foils on the substrate strip temperature; *1* and *2* – microhardness on the side of the vaporizer and the substrate strip, respectively

As the substrate temperature increases from 500 °C to 600 °C, elongation δ increases from 0.5 to 1.0 % while the subsequent temperature rise does not affect it. The tensile strength in the studied temperature range is almost constant being 114 kgf /mm^2. Neither does microhardness of the foil alter with the changing of the substrate strip temperature. On the side facing the vaporizer it is 360 kgf/mm^2.

The X-ray microanalysis results of copper distribution across the foil are shown in Fig. 5.2.

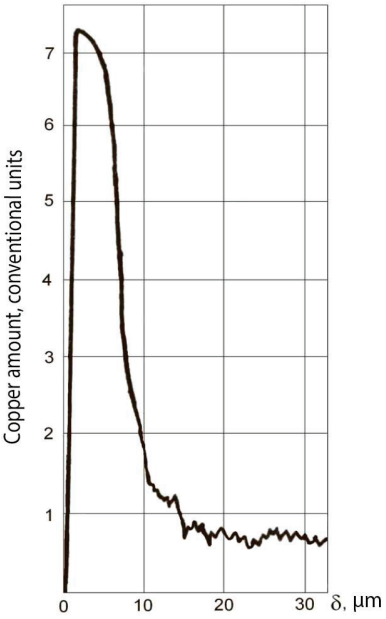

Fig. 5.2. Copper distribution across the BT6 alloy foil obtained by vapor condensing onto the pickled copper substrate

It is apparent that the foil side facing the substrate is rich in copper. The copper concentration decreases with the distance from the foil surface. Integral copper content in the foil is 4.7... 7.4 %. These values by far exceed the value of copper in titanium solubility limit [120]. The presence of intermetallic inclusions in the foil is also proved by about 160 kgf/mm^2 higher values of its microhardness on the foil side facing the substrate (see Fig. 5.1). As seen in Fig. 5.2, the copper enriched area is almost one-third of the foil thickness.

Copper diffusion from the substrate strip into the condensate makes the foil brittle, while increasing amount of intermetallic inclusions at higher temperatures of the substrate, causing the foil embrittlement, is compensated by ductility growth due to reduced internal stress in the foil and improvement of its structure. This is why the foil ductility is constant at growing substrate temperature. The experimental data show that foil production by condensing vapor onto a subsequently pickled substrate strip does not allow to make a sufficiently ductile foil due to the interdiffusion of the substrate and the condensate materials . Therefore, we rejected the technology of manufacturing titanium foil by vapor deposition onto a subsequently pickled substrate strip.

We used 12X18H9 steel strip manufactured by several Russian plants as the substrate strip material for titanium foil production. In accordance with TOR, this strip is made with a high quality surface and has sufficiently good mechanical properties at elevated temperatures ($\sigma_в$(800 °C) = 13 MPa/mm^2).

To study the possibility of multiple using of such strip we conducted its mechanical tests after cyclic heating to the temperature of 900 °C and exposing the strip to this temperature for 5 min. The heat treatment cycle simulated the operation mode of the strip during the foil manufacturing process. It was found that after such thermocyclic treatment, the strip mechanical properties virtually did not deviate from the initial values.

The selection of antiadhesive material was based on the following requirements:

– ensuring the separability of the foil from the substrate strip after passing through the condensation zone;

–sufficiently strong adhesion of the materials of the substrate strip and the condensate through a layer of antiadhesive during condensation to prevent premature separation of the condensate from the substrate strip above the vaporizer and avoid the condensate destruction due to its overheating;

– chemical inertness of the antiadhesive material regarding the substrate strip and the foil materials.

Recommendations found in patent and technical literature include organic compounds, oxides and salts of metals as antiadhesives [68, 121]: Cs, NaCl, $BaCl_2$, etc. [122]; fluorides of Sr, Ba, Mg, Ca [123] .

This work offers the study of the following groups of substances as potential antiadhesives: metals, oxides, halides [124, 125]. Table 5.2 shows some characteristics of the metals that do not react with titanium (see Table 5.1) such as Li, Na, K, Rb, Cs, Mg, Ca, Sr, Ba. Mg, Ca, Sr, and Ba with melting temperature over 600 °C are the most promising antiadhesives for titanium foil production. However, the use of these materials is impeded by their re-evaporation at temperatures of the substrate strip in the range of 400...600 °C.

To determine oxides that may be used as antiadhesive for titanium foil production let us arrange them in the descending order of their affinity for oxygen according to the free energy of oxide formation (Table 5.3):

– in the class of monooxides – Ca, Be, Mg, Sr, Ba, Ti, Th, V, Mn, Zn, Fe, Sn, Co, Ni, Cd, Pb, Bi, Cu, Al;

– in the class of sesquioxides – Y, Sm, Nb, Ce, La, Ti, B, V, Cr, Mg, Fe, Sb, Al, Bi, K;

– in the class of dioxides – Th, Hf, Zr, Ce, Ti, Si, Nb, W , Mo, Sn, Mn.

Oxides of elements located to the left of titanium in these series shall be inert relative to titanium. Some properties of the oxides are given in Table 5.3. The most available of these oxides are those of Ca, Be, Mg, Y, Al, Zr.

Table 5.2

Some physical and chemical characteristics of metals that do not interact with titanium [91, 126]

Metal	Molecular weight, g/mol	Atomic radius, Å	Melting point, °C	Evaporation temperature,°C at P = 10–2 mm Hg. (1.33 Pa)
Li	6.94	1.57	181	534
Na	22.99	1.92	98	290
K	39.09	2.38	63	208
Rb	85.47	2.51	38	176
Cs	132.91	2.70	29	152
Mg	24.31	1.60	649	442
Ca	40.08	1.97	839	592
Sr	87.62	2.15	770	531
Ba	137.34	2.24	729	617

Table 5.3

Free energy and melting temperature of the oxides [127]

Class	Oxide	ΔF0, 295 K	ΔF0, 1000 K	Melting point, K
Monooxides	CaO	–144 350	–127 200	2873
	BeO	–136 100	–119 750	2853
	MgO	–136 100	–118 050	3178
	SrO	–133 850	–117 400	2688
	BaO	–126 300	–101 100	2293
	TiO	–116 900	–101 100	2293
Sesquioxides	Y2O3	–433 450	–385 000	2500
	Ce2O3	–411 500	–356 500	1960
	La2O3	–402 600	(–342 400)	2600
	Al2O3	–378 000	–325 200	2313
	Ti2O3	–344 000	–297 000	2400
Dioxides	ThO2	–279 450	–247 450	3225
	HfO2	–251 750	–219 700	3063
	ZrO2	–247 750	–216 000	2950
	CeO2	–245 940	(–213 200)	2873
	TiO2	–212 400	–182 350	2123

We refer to the abovementioned data on using halide salts as antiadhesive [123]. However, these patents do not mention any modes of antiadhesive deposition and properties of the resulting foils. This prompted us to study the class of halides more thoroughly.

Physical and chemical properties of halides are shown in Table 5.4. These data show that the most refractory are compounds of the fluoride class, especially those of magnesium, calcium, barium and strontium. However, their disadvantage is the difficulty of antiadhesive removal from the surface of the steel strip due to their persistence in water solutions.

Thus, the analysis allowed to reduce significantly the range of possible materials that can be used as antiadhesives for titanium foil manufacturing.

The most promising ones include:

– from metals – Mg, Ca, Ba;
– from oxides– oxides of Ca, Be, Mg, Y, Zr, Al;
– from halides – fluorides Mg, Ca, Ba, Sr.

Based on the results of experimental studies on vacuum deposition of Mg, ZrO_2, Y_2O_3, MgF_2 and CaF_2 onto 12X18H9 steel substrate strip, subsequent deposition of titanium condensates, their separation from the substrate and assessing the separability of the foil from the substrate, the condition of the substrate surface and antiadhesive after separation of the foil and the mechanical properties of the foil the preference was given to the magnesium fluoride.

A very difficult task, along with the selection of optimum antiadhesive thickness and condensation temperature, was developing an antiadhesive evaporation technology.

In addition, we developed a technology of preparation of initial materials − the substrate strip and antiadhesive, including vacuum annealing of the substrate prior to the alloy deposition without depressurization of the vacuum chamber and pre-remelting of the magnesium fluoride powder in inert gas atmosphere.

We developed a technology of electron beam heating of the substrate strip comprising a programmable electron beam scan across the substrate width, and the technology of radiant heating of thin substrate strip.

Therefore main technological parameters of the manufacturing process can be selected for a given foil alloy on the basis of our findings concerning the specifics of high-speed evaporation, replication of the chemical composition during multi-component alloys evaporation from one source with continuous feeding of the molten metal, formation of vacuum con-

Table 5.4

Physical and chemical properties of halides [127]

The class of compounds	Equation	Molecular weight, g/mole	Density, g/m^3	Melting point, °C	Boiling point, °C	$\Delta F_{1000°K}$, cal	$\Delta H_{vaporization}$, cal/mole	Solubility in water, g/100g
Fluorides	LiF	25.94	2.640	845; 870	1670; 1679	–123 300	50 970	~0.14
	NaF	41.99	2.558	997; 1040	1705	–11 800	53 260	~4.20
	CaF_2	78.08	3.180	1360; 1418	1872	(–249 750)	83 000	~0.002
	MgF_2	62.31	2.9–3.2	1263; 1396	2239; 2250	–221 950	65 000	~0.008
	SrF_2	125.6	4.18	1400	2460; 2489	–247 900	71 000	~0.001
Chlorides	NaCl	58.44	2.165	800	1413	–76 250	40 800	~36
	$SrCl_2$	158.53	3.085	873	(2027)	–162 000	(55 000)	52.7
	$CaCl_2$	111.08	2.15	772; 782	(2027)	–155 700	(55 000)	74.5
	$MgCl_2$	95.21	2.316	708; 714	1412	–115 150	32 700	54.6
Bromides	LiBr	86.85	3.464	547	1265	(–70 450)	35 400	166.7
	NaBr	102.89	3.211	750	1392	(–68 000)	37 950	~90
	$SrBr_2$	247.44	4.216	643	(1877)	(–141 900)	(50 000)	87.9
	$CaBr_2$	199.90	3.353	760	(1827)	(–133 500)	(50 000)	142
	$MgBr_2$	184.13	3.72	700	(1227)	(–92 450)	(35 000)	101

densate structure and its connection with the foil properties, and accounting for customer needs regarding the foil.

The process flow for manufacturing titanium alloy foil comprises the following steps:

− preparation of the substrate strip including separation of the paper protector, strip degreasing and placing it into the foil-making plant;

− remelting the antiadhesive in inert gas atmosphere, its placement in the antiadhesive evaporation device;

− sealing the foil-making plant, vacuum annealing of the substrate strip;

− sequential deposition of vaporized antiadhesive and alloy onto a heated substrate strip;

− depressurization of the vacuum chamber, mechanical separation of the foil from the substrate strip (peeling it off), preparation of the substrate strip for its re-use;

− foil quality control.

Depending on the customer's requirements, the process of making titanium foil by vacuum deposition also included vacuum pre-annealing of the evaporated billet and vacuum annealing of the finished foil.

Chapter 6. THROUGH POROSITY OF THE FOIL MADE BY THE VACUUM CONDENSATION TECHNIQUE

The problem of the formation of through porosity in foils is not only of scholar significance but also of considerable practical importance as it largely determines possible applications of the foil material.

Some information on micro-porosity in vacuum condensates is available in literature, e.g. [128, 129]. The emergence of fine pores depends on the structural specifics of the vacuum condensates formation [130−138].

In [133] it is shown that through cylindrical pores in thin vacuum condensates are caused by the diffusion and subsequent condensation of non-equilibrium vacancies. Many of micro-pores appear in the early stages of condensate formation along the boundaries of coalescing insular particles. The dependence of the micro-pore formation on the temperature of the substrate strip shows that the adsorbed gas atoms also play an important role in the formation of micro-pore nucleation centers or in decelerating the surface diffusion of the condensed atoms. These are the two key factors of micro-pores nucleation and growth.

Large pores appear, in particular, when foreign particles get into the foil during the condensation process, including melt droplets from the pool [138], or due to the substrate strip roughness [139−141].

Pollution with volatile substances (e.g. oil spots) can also cause the formation of through holes, because these contaminants evaporate from the substrate surface during the foil making process, preventing the metal vapor condensation. Therefore in our work to eliminate the influence of this factor the substrate strip was not only thoroughly degreased but also annealed in vacuum at higher temperatures prior to the deposition of the alloy vapor on its surface.

The dependence of porosity on coating thickness is observed in pores of all sizes [128, 134].

The authors of the work [142] think that pores are formed when two conditions coincide: there must be a geometric shielding of the vapor flow by projections on the condensation surface, as well as a low mobility of the condensed atoms.

The through porosity of the foils made by vacuum deposition was studied to a much lesser extent by the time of this work.

In our work, along with traditional methods of through porosity studies such as the determination of specific through porosity by translucence and metallographic measurement of through pores dimensions [143], a quantitative method for through porosity evaluation, i.e. the measurement of the vacuum-tightness (permeability) of the foil. The influence of the main technological parameters of the vacuum deposition process, as well as the substrate strip roughness and the gas content of the evaporated billet on the through porosity characteristics of the foil alloy BT6 was studied. To ensure practical applications of the obtained results on through porosity characteristics, and to expand the areas of using the foil with regulated through porosity, methods of calculating the required values of vacuum tightness and gas permeability of multi-layer porous foil screens at a higher temperatures were suggested.

6.1. Vacuum tightness and through porosity of the foil

In some fields of science and technology the concept of vacuum tightness is used to assess the suitability of particular material, and foils among them, as a wall of the vacuum chamber, in which it is necessary to maintain a predetermined rarefaction [144].

This characteristic is especially important when using the foil made of light alloys in devices ensuring an electron beam output from a vacuum chamber to atmosphere (exhaust ports) [145]. In this case the foil should ensure both the minimum losses of an electron beam passing through it and the desired tightness of the vacuum chamber.

Foil vacuum tightness was usually estimated indirectly, empirically, or by comparing the vacuum in the vacuum chamber with the foil window, with the desired vacuum level, or by the absence of any leaking defined by the leak detector when blasting the foil window with helium. The quantitative relation between the vacuum tightness and the foil through porosity was not found as well.

The introduction of quantitative criteria to evaluate vacuum tightness is also necessary in order to improve the foil making technology, because without this it would be difficult to estimate the impact of the foil making parameters on the through porosity not detectable by translucence.

6.1.1. A quantitative criterion of the foil vacuum tightness

There is a well-known criterion for evaluating the permeability of the material for a particular gas – gas permeability Π, $\frac{\mathrm{m}^3(\mathrm{NTP})}{\mathrm{m}^2 \cdot \mathrm{c} \cdot \mathrm{Pa}}$, equal to the gas amount at normal temperatures and pressure Q, m^3 (NTP), passing in the time unit through the membrane unit area at the pressure difference on both sides of the membrane equal to 1 Pa:

$$\Pi = \frac{Q}{St\left(P_1 - P_2\right)}, \tag{6.1}$$

where S – membrane surface area, m^2; t – time, s; $(P_1 - P_2)$ – pressure difference on the opposite sides of the membrane, Pa.

Since the vacuum tightness is understood as the material ability to resist gas penetration through it, let us determine vacuum tightness R, $\frac{\mathrm{m}^2 \cdot \mathrm{s} \cdot \mathrm{Pa}}{\mathrm{m}^3(\mathrm{NTP})}$ as the value inversely proportional to gas permeability

$$R = \frac{1}{\Pi} = \frac{St\left(P_1 - P_2\right)}{Q}. \tag{6.2}$$

The gas permeability value Π consists of two components − the permeability of the material itself, Π_m, and the gas permeability of through holes in the foil, Π_o:

$$\Pi = \Pi_m + \Pi_o \tag{6.3}$$

Literature offers a very limited number of works on metal gas permeability [126, 146].

Without experimental data, the value of gas permeability of a metal can be approximately calculated using the following equation

$$\Pi_m = DS_g, \tag{6.4}$$

where D – gas diffusion coefficient, m^2/s; S_g – gas solubility in the metal.

The second member of Equation (6.3), Π_o, can be determined by calculation if the average diameter of through pores in the foil d, m, the specific

through porosity n, m^{-2}, the foil thickness δ, m, and the pressure on both sides of the foil P_1, P_2, Pa, are known.

To do this, let us consider through pores in the foil as pipelines.

The gas flow through the pipeline per unit of time is

$$Q = U(P_1 - P_2),\ \frac{\text{m}^3}{\text{s}}; \tag{6.5a}$$

$$Q = \frac{22.4 \cdot 10^{-3}}{8.31T} U \Delta P,\ \frac{\text{m}^3\,(\text{NTP})}{\text{s}}, \tag{6.5b}$$

where U – pipeline transfer capacity at $\Delta P = 1$, m^3/s; 8.31 – universal gas constant, $m^3 \cdot Pa/(mole \cdot K)$.

For the molecular flow mode of the gas with the molecular weight M_i the transfer capacity of a short pipeline ($\delta < 20d$), U_{sp},

$$U_{\text{sp}} = 10 \left(\frac{T}{M_i} \right)^{1/2} d^2 \left(\frac{\delta}{3.8d} + 0.35 \right)^{-1} \tag{6.6}$$

For a long pipeline ($\delta > 20$d) transfer capacity, U_{lp},

$$U_{\text{lp}} = 38 \left(\frac{T}{M_i} \right)^{1/2} \frac{d^3}{\delta}. \tag{6.7}$$

When the pipe diameter exceeds the foil thickness, for air at $T = 293$ K it can be approximated as follows

$$U_0^{(i)} \cong 1.16 \cdot 10^2 F_i' \tag{6.8}$$

where F_i' – the hole area, m^2.

At room temperature, the first member of Equation (6.3) can be neglected, and the total transmissivity of the foil, U_f, can be considered as the sum of transmissivities of the through holes in the foil

$$U_{\text{f}} = \sum U_0^{(i)} = 1.16 \cdot 10^2 \sum F_i' \tag{6.9}$$

The foil through porosity is the ratio of the total area of through holes to the total foil area

$$F = \frac{\sum F_i'}{S}, \tag{6.10}$$

hence U_f

$$U_f = 1{,}16 \cdot 10^2 \cdot F \cdot S. \tag{6.11}$$

From (6.1), (6.2), (6.5), (6.8) and (6.11)

$$R = \frac{S\Delta P \cdot 8.31 \cdot T}{22.4 \cdot 10^{-3} \cdot U_f \Delta P} = \frac{8.31 \cdot TS}{22.4 \cdot 10^{-3} \cdot 1.16 \cdot 10^2 \cdot FS} = \frac{9.37 \cdot 10^2}{F} \tag{6.12}$$

Equation (6.12) establishes the relation between vacuum tightness R and foil through porosity F.

To improve the accuracy of this calculation, it is necessary to substitute the U values from Equations (6.6) or (6.7) for the value U_0 from Equation (6.8).

6.1.2. Experimental determination of foil vacuum tightness

To determine the vacuum tightness of coiled foil up to 400 mm wide, a universal vacuum plant (UVP) was developed, the layout of which is shown in Fig. 6.1.

The plant includes:

– vacuum chamber;

– pumping apparatus;

– foil rewind mechanism;

– devices for pressing and sealing an isolated rectangular foil "specimen" without breaking the strip integrity;

– power and control units of the vacuum system;

– equipment for vacuum control and measurement.

Foil strip (*10*) is pressed by flange (*3*) to chamber body (*1*). Then volume (*7*) and vacuum chamber (*1*) are pumped out mechanically keeping valve (*8*) and valve (*12*) closed, and valves (*4*), (*5*), and (*6*) open. The vacuum of 1.33 Pa having reached, valves (*5*) and (*6*) get closed and valve (*8*) open, thus connecting pumped volume (*1*) with the oil-vapor pump.

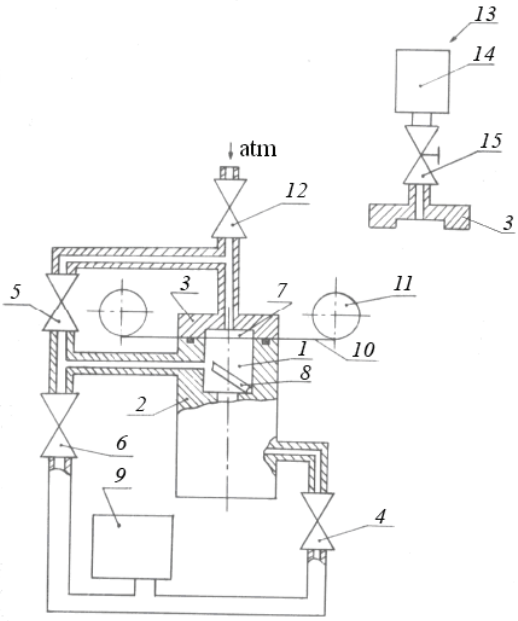

Fig. 6.1. The UVP plant layout to determine foil vacuum tightness: *1* – vacuum chamber; *2* – high vacuum unit; *3* – clamping flange; *4*, *5*, *6*, *12* – valves; *7* – volume formed by the clamping flange; *8* – vacuum system valve; *9* – fore-vacuum pump; *10* – foil strip; *11* – mechanism for rewinding and moving the foil strip; *13* – plant calibration device; *14* – calibrated volume; 15 – leak valve

Firstly, the vacuum in chamber (*1*) is measured. Then valve (*12*) is opened to let air into volume (*7*) and vacuum P_2 in volume (*1*) is measured again.

The vacuum tightness can also be measured in the "backing pump" mode. To do this, volume (*1*) is continuously pumped out not with the high vacuum oil-vapor pump, but with the fore-vacuum pump. At that valve (*8*) is closed, valve (*5*) is closed and valve (*6*) is open.

The amount of gas which passes through the foil during time t equals to:

$$Q = K_1 \int_0^t (P_2 - P_2^0)\mathrm{d}t, \quad (6.13)$$

where K_1 – constant, $m^3/(Pa \cdot s)$; P_2^0 – gas pressure in the vacuum chamber with no foil (in the case of solid walls).

During continuous pumping out volume (*1*) and reaching the stationary state $P_2 - P_2^0 = \text{const}$ and Equation (6.13) takes the form

$$Q = K_1 \left(P_2 - P_2^0 \right) t, \quad (6.14)$$

hence

$$\frac{Q}{t} = K_1 \left(P_2 - P_2^0 \right) \quad (6.15)$$

The substitution of (6.15) in (6.2) gives

$$R = \frac{S\left(P_1 - P_2\right)}{K_1\left(P_2 - P_2^0\right)}. \tag{6.16}$$

If $P_1 >> P_2$, then

$$R = K_2 \frac{P_1}{\left(P_2 - P_2^0\right)}, \tag{6.17}$$

where $K_2 = \frac{S}{K_1}$.

The value of K_1, characterizing the pump system, was determined in a special experiment using (6.13) by evacuating a known amount of the gas from the calibrated volume (see (*14*) in Fig. 6.1), recording dependence $P_2 = f(t)$ and then integrating function $(P_2 - P_2{}^0) = f(t)$.

For our plant the K_1 value was $4.97 \cdot 10^{-9}$ and $7.8 \cdot 10^{-7}$ $m^3/(Pa \cdot s)$ in the pressure intervals of $P_2 = 1 \ldots 5$ and $1 \cdot 10^{-2} \ldots 5 \cdot 10^{-2}$ Pa, respectively.

Using these values of K_1, value S = $3.16 \cdot 10^{-3}$ m^2 and the atmospheric pressure P_1, from Equation (6.17) for gas permeability $R, \frac{m^2 \cdot Pa \cdot s}{m^3(NTP)}$, we'll have

$$R = \frac{6.35 \cdot 10^8}{(P_2 - P_2^0)}, \tag{6.18}$$

within the pressure range of $1 < P_2 < 5$ Pa, and

$$R = \frac{4.05 \cdot 10^6}{(P_2 - P_2^0)} \tag{6.19}$$

in the pressure interval of $1 \cdot 10^{-2} < P_2 < 5 \cdot 10^{-2}$ Pa.

The vacuum tightness calculated using the stationary state value P_2 for a given foil specimen by Equations (6.18) or (6.19), depending on what pressure interval the value P_2 was in.

6.2. The influence of vacuum deposition parameters on the characteristics of through porosity in the foil

We studied the effects of substrate strip temperature, condensation rate, rarefaction, condensate and anti-adhesive layer thickness, substrate strip roughness as well as initial materials preparation on the foil through porosity characteristics.

The distribution of through pores by size is shown in Fig. 6.2. The most common are pores 50 μm in diameter, which substantially exceeds the thickness of the studied foils.

The dependence of through porosity and vacuum tightness on foil thickness at various substrate strip temperatures are presented in Fig. 6.3 and 6.4.

As the foil thickness increases, its through porosity decreases within the studied temperature range of 500...950 °C. The vacuum tightness of the foil is changed similarly.

At the substrate temperature of 850 °C, a double increase in the foil thickness (from 10 to 20 μm) causes a reduction of through porosity by 9 times. At the same time, the vacuum tightness increases more than by 10 times.

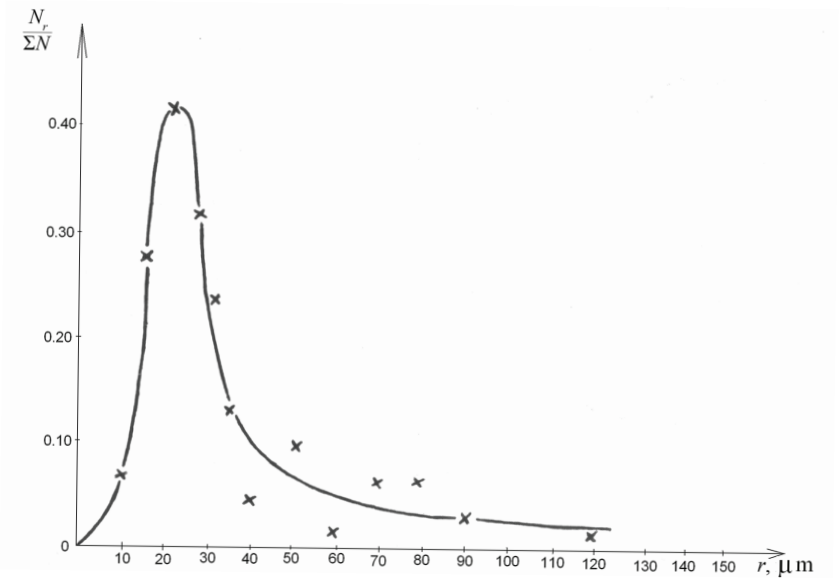

Fig. 6.2 The size distribution of through pores in titanium foil

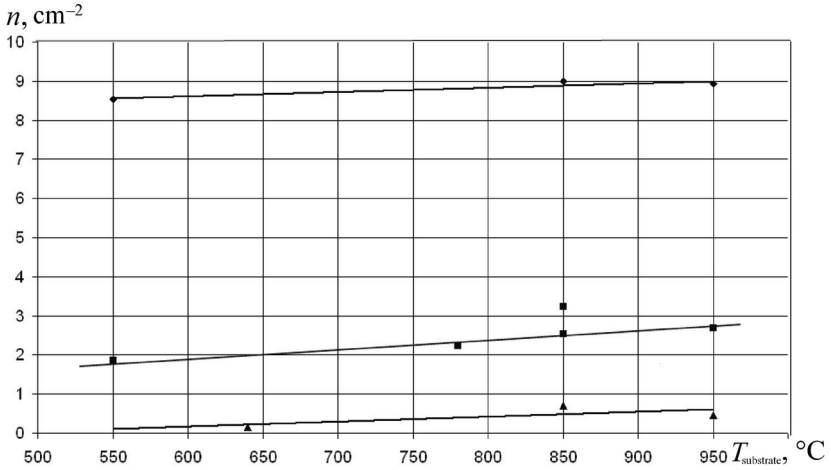

Fig. 6.3 The dependence of specific through porosity (n)
on substrate strip temperature and foil thickness:
◆ – δ = 10 μm; ■ – δ = 15 μm; ▲ – δ = 20 μm

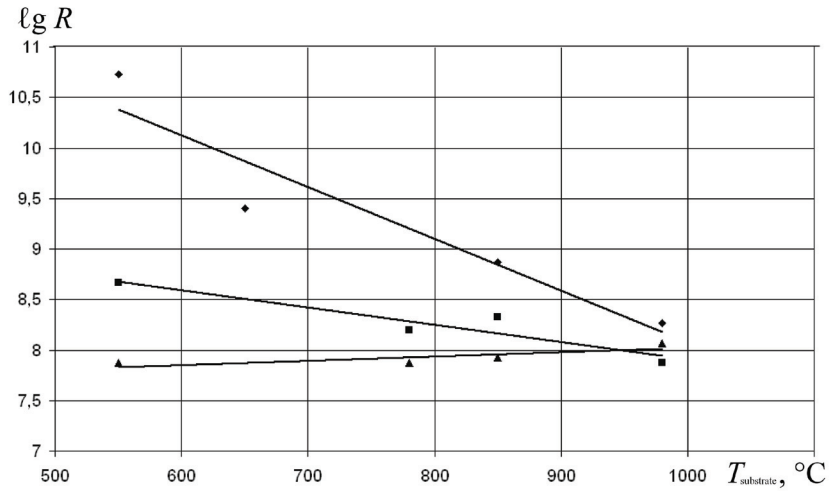

Fig. 6.4 The dependence of vacuum tightness
on substrate strip temperature and foil thickness:
◆ – δ = 10 μm; ■ – δ = 15 μm; ▲ – δ = 20 μm

The change of through porosity characteristics depending on the substrate strip temperature is largely determined by the foil thickness.

For the 10 μm thick foil an increase in the substrate strip temperature has virtually no effect on the specific through porosity as well as on the vacuum tightness of the foil. For the 15 μm thick foil an increase in the substrate temperature causes an increase in the specific through porosity, while the vacuum tightness decreases. For the 20 μm thick foil the level of through porosity is lower than that of the 15 μm thick foil, however, the growth of the specific through porosity along with the increase in the substrate temperature is expressed less sharply. At the same time, the vacuum tightness of the 20 μm thick foil decreases with the increase in the substrate temperature more sharply than in the case of the 15 μm thick foil.

It is noteworthy that with increasing substrate temperature the vacuum tightness dependence on the foil thickness becomes less pronounced, and at the substrate temperature of 950 °C this through porosity characteristic is about the same for all the foils of 10...20 μm thick (Fig. 6.4).

The anti-adhesive layer thickness significantly affects the level of the foil through porosity (Table 6.1). Thus, for the 1.0 μm thick layer the through porosity is $5 \cdot 10^{-5}$ %, while decreasing layer thickness up to 0.3 μm causes the through porosity increase by 20 times.

Table 6.1

The impact of anti-adhesive layer thickness and initial billet conditions on through porosity and droplet phase in titanium foil

	Anti-adhesive layer thickness, μm			Evaporated billet conditions	
	0.3	0.5	1.0	Without pretreatment	After vacuum heat treatment
Through porosity, %	$1 \cdot 10^{-3}$	$2 \cdot 10^{-4}$	$5 \cdot 10^{-5}$	$1 \cdot 10^{-3}$	$2 \cdot 10^{-4}$
Droplet phase, %	$1 \cdot 10^{-3}$	$1 \cdot 10^{-3}$	$1 \cdot 10^{-3}$	$1 \cdot 10^{-2}$	$1 \cdot 10^{-3}$

The degree of rarefaction affects the through porosity characteristics to a much lesser extent. As the rarefaction increases from $4 \cdot 10^{-5}$ to $2 \cdot 10^{-5}$ mm Hg, the specific through porosity drops from 1.2 to 0.7 cm^{-2}, while the vacuum tightness (lg *R*) increases from 8.6 to 8.9.

The droplet phase and through porosity are greatly influenced by the gas content of evaporated billet.

In oder to change the billet hydrogen content, the vacuum annealing of initial ingots, 100 mm in diameter, at the temperature of 1400 °C for 25...100 hrs was used. The vacuum annealing allowed reducing the ingot hydrogen content from 0.015 to 0.005 %. This caused a 10 times decrease

in the droplet phase amount, while the foil through porosity decreased by ~5 times, i.e. from $1 \cdot 10^{-3}$ to $2 \cdot 10^{-4}$ % (Table 6.1).

Similar results were obtained in the experiments of feeding the molten metal pool with wire. The preliminary vacuum annealing at 800 °C for 1 hr causes a decrease in the wire hydrogen content by 3...6 times, while the droplet phase amount in the foil reduced sharply (Table 6.2).

Table 6.2

The effect of vacuum annealing of the 2B alloy wire on the droplet phase amount in the foil

Annealing mode	Wire hydrogen content, %	Droplet phase, cm^{-2}
No annealing	0.006	3
800 °C, 2 hours	0.001	0.03

The absence of through pores, detected by the foil translucence, did not guarantee the vacuum tightness of the foil.

Table 6.3 presents the data on the percentage of the foil specimens with no "translucent" through pores but with the value of lg $R > 14$, which may well be considered as vacuum-tight.

No "translucent" through pores were found in the 15 μm thick foil, however, virtually no researched specimens were vacuum-tight. Yet, more than two-thirds of the 35 μm thick specimens with no "translucent" through pores were vacuum-tight.

Table 6.3

The share of vacuum-tight foil specimens (lg $R > 14$) with no through pores detected by the foil translucence

Thickness , μm	Share of vacuum-tight specimens, %
15	0
25	23
35	71

The characteristics of the foil through porosity are substantially influenced by the roughness of the substrate strip surface (Table 6.4).

Table 6.4

The influence of substrate strip surface conditions on the through porosity level in titanium foil

	Substrate strip surface conditions			
	Polished (∇10)	Ground (∇8)	Sanded (∇4)	With boron powder
Through porosity, %	$1 \cdot 10^{-4}$	$2 \cdot 10^{-4}$	$4 \cdot 10^{-3}$	$5 \cdot 10^{-2}$

As compared to grinding, polishing the substrate surface brought a two-fold reduction of the foil through porosity, while sanding the substrate surface increased the foil through porosity by a factor of 20.

The most effective means of increasing the through porosity was pre-coating the substrate strip with 15…20 μm boron powder. This caused the through porosity increase by a factor of 250.

The through porosity affects the value of the actual surface of the foil. But we have not found any literature data on the true value of the surface area of the foil made by vacuum deposition.

For titanium foils this value was determined by the procedure, using the BET method [147] based on measuring the krypton adsorbed by the foils at the liquid nitrogen temperature (–196 °C).

The amount of the adsorbed krypton was determined by the change in the gas pressure above the foil. Krypton was used owing to its low saturated vapor pressure at the liquid nitrogen temperature ($P_s \approx 1.78$ mm Hg) (237.2 Pa). This allows improving the accuracy of the area assessment for the materials of low specific surface area. The detection limit of this method is $1.2 \cdot 10^{-4}$ m^2/g, with the reproducibility of 15 % rel.

The foil specific surface area obtained by BET method, S_{BET}, gives the equation

$$S_{\text{BET}} = \frac{a_{\text{M}}}{M} N_{\text{A}} \omega_m \cdot 10^{-20}$$

where a_{M} – adsorbate amount, g per 1 g of the foil; M – molecular weight of the foil material; N_{A} – Avogadro's number; ω_m – cross-section area of the adsorbate molecule, Å^2.

The value a_{M} was determined by the "single point" method [148]

$$a_{\text{M}} = a\left(1 - \frac{P}{P_0}\right)\left\{1 + \frac{\frac{P_0}{P} - 1}{C}\right\},$$

where a – adsorption value, mole/g; P – partial vapor pressure of the adsorbate; P_0 – saturated vapor pressure of the adsorbate; C – constant.

Strips, 60 mm wide and 700...850 mm long, tightly coiled into Ø10 mm tubes, were used as foil specimens.

As each external coil layer of the foil is a heat shield for the internal layers, plus low heat conductivity of titanium and, consequently, the temperature gradient across the diameter of the tube specimen, at first the ratio of the specific surface area of the vacuum deposited foil, S_{vac}, to the specific surface area of the rolled foil, S_{rolled}, as measured by the same BET-method, was determined. Then, knowing the value of the surface roughness of the rolled foil which is equal to 6 [149], we defined the roughness coefficient and the true surface area of the vacuum deposited foil (Table 6.5).

Table 6.5

The true surface of the vacuum deposited foil compared to the rolled foil

Foil production method	Specific through porosity, %	Specific surface area of the foils S_{BET}, m^2/g	S_{vac}/S_{rolled}	Roughness coefficient of the foils	True surface area, m^2/g
Rolling	0	0.01	1	6	0.18
Vacuum deposition	$8.3 \cdot 10^{-6}$	0.04	4	24	0.72
Vacuum deposition	$5.0 \cdot 10^{-3}$	0.09	9	54	1.62

It is obvious that the surface of the foil made by vacuum deposition is substantially more developed (here – up to 9 times) than the rolled foil surface.

Increasing through porosity of the vacuum deposited foil causes tangible growth of the true foil surface area, which is likely to affect directly its sorption characteristics, in particular, when using the foil in high-temperature membrane technologies.

6.3. The model of through porosity formation in the foil

Experimental results of our work allow us to conclude that through porosity in the foil, obtained by alloy vacuum deposition, is formed due to three main factors:

1) discontinuities at the crystallite boundaries;
2) substrate strip surface roughness;
3) droplets of molten metal on the condensation surface.

The impact of the first factor is confirmed by the results of measuring the vacuum tightness of the foil, which has no translucent pores, as well as by the studies of the cross section structure of the foils obtained at a relatively low (600 °C) substrate strip temperature.

The through porosity caused by this factor is obviously typical both for foils and coatings made by vacuum deposition. However, one of the most significant factors of through porosity formation are molten metal droplets getting on the condensation surface.

Droplets formation (boiling and splashing of the melt in the vaporizer) during the electron-beam evaporation is caused both by heterogeneous nucleation centers of the vapor phase and by fluctuation nuclei when the molten metal pool is overheated [150−154]. This process is enhanced by the formation of dissolved gas bubbles, pores, foreign particles, etc. Work [155] mentions oxide inclusions and chemical heterogeneity of the evaporated billet as factors contributing to the droplet phase formation.

Our findings include three kinds of through pores caused by droplets of the molten metal from the vaporizer getting on the substrate strip during the foil production:

1) pores resulted from crumbling out of the solid drops which are barely adhered to the foil and to the substrate surface;

2) pores formed by "shadowing" of the vapor flow by the drops on the condensation surface;

3) pores formed during the mechanical separation of the foil from the substrate at the points of drops hitting the substrate surface.

Fig. 6.5 shows a droplet and a circular through pore with smooth edges, closely located in the foil. Since the pore size is comparable to the size of the crystallized droplet, it can be assumed that this pore was formed by crumbling out of a similar droplet.

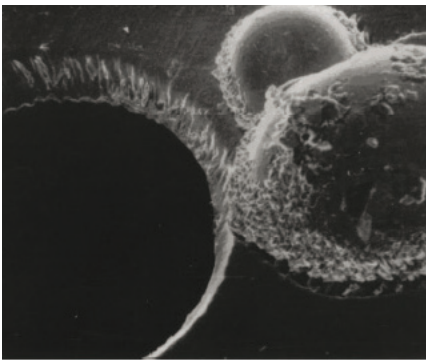

Fig. 6.5. A droplet and a through pore in the foil. View on the side of the foil facing the vaporizer (×200)

Fig. 6.6. A droplet on the foil surface facing the vaporizer (×200)

Fig. 6.6 shows clearly discontinuities on the border between the droplet and the foil resulted due to the drop shielding the vapor flow. Small crystallites formed during the vapor condensation at the final stages of the vacuum deposition are visible on the surface of this droplet.

Apparently, discontinuities similar to the one shown in Fig. 6.6 that are formed by droplets shielding the vapor flow, contribute to the crumbling out of droplets and the appearance of pores of the first type.

The first two types of through pores can be observed both in vacuum coatings and in foils.

The third type of through pores, apparently, is typical of foils made by mechanical separation of the condensate from the substrate strip, being absent in vacuum coatings and condensates separated by pickling the substrate.

a

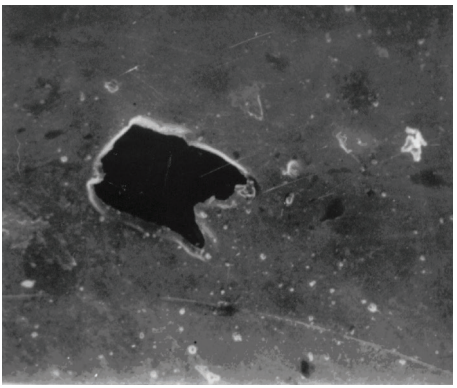

b

Fig. 6.7 A droplet on the surface of the substrate strip after separating the foil (*a*) and a through pore in the foil caused by this droplet (*b*)

Fig. 6.7, *a* shows a droplet on the substrate strip surface after the separation of the foil, and Fig. 6.7, *b* shows a through pore made by this droplet at the point where it hit the condensation surface.

A wider rim with smooth surface on the substrate around the droplet (see Fig. 6.7, *a*) indicates that the droplet partially got flattened as it collided with the substrate strip. Non-separated pieces of the foil can be seen on the droplet surface. The flat surface of the droplet top was formed, apparently, as the substrate strip was coiled up together with the foil. The winding force was sufficient to deform the crystallized droplet.

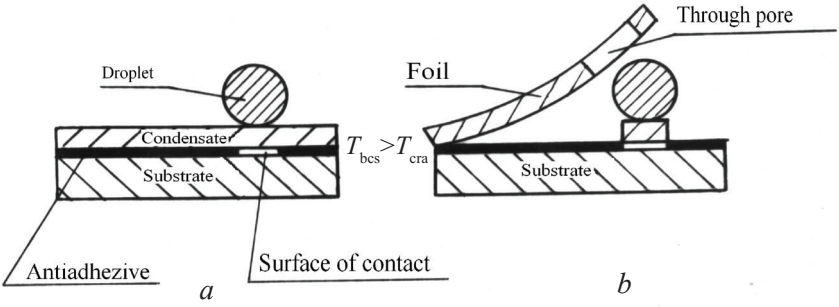

Fig. 6.8 The mechanism of through porosity formation in the foil

The pore with ragged edges, which is elongated along the direction of the foil separation (see Fig. 6.7, *b*) is typical of the third type of through pores.

We suggested the following formation mechanism for through pores of this type. During vacuum deposition, a liquid droplet, ejected from the vaporizer, hits the substrate strip with the condensate thereon and heats the condensate just in the area adjacent to the droplet (Fig. 6.8, *a)*. And the temperature at the boundary between the condensate and the substrate strip (T_{bcs}) may exceed the critical temperature for a given anti-adhesive material (T_{cra}). The critical temperature is meant as the maximum temperature at which the selected anti-adhesive material maintains its barrier properties. For magnesium fluoride this temperature is 1100 °C.

If the local temperature on the condensate-substrate border exceeds a certain critical value, then the diffusion welding of the condensate and the substrate at this point will occur.

Thus, the condition for the formation of a diffusion contact on the border between the condensate and the substrate is represented as follows:

$$T_{bcs} > T_{cra} \tag{6.20}$$

The mechanical separation of the condensate from the substrate strip may cause the formation of a through pore at the point of their diffusion welding (Fig. 6.8, *b*).

Let us formulate the condition for the through pore formation, based on the above mechanism:

$$\sigma_t \cdot \pi r^2_{\text{cont.surf.}} \geq F_{\text{br.out}} \geq \tau \cdot 2\pi r_{\text{cont.surf.}} \cdot \delta, \tag{6.21}$$

where $F_{\text{br.out}}$ – breakout force of the foil separation from the substrate strip, kg; $r_{\text{cont.surf}}$ – radius of the contact surface, m; σ_t – tensile strength, MPa; τ – shear strength, MPa; δ – foil thickness, m.

Hence

$$\frac{\sigma_t}{2\tau} \geq \frac{\delta}{r_{\text{cont.surf.}}} \tag{6.22}$$

Equation (6.22) expresses the condition for the formation of through pores of the third kind in the foil.

For the plane-stress state (thin sheet and foil) [156]

$$\tau \approx \frac{\sigma_t}{2} \tag{6.23}$$

Substituting (6.23) into (6.22), we'll finally have

$$\frac{\delta}{r_{\text{cont.surf.}}} \leq 1 \tag{6.24}$$

For separating the foil without forming a through pore

$$\tau \cdot 2\pi r_{\text{cont.surf}} \cdot \delta \geq F_{\text{br.out}} \geq \sigma_t \cdot \pi r^2_{\text{cont.surf.}}, \tag{6.25}$$

or

$$\frac{\sigma_t}{2\tau} \leq \frac{\delta}{r_{\text{cont.surf.}}}. \tag{6.26}$$

The substitution of (6.23) into (6.26) gives

$$\frac{\delta}{r_{\text{cont.surf.}}} \geq 1 \tag{6.27}$$

In other words, the main criterion for the formation of a through pore due to a melt droplet hitting the condensation surface is the ratio of the foil thickness to the radius of the contact surface [157].

The above-mentioned experimental results confirm this conclusion.

The increasing share of the droplet phase prompts a rise in through porosity in the foil (see Table 6.1). A thicker condensate layer causes the

left-hand part of the relation (6.24) to increase, hence the through porosity of the foil is reduced (see Fig. 6.3).

A thinner layer of the anti-adhesive material translates into a bigger area of the contact surface, which causes a reduction of the left-hand side of the relation (6.24) and, consequently, an increase in through porosity of the foil (see Table 6.1).

Reducing the gas content of the initial materials by vacuum annealing helps diminish the splashing of the molten metal pool (see Table 6.1) and, therefore, curtails the through porosity.

The proposed model suggests that with increasing substrate temperature (at constant size and temperature of a droplet) the diffusion contact area will increase and, consequently, the left-hand part of Equation (6.24) will reduce; therefore, the through pores number is supposed to grow. Indeed, as follows from Fig. 6.3, the specific through porosity, estimated by the number of detectable pores, increases at higher substrate strip temperatures.

Similar results were obtained when studying the foil vacuum tightness (see Fig. 6.4): the vacuum tightness of 15...20 μm thick foils decreases as the substrate strip temperature increases.

At reaching the substrate strip temperature close to the critical one (T_{cra}), virtually every droplet hitting the substrate strip will cause the formation of a through pore. In addition, the influence of the foil thickness on the through pore formation is likely to decrease.

This is confirmed by the data shown in Fig. 6.4. At the substrate strip temperature of 960 °C, which is close to T_{cra} for this particular anti-adhesive material (~1100 °C), the vacuum tightness of 10, 15 and 20 μm thick foils differs slightly.

From the proposed model it follows that for a given vaporizer, which is characterized, in particular, by the number and the size of melt droplets per unit area and per unit time, there should be a certain critical foil thickness δ_{cr}, below which the number of the through pores considered, is constant. In other words, if the foil thickness is small enough, then almost every droplet falling onto the condensation surface will cause the formation of a through pore. Therefore, at a high enough substrate temperature ($\sim T_{cra}$) this through porosity should not significantly depend on the foil thickness at $\delta \leq \delta_{cr}$. This phenomenon is illustrated by Fig. 6.4: the through porosity of 10, 15 and 20 μm thick foils tends to be similar as the substrate strip temperature increases up to ~960 °C. Obviously, this indicates to the main

role of the proposed mechanism of through pore formation in all the foils at a given set of the process parameters.

This results allows concluding that increase in foil through porosity will be enhanced by using an anti-adhesive having a lower critical temperature, by increasing droplet phase share as well as by rising size, temperature and start speed of the droplets ejected from the vaporizer, and by reducing the distance from the vaporizer to the substrate strip.

The influence of the substrate surface roughness on the porosity of vacuum coatings, condensates separated by substrate pickling or by mechanical separation of the condensate from the substrate strip, is somewhat different. Work [138] notes that the surface roughness of the substrate strip and the presence of impurities, in particular, dust particles on this surface, leads to the formation of pores less than 6...11 μm in size in vacuum condensates, while these factors are irrelevant as far as the formation of larger through pores is concerned.

The influence of the substrate strip surface roughness on the formation of larger through pores, established in our research, is due, possibly, to the fact that the protrusions on the condensation surface play the role of stress concentrators when the foil is mechanically separated (peeled off) from the substrate strip. This can explain the difference with the findings in [138] that did not reveal such a strong dependence of through porosity on substrate strip roughness in the case of vacuum coatings.

The same reason can explain differences in the influence of particles located on the substrate surface on the through porosity in vacuum coatings [138] and that in foils obtained by mechanical separation of the condensate from the substrate strip (see Table 6.4).

Our results show that foil through porosity can be widely controlled by varying the parameters of the vacuum deposition process, as well as by changing the substrate strip surface roughness and the gas content in the evaporated materials.

The data in Table 6.3 as well as the results of the customer foil tests showed that using a highly intensive electron-beam deposition process can yield vacuum-tight titanium alloy foil of a thickness exceeding 20 μm. At the same time, the results obtained lead to the conclusion on the possibility of using the vacuum deposition technique to make even thinner vacuum-tight foil.

To reduce through porosity, it is necessary, along with a thorough preparation of the substrate strip surface and smoothing its roughness,

to diminish drastically the share of the droplet phase. The latter can be achieved by evaporating the metal from a "blind" (not pass-through) crucible without additional feeding the melt. At first, it is necessary to remelt and to degas the pool keeping the throttle between the crucible and the substrate closed, and then, having reduced the power of the electron beam gun, open the throttle to deposit the vapor on the substrate.

However, this method is not sufficiently productive because the lower vaporizer power, while decreasing the splashing of the molten metal, will substantially slow down the evaporation rate.

Furthermore, no feeding of the pool along with a lower cycle time will make the application of this technique not feasible for the manufacture of vacuum-tight foil from alloys due to changes in the pool chemical composition during the evaporation process.

6.4. Calculation of the preset vacuum tightness of the foil

Our method of the quantitative estimation of through porosity based on foil vacuum tightness allows formulating reasonable requirements to the foil quality (and, respectively, to the foil making process) in accordance with customers' demands.

Let us find the relationship between the main structural characteristics of devices, which use foil material, and the foil vacuum tightness. The required values of the foil vacuum tightness will be calculated separately for devices with continuous pumping of the vacuum chamber and closed-volume devices.

The main practical criterion of foil suitability is the the vacuum deterioration value, ΔP_2, for the plant using a foil window

$$\Delta P_2 = P_2 - P_2^0, \tag{6.28}$$

where P_2 – pressure in the vacuum chamber with the foil wall;

P^0_2 –background pressure in the vacuum chamber when the foil is replaced with a massive plug.

In other words, ΔP_2 – is an excess pressure in the vacuum chamber due to gas inleakage through the foil. It is typical to specify the maximum allowable value ΔP_2^m by which the vacuum can be deteriorated when using the foil.

According to Equation (6.1), the quantity of the gas which has passed through the foil per time t at constant pressures of P_1 and P_2 will be

$$Q = \Pi S t \left(P_1 - P_2 \right), \tag{6.29}$$

where Π – gas permeability; P_1 – pressure outside the vacuum chamber;
P_2 – pressure inside the vacuum chamber.

On the other hand, the amount of the gas pumped from the vacuum chamber is

$$Q = K_1 \int_0^t \Delta P_2 dt,$$

where K_1 – pumping rate in the cross section of the vacuum sensor, $m^3/(Pa \cdot s)$; t – time, s.

For devices of the first type in the stationary state

$$Q = K_1 t \cdot \Delta P_2. \tag{6.30}$$

From (6.29) and (6.30), taking into account (6.2) and (6.28), it follows that

$$\Delta P_2 = \frac{P_1 - P_2^0}{1 + \dfrac{K_1 R}{S}}. \tag{6.31}$$

If $P_1 >> P_2{}^0$, then

$$\Delta P_2 = \frac{P_1}{1 + \dfrac{K_1 R}{S}}. \tag{6.32}$$

Equation (6.32) makes it clear why foils with the same value of vacuum tightness R are either usable or useless depending on a given case.

Except for vacuum tightness, the value of vacuum deterioration is influenced by:

– pumping rate characterized by value K_1;

– vacuum in the vacuum chamber created by continuous pumping without foil (with a plug) $P_2{}^{0;}$

– foil surface area S;

– pressure outside the vacuum chamber P_1.

From Equation (6.32) the required value of vacuum tightness is

$$R \geq \frac{S}{K_1}\left(\frac{P_1}{\Delta P_2^m} - 1\right). \tag{6.33}$$

If $P_1 >> P_2$, then

$$R \geq \frac{SP_1}{K_1 \Delta P_2^m}. \tag{6.34}$$

ΔP_2^m in Equation (6.34) is preset while other values, except for K_1, are known. Value K_1 is the pumping rate in the cross section of the vacuum measurement sensor. This value can be determined both by calculation [158] and experimentally [146]. In the latter case, it is possible to use the method described above in p. p. 6.1.2.

For devices of the second type, considering that the cycle time t is sufficiently high as compared to the time needed for establishing a stationary gas flow (by inleakage) through the foil, it can be written that

$$Q = \Pi\left(P_1 - P_2\right)St$$

and

$$\Delta P_2 = \frac{\Pi\left(P_1 - P_2\right)St \cdot 8.31 \cdot T}{22.4 \cdot 10^{-3} V} \tag{6.35}$$

where V – volume of the vacuum chamber, m^3; 8.31 $Pa \cdot m^3/(K \cdot mol)$ – the universal gas constant; T – temperature, K.

Hence

$$R \geq \frac{3.7 \cdot 10^2 \left(P_1 - P_2\right)STt}{V \cdot \Delta P_2^m} \tag{6.36}$$

If $P_1 >> P_2$, then

$$R \geq \frac{3.7 \cdot 10^2 P_1 STt}{V \cdot \Delta P_2^m} \tag{6.37}$$

These equations establish the relationship between foil vacuum tightness and main structural characteristics of the devices using foil outlet windows.

Thus, already at the device design stage, using Equations (6.34) and (6.37), one can formulate specific requirements to the foil vacuum tightness. Alternatively, knowing the attainable vacuum tightness of the foil made of the required material, one can calculate the main characteristics of the plant, reasonably select the pumping means and determine the design of the vacuum chamber.

6.5. Calculation of the gas permeability of porous foil screens at high temperatures[1]

In section 6.4 we discussed the use of thin foil in the cases where the main requirement was to ensure vacuum tightness and, therefore, the minimal level of through porosity. However, there are foil applications where the presence of foil through porosity is one of the main requirements. In particular, this holds for foils used in the high-temperature membrane technology that may need multi-layer screens made of porous foil.

To implement this possibility in practice it was necessary to establish interrelations between the characteristics of the controlled through porosity of foils and the gas permeability of multi-layer screens made of such foils.

The calculations assume that the rarefied gas is pumped out of the closed space one wall of which is formed by a system of porous screens. It is also accepted that a gas molecule colliding with the surface of any of the screens gets absorbed by this surface. This model is correct, in particular, for the case of the penetration of oxygen, hydrocarbons and the like through titanium alloy foil at high temperatures. The collision of their molecules with the heated titanium surface will lead to the formation of chemical compounds. Thus, only those molecules penetrate through the system of consecutive porous screens whose trajectory passes exactly through the pores in each of the screens.

From this point on we will adhere to the model of gas dynamics adopted in classical statistical physics [160−162].

[1] The work was performed in collaboration with M.R. Soloveitchik and V.R. Soloveitchik [159].

The Ideal Gas is defined as a random Poisson field in the physical phase space X coordinates (q) − velocities (v):

$$X = \{(q, v) : q, v \in \mathrm{R}^3\}.$$

Let us assume that the main configuration space of the gas is a half-space R:

$$\mathrm{R}^3 = \{(x, y, z) : x \le 0\}.$$

The average measure of the considered Poisson field

$$n(\mathrm{d}q, \mathrm{d}v) = \left(\frac{m\beta}{2\pi}\right)^{3/2} \rho \exp\left(-\beta \frac{m|v|^2}{2}\right) \mathrm{d}q\mathrm{d}v,$$

where $\beta = \frac{1}{TK}$; K − Boltzmann constant, T – absolute temperature,

m – mass of a particle (molecule), ρ – gas density (the average number of gas particles in a volume unit).

$q = \{x, y, z\}$, $v = \{v_x, v_y, v_z\}$ − a three-dimensional coordinate and the velocity of the particle, respectively.

A random gas configuration is a locally finite sequence of points ω in the phase space $\mathrm{R}^3 \times \mathrm{R}^3$, whereas the probability that the number of particles in a subset A of the phase space is equal to κ, corresponds to the Poisson distribution

$$\mathrm{Prob}\{\mathrm{card}(\omega \cap A) = \kappa\} = \exp(-n(A)) \frac{n(A)^{\kappa}}{\kappa!}$$

If two subsets A and B of the phase space do not intersect, then configurations of particles $\omega \cap A$ и $\omega \cap B$ are statistically independent.

The dynamics of gas configuration corresponds to a free motion of particles without any collisions:

$$S^t(\omega) = \{(q, v) : (q - tv, v) \in \omega\}.$$

Configuration $\tilde{\omega} = S^t(\omega)$ is the configuration ω after time t.

The geometry of screens

The term "screen" denotes the following region in the configured space:

$$D_i = \{(x, y, z) : 0 \le a_i \le x \le b_i,\ b_i < a_{i+1}\},\ i = 1, \ldots, N;\ a_1 = 0.$$

In this case, "screens" are a finite collection of vertical "walls". Then let us assume that every i-screen D_i has randomly distributed horizontal holes of radius r_i, and the random configuration of holes in each screen is statistically independent of the ideal gas and of the holes in the other screens.

In more formal terms, let us denote by $w^{(i)}$ – the random field of the centrums of the holes on the screen D_i projected onto the coordinate plane $\{Y, Z\}$.

Let us accept the following assumptions regarding the field $w^{(i)}$:

– every field $w^{(i)}$ is invariant with respect to the translations. That is

$$\mathrm{Prob}\{\mathrm{card}(w^{(i)} \cap A)\} = \mathrm{Prob}\{(\mathrm{card}(w^{(i)} \cap \tau_\xi(A)\},$$

where $\xi = (\xi_y, \xi_z) \in \{Y, Z\}$ and $\tau_\xi(A)$ is the translation: $\tau_\xi(A) = \{(y+\xi_y, z+\xi_z)\} : (y, z) \in A$;

– the field $w^{(i)}$ has density χ_i:

$$\lim_{l \to \infty} \frac{\mathrm{card}\{w^{(i)} \cap \{|y| < l, |z| < l\}\}}{4l^2} = \chi_i,$$

– the field $w^{(i)}$ has a finite radius of statistical dependence, i.e., there exists a constant $d_i > 0$, that if $A,B \subset (Y, Z)$ and $\mathrm{dist}(A,B) > d_i$ then $w^{(i)} \cap A$ and $w^{(i)} \cap B$ are statistically independent.

Let Φ denote the union of all holes of all the screens, and let $\tilde{D} = \cup D_i \backslash \Phi$ denote the solid body of all the screens; let $(q, v) \in \omega$, $q_x < 0$ be a gas particle in the left half-space. We say that the particle (q, v) percolates through the screens during the time $t > 0$ if $q_x + tv_x > b_N$ and $q + sv \cap \tilde{D} = \varnothing$ for any $s \le t$.

Formulation of the Problem

We are interested in the intensity of the gas percolation through the system of screens described above.

Let us consider the region $\Sigma \subset \{x = b_N\}$ in the right boundary of the last screen. Let S be the area of Σ. For instance,

$$\Sigma = \{x = b_N, |y| < l, |z| < l\},\ S = 4l^2.$$

Denote by $\mathbf{N}(T,\Sigma)$ the number of particles (gas molecules) penetrating through the screens within time T and cross the last screen through the region Σ. We are interested in investigating the limit

$$\lim_{T\to\infty,S\to\infty} E(\mathbf{N}(T,\Sigma))/TS$$

where $E(\mathbf{N}(T,\Sigma))$ denotes the mathematical expectation.

One screen case (N = 1, therefore, the screen numbering indices are not specified)

1. Let us consider all gas particles in the left half-space $q_x < 0$ which intersect the rear surface of the screen during the interval $[0,\infty]$.

To this end it is convenient to introduce new coordinates in the one-particle phase space. For the point (q, v) let

$$\tau(q,v) = \frac{b-q_x}{v_x}$$

be the time when the trajectory of the particle (q, v) intersects the subspace $x = b$.

Let (ξ_y, ξ_z) denote the (Y, Z) coordinates of the particle at the moment τ:

$$\xi_y = q_y + \tau(q, v)v_y,\ \xi_z = q_z + \tau(q, v)v_z.$$

Let us take (ξ, τ, v) as new coordinates. The condition $q_x < 0$ in the new coordinates will be represented as $\tau v_x > b$. Particle configuration ω in the new coordinates is a Poisson random field with the average measure:

$$n(\mathrm{d}\xi\mathrm{d}\tau\mathrm{d}v) = \rho\left(\frac{m\beta}{2\pi}\right)^{3/2}\exp\left(-\beta\frac{m|v|^2}{2}\right)|v_x|\mathrm{d}\xi\mathrm{d}v\mathrm{d}\tau.$$

We are interested in the restriction of this field to the region $\tau v_x > b$, that is a Poisson random field with the average measure

$$n(\mathrm{d}\xi,\ \mathrm{d}\tau,\ \mathrm{d}v)I_{\{\tau v_x > b\}}.$$

Given the condition $\tau = t > 0$, the *conditional* distribution of particles touching the screen at time t becomes a Poisson field on the space $(Y, Z) \times \mathrm{R}^3$ with the average measure

$$n(d\xi dv|t) = \rho\left(\frac{m\beta}{2\pi}\right)^{3/2} I_{\{v_x > b/t\}} \exp\left(-\beta\frac{m|v|^2}{2}\right)|v_x|\, d\xi dv. \qquad (6.38)$$

In what follows, we assume that the time t is a large parameter, for we are studying the gas percolation during a large time period. Therefore, in (6.38)

$$I_{\{v_x > b/t\}} \approx I_{\{v_x > 0\}}.$$

The assumption making this approximation feasible is that the average distance of a particle displacement during the considered time period projected on the axis X is much larger than the width of the region containing the screens:

$$|q_x(t) - q_x(0)| >> |b_i|, |a_i|.$$

2. In the set of all gas molecules (from the left half-space $q_x < 0$) intersecting the plane $x = b$ let us consider those crossing the screen through a given horizontal hole (Fig. 6.9).

The condition that the particle with a given velocity direction will cross the screen through a hole is equivalent to the condition that the particle will touch the rear surface of the screen inside a special region, defined by the screen geometry and the direction of the particle velocity. This region is the intersection of two circles of radius r, the distance between the centers of which is equal to

$$h \tan\varphi = (b - a) \tan\varphi,$$

where $\varphi = \varphi(v)$ is the angle between the particle velocity v and the axis X and h is the width of the screen;

$$\tan\varphi = \sqrt{\frac{\left(v_y^2 + v_z^2\right)}{|v_x|}}$$

The area of this region (the intersection of two partially overlapping circles) is equal to

$$r^2[2\Theta - \sin(2\Theta)],$$

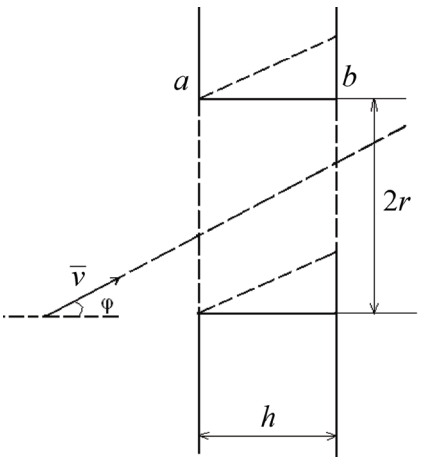

Fig. 6.9. The scheme of a particle passing through the screen

where $\Theta = \arccos(h \tan\varphi /(2r))$ and $\tan\varphi < 2r/h$.

The part of screen Σ with the area S contained the average number of $\chi \cdot S$ holes. The total area of all of the regions (considered above) corresponding to those holes is

$$\chi S r^2[2\Theta - \sin(2\Theta)].$$

Set $G(v) = 2\Theta - \sin(2\Theta)$ if $\cos\Theta = h \tan(\varphi(v)) /(2r) \in [0,1]$ and $G(v) = 0$ otherwise.

The arguments discussed above suggest that the average number of particles penetrating the screen through the region Σ during the large time intervals $T > 0$ is equal to

$$\mathbf{N}(S,T) = T\chi S r^2 \rho \left(\frac{m\beta}{2\pi}\right)^{3/2} \int I_{\{v_x > 0\}} \exp\left(-\beta \frac{m|v|^2}{2}\right) G(v) v_x \mathrm{d}v. \quad (6.39)$$

Equation (6.39) may be simplified by transition to the polar coordinates: $v_x = |v|\cos\varphi$, $v_y = |v|\sin\varphi\cos\psi$, $v_z = |v|\sin\varphi\sin\psi$; $d^3v = |v|^2 \sin\varphi \mathrm{d}\varphi \mathrm{d}\psi \mathrm{d}|v|$.

Taking into account that $G(v) = g(\varphi(v))$, we get

$$\int I_{\{v_x > 0\}} \exp\left(-\beta \frac{m|v|^2}{2}\right) G(v) v_x \mathrm{d}v = \frac{2\pi}{(m\beta)^2} \int_0^{+\frac{\pi}{2}} g(\varphi)\sin(2\varphi)\mathrm{d}\varphi.$$

Finally, substituting this into (6.39) we get

$$\mathbf{N}(S,T) = \frac{T\chi S r^2 \rho}{\sqrt{2\,\pi\, m\beta}} \int_0^{+\frac{\pi}{2}} g(\varphi)\sin(2\varphi) d\varphi. \quad (6.40)$$

Generalization. Case of N screens

Let (v,ξ,τ) be the same coordinates in the phase space as those introduced in the previous section, but with τ denoting the time when a particle crosses the rear surface of the last (rightmost) screen, $x = b_N$.

Following the same way of reasoning as above we get down to computing the value

$$T\rho\left(\frac{m\beta}{2\pi}\right)^{3/2} E\left(\int \exp\left(-\beta \frac{m|v|^2}{2}\right) v_x I_{\{v_x > 0\}} I_{\Sigma}(\xi) J(v,\xi,\bullet)\mathrm{d}v\mathrm{d}\xi\right), \quad (6.41)$$

where $I_\Sigma(\xi)$ – indicator of set $\Sigma \subset (X,Y)$, E – operator of mathematical expectation, $J(v,\xi,\bullet)$ – *random* indicator function which takes values in $\{0, 1\}$ and is equal to 1 if the trajectory of the particle intersecting the rear surface of the last screen at point ξ and having velocity v penetrates through all N screens. More specifically J depends on the random (holes) configurations w_k, $k = 1, .., N$:

$$J = J(v,\xi,w_1,...,w_N),$$

and the expectation operator E is nothing but the statistical averaging over the configurations $w_1, ...,w_N$:

$$E(...) = \int \ldots \Pr(dw_1,...,dw_N).$$

Since the probability distribution $\Pr(dw_1,...,dw_N)$ is translation invariant we can assume that the $J(v,\xi,w_1,...,w_N)$ is statistically independent of the position ξ. More precisely the induced distribution appears as follows

$$J(v,\xi,w_1,...,w_N)\Pr(dw_1,...,dw_N) = J(v,w_1,...,w_N)\Pr(dw_1,...,dw_N).$$

The condition that a specific particle trajectory penetrates through all N screens means that the indicator J can be decomposed into the following product:

$$J(v,w_1,...,w_N) = J_1(v,w_1) \ldots J_N(v,w_N),$$

where $J_k(v,w_k)$ is the indicator of the event, that a particle penetrates through the screen number k.

The final observation towards simplifying the expression (6.41) is that the configurations $w_1,...,w_N$ are statistically independent:

$$\Pr(dw_1,...,dw_N) = \Pr(dw_1) \ldots \Pr(dw_N)$$

and thus

$$J(v,w_1,...,w_N)\Pr(dw_1,...,dw_N) = J_1(v,w_1)\Pr(dw_1) \ldots J_N(v,w_N)\Pr(dw_N).$$

Therefore the averaging over the configurations $w_1,...,w_N$ may be reduced to the product of the single-screen operators already calculated above:

$$\int J(v,w_1,...,w_N)\Pr(dw_1,...,dw_N) = \prod_{k=1}^{N} \int J_k(v,w_k)\Pr(dw_k).$$

Substituting this expression into (6.41), we'll obtain the final expression for the average number of gas particles penetrating through a sequence of parallel screens

$$\mathbf{N}(S,T) = TS\rho \frac{\prod_{k=1}^{N} \chi_k r_k^{\,2}}{\sqrt{2\,\pi\, m\beta}} \int_0^{\frac{\pi}{2}} \sin(2\varphi) \prod_{k=1}^{N} g_k(\varphi)\, d\varphi, \qquad (6.42)$$

where functions g_k contain information on the screens geometry:

$$g_k(\varphi) = 2\theta - \sin(2\theta),\ \theta = \arccos\{h_k \tan(\varphi)/(2r_k)\}$$

if $\cos\theta = h_k \tan(\varphi)/(2r_k) \in [0, 1]$ and $g_k(\varphi) = 0$ otherwise.

For numerical calculations in this formula it is convenient to take as the upper limit of integration in (6.42) not $\pi/2$, but $\varphi_{max} = \max \arctan (2r_k /h_k)$. In this case, the average number of particles crossing the system of screens per unit area and per unit time will be

$$\mathbf{N} = \rho \frac{\prod_{k=1}^{N} \chi_k r_k^{\,2}}{\sqrt{2\,\pi\, m\beta}} \int_0^{\varphi_{max}} \sin(2\varphi) \prod_{k=1}^{N} g_k(\varphi)\, d\varphi. \qquad (6.43)$$

Calculation equations

Let us transform Equation (6.43) into the form suitable for the calculations. First of all, let us turn to the more conventional thermodynamic parameters of gases, i.e. pressure and temperature. To this end let us note that according to the equation of state of an ideal gas

$$PV = \frac{M}{\mu} RT, \qquad (6.44)$$

where V – gas volume, M − total mass of the gas, μ − molar mass of the gas, R − universal gas constant, P – pressure.

The particle number density ρ, that is present in (6.43), can be now written as follows:

$$\rho = \frac{M}{\mu V} N_A = \frac{P}{KT}, \tag{6.45}$$

where K − Boltzmann constant, N_A − Avogadro's number, $m = \mu/N_A$ − mass of a gas molecule.

Substituting (6.44), (6.45) into Equation (6.43) gives

$$\mathbf{N} = \frac{P\sqrt{N_A}}{\sqrt{2\pi KT\mu}} \prod_{k=1}^{N} \chi_k r_k^2 \int_0^{\varphi_{\max}} \sin(2\varphi) \prod_{k=1}^{N} g_k(\varphi) d\varphi . \tag{6.46}$$

If the gas penetration rate is calculated in kg/(m^2·sec) then.

$$\mathbf{N}_m = \frac{P\sqrt{\mu}}{\sqrt{2\pi RT}} \prod_{k=1}^{N} \chi_k r_k^2 \int_0^{\varphi_{\max}} \sin(2\varphi) \prod_{k=1}^{N} g_k(\varphi) d\varphi . \tag{6.47}$$

Eventually, we obtained an explicit analytical dependence for the permeability of multilayer porous screens both on the thermodynamic parameters of the penetrating gas and on the geometry of the foil screens. It was used for practical calculations of a multilayer shielding device made of ultra-thin foil with the regulated through porosity (see Chapter 8).

Chapter 7. SCIENTIFIC AND PRACTICAL RESEARCH TO DEVELOP THE PROCESS OF PRODUCING THIN FOIL BY VACUUM VAPOR DEPOSITION ONTO A MOVING SUBSTRATE STRIP

In accordance with the criteria formulated in 1.3, one of promising materials for making thin foil by the method of vacuum deposition is titanium and moderately doped titanium-base alloys (primarily, α- alloys and pseudo α- alloys).

Specific features that contribute to the fairness of this statement are:

– unique physical and mechanical properties of titanium and its alloys, combining high specific strength and high resistance to aggressive chemical effect of the environment, thus expanding the possibilities of their use as a structural material;

– technological complexity of making foil from titanium and its alloys by cold rolling, which becomes substantially more difficult as the preset thickness of the foil decreases and the width of the final product increases;

– the possibility of obtaining, in the case of vacuum deposition of titanium and its α-alloys and pseudo-α-alloys, an axial texture with the axis direction $<0001>_{\alpha}$, perpendicular to the foil plane, which ensures, in particular, an improved formability of the foil compared to a cold-rolled material, for a typical texture of which the direction $<0001>_{\alpha}$ forms with the plane of the foil an angle ~30° [163, 164];

– the ability of broadly changing the level of strength and ductility of alloys by alloying it with substitution elements, while maintaining the favorable axial texture of condensate $<0001>_{\alpha}$ to improve the foil formability, which is due to a rather wide concentration area of existence of the alloys where the α-phase having hexagonal close-packed crystal lattice is the basic one.

Many of the general statements discussed in Chapters 1 – 6, which are essential for launching industrial production of thin foil by vacuum deposition and ensuring the required properties of the end product, can be explicitly and adequately illustrated by titanium and its alloys. Apart from immediate practical importance of this group of alloys, their additional advantage as “illustrative” object is the existence of polymorphic transformation in these alloys. This allows to consider also the matters of influence

of process parameters on the structure and structure-sensitive properties of vacuum condensates, which are able to condense vapor into solid phases with different crystal lattices but the identical chemical composition.

7.1. The choice of alloys concentration range for practical applications

Pure (iodide) titanium has low strength and high ductility properties at ambient temperature $\sigma_в \approx 250…300$ MPa, $\delta \approx 50…60$ %). The presence of small amounts of interstitial impurities (especially oxygen and nitrogen) increases the strength and significantly reduces the ductility properties of titanium. Thus, for industrial titanium grade BT1-00 $\sigma_в \approx 300…450$ MPa and $\delta \approx 25$ %. Most titanium alloys are alloyed with aluminum, because it is widely available, has a low specific weight and increases the specific strength of the alloys, effectively strengthens α- and β-phases, while maintaining their satisfactory ductility, increases the elastic moduli and heat resistance of the alloys.

Titanium, α- and pseudo-α-alloys, containing a small amount of β-phase (according to the existing classification – below 5 %, the rate of stabilization of the β-phase $K_β \leq 0.25$), are prone to hydrogen embrittlement. Alloying of titanium with aluminum significantly reduces hydrogen embrittlement of α-alloys of titanium. For instance, the critical hydrogen content increases due to the introduction of ~5 % Al (α-alloy BT5) from from ~0.01 to ~0.035 % H.

Vanadium, unlike most of other alloying elements (e.g. Al, Mn, Cr, etc.), increases not only the strength but also the ductility of the α-phase in alloys Ti–Al. Furthermore, it impedes the formation of superstructure Ti_3Al (α_2), which in binary alloys Ti–Al can occur even at ~6 % Al and result in embrittlement. Being a β-stabilizer, vanadium, at the appropriate amount, leads to a two-phase (α+β) structure, thus increasing the processing ductility of the deformed alloys [37].

As the hardener and β-stabilizer in producing condensates, vanadium is more preferable than manganese, which is widely used in pseudo-α-titanium alloys, since its vapor pressure is less different from titanium than manganese [91], which simplifies the reproduction of the ingot chemical composition of the in the condensate.

No complication of the alloying system and volume is desirable, because it hinders the obtaining of the appropriate chemical composition and its homogeneity throughout the condensate volume.

In accordance with the foregoing, we focused our studies of applications of metal foil condensates on Ti–Al–V alloys containing up to ~6 % Al and up to ~5 % V. Maximum alloying corresponded to the alloys of BT6 (Ti ~6 % Al ~ 4 % V) type with the level of mechanical properties of massive specimens in annealed condition $\sigma_в \approx 850...1000$ MPa, $\delta \approx 8...12$ % and phase composition of α + (7...10) % β. For these alloys the coefficient $K_\beta \approx 0.27$, i.e. chemically they belong to the group of (α+β) alloys, being immediately adjacent to the concentration area of pseudo-α-titanium alloys.

The temperature of polymorphic β/α-transformation (T_{pt}) in titanium is ~882 °C, the alloying of titanium with aluminum allows to stabilize the α-phase, while alloying with vanadium ensures a stable β-phase) [37]. A slow (or gradual) cooling of the BT6 alloy from the β-area leads to the appearance of α-phase at temperatures below $A_3 \approx 980$ °C. The incubation period prior to the start of diffusion transformation β→α near the A_3 temperature apparently may substantially increase as the temperature of pre-heating of the alloy in the β-area becomes higher (with increasing size of β-grains and homogenization of the alloy), but at ~900 °C the role of this factor is insignificant and the appearance of the first α-crystals is observed after 3...5 seconds of isothermal time. The temperature of the beginning of diffusionless martensite transformation β→α′ at quenching the alloy BT6 (M_s), apparently, is in the range of ~780...840 °C, but in one of the earlier works $M_s \approx 920$ °C was reported [165−167].

7.2. Substrate strip and antiadhesive − materials, structures and structural interaction

According to the general points in Chapter 5 and taking into account the results of additional simulation experiments, we selected the 12H18N9 steel as the substrate material for the titanium alloys deposition onto a moving strip, and halide MgF_2 as the antiadhesive material.

Eventually, the implemented flowsheet included the substrate strip stabilizing annealing at the temperature ≤1000°C for 5 min and the subsequent antiadhesive layer vacuum deposition onto the strip as the major preliminary operations. Both operations were carried out in the operation plant chamber just prior to the vacuum deposition of thin foil.

In the annealed condition, the substrate strip had a fully recrystallized austenitic structure with numerous annealing twins, which are typical for the 12H18N9 steel type. The antiadhesive has a fine crystalline structure with a grain size of ~0.1 μm (Fig. 7.1, *a*).

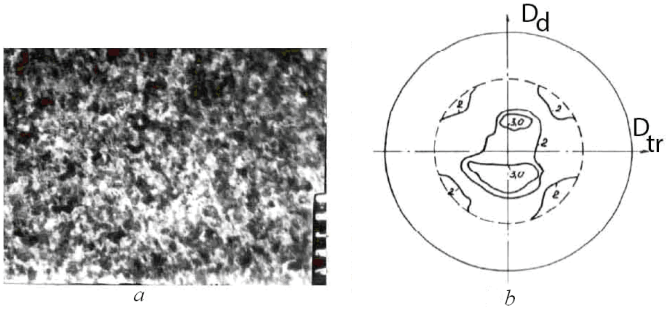

Fig. 7.1. Microstructure (*a*)(×6000) and pole figure {111} (*b*) of antiadhesive MgF_2
D_d – the draw direction; D_{tr} – transverse direction

For the certification of the substrate strip and antiadhesive, as well as for the assessment of their influence on the foil structure, we obtained some information on the substrate strip and antiadhesive textures.

The pole figures $\{111\}_\gamma$ and $\{110\}_\gamma$ typical for a substrate strip are shown in Fig. 7.2. The evaluation of such pole figures has revealed the presence of substrate textures $\{112\}<111>_\gamma$ and $\{100\}<001>_\gamma$. The pole figure $\{111\}_{MgF_2}$ is shown in Fig. 7.1, *b*. Apparently, the pole figure of magnesium fluoride is similar to $\{111\}_\gamma$, i.e. the pole figure of austenite substrate, but is characterized by a broader blurring of the texture maxima. This suggests the presence of partial epitaxy of the antiadhesive MgF_2, having a tetragonal lattice (a = 0.467 nm, c = 0.309 nm [168]), at its condensation onto 12H18N9 austenitic steel surface. Accordingly, one should bear in mind the possible influence (indirectly, through the antiadhesive texture) of the substrate strip texture on the foil texture formation.

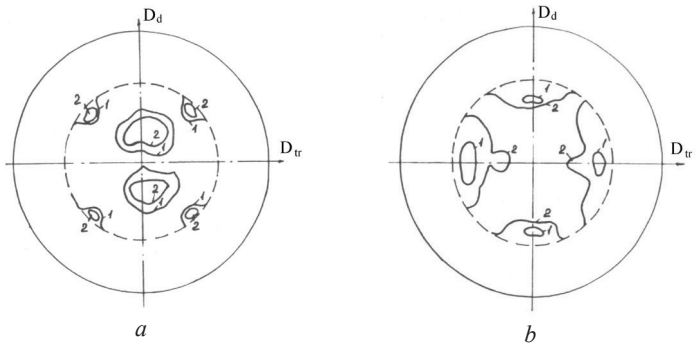

Fig. 7.2. Pole figures {111} (*a*) and {110} (*b*) of X18H9T steel substrate strip

7.3. The influence of vacuum deposition process parameters on the condensate structure

As noted in Chapter 1, the main parameters of the vacuum deposition process include the substrate strip temperature ($T_{substrate}$), the pressure of residual gases in the working volume (P_{res}) and the condensation rate ($W_к$). Find below the results of our studies that illustrate the influence of these factors on titanium alloy condensates in the considered range of their alloyng.

Preliminary experiments have shown that the use of low temperatures of the substrate for industrial production of foil by vacuum deposition onto a moving strip is impractical as far as titanium alloys are concerned, in particular, due to the lack of plasticity of the finished foil, which creates additional difficulties of its separation from the substrate and winding it into coils. Therefore systematic studies of the foil structure and properties were performed for $T_{substrate} \geq 600$ °C [169, 170].

Further mention of $T_{substrate}$ will mean maximum temperature achieved on the moving substrate strip at the end of the plant condensation zone (see Chapter 1). Obviously, the presence of an antiadhesive layer and the use of rather high condensation rates make the condensation surface temperature differ from $T_{substrate}$, thus affecting the temperature gradient across the condensate thickness. All this impedes (makes it to a certain extent conditional) the correlation of observed effects with a specific temperature. Hence, the development of real production processes requires a significant amount of experiments to determine the temperature dependences of foil properties in a rather wide range of temperature change of the substrate strip area where the temperature can be relatively reliably measured and controlled (used for production process control).

7.3.1. Substrate strip temperature

Grain structure. Optical and electron microscopy was used to obtain information about the influence of substrate strip temperature on grain size and shape in the foil, 25...30 μm thick, made of alloys BT1-00 (titanium with a small amount of impurities), 2B (Ti–2%Al–1.5% V) and BT6 (Ti–6%Al–5% V) in the interval of $T_{substrate}$ = 600...1000 °C at condensation rate $W_к \approx 0.2$ μm/s and residual gas pressure $P_{res} = (1.3...2.6) \cdot 10^{-3}$ Pa.

A common feature of the structure of alloys is the columnar form of grains of α-phase, which is clearly observed in the cross section of foils for a wide range of temperatures $T_{substrate}$. The presence of slanted columnar α-crystals, falciform and approximately perpendicular to the foil plane, in the 2B-alloy foil, 25...30 μm thick, is illustrated in Fig. 7.3.

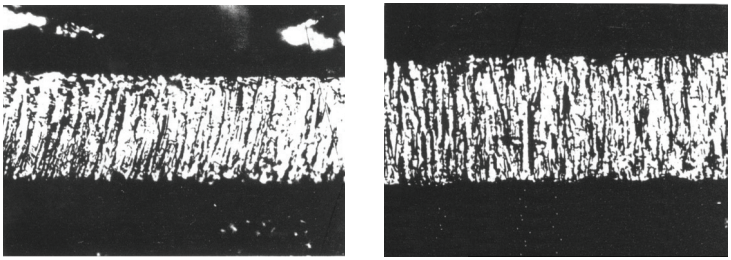

a *b*

Fig. 7.3 The microstructure of the cross section of 2B alloy foil (×800):
a – $T_{substrate}$ = 600 °C; *b* – $T_{substrate}$ = 840 °C

In the section parallel to the foil plane, the columnar crystals have a virtually equiaxed polyhedral form. The temperature dependence of their "diameter" *D* in the plane of the foil for alloys BT1-00 and BT6 is presented in Fig. 7.4. These dependences are qualitatively similar: for each alloy with increasing $T_{substrate}$ the rise of *D* is observed; the rise begins at a slow rate, but having reached a certain temperature it becomes much more steep. However, alloyng causes significant quantitative differences in the dependence of *D* on $T_{substrate}$. The grain size of BT1-00 is about an order of magnitude greater than that in BT6, and the transition temperature from a slow to an accelerated pace of *D* growth in BT1-00 is by ~150 °C lower than that in BT6.

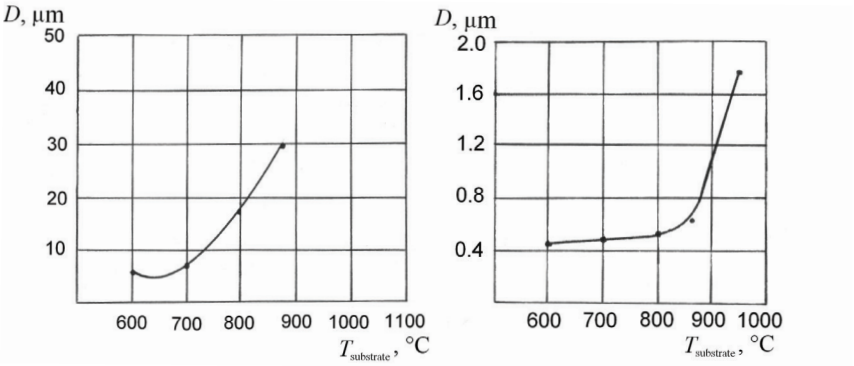

a *b*

Fig. 7.4. The influence of the substrate temperature
on the grain size in the plane of the foils BT1-00 (*a*) and BT6 (*b*)

It is clear that the fast growth of D with increasing $T_{substrate}$ in BT1-00, beginning at $T_{substrate}$. ≈ 700 °C << T_{pt} (≈ 882 °C) and resulting in the grains diameter comparable with the foil thickness (~30 μm) at $T_{substrate}$ ≈ 850 °C, is not connected with the polymorphic transformation and cannot be explained by the temperature dependence of the surface density of condensate nucleation. Therefore, the main cause of this effect is the temperature (temperature−time) dependence of the start and intensity of the collective recrystallization process in titanium condensate.

A similar conclusion is probably true for the alloy BT6, although the high temperature of the start of accelerated growth of D ($T_{substrate}$ ≥ 850 °C, see Fig. 7.4, *b*) does not allow to exclude a possible influence of diffusion acceleration near the phase transition temperature on the intensity of the recrystallisation processes. Moreover, a small grain diameter of this alloy can be due not only to the alloying of α- and β-solid solutions (as the recrystallization processes are influenced by the surface diffusion deceleration, grain boundary segregation and/or formation by alloying elements of dispersed grain boundary phases – oxides, etc.), but also due to the appearence of β-phase in the condensate structure at $T_{substrate}$ > 600 °C (see further Fig. 7.9). However, the role of this last factor, apparently, is relatively small, as evidenced, for example, by effective (comparable to that observed in the alloy BT6) reduction of α-grains size in single-phase alloys Ti–Al by the aluminum content increasing (Fig. 7.5).

Separate influence of alloying titanium with aluminum and vanadium (up to 5 %) on condensate grain diameter for $T_{substrate}$ ≈ 850 °C is presented in Fig. 7.5. The dependences $D(T_{substrate})$ for alloys Ti–Al and Ti–V qualitatively and partly, quantitatively, are similar: the most dramatic decrease in grain size is observed in the area of small concentrations of Al and V, and at 4...5 % content of the alloying element, the average grain size is virtually fixed at the same level of ~1.5 μm. However, vanadium is by far a more effective grain size reducer than aluminum, which becomes especially apparent when mass concentrations are replaced with atomic concentrations.

This result corroborates the ideas concerning the influence of alloying elements on the recrystallization of condensate systems Ti–Al and Ti–V based on researching alloys of other systems. According to these findings, alloying elements typically increase the recrystallization start temperature, and the more effectively the larger the difference of atomic radii of the matrix and alloying elements is and the lower its solubility in the solid solution is [171]. According to [172], the same size factor affects the uni-

formity of the element distribution through the grain and the mobility of grain boundaries in condensates. The atomic radii of titanium, aluminum and vanadium are ~0.147, 0.143 and 0.136 nm, respectively [173], and the vanadium solubility in α-titanium, unlike the aluminium solubility, is low and decreases with increasing temperature (from ~3.5 % at 600 °C to zero at 882 °C [174]). Therefore, vanadium alloying must be more effective than aluminum alloying in raising the recrystallization start temperature and impeding the migration of grain boundaries, i.e. to produce smaller grains at a given substrate temperature higher than the recrystallization start temperature of the alloys, as observed experimentally (see Fig. 7.5).

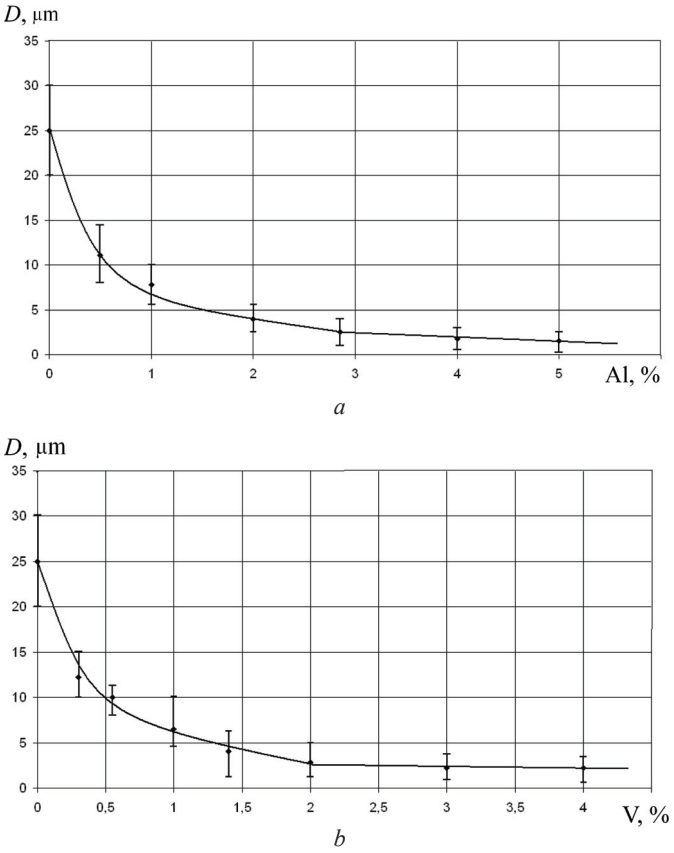

Fig. 7.5. The effect of aluminum and vanadium on grain size in the plane of the Ti–Al (*a*) and Ti–V (*b*) foil ($T_{substrate}$ = 850 °C)

Fig. 7.5 shows that for the considered condensation modes and the foil thickness of 25...30 μm (corresponding to the process duration) the alloying of titanium with aluminum or vanadium in the amount of ~5 % hinders efficiently the collective recrystallization, at least up to $T_{substrate} \approx 850$ °C. By comparing Fig. 7.5 and Fig. 7.4, *b* we see that additional alloyng of binary alloys Ti–5%(Al or V) with a third element in the Ti–Al–V system in the amounts corresponding to the BT6 alloy, may result in a slight decrease of the average grain size at $T_{substrate} \leq 850$ °C, but does not increase the start temperature of collective recrystallization, which is around 850 °C for alloy BT6. In principle, we may assume that additional alloying can even reduce this temperature compared to the temperature typical for one of the two or each binary system (in the former case − due to controlling the collective recrystallization process by alloyng with only one element, i.e. aluminum or vanadium, in the latter case − due to a less stable primary grain structure of the condensate in the additionally doped alloy), but we have not verified these assumptions.

The influence of the substrate temperature on the grain structure of the alloy BT6 is shown in Fig. 7.6, which presents electron microscopic information on the foil layer located approximately half-way through its thickness.

It is noteworthy that at $T_{substrate} = 930$ °C there is a significant increase of the α-grain diameter compared to the one obtained at $T_{substrate} = 600$ and 800 °C (see Fig. 7.4, *b*), but the structure with packets of plane-parallel α-plates, which can result only from the transformation β→α when cooling from the β area, do not exists in a foil 25...30 μm thick at $T_{substrate} = 930$ °C (Fig. 7.6, *c*). At $T_{substrate} = 1000$ °C, the lamellar α-structure exists along with large α-grains (Fig. 7.6, *d*); β-phase is present in the foil in the form of interlayers of various thickness between the α grains (Fig. 7.6, *e*).

Fig. 7.7 shows the structure in the cross-section of the BT6 foil obtained at $T_{substrate} = 930$ °C in the foil not 25...30 μm but ~70 μm thick. In this case, under the thin fine-grain layer on the facing vaporizer foil surface (the "vaporizer face") a subsurface layer ≤ 30 μm thick with a much coarser crystallite structure, containing among other things the packets of plane-parallel α-phase plates, is formed. Further on, up to the foil surface adjacent to the substrate strip, the layer ≥ 30 μm thick has a relatively dispersed grain structure, having a sporadic morphological resemblance with columnar α-structure and generally similar to the structure of the foil 25…30 μm thick at the same temperature $T_{substrate} = 930$ °C.

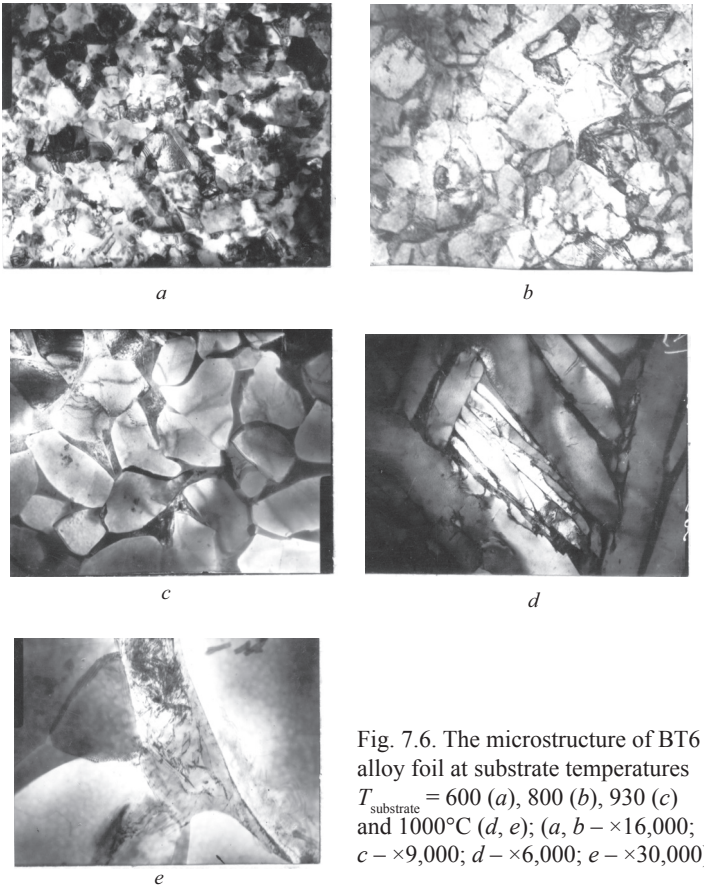

Fig. 7.6. The microstructure of BT6 alloy foil at substrate temperatures $T_{substrate}$ = 600 (*a*), 800 (*b*), 930 (*c*) and 1000°C (*d*, *e*); (*a*, *b* – ×16,000; *c* – ×9,000; *d* – ×6,000; *e* – ×30,000)

Fig. 7.7 clearly illustrates the fact that due to the polymorphic transformation in the alloy the overheating of the condensate surface facing the vaporizer, which occurs in the real foil making process, can not only cause quantitative changes in the average size of α-grains, but, at relevant $T_{substrate}$, can also cause qualitative morphological changes in the final structure for a greater or

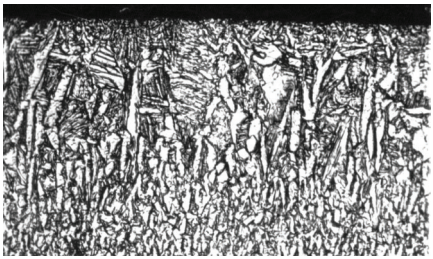

Fig. 7.7. The heterogeneity of the microstructure in the cross-section of the BT6 foil ~70 thick at $T_{substrate}$ = 930 °C (×850)

smaller part of the foil thickness. The probability of occurrence of this effect increases with foil thickness, which requires a denser beam or a longer condensation time with the consecutive rise of the condensation surface temperature relative to the substrate strip temperature, which is the case of the transition from 25…30 μm to ~70 μm foil thickness.

Substructure and phase composition. During condensation, apart from the influence on the grain size and the morphological features of the condensate grain structure, the substrate strip temperature and temperature variance throughout the foil cross-section cause a regular change in the crystal substructure and phase composition of the multiphase alloy condensate [175−177].

Fig. 7.8 presents the temperature dependence of the integral characteristic of crystal structure faults, i.e. physical broadening B of the X-ray α-phase line of the researched alloy condensates. The absolute value of B (and, accordingly, the density of crystal structure faults within the α-phase) for each specific temperature $T_{substrate}$, as well as the start temperature of the sharp *B*-decline and its value at rising $T_{substrate}$ increase with alloying. When comparing the data in Fig. 7.8 and Fig. 7.4, *b* for alloy BT6 we may see that the start temperatures of the sharp B-decline and the sharp increase in grain size coincide, which in this particular case indicated interconnection between the processes of α-grains growth and fault reduction. Other alloys behave in a similar way, but in pure titanium and alloy Ti–1% Al the recrys-

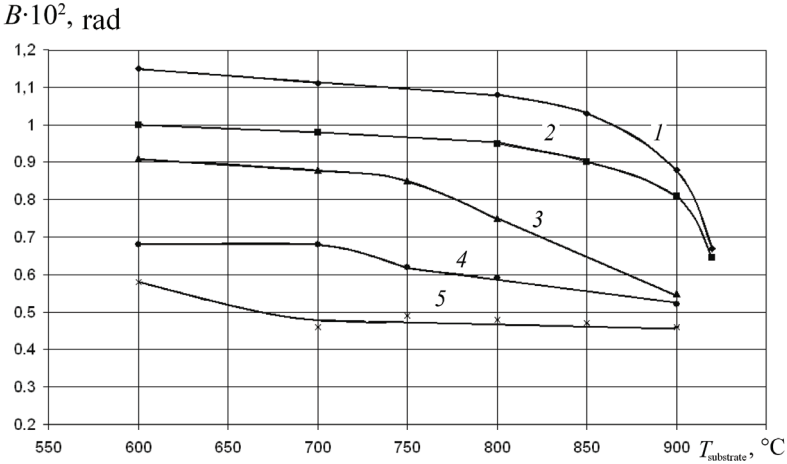

Fig. 7.8. The influence of substrate temperature on physical broadening of line {2131} for BT6 alloy foils (*1*, *2* – substrate and vaporizer face, respectively), 2B (*3*), Ti-1%Al (*4*) and BT1-00 (*5*)

tallization processes ensure a great reduction of B (the density of defects) already at $T_{substrate} \approx 600$ °C. Therefore, subsequent grain growth occurring at $T_{substrate} > 600$ °C (even significant growth, as in pure titanium, see Fig. 7.4, *a*) does not cause considerable changes in the substructure and B value.

For the considered $T_{substrate}$ range, there is no difference of *B* on the opposite surfaces of the pure titanium foil, which is the evidence of the effective reduction of crystal structure fault density across the titanium foil thickness already at $T_{substrate} \approx 600$ °C, and the difference is the most obvious in alloy BT6 with the maximum content of alloyng elements. Quantitative data on this alloy is shown in Fig. 7.8.

Lower B values on the vaporizer side in the range of $T_{substrate} = 600...800$ °C may be mainly due to a higher condensation temperature on this surface, which reduces crystalline flaws both by changing condensation conditions (see Chapter 1) and by more effective annealing of primary defects in the "hot" sub-surface condensate layer. The role of a possible grain boundary migration (differences in the process development) is apparently insignificant in this case, as evidenced by the consistency of the differences in B values on the opposite foil surfaces at $T_{substrate} = 600...800$ °C. Recrystallization leads to equal B-values on these surfaces, i.e. to the same crystal defect densities of α-grains through all foil thickness (see $T = 930$ °C in Fig. 7.8 and 7.4, *b*).

Fig. 7.9 illustrates the characteristic influence of temperature and its gradient through the foil thickness on the β-phase amount in two-phase titanium alloys by the example of (α+β)-alloy BT6 for which the presence of ~10 % β-phase is common in the equilibrium state (due to the textured nature of the object, we have used a semi-quantitative radiographic evaluation technique to determine the phase composition [163]).

According to our results, at $T_{substrate} \leq 600$ °C no β-phase is found in the condensate of alloy BT6, and $T_{substrate}$ increasing from ~600 to 900 °C results in a gradual increment of its quantity, and, moreover, the share of β-phase in the condensate structure is higher on the side facing the substrate strip (the "substrate face") than that on the "vaporizer face".

The absence of β-phase at $T_{substrate} \leq 600$ °C (proved by electron-microscopic examination of thin foils) points out to the formation of α-phase being substantially supersaturated with vanadium, which does not have enough time to decompose into a more equilibrium mixture of α and β phases during the foil condensation and its cooling at a sufficiently low temperature $T_{substrate}$. The emergence and growth of the total β-phase quantity in the foil observed at a higher $T_{substrate}$, is naturally explained by a faster decomposition of supersaturated α-phase due to a faster diffusion.

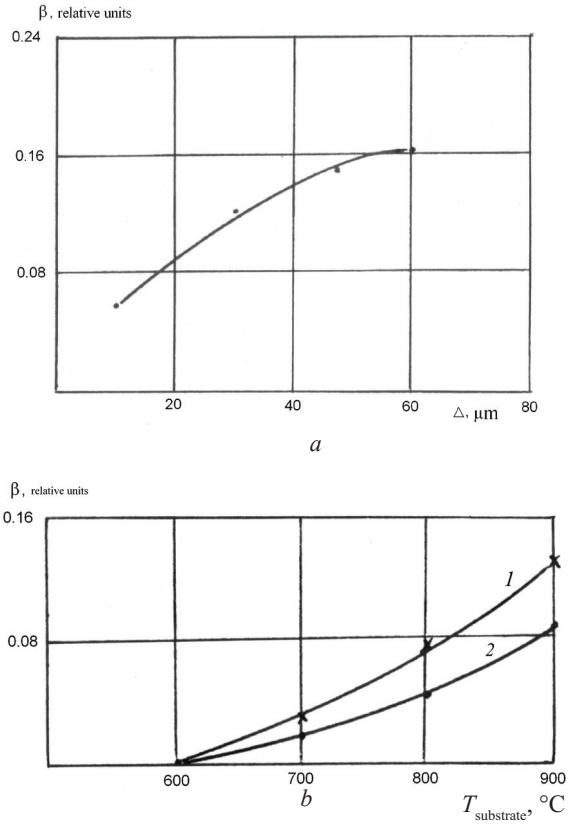

Fig. 7.9. The amount of β-phase in the alloy BT6: dependence on foil thickness at $T_{substrate}$ = 900 °C (*a*) and on substrate temperature (*b*): *1* – the "substrate face"; *2* – the "vaporizer face"

It is less obvious, though, why the β-phase prevails in the "substrate face" as opposed to the "vaporizer face". Indeed, a certain increase in vanadium super-saturation of α-phase and its faster decomposition (diffusion) due to the high temperature of the "vaporizer face" could result in the opposite effect. However, our experimental findings demonstrated that the factors, inherent in the "substrate face", prevail in solid solution decomposition and phase composition formation during alloy condensation. Such factors may include a faster diffusion of vanadium from the volume to the α-grain boundaries where the formation of β-phase takes place (due to a higher density of defects in α-phase, see Fig. 7.8), a higher density of grain boundaries and, consequently, shorter diffusion paths thereto (this being likely the consequence of a somewhat smaller average size of α-grain on this side compared to that on the vaporizer side) and a longer dwell of condensate layers adjacent to the substrate strip at high temperature.

Textural effects. Specifics of the texture formation are defined both by the production process parameters and the condensation mechanism [178]. Fig. 7.10 presents the ratio and the intensity alteration of the first X-ray lines of the α-phase in titanium BT1-00 and BT6 alloy foils depending on the substrate

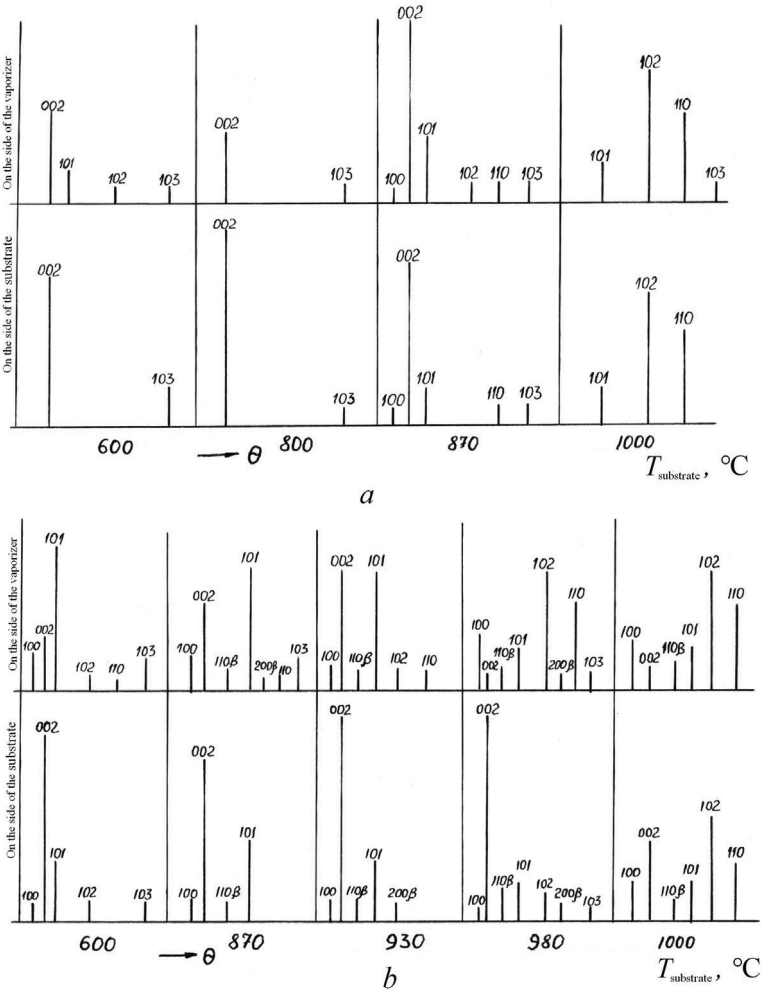

Fig. 7.10. The influence of the substrate temperature on the intensity of X-ray diffraction lines (bar-chart) in the foils of alloys BT1-00 (*a*) and BT6 (*b*)

strip temperature and the foil surface to which the experimental data refer (foil thickness 25...30 μm, radiation CrKα, informative layer thickness ~2...3 μm).

For non-textured α-titanium the ratio of the line intensities $I_{100} : I_{002} : I_{101} : I_{102} : I_{110} : I_{103}$ shall be ~0.27 : 0.20 : 1.00 : 0.13 : 0.13 : 0.13 [162]. Deviations from these ratios are due to the crystallographic texture inherent to the experimental objects.

The bar-charts in Fig. 7.10, *a*, indicate that the condensate texture in titanium BT1-00 is generally quite uniform across the foil thickness throughout the studied range of $T_{substrate}$ = 600...1000 °C − the line intensity ratios on the opposite surfaces of the foil are not fundamentally different.

The experiment also demonstrated that the texture type of titanium foil remains constant at increasing $T_{substrate}$ in the temperature range of 600…870 °C, but it changes drastically at the transition from 870 °C to 1000 °C: at $T_{substrate} \leq$ 870 °C to the foil plane is mainly parallel to the crystallographic plane $\{002\}_{\alpha}$, and at $T_{substrate}$ = 1000 °C – to the planes of types $\{102\}_{\alpha}$ and $\{110\}_{\alpha}$. Obviously, such a texture change may be caused, first of all, by titanium polymorphism. Indeed, at $T_{substrate} < T_{pt}$ (≈ 882 °C) it is natural to expect vapor condensation into the low-temperature α-modification of titanium and formation of the texture typical of this particular phase, while at $T_{substrate}$ = 1000 °C >> T_{pt} the vapor is condensed into the high-temperature β-phase, and, therefore, the α-texture observed at the ambient temperature is the result of the transformation of β-condensate into α-phase during foil cooling.

The transition from pure titanium to the alloy BT6 significantly changes the ratio of the intensities of X-ray lines (bar-charts) for the opposite surfaces of the foil (Fig. 7.10, *b*).

On the substrate face, as in pure titanium, the "low-temperature" texture with plane $\{002\}_{\alpha}$, parallel to the surface of the foil, prevails and exists up to $T_{substrate}$ = 980 °C . At $T_{substrate}$ = 1000 °C it is replaced by the texture having a significantly weakened "low-temperature" component $\{002\}_{\alpha}$ along with sufficiently distinct "high-temperature" components $\{102\}_{\alpha}$ and $\{110\}_{\alpha}$ that are identical to the main texture components of titanium BT1-00 foil at the same $T_{substrate}$ = 1000 °C.

Thus, on the "substrate face" of BT6-foil mainly the expansion of the primary low-temperature texture area $\{002\}_{\alpha}$ towards higher $T_{substrate}$ is observed, as compared to the area of this texture throughout the thickness of the pure titanium foil. The similarity of the BT6 alloy textures with the titanium textures allows to conclude that the low-temperature and high-temperature textures of this alloy are connected with the vapor condensation into α-phase and β-phase, respectively.

At $T_{substrate} \leq$ 980 °C, the bar-charts of the BT6 "vaporizer face" differ radically from the bar-charts of the "substrate face" for the same $T_{substrate}$, and, respectively, from the bar-charts of pure titanium: here the most intensive are lines $\{101\}_{\alpha}$ (for $T_{substrate} \leq$ 930 °C) or $\{102\}_{\alpha}$ and $\{110\}_{\alpha}$ (for

$T_{substrate}$ = 980 °C), but not the $\{002\}_{\alpha}$ line. For $T_{substrate}$ = 600 °C, the intensity ratios of α-phase lines is close to the calculated value for a non-textured material. As $T_{substrate}$ increases from 600 to 930 °C, one observes a tendency of decreasing the intensity of line $\{101\}_{\alpha}$ and, simultaneously, of increasing the intensity of line $\{002\}_{\alpha}$, i.e. the tendency of approaching to the texture of the "substrate face". However, this trend is completely destroyed as the temperature rises further up to $T_{substrate}$ = 980 °C: line $\{002\}_{\alpha}$, which prevails on the substrate side at $T_{substrate}$ = 980 °C, almost disappears while intensive lines of "high- temperature" texture components $\{102\}_{\alpha}$ and $\{110\}_{\alpha}$ emerge. Lines $\{100\}_{\alpha}$ and $\{101\}_{\alpha}$ are also quite intensive. The bar-charts for the "vaporizer face" at $T_{substrate}$ = 980 and 1000 °C are almost identical, and differ from the chart for the "substrate face" at $T_{substrate}$ = 1000 °C mainly by the presence on the "substrate face" a tangible, though not dominant component $\{002\}_{\alpha}$.

The bar-charts for alloy BT6 at $T_{substrate}$ > 600 °C also have bleak lines $\{110\}_{\beta}$ and $\{200\}_{\beta}$ of β-phase, the intensity of which on the "substrate face" is slightly higher than that on the "vaporizer face".

Additional information on the types and temperature dependence of the BT6-foil texture is shown in Fig. 7.11 and 7.12.

The pole figures in Fig. 7.11, *a*, *b*, indicate that at $T_{substrate}$ = 600 °C the intensive axial base texture with axis <0001>α deviating from the foil plane normal by the angle of ~15° along line D_d (the drawing direction of the substrate strip during foil production) is formed on the foil side facing the substrate. The magnitude and the direction of this deviation correspond to the vapor flow direction at the entry to condensation window of the foil production plant, and, accordingly, to the growth direction of the crystals in the first condensate layer which are the source of our experimental data.

In the case of alloy BT6, at $T_{substrate}$ rising above ~ 800 °C, the deviation angle of the base texture axis from the foil plane normal is significantly reduced (from ~ 15° to ~ 4° at $T_{substrate}$ = 900 °C), which corresponds to the general regularities of $T_{substrate}$ influence on the orientation of the growth direction of columnar crystals (see Chapter 1) and is due to increasing diffusion mobility of the atoms on the condensation surface and intensification of the condensate recrystallisation processes.

The pole figure in Fig. 7.11, *c* shows that in the BT6 alloy at $T_{substrate}$ = 1000 °C, just as at $T_{substrate}$ = 600 °C, appearse an axial texture, or at least, a rather intensive axial texture component, but, unlike the

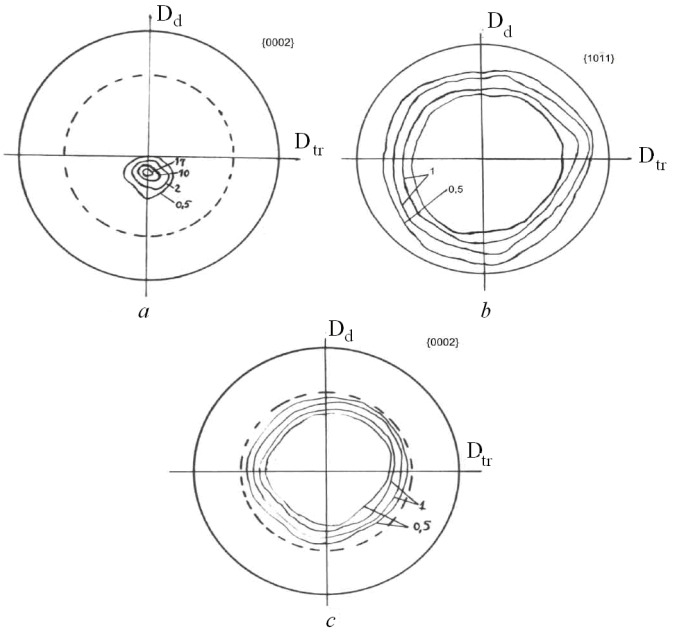

Fig. 7.11. The pole figures of BT6 alloy foil at $T_{substrate}$ = 600 (*a*, *b*) and 1000°C

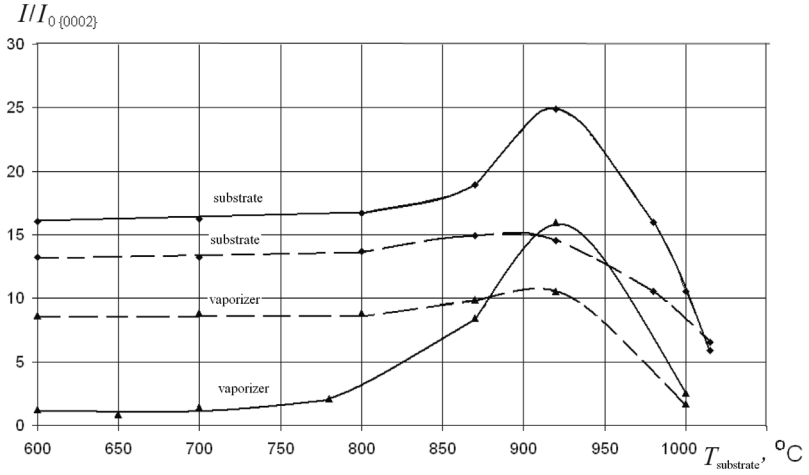

Fig. 7.12. The influence of substrate temperature
on the texture maximum intensity for BT6 alloy foils
(——— thickness 30 μm; — — — — thickness 10 μm)

$T_{substrate}$ = 600 °C, the axis of this texture does not match the direction close to $<0001>_{\alpha}$ but forms with this direction the angle of ~55°.

This textural data illustrates the following facts:

– alloying of titanium leads to diffusion slowing down, rising critical temperatures and impeding recrystallization processes, and, thus, causes inhomogeneity of crystallographic characteristics of the structure throughout the thickness of the condensed foil (it must be noted that the magnitude of respective effects depends on the substrate strip temperature: at low and high $T_{substrate}$ this heterogeneity can be negligibly low);

– titanium polymorphism causes (may cause) radical alteration of the texture type of the final α-phase throughout the foil thickness in the cases when rising temperature of the condensation surface leads to the transition from the "vapor → low-temperature α-phase" condensation to the "vapor → high-temperature β-phase" condensation;

– the existence of axial texture $<0001>_{\alpha}$ in a wide temperature and concentration range, which, according to our and literature data, is typical for titanium condensates when using different substrates, indicates that the antiadhesive texture has no influence on the foil texture.

Substrate strip temperature, foil structure and phase transformations. Basing on the above results of microstructural and textural studies, let us consider in detail the possibilities of the substrate temperature influence on the condensate structure features caused by titanium alloy polymorphism.

Undoubtedly, at sufficiently high temperatures of the substrate strip, vapor condensation into the high-temperature β-phase takes place. In this case, the low-temperature α-phase emerges only by β→α transformation during the finished foil cooling. Onwards we will assume that the foil cooling rate after the condensation ensures the absence of any significant (regarding the alteration of relative stability of β- and α-phases) redistribution of alloying elements in the β-phase in two-phase alloys like BT6 before the transformation β→α. The temperature of such polymorphic transformation T_{pt} corresponds to the metastable thermodynamic equilibrium of β- and α-phases having the same chemical composition, and, therefore, may correspond to the boundary temperature for condensation variants "vapor →β" ($T_{substrate} > T_{pt}$) and "vapor→α" ($T_{substrate} < T_{pt}$).

It is known that for pure titanium $T_{pt} \approx 882$ °C. Apparently, there is no experimental or calculated data for alloy BT6. It is evident that this temperature is within the range of $M_s < T_{pt} < A_3$. Using the average temperature of the temperature range as a first approximation, we'll have $T_{pt} \sim 900$ °C, but this estimation is too imprecise to evaluate the available structural information.

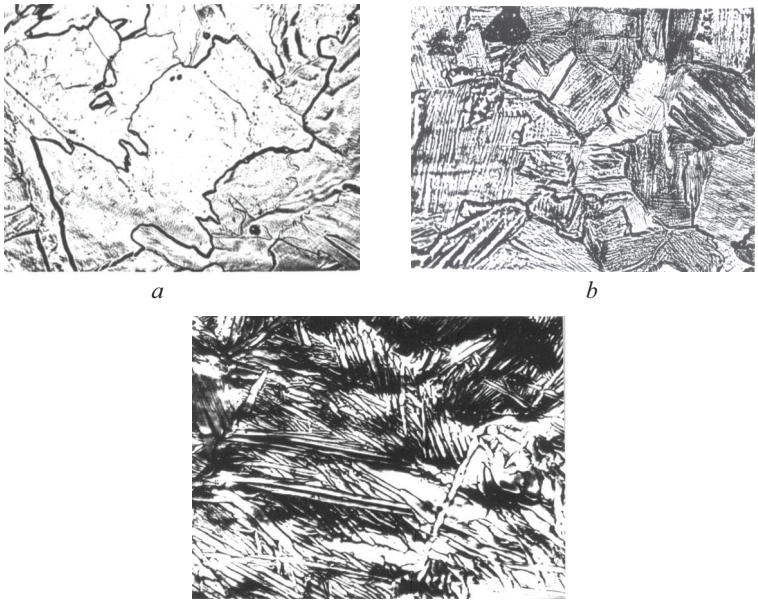

a *b* *c*

Fig. 7.13. Microstructure of the foil of alloys BT1-00 (*a*), 2B (*b*) and BT6 (*c*) at $T_{substrate} > T_{pt}$ (*a, b* – ×400, *c* – ×800)

Fig. 7.13 shows the general view of the condensate structures of titanium BT1-00 and alloys 2B and BT6 obtained at $T_{substrate} > T_{pt}$. In each of the three materials large grains of β-phase were formed at the condensation temperature, but cooling the alloys caused the formation of a martensite-like lamellar α-structure, whereas the β→α titanium transformation lead to α-phase grains having an irregular shape and sharply curved boundaries, which indicates the formation of multiple independent α-grains within a single initial β-grain (phase transformations involving such morphological features are sometimes called "massive").

It is known that for lamellar structures of titanium alloys between the cristal lattices of phases β and α (BCC and HCP, respectively) the Burgers' orientational relationship is fulfilled, according to which $\{110\}_{\beta}$ // $\{001\}_{\alpha}$ and $<111>_{\beta}$ // $<100>_{\alpha}$. For such orientation relationship (OR) in one (each) β-phase grain there may emerge up to twelve different HCP-lattice orientations of the α-phase lamellars. Respectively, the primary condensate texture, which is determined by the intensity and the number of β-phase

texture components, can be significantly weakened and modified due to the β → α transformation during the condensate cooling. However, if there are factors causing the formation of only some of the 12 possible α-orientations in each cooled β-phase grain, then an intense texture of the α-phase may occur not only in a textured β-condensate, but, in principle, in a β-condensate without any texture. Indeed, in our case there are such factors that select the normal to the foil surface as the special direction within the entire condensate volume. These include temperature gradient during foil cooling, shape anisotropy (e.g. columnarity) of primary β-crystals (grains) and anisotropy of various stresses and conditions of their relaxation associated with the thin plate form of the condensate.

For the "massive" phase transformations, the problems of the crystallographic relationships of the original high-temperature and the phase formed at cooling, as well as the influence of external factors on the occurrence of specific orientations of crystals of low-temperature phase, usually are not considered. It is believed that the role of the crystallographic factors in the structure formation at such transformations is relatively small.

The bar-charts (see Fig. 7.10, *a*) for $T_{substrate}$ = 1000 °C prove quite definitely the presence of the intense α-phase texture in titanium BT1-00 resulted from the β→α transformation when cooling the condensate from the β-area. The origin of the two major components of this texture, for which the planes of $\{102\}_\alpha$ and $\{110\}_\alpha$ types are parallel to the surface of the condensate (and the substrate), can be explained by assuming that, firstly, condensing at $T_{substrate}$ = 1000 °C causes formation of a sufficiently intense axial β-phase texture, for which the surface of the condensate is parallel (close to) the plane of the $\{100\}_\beta$ type, and, secondly, that at the β→α transformation in the cooled condensate the crystal lattices of β- and α-phases follow the Burgers' OR. The minimum estimated angle of the $\{100\}_\beta$ plane with the $\{102\}_\alpha$ and $\{110\}_\alpha$ planes is equal to ~4.4° and ~5.2°, respectively; therefore, the $\{102\}_\alpha$ and $\{110\}_\alpha$ lines may appear on the bar-charts quite likely because of a non-strict parallelism of the plane $\{100\}_\beta$ and the condensate surface and/or the existence of some scattering of the original β-phase texture. Thus, the two assumptions made above have a convincing experimental confirmation.

It should be noted that since at the Burgers' OR planes $\{100\}_\beta$ are almost parallel to planes $\{102\}_\alpha$ or $\{110\}_\alpha$, and only to the planes of these two types for all twelve α-orientations that are theoretically possible in each β-phase grain, then the interpretation of these bar-charts does not re-

quire any assumptions (and is not an evidence) concerning the preferred emergence (selection) of certain α-orientations during the β→α transformation in the cooled condensate, but such possibility is not excluded.

The presence and a relatively high (abnormal for untextured material) intensity of the same lines $\{102\}_\alpha$ and $\{110\}_\alpha$ on the bar-charts (see Fig. 7.10, b) at $T_{substrate}$ = 1000 °C indicates that alloy BT6 has the same regularities of high-temperature condensation vapor→β and subsequent transformation β→α in the cooled condensate that were determined above for titanium BT1-00.

At the same time, the presence of a relatively intense line $\{100\}_\alpha$ on the bar-charts of BT6 alloy can be explained by the assumption of the occurrence, at the condensation of this alloy, one more component of β-texture, for which the planes $\{110\}_\beta$ are approximately parallel to the condensate surface: for Burgers' OR the minimum angle of the planes $\{110\}_\beta$ and $\{100\}_\alpha$ is equal to ~5.3°. The lines $\{002\}_\alpha$, $\{101\}_\alpha$ and $\{110\}_\beta$, present in the bar-charts of BT6 alloy at $T_{substrate}$ = 1000 °C, can be also associated with this texture component, but they may have alternative interpretations. Thus, the $\{002\}_\alpha$ line may be the result of the partial "vapor → α-phase" condensation, if for BT6 alloy the temperature T_{pt} is close to 1000 °C, and the lines $\{101\}_\alpha$ and $\{110\}_\beta$, that are the most intense X-ray lines for the phases α and β, can match untextured foil parts.

The idea, that in the BT6 alloy condensate at $T_{substrate}$ = 1000 °C the two-component texture $\{100\}_\beta$+$\{110\}_\beta$ arises, is qualitatively consistent with the pole figure shown in Fig. 7.11. The apex angle of the circular (in the first approximation) cone of maximum intensity on this pole figure is ~55°. For one-component $\{100\}_\beta$ texture at Burgers' OR it must be ~43°, and for one-component texture $\{110\}_\beta$ – ~61°. It is obvious that the imposition of texture maxima of two texture components can improve the affinity of the estimated results obtained for a one-component texture $\{100\}_\beta$ and the experimental results.

In general, the emergence of the texture component $\{110\}_\beta$ seems quite likely, especially at lower condensation temperatures when the textures with densely packed planes in parallel to the condensation surface dominate (see Chapter 1), but the experimental data available is not enough to prove this assertion.

Let us consider some possible microstructural consequences of polymorphism based on Fig. 7.7.

The packets of lamellar α-structure in the subsurface layer of the "vaporizer face" indicate the following:

– the vapor is condenced into a high-temperature β-phase;

– temperature and time conditions in this layer enable the emerged nuclei growth as the foil thickness increases, resulting in the formation of β-grains ~10 μm in size;

– β-grains are stable until the release of the foil from the condensation area when a sharp temperature drop causes the transformation β→α with the formation of a packet α-structure.

It is obvious that under the layer of packet α-structure there can be a layer where the β-phase also occurs during condensation (possibly along with the α-phase), but because of the lower condensation surface temperature, corresponding to a lower (intermediate) foil thickness, no significant increase in the β-grains diameter by recrystallization occurs, while their growth towards the vapor flow causing the columnar β-structure formation is quite consistent with the general regularities of the condensation process. In this particular case, the transformation β→α can occur both during the time (relatively long) of increasing the foil thickness and at the foil cooling after its exit of the condensation area. Apparently, the role of the first scenario becomes more important as the foil layer approaches the substrate strip: the foil near the substrate strip has the minimal average temperature and the grain size (and hence − the lowest β-phase stability), plus it has the maximum duration of the temperature exposure. But in either of the two cases the transformation β→α will not result in a packet-lamellar morphology of the final α-structure: such morphology is not associated at all with the high-temperature isothermal transformation, and the formation of the packets of plane-parallel α-plates during the foil cooling is not expected to be due to the small transverse size of columnar β-crystals. Under either scenario, the resulting structure will (may) have more or less clear-cut features of the columnar structure of the primary β-phase on its metallographic images.

Certainly, the above study does not exclude the possibility of partial or even complete formation of the adjacent substrate strip layer of the 70 μm BT6 foil at $T_{substrate}$ = 930 °C by vapor condensation directly into the α-phase. However, it is clear that the absence of the packet α-structure in the 25...30 μm thick foils of alloy BT6 at the same temperature, at least, is not an unambiguous evidence of the vapor condensation into the α-phase. The problem of the primary phase during the titanium alloys condensation, and especially – during the condensation at $T_{substrate}$ close to the equilibrium temperature of phases β and α, requires additional experimental data to be solved.

To conclude, we have to note that the studied examples of the influence of the substrate strip temperature on the characteristics of condensates, of course, are not exhaustive. Subsequently the role of this factor will be considered in conjunction with other process parameters.

7.3.2. Residual gases pressure and condensation rate

The pressure and the composition of residual gases in the condensation chamber can affect significantly the gas content and density (porosity) of the condensates, the grain structure formation during the condensation process and the growth of the deposited layer thickness, and, consequently, – all structure-sensitive properties of the foil. This is especially true in the case of titanium alloys marked by a very active interaction with gases [179].

In our experiments, we considered the air environment whose pressure was adjusted within $P_{res} = 1.3 \cdot 10^{-3} ... \ 1.3 \cdot 10^{-2}$ Pa. The substrate strip temperature varied in the range of $T_{substrate} = 600...1000$ °C.

The nature of the residual pressure influence on the gas content in the condensate, its density ρ and porosity P, as well as the dependence of these foil characteristics on the substrate temperature are illustrated by the data in Table 7.1 and Fig. 7.14 for alloy BT1-00 [180]. The pressure rise drives up the content of all gases in the foil, decreases the condensate density and increases the porosity of the condensate as compared to the analogous characteristics of the original solid billet.

Table 7.1

The gas content in condensate BT1-00
(numerator – P_{res} = ~1.3 · 10^{-3} Pa, denominator – P_{res} = ~1.3 · 10^{-2} Pa)

Admixture,%	$T_{substrate}$, °C					The source wire, %
	600	700	800	850	1000	
Oxygen	0.12/0.22	0.10/0.19	0.08/0.15	0.10/0.16	0.12/0.18	0.08
Nitrogen	0.007/0.008	0.007/0.009	0.008/0.009	0.008/0.010	0.008/0.010	0.006
Carbon	0.035/0.051	0.035/0.056	0.036/0.053	0.040/0.060	0.044/0.062	0.035
Hydrogen	0.004/0.006	0.004/0.006	0.003/0.005	0.003/0.004	0.002/0.004	0.003
Total impurities	0.166/0.285	0.146/0.261	0.127/0.217	0.151/234	0.174/0.256	0.124

According to Table 7.1, titanium foil is saturated with oxygen more than with other gases. A tangible increase in the carbon saturation of the

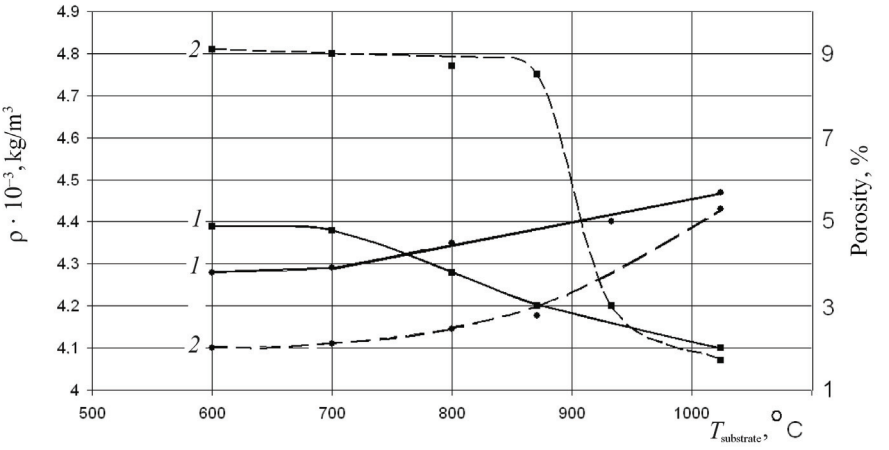

Fig. 7.14. The influence of residual pressure and the substrate strip temperature on the density and porosity of the BT1-00 foil: (■ −porosity; ● − density)
1 – P_{res} = ~2·10^{-3} Pa; *2* – P_{res} = ~1.25·10^{-2} Pa

condensate with growing P_{res} from ~1.3·10^{-3} to ~1.3·10^{-2} Pa can be largely linked to the characteristics of the oil-vapor diffusion pumps and the diffusion oil vapors traps.

Temperature dependencies of the content of various gases in the condensate for the $T_{substrate}$ range of 600...1000 °C are not identical. Higher values of $T_{substrate}$ cause carbon and nitrogen concentration slightly increase, while hydrogen content decreases, and oxygen content firstly decreases (to $T_{substrate} \approx 800$ °C) and then increases again. The total content of gas impurities in the condensate of titanium is mainly determined by the oxygen, and therefore it is minimal at $T_{substrate} \approx 800$ °C.

Increasing residual gas pressure decreases the foil density, while its porosity increases (the foil density was measured by hydrostatic weighing, and the porosity was calculated by the deviation of the foil density from the density of the massive material).

The temperature dependence of ρ and P is barely expressed at low $T_{substrate}$, but it becomes significant in the high-temperature area. The transition temperature from the low-temperature to the high-temperature area, as well as the absolute magnitude of changes in ρ and P significantly increases along with growing P_{res} (see Fig. 7.14).

By comparing the data in Table 7.1 and Fig. 7.14, we see no correlation between temperature dependences of the total gas quantity or the amount of a particular gas in the condensate and its density (porosity) within the entire range of $T_{substrate}$.

This discrepancy is due to the general regularities of the processes of vacuum condensate formation. Thus, high $T_{substrate}$ enables conditions for obtaining dense (nonporous) vacuum condensates (see Chapter 1). But simultaneously it increases the maximum gas content in the metal due to rising gas solubility in the solid solution. Consequently, the increase of the residual pressure within certain limits will not affect the density (porosity) of the condensate, which is observed at $T_{substrate} \approx 1000$ °C. At low $T_{substrate}$, when gas solubility in metal is relatively small and their diffusion in the crystal lattice of the condensed metal is impeded, the formation of micropores typically occurs along the grain boundaries of the condensate; moreover, the growth of P_{res} causes an increase in the number of such pores up to complete separation of the crystallites. Accordingly, for these temperatures one can expect correlation between the total gas content and the porosity of the condensate, as well as significant influence of the residual pressure on the condensate density, as was observed in the experiment.

Table 7.2 shows the data describing the influence of the pressure of residual gases on the grain size of the BT1-00 condensate obtained at $T_{substrate} = 840$ °C. These data illustrate the fact that for "intermediate" temperatures of condensation the value P_{res} can have a significant impact on the foil grain structure: the residual gas role is negligible at $P_{res} \sim 1.3 \cdot 10^{-3}$ Pa, when the average grain size is determined (limited) by the foil thickness, but increasing pressure causes a consistent and significant decrease of the grain diameter.

Table 7.2

The grain size of BT1-00 condensate at $T_{substrate} = 840$ °C

P_{res}, Pa	D, μm
$\sim 1.3 \cdot 10^{-3}$	28
$\sim 7 \cdot 10^{-3}$	18
$\sim 1.3 \cdot 10^{-2}$	10

Fig. 7.15 demonstrates the influence of alloying elements, substrate temperature, residual gas pressure and condensation rate on pore formation in condensates of the Ti–Al–V system. The position of the shown po-

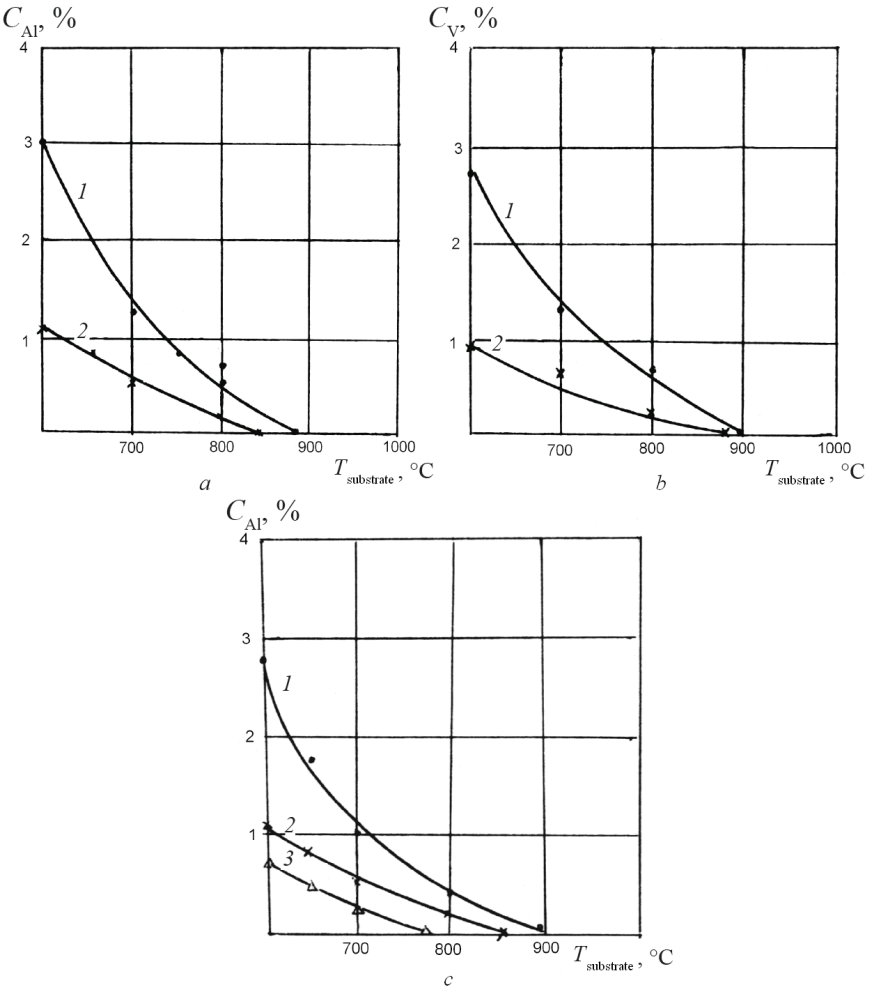

Fig. 7.15. The influence of alloying and deposition process parameters on the location of boundaries of the porous microstructure in titanium alloys foil: *a, b* – W_c = 0.2 μm/s, P_{resid} = ~7·10^{-3} Pa (*1*) and ~1.25·10^{-2} Pa (*2*); *c* – P_{resid} ~7·10^{-3} Pa, W_c = 0.1 μm /s (*1*), 0.2 μm /s (*2*) и 0.3 μm /s (*3*)

rosity borders was determined metallographically. It is seen that alloyng both with aluminum and vanadium suppresses pore formation in the condensate: adding a sufficient quantity of these elements into the alloy allows

eliminating the porosity which exists in pure titanium at the same values of $T_{substrate,}$ P_{res} and W_c. The increase in W_c reduces porosity, i.e., in qualitative terms, its effect is similar to that of the P_{res} reduction (Fig. 7.15, *c*).

7.4. The influence of condensation process parameters on condensate mechanical properties

The results presented in Fig. 7.16–7.18 illustrate the following regularities of the mechanical property dependence on substrate strip temperature, residual gas pressure and chemical composition of condensates:

– strength characteristics within the considered alloying range decrease with the growth of the substrate temperature from 600 °C to ~ 700...750 °C and remain almost unchanged at further rise of $T_{substrate}$;

– the dependence of ductility on the substrate temperature is non-monotonic: within the considered range of $T_{substrate}$ for all alloys there is a maximum of the relative elongation;

– increasing content of the alloying elements causes an increase in the strength and a reduction in the ductility properties of the condensate;

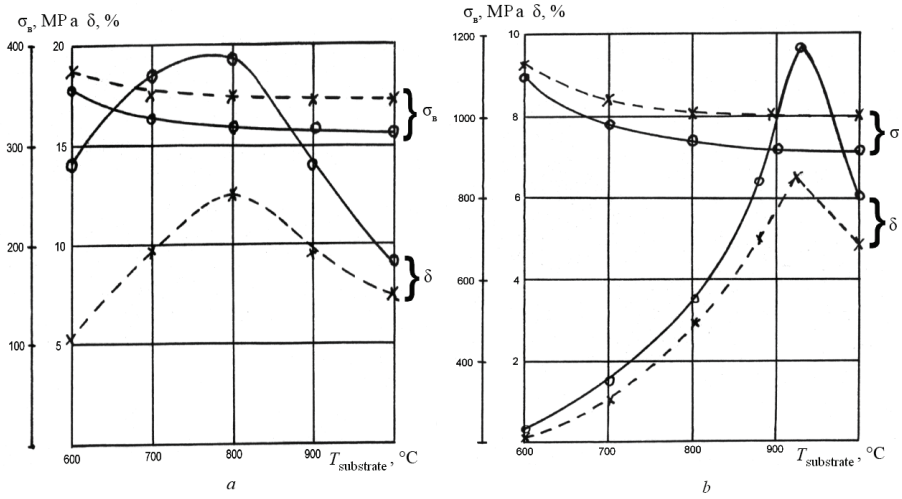

Fig. 7.16. The influence of the substrate temperature and the residual gas pressure on the mechanical properties of 25 μm thick foils of BT1-00 (*a*) and BT6 alloy (*b*): o – P_{res} = ~2·10^{-3} Pa; x – P_{res} = ~1.25·10^{-2} Pa

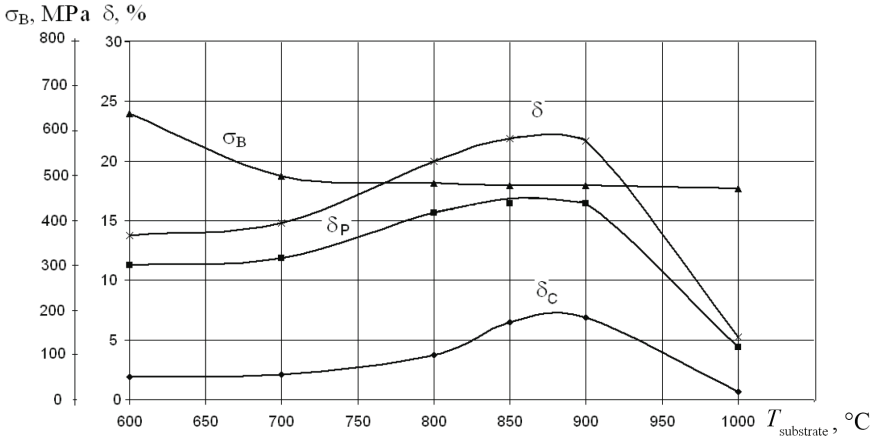

Fig. 7.17. The influence of substrate temperature
on the mechanical properties of the 2B alloy foil

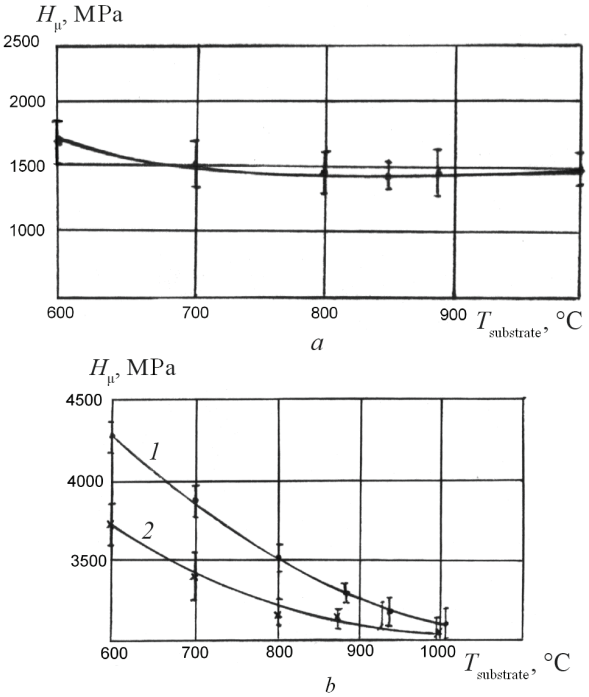

Fig. 7.18. The influence of the substrate temperature
on the microhardness of alloy foils BT1-00 (*a*) and BT6 (*b*):
1, *2* – measured on the sides of the substrate and the vaporizer, respectively

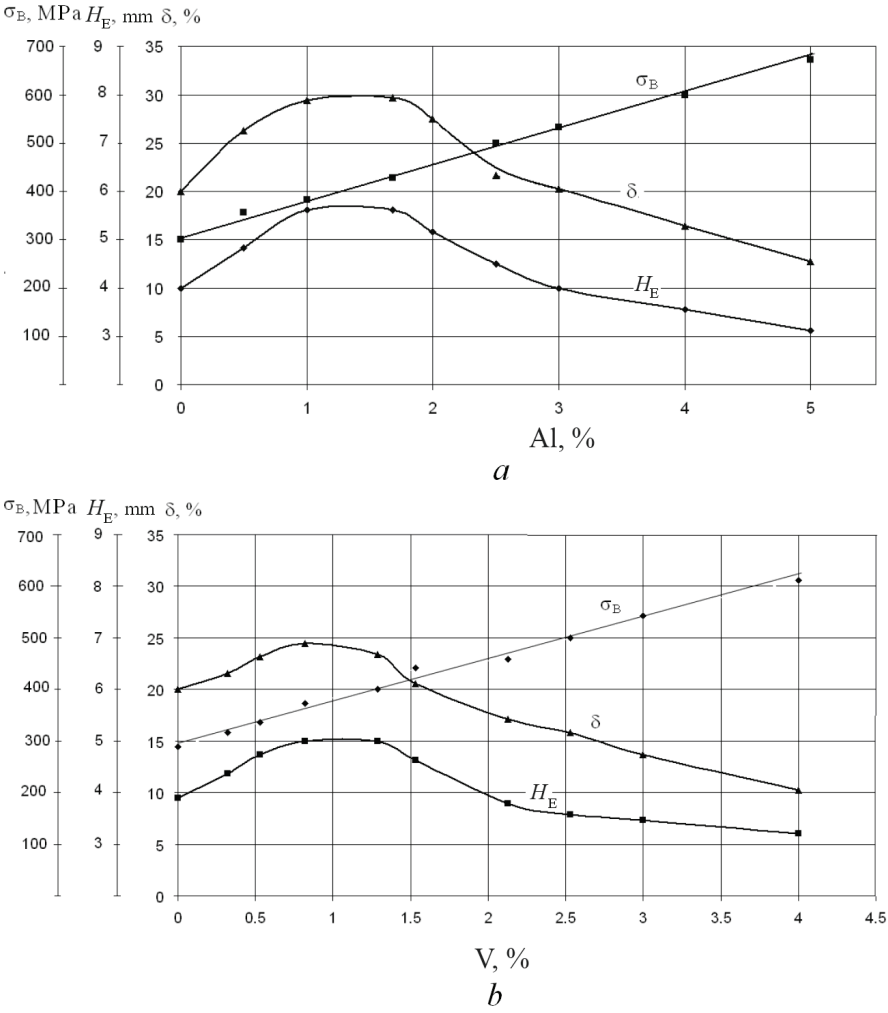

Fig. 7.19. The effect of aluminum and vanadium on the mechanical properties of Ti–Al (a) and Ti–V (b) alloy foils ($T_{substrate}$ = 850 °C)

– the higher the alloying, the narrower the $T_{substrate}$ temperature range of the increased condensate ductility, which shifts towards higher temperatures;

– an increase in the residual gas pressure in the range of $1.3 \cdot 10^{-3}$...$1.3 \cdot 10^{-2}$ Pa causes an increase in strength and decrease in ductility condensate properties;

– alloying may lead to different mechanical properties throughout the foil thickness: microhardness of the BT1-00 condensate is the same all over the foil cross section, whereas for the BT6 alloy the foil hardness on the substrate side is substantially larger than that on the vaporizer side, and this difference increases as $T_{substrate}$ decreases.

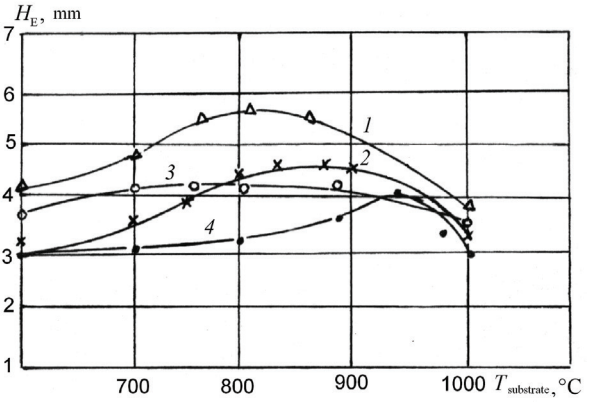

Fig. 7.20. The effect of chemical composition and substrate temperature on the drawing depth (according to the Erickson test) for 25 μm thick foils of alloys 2BΦ (*1*), 2B (*2*), BT1-00 (*3*) and BT6 (*4*)

An extreme kind of temperature dependence $\delta(T_{substrate})$ caused by the initial increase in ductility with growing $T_{substrate}$ due to the development of the processes of tempering and/or recrystallization in the condensate, which is replaced by a ductility decrease due to an excessive grain coarsening of the α-structure, when the grain size becomes comparable to the foil thickness (in pure titanium), or as the result of the formation of a less ductile lamellar α-structure in the foil cooled from the β-area in the case of a sufficiently high temperature $T_{substrate.}$.

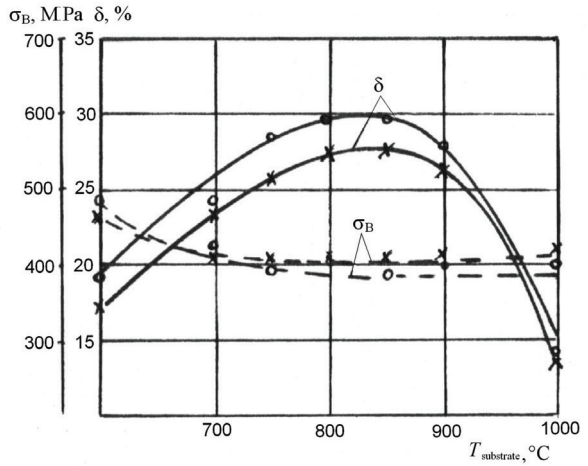

Fig. 7.21. The influence of substrate temperature and residual gas pressure on the mechanical properties of the 2BΦ alloy foil:
○ – $P_{res} = \sim 2 \cdot 10^{-3}$ Pa; x – $P_{res} = \sim 6 \cdot 10^{-3}$ Pa

Separate influence of alloying titanium with aluminum and vanadium on standard mechanical properties and fabrication ductility (depth of the extrusion according to Eriksen, H_E) of condensates is presented in Fig. 7.19. At constant temperature $T_{substrate}$ = 850 °C the strength of the alloys increases linearly along with increasing amounts of Al and V, whereas the ductility has a maximum corresponding to ~1.5 % Al and ~1 % V. A simultaneous increase in strength and ductility which is observed at moderate alloying is due to a sharp decrease of the condensate grain size (see Fig. 7.5). Further alloying results in the common decrease in ductility with increasing strength.

The influence of the substrate temperature and the chemical composition on the fabrication plasticity for the considered alloying range of the condensates is illustrated in Fig. 7.20. The maximum drawing depth by the Erikson test was shown by alloy 2ВФ (~Ti–1.5% Al) [181]. The influence of $T_{substrate}$ and P_{res} on the standard mechanical properties of this alloy condensate is given in Fig. 7.21.

7.5. The use of heat treatment of condensates

For the considered alloys of the Ti−Al−V system the expedience of heat treatment in the case of thin foil vacuum deposition onto a moving substrate strip is determined by the following main factors [182]:

− under typical temperature−time conditions of foil production the structure of condensates differs throughout its thickness, and the structural heterogeneity gets higher with decreasing substrate temperature and increasing content of the alloying elements;

− at a low substrate temperature (~ 600 °C) the alloy condensates with a higher content of the alloying elements are highly defective as far as their crystal structure and microporosity are concerned, which deteriorates the foil ductility;

− rising the substrate temperature from 600 to ~800...850 °C, which enhances the structural homogeneity of the condensates throughout the foil thickness (especially in the case of titanium and low-doped alloys) and leads also to lower crystal defectiveness and porosity, simultaneously reduces the substrate strip resistance and limits its multiple usability, i.e., worsens the economic characteristics of the production process;

− in principle, homogenization of the condensate structure, obtained at low $T_{substrate}$, as well as the foil ductility improval, can be achieved by adding heat treatment of the condensate into the production process.

The effect of heat treatment on the structure and properties of titanium alloys is demonstrated on the example of 25...30 μm thick condensates that were obtained at $T_{substrate}$ = 600 °C, i.e. at the minimum substrate strip temperature of the above-mentioned temperature range.

Vacuum annealing results in a bigger grain diameter in the foil plane (Table 7.3 and Fig. 7.22) and alters the crystallite shape along the foil cross-section, where the transition from a columnar to a more equiaxial crystal structure takes place (Fig. 7.23 and Fig. 7.24).

Table 7.3

The effect of annealing on the grain size in alloys

Alloy	Annealing conditions	Grain size, μm
2B	–	1.1
	850 °C, 3 hrs	4.2
	850 °C, 6 hrs	6.3
BT6	–	0,4
	800 °C, 1 h	1.6
	850 °C, 1 h	2.4

The influence of annealing temperature $T_{annealing}$ on the basic texture intensity for various alloy foils is shown in Fig. 7.25. The increasing of $T_{annealing}$ in the range of 600...850 °C makes virtually no change in the foil texture of pure titanium BT1-00 due to the formation of a practically stable recrystallization texture already in the process of condensation. In other alloys, recrystallization processes lead to the base texture strengthening with growing $T_{annealing}$, being more significant with at a higher content of alloying elements.

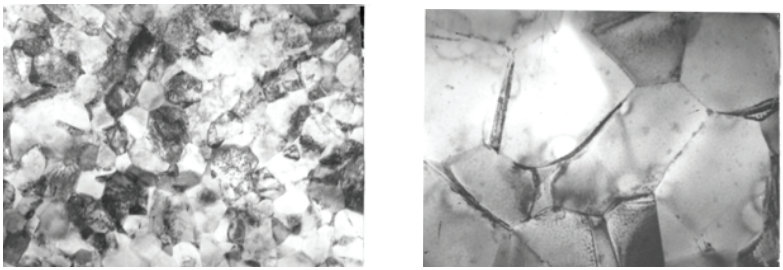

a *b*

Fig. 7.22. The microstructure of BT6 alloy foil before and after the heat treatment: *a* – $T_{substrate}$ = 600 °C; *b* – annealing 850 °C, 1 h

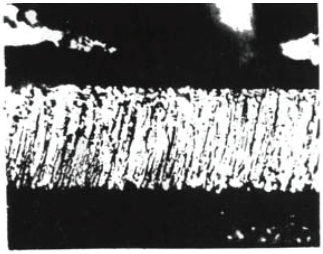

a

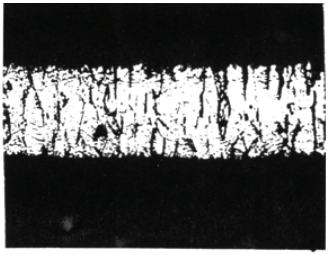

b

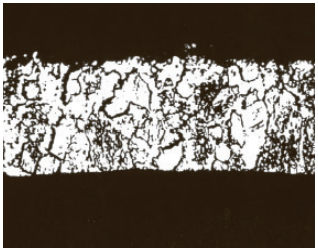

c

Fig. 7.23. The influence of annealing on the structure of 2B alloy foil (×800):
a – $T_{substrate}$ = 600 °C; *b* – annealing 850 °C, 1 h;
c– annealing 850 °C, 3 hrs

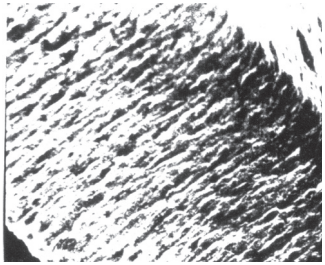

a

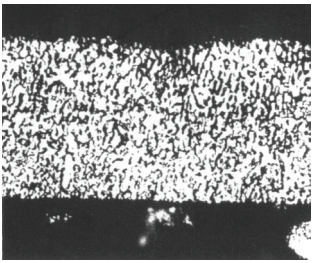

b

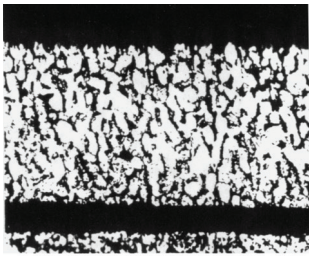

c

Fig. 7.24. The influence of annealing
on the structure of BT6 alloy foil:
a – $T_{substrate}$ = 600 °C; *b* – annealing 800 °C, 1 h;
c – annealing 850 °C, 1 h;
(*a* – ×1500; *b*, *c* – ×800)

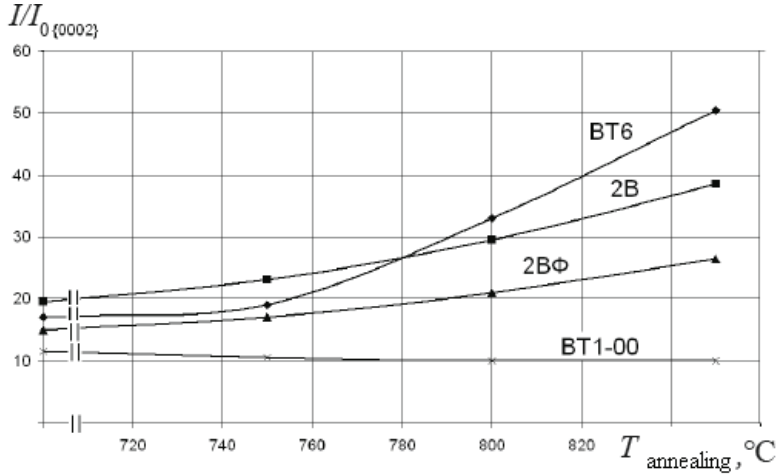

Fig. 7.25. The effect of annealing temperature
(t = 1 h) on the base texture intensity of alloyed foils

The metastability of the phase composition of the BT6 alloy condensate obtained at $T_{substrate}$ = 600 °C makes possible the occurrence of the β-phase, the amount of which rises with increasing temperature of the isochronous one-hour annealing (Fig. 7.26).

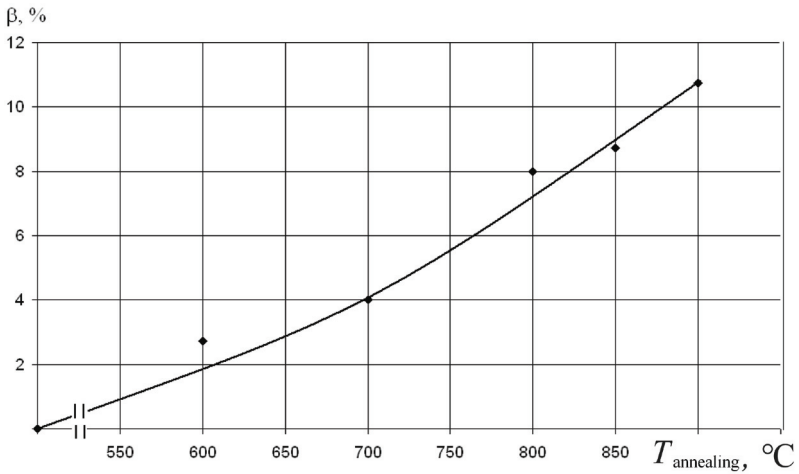

Fig. 7.26. The effect of annealing temperature (t = 1 h) on the amount
of β-phase in BT6 alloy foil produced at $T_{substrate}$ = 600 °C

The effect of annealing on the regular mechanical properties ($\sigma_в$, δ) is illustrated in Fig. 7.27. The growth of $T_{annealing}$ in the range of 600...900 °C leads to a monotonic decreasing of the strength properties of the alloys annealed for ≤ 0.5 h, while at a longer annealing time their alteration is described by the curve with a minimum. The dependence of plasticity on $T_{annealing}$ is qualitatively identical for all the alloys and heat treatment modes considered. The dependence of δ on $T_{annealing}$ for each of the three isochronous annealing durations (0.5; 1 and 2 h) is described by the curve with

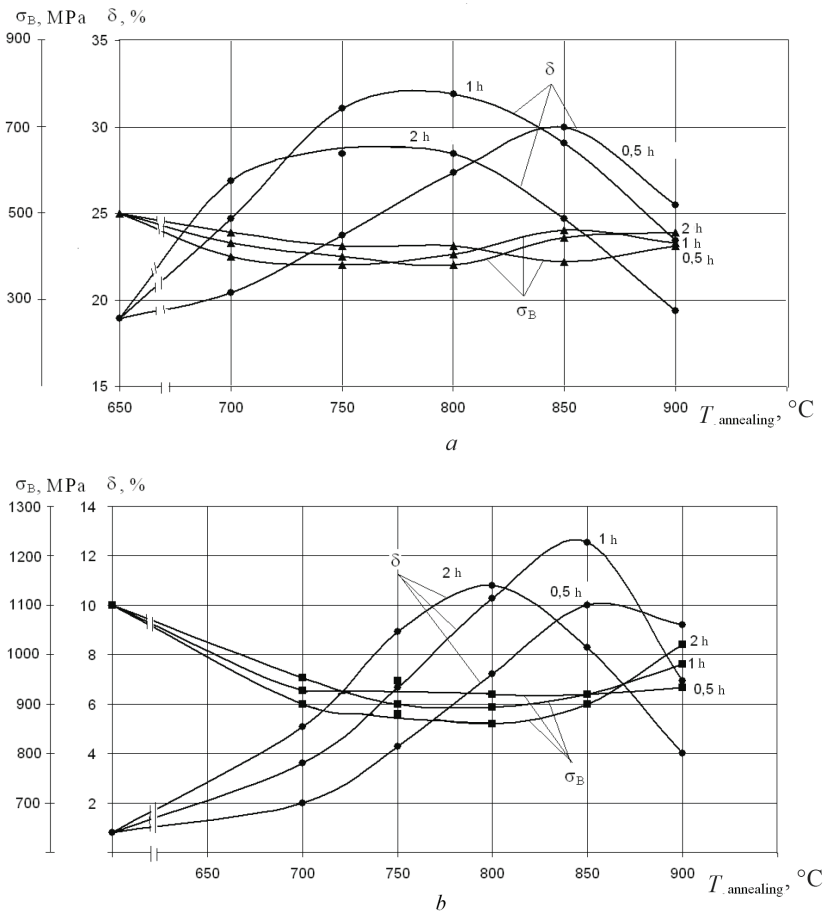

Fig. 7.27. The effect of annealing temperature and duration on the mechanical properties of 2BF (*a*) and BT6 (*b*) alloy foil obtained at $T_{substrate}$ = 600 °C

a maximum, shifting towards higher temperatures with decreasing annealing time and increased alloying. The extreme values of δ were observed at the «intermediate» annealing time of 1 hour.

The plasticity growth and the strength decrease, that take place at $T_{annealing}$ increment, are caused by the recrystallization processes during the condensate annealing [183, 184], while the strength increasing and the ductility lowering are due to the gas absorbtion (primarily oxygen) by the foil metal from the residual atmosphere in the vacuum chamber in the annealing process. The position and the absolute maximum values of δ on the curves (cf. Fig. 7.27) are determined by the temperature-, time- and concentration-specific dependencies of the recrystallization processes, on one hand, and the processes of gas saturation of the annealed foil, on the other hand. For alloy BT6, an additional factor influencing the mechanical properties of the foil can be the thermal and temporal dependence of the changes in the initial condensate phase composition, whereas for low-doped alloys the additional reduction of ductility at the maximum annealing temperatures may be caused by excessive coarsening of the grain structure.

Figure 7.28 shows the influence of annealing temperature on fabrication ductility of 2B and BT6 alloy foils annealed for 1 hour, at which the absolute maximum δ-values were obtained. The comparison of this figure and Fig. 7.20 evidences that the use of low-temperature deposition ($T_{substrate}$ = 600 °C) followed by vacuum annealing of the condensate allows obtaining even a higher ductility of the foil than using high-temperature ($T_{substrate}$ > 800 °C) condensation. By that, the annealing temperature, ensuring maximum ductility of the 2BΦ, 2B and BT6 alloy foils, is more than by 50 °C below $T_{substrate}$, at which the maximum ductility of

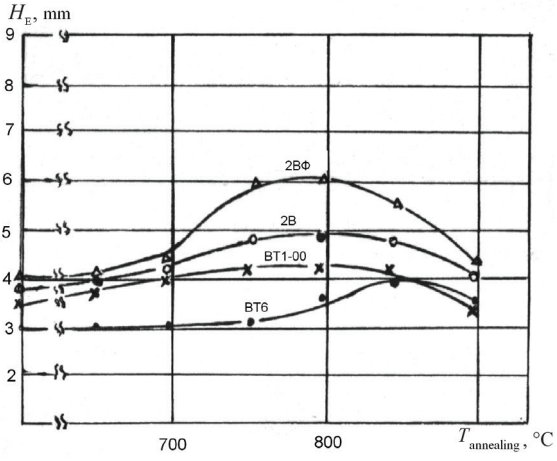

Fig. 7.28. The influence of annealing temperature (t = 1 h) on the drawing depth (according to the Erickson test) of 2BΦ (*1*), 2B (*2*), BT1-00 (*3*) and BT6 (*4*) alloy foils

the same alloys is reached at high-temperature condensation. The comparison of Fig. 7.16, *b* and Fig. 7.17 with Fig. 7.27 leads to qualitatively similar conclusions on the correlation of the maximum δ-values at "high-temperature" and "low-temperature + annealing" technologies of foil production.

Thus, including the heat treatment operation for the condensates of the Ti–Al–V system allows using a relatively low substrate strip temperature, which is favorable for the strip multiple use, and obtaining a more homogeneous and stable foil structure with improved ductile properties.

7.6. The influence of condensation conditions on the foil surface

The surface of the foil made by vacuum condensation depends on the alloy chemical composition, condensation conditions (temperature and microrelief of the substrate strip, condensation rate, the presence of residual gases) and the type of resulting condensate structure [33, 185−188]. In turn, the surface condition has a significant influence on the adhesion, gas saturation of vacuum condensates, their behavior at soldering and diffusion welding [113, 168, 189−191, 192]. Titanium condensate surface was the object of many researches [32, 43, 193, 194].

We researched the influence of the relief of the substrate strip surface and of the vacuum deposition conditions on the surface morphology of the BT6 foil.

The roughness of the foil and substrate strip surfaces was studied with a profilograph − a surface profilometer with the vertical magnification of 20,000, horizontal magnification of 400 and the tip radius of 2 μm. The quantitative roughness of the surface was estimated (according to the standard GOST 2789−93) through arithmetic mean deviation of the surface relief (R_a) and the arithmetic mean value of the irregularity pitch of the surface peaks (*S*).

To study the foil surface structure, scanning and transmission electron microscopy was used. The height of the surface microstructure elements (*H*) was evaluated on the base of electron microscopic images of carbon replicas, obtained at the shading angle of 15°.

It was found that the substrate strip surface had a more developed relief in the direction perpendicular to the rolling direction. Accordingly, the foil relief was also more developed in this direction. Therefore, the surface roughness was rated (by the method of surface profilography) mainly in this direction.

Irregularities in the substrate strip surface cause the emergence of outgrowths, i.e. groups of crystallites projecting over the condensate surface. These outgrowths are globular (Fig. 7.29) and are formed due to the shielding of the vapor flow by the projections formed on the condensation surface, thus enhancing a predominant growth of crystallites on these outgrowths.

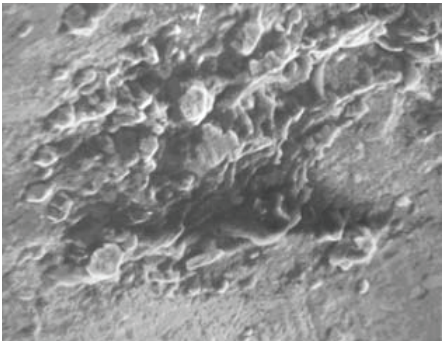

Fig. 7.29. Globular outgrowths on the foil surface, alloy 2B (×500)

Along with globular outgrowths, the condensate surface displayed lamellar outgrowths resulting from inadequate cleaning of the substrate strip surface from organic contaminations (Fig. 7.30).

Unlike globular outgrowths, the formation of lamellar ones in organic contamination spots on the substrate strip is caused by a number of other reasons apart from the shading effect. It was observed that the size of the lamellar outgrowths varies due to chemical composition of the condensate. For instance, the BT1-00 foil had lamellar outgrowths of average size ~30 μm, while the outgrowths in the 2B foil − ~5 μm, which correlates with the transverse size of crystallites in these alloys. Apparently, the lamellar outgrowths formation is caused by the interaction of the condensate with carbon and oxygen in the organic contamination spots on the substrate strip. More research is needed to present a detailed picture of the mechanisms causing the formation of lamellar crystals.

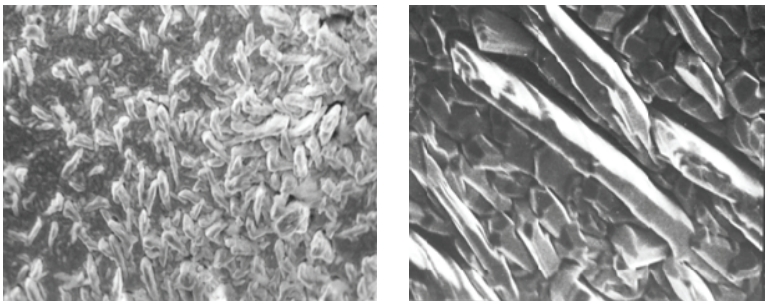

a *b*

Fig. 7.30. Lamellar outgrowths on the foil surface, alloy 2B (*a* –×500; *b* – ×1500)

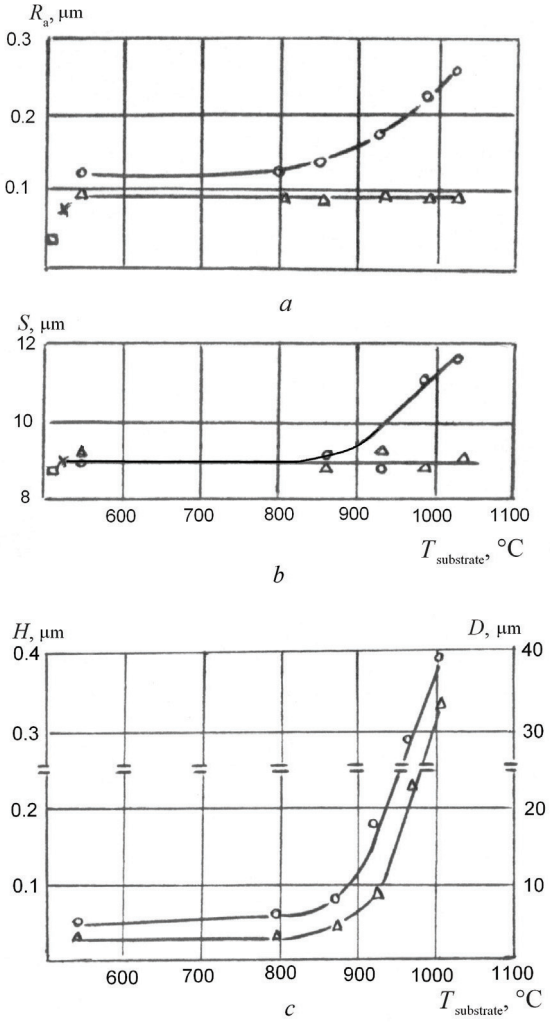

Fig. 7.31. The influence of the substrate strip temperature on the foil surface roughness (*a*, *b*), the height of microstructure elements, and the average grain size (*c*). The alloy BT6: o—o – the "vaporizer face", Δ—Δ – the "substrate face"; □ and x – the substrate strip without and with an antiadhesive layer, respectively

Fig. 7.31 presents our research results on the surface relief of the BT6 foil, which was produced by condensation onto a substrate strip covered with an antiadhesive layer.

As shown in Fig. 7.31, *a*, *b*, within the studied temperature range, the R_a value is higher on the foil side facing the vaporizer than on the "substrate face", and R_a of the "substrate face" is greater than in the case of the substrate strip without the antiadhesive layer, being identical to the R_a value for the substrate strip coated with an antiadhesive layer. At that, the R_a value for the "substrate face" remains constant throughout the entire temperature range. The value of *S* also is constant being equal to the value of *S* on the substrate strip.

The values of R_a and *S* measured on the "vaporizer face" remain virtually unchanged within the temperature range of ~550...900 °C, but they increase at a higher substrate strip temperature. At that the relief of the

"vaporizer face" is changed significantly. At the temperature above 930 °C it becomes identical in the longitudinal and transverse rolling direction, while the distance between the outgrowths becomes greater compared to the *S* value of the substrate strip.

The height *H* of the microstructure elements of the "vaporizer face" is virtually the same within the temperature range of 550...870 °C, and it increases rapidly as the substrate temperature goes up, reaching the value commensurable with the values of R_a at the same temperatures (Fig. 7.31, *a*, *c*). The change of *H*, caused by the temperature rise up to 930 °C, is similar to the change of the width *D* of the columnar crystals which form the foil cross-section structure.

In the temperature range of 550...930 °C, the relief of the "vaporizer face" may be described as "finely granulose", where the transverse size of the granules coincides with the transverse size of the condensate grain and, respectively, it increases along with the rise in the substrate strip temperature. At temperatures above 930 °C, the surface mic rostructure changes radically, being dominated by the helically-formed condensate growth. At the same time the height of the microstructure elements varies by more than a factor of 10. It was found out that the type of the helically-formed relief remains constant within the boundaries of a single initial grain of the β-phase, which is predominant at high temperatures, but it is altered greatly from grain to grain.

Thus, the "substrate face" relief pattern is almost entirely determined, within the studied temperature range, by the substrate strip relief (i.e. by the rolling traces on its surface) and partly by the presence of the antiadhesive layer.

The morphology of the "vaporizer face" is defined both by the relief of the substrate strip surface and the condensate growth pattern.

In the temperature range of 550...930 °C the height of micro-irregularities depends mainly on the columnar crystallite size. The fact that the size of the crystallites is comparable to the height of the rolling traces on the substrate strip surface means that the substrate strip is a significant factor of the foil relief formation in this temperature range. Despite the increase in the crystallite size at higher temperatures and a greater height of micro-roughness, the value of *S* in the "vaporizer face" does not depend on the temperature and coincides with *S* of the substrate strip. This is because the tip radius of the profilometer needle is greater than the transverse

size of crystallites within this particular temperature range. Therefore the profilometer does not measure the height of the microstructure elements formed through the growth of crystallites; instead it just detects higher roughness caused by rolling traces, the distance between which exceeds significantly the needle tip radius.

In this case, the value of R_a also is not supposed to change with temperature, since its value would be determined by the height of the rolling traces reproduced through the growth of the fine-grained condensate. The observed higher values of R_a indicate a shadowing mechanism in the form of predominant growth of protrusions on the surface. Moreover, the operation of this mechanism is supposed to become more intense as the columnar crystallites grow in size.

At temperatures above the temperature of the (α+β)/β phase transition the "vaporizer face" relief changes abruptly. The morphology of the foil surface in this case is controlled mainly by the crystallographic features of the original β-phase grains. This is confirmed by the relief structure variance from grain to grain, by a sharp increase in R_a, which is fully determined by the growth of H, and the identity of the relief in the directions that are perpendicular and parallel to the rolling direction [195].

The diagram of the foil surface relief formation is shown in Fig. 7.32.

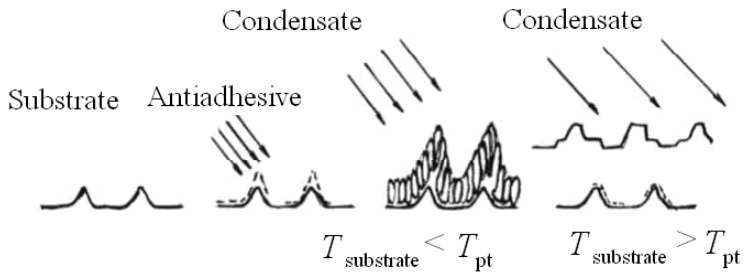

Fig. 7.32. Schematic view of the formation of the foil surface relief

Fig. 7.32 shows how the shadowing effect causes the outgrowths building-up on the condensation surface during the sequential antiadhesive and alloy deposition processes, as well as the change in the foil surface relief formation when the substrate temperature is above the temperature of the phase transformation in the foil.

Chapter 8. USING THE WORK RESULTS TO ADRESS CHALLENGES OF INDUSTRY

Our researches and inventions allowed us to solve a number of important applied problems, including the development of a high-temperature membrane technology preventing titanium apparatus from gas saturation in the course of vacuum annealing and the creation of a multi-layered gettering material to protect blades of gas turbine engine from gas saturation during high-temperature annealing. Ultra-thin foil obtained by vacuum deposition was used in a number of specialized products, including microelectronics, laser units and electron beam output devices.

One of the key technological operations of manufacturing a large welded titanium apparatus is vacuum annealing, ensuring the removal of internal stress, dehydrogenation and framework correction. However, the annealing process involves the interaction of framework surfaces with residual gases and the formation of the brittle alpha case layer, which dramatically reduces the life span and the reliability of the product in general [196]. Therefore it is necessary either to prevent the alpha case layer formation during the annealing process, or to remove this layer after the framework annealing. In practice the degree of alpha case formation is quantitatively characterized by the excessive microhardness of the surface compared to the core for witness-specimens of the same alloy ΔH_{μ}.

Fig. 8.1 shows the dependence of exceeding microhardness on the carbon content on the specimen surface, obtained in the A. N. Tupolev Interbranch Scientific and Technical Complex. It was demonstrated that as the carbon content in the surface layer rises by a factor of 30 and the oxygen content – by a factor of 2 to 5, then carbonization of the surface becomes one of the main reasons resulting in increase of microhardness after vacuum annealing. The sources of hydrocarbon vapors within the furnace volume are the contamination of the surface of the furnace structural elements and the metal charge plus the counterflow of oil vapor into the furnace chamber from the preevacuation and oil-diffusion pumps.

The attempts to prevent alpha case formation in the annealed metal by using the AVED high-vacuum oil-free pumps failed.

In large furnaces of a UVN4500 type equipped with AVED pumps the increase of microhardness of the titanium construction surfaces after annealing (ΔH_{μ}) reached 70 %, the alpha case layer depth was 25 μm. That is why ear-

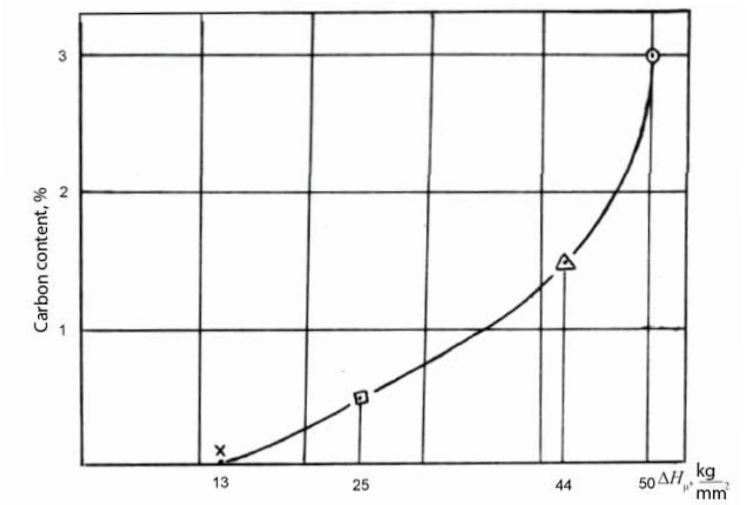

Fig. 8.1. The dependence of the excessive microhardness after vacuum annealing ΔH_μ on carbon content on the surface of titanium specimen

lier it was suggested to remove the alpha case layer formed in the process of vacuum annealing by pickling it off with a hydrofluoric acid based solution.

The implementation of this technology for this case required building of several 18-meter-long titanium pickling baths. This involved not only a lot of capital investments and created substantial environmental problems but also delayed significantly the completion of high-duty products. In addition, the introduction of another labor-intensive operation greatly extended the time of building such apparatus. It should also be noted that this prickling technology did not ensure the required reliability of alpha case layer removal since a number of structures had lap joints with hard-to-reach gaps and pockets.

These shortcomings required a brand new solution to the problem of eliminating gas saturation of titanium aggregates during vacuum annealing. To omit pickling it was necessary to prevent the surface alpha case formation in annealing operations.

This problem was solved by inventing a high- temperature membrane technique[1], HMT, which include shielding the furnace charge with a spe-

[1] We appreciate the contribution to the development and implementation of HMT by Y.V. Gorshkov, O. N. Sankov, L. I. Korseladze and A. V. Bushuev.

cial membrane shielding device based on ultra-thin titanium alloy foil with regulated through porosity.

It must be noted that attempts to protect the furnace charges with screens made of rolled titanium sheets and titanium chippings had been experienced earlier. However, the chipping screens turned out to be not suitable for furnaces with the working volume of more than 20 m^3 due to screen overweight and heat insulation properties of these screens resulting in additional energy consumption and unacceptable extension of the annealing cycle. Sheet shields did not protect adequately the metal charge in the furnace from gas saturation, mainly due to the deformation of the sheets and gaps between them [197].

Our high-temperature membrane technology is fundamentally different from the widely used low-temperature membrane technology based on organic porous membranes.

In the low-temperature membrane technology, gas mixture molecules are separated exclusively according to a geometrical factor, i.e. the size of the holes in the organic membrane is selected so that molecules of one kind could pass through these holes, while other molecules are trapped there. This technology has a number of shortcomings.

A small diameter of cut-through holes, comparable to the size of molecules, means a low permeability of the membrane and, respectively, insufficient efficiency of this technique. There is no way to control the membrane permeability within a wide range. Using organic membranes does not allow applying this technology for separation of mixtures at high temperatures.

Let us formulate the requirements concerning the use of high-temperature membrane-shielding devices meant to prevent gas saturation of the metal charge in the furnace during vacuum annealing.

1. At low temperatures the device must not impede the build-up (within a relatively short time) of a high vacuum in the entire volume of the furnace and in the area adjacent to the metal charge, i.e. the device must have a high gas permeability at low temperatures.

2. At high temperatures the device must prevent the penetration of hydrocarbons and oxygen from the furnace volume to the charge surface, while enabling the removal of the hydrogen, released by the annealed titanium structures from the volume adjacent to the charge. In other words, at high temperatures this device must separate the gas mixture, i.e. let hydrogen flow out (from the charge) while impeding the penetration of the hydrocarbon vapors and oxygen atoms to the charge from the external

furnace volume. Requirements *1* and *2* imply that the device should have temperature-dependent conductivity.

3. The device should not trap much heat to allow reduced energy consumption at annealing operation.

4. To avoid using a massive frame, the device must be lightweight and flexible.

The device should provide reliable protection of the charge and prevent the formation of gaps in the screen in the annealing process, also it must be easy to assemble.

Based on these requirements we developed a device [198−203], whose operation principle is schematically shown in Fig. 8.2 and may be described as follows.

At low temperatures, as the furnace volume is pumped out in the viscous flow mode, the charge volume is vacuumized by the residual gas efflux through the holes in the double-layer titanium alloy foil screen. The residual gas molecules penetrate through the open holes in foil layer *2* to the surface of foil layer *1*, then migrate along this surface and are removed through the open holes in the foil layer *1* into the pumped volume of the furnace.

As the charge is heated in the furnace, the hydrocarbon and oxygen molecules, partly entering from the furnace volume through the holes in the foil layer *1*, are effectively absorbed by foil layer *2* and do not go into the charge volume (cf. 6.5). At the same time, some part of the hydrogen molecules formed during the degassing of the charge may be absorbed by foil layer *2*, but major part of the remained molecules, over-equilibrium for the temperature, that have passed through the open holes in layer *2* and touched the surface of layer *1*, migrate over the surface and are removed through the open pores in foil layer *1*. Thus the gas permeability of this device is controlled by the furnace temperature.

To meet the requirements to elasticity, lightness, insignificant heat-trapping capacity, and to exclude the formation of any gaps in the process of vacuum annealing of large-size semi-finished products we suggested to make screen layers of ultra-thin foil.

It is known that the elasticity of titanium foil of 5...15 μm thick is close to that of woven materials. For the foil of such thickness to be used as a construction material it must be made of high-strength titanium alloys, such as BT6.

In order to facilitate the manufacture of a sizeable device for shielding large aggregates it is necessary to use coiled foil, at least 400 mm wide.

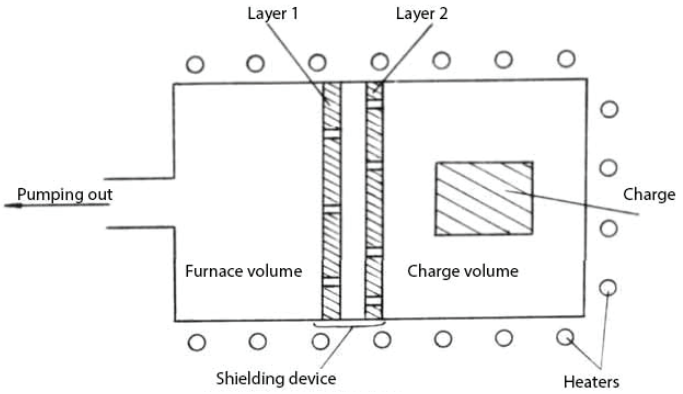

Fig. 8.2. Layout of shielding device location
at vacuum annealing of titanium structures

The basic parameters of the shielding device were selected by calculating the device gas permeability (see Chapter 6). These include foil thuough porosity characteristics − specific thuough porosity P, m^{-2}, average pore size *d*, m, numder of shields N and the distance *L*, m,between them atthe selected foil thickness *h*, m.

For the desired increase of the charge pumping rate it is necessary to increase the device gas permeability, for example, by increasing P and lowing N at given *d* and *h*. On the other hand, to prevent the penetration of gas impurities from the furnace volume to the charge, it is advisable to reduce the device gas permeability by decreasing P and increasing N. Hence, a certain optimal set of the device parameters which ensures the desired performance of charge pumping and reliable protection of the charge surface against the ingress of gas impurities from the furnace volume must be chosen.

Based on the gas permeability calculation (see Chapter 6), the optimum values of main shielding device parameters were selected:

average size of through pores, *d*	30…50 μm
pecific through porosity, P	1...10 cm^{-2}
number of screens, N	2
distance between screens, *L*	0.2...0.3 cm

To ensure the required distance and to improve the device structural characteristics it was suggested to use a special carrier material placed between foil layers. This material should meet the following requirements:

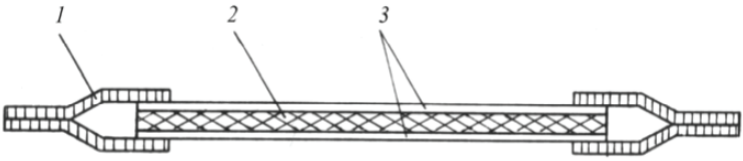

Fig. 8.3. The shielding device layout:
1 − foil with h = 80 μm; 2 − silica fabric KT-11; 3 − foil with h = 5...7 μm

− the thickness of the material must match the required distance between foil layers;

− the material must be chemically inert at the annealing temperature of titanium semi-finished products, flexible and sufficiently strong.

In addition, the carrier must not resist the gas flow through the shielding device, i.e. the through porosity of the carrier has to be several times higher than that of the foil. The selected carrier was silica fabric KT-11 of 0.3 cm thick, 0.2 cm mesh. Ultrathin foil of alloy BT6 with specified porosity was produced using the previous studies of the influence of vacuum deposition process parameters on the foil through porosity (see Chapter 6).

A layout of the shielding device is shown in Fig. 8.3. The device consists of two layers of ultrathin porous titanium foil with the silica fabric carrier in between.

The efficacy of applying the high-temperature membrane technology to reduce the gas saturation of titanium structure surfaces was assessed by comparing the excessive surface microhardness to the core microhardness of the BT6 alloy witness-specimens after vacuum annealing. The witness-specimens were placed either under the shielding device together with the furnace charge, or in the outer furnace volume. Table 8.1. shows the results of an industrial application of this process.

It is evident that the proposed shielding device ensures an effective protection of the charge surface from the gas saturation during the vacuum annealing.

The increase of the surface microhardness after annealing is about three times lower than the value allowed by the technical specifications, while the oxygen and carbon concentration in the surface layer is within the specified requirements. This process has been used in experimental production and industrial applications over several years and has proved to be highly efficient and reliable.

Table 8.1

The results of the industrial application of the vacuum annealing process

Description of technology of gas saturation of the furnace charge surface	No shielding	With the suggested shielding device	Technical specifications
Increasing microhardness, ΔH, %	41…72	1…7	25
Oxygen concentration, %	0.25	0.05	–
Carbon concentration, %	3.0	0.08	0.1

It happened once that the industrial furnace charge suffered an accidental vacuum drop in the furnace volume from $5 \cdot 10^{-5}$ to $2.5 \cdot 10^{-2}$ mm Hg ($6.67 \cdot 10^{-3}$... of 3.33 Pa) at the charge temperature of 490 °C. However, also under these conditions, the use of new shielding devices ensured an effective protection of the charge, the maximum excess of the surface microhardness being 14 %.

The implementation of HMT allowed not only to provide the required service life of the product, but also to withdraw the earlier decision about the construction of a special titanium pickling line.

Arguably among the applicable results of our work there are 12 production manufacturing specifications and technical specifications for new materials made by vacuum deposition including ОПУ-6-09-89, ВТИ ОПУ-6-10-89, ВТИ ОПУ-6-07-89, ВТИ ОПУ6-11-89.

We have also made a number of recommendations concerning the future applications of our results and the vacuum deposition process, such as:

– to use the technique of determining the components activity not only for the titanium-based melts but also for other metals, including refractory ones;

– to continue researches on the production of vacuum-sealed foil from hard-to-deform alloys;

– to conduct works on making wide foil-based ribbon solders;

– to explore the possibility of obtaining thick vacuum condensates of the aluminum-based alloys having high mechanical properties.

Our achievements have bee registered in author's certificates for inventions [110, 181, 198–207].

CONCLUSION

The presented results of our researches of the processes of heat and mass transfer at high-rate vacuum evaporation and vapor condensation onto a moving substrate strip; the regularities of multi-component alloy evaporation under continuous feeding of molten metal; the principles of substrate strip and antiadhesive material selection; structure formation during the alloy crystallization out of a vapor phase and the relationship between foil structure and its properties; the characteristics of through porosity formation in foil, allow defining the main parameters of foil production out of various metals and alloys with preset properties, including the rational choice of substrate strip and antiadhesive materials, the calculation of initial molten pool composition, ingot feed rate, substrate strip motion rate, the special screen configuration reducing the foil thickness variance, the program of electron beam scanning along the substrate strip and a number of other parameters.

In addition, new opportunities arising from the crystallization out of a vapor phase enable the use of the present results in working out and research of completely new alloys with unique characteristics.

The established regularities provided the scientific basis for the development of a technology for manufacturing ultra-wide foil from hard-to-deform alloys, including titanium-based ones, for creating a specialized equipment complex to study the process and to produce such foil, as well as for the development of vacuum engineering devices acting somewhat like semiconductors.

REFERENCES

1. Палатник Л.С., Папиров И.И. Ориентированная кристаллизация. М.: Металлургия, 1964. (Palatnik L.S., Papirov I.I. Directed crystallization. M.: Metallurgy, 1964.)

2. Палатник Л.С., Фукс М.Я., Косевич В.М. Механизм образования и субструктура конденсированных пленок. М.: Наука, 1972. (Palatnik L.S., Fuks M.IA., Kosevich V.M. Nature of formation and substructure of condensed films. M.: Nauka, 1972.)

3. Комник Ю.Ф. Физика металлических пленок. Размерные и структурные эффекты. М.: Атомиздат, 1979. (Komnik Yu.F. Physics of metal films Dimensional and structural effects. M.: Atomizdat 1979.)

4. Мовчан Б.А., Малашенко И.С. Жаростойкие покрытия, осаждаемые в вакууме. Киев: Наукова думка, 1983. (Movchan B.A., Malashenko I.S. Heat-resistant vacuum-deposited coatings. Kiev: Naukova Dumka, 1983.)

5. Ройх И.Л., Колтунова Л.Н., Федосов С.Н. Нанесение защитных покрытий в вакууме. М.: Машиностроение, 1976. (Roikh I.L., Koltunova L.N., Fedosov S.N. Protective coatings in Vacuum. M.: Mashinostroyenie, 1976.)

6. Wood R.W. // Phil. Mag., 1915. 30. 300; Phil. Mag. 1916. 32. 364.

7. Knudsen M. // Ann. Phis. 1916. 50. 472; Phys. Rev. 1916. 8. 149.

8. Langmuir J. // Proc. Nat. Acad. Sci. 1917. 3. 141.

9. Мак-Каррон Б., Эрлих Т. Взаимодействие газов с поверхностями. М.: Мир, 1965. (Mak-Karron B., Erlikh T. Interaction of gases with surfaces, M.: Mir, 1965.)

10. Cabrera N. // Disc. Farad. Soc. 1959. 28. 16.

11. Zwanzing R. //J. Chem. Phys. 1960. 32. 1173.

12. Хирс Д., Хруска С.Д., Паунд Г.М. Монокристаллические пленки. М.: Мир, 1966. (Khirs D., Khruska S.D., Paund G.M. Monocrystal films.M.: Mir, 1966.)

13. Chariton J., Semenov N. // Z. Phis. 1924. 25. 287.

14. Frencel J. // Z. Phis. 26. 117.

15. Семенов Н.Н. // Журн. русского физ.-хим. общества. 1930. 62. 33. (Semenov N.N.// Journal of the Russian physical-chemical society. 1930. 62. 33.)

16. Родин Т., Уолтон Д. Монокристаллические пленки. М.: Мир, 1966. (Rodin T., Uolton D. Monocrystal films. M.: Mir, 1966.)

17. Хирс Д., Паунд Г. Испарение и конденсация. М.: Металлургия, 1966. (Khirs D., Paund G. Vaporization and condensation. M.: Metallurgy, 1966.)

18. Физика тонких пленок. Т. 1. М.: Мир, 1967. (Physics of thin films. V. 1. M.: Mir, 1967.)

19. Чопра К. Электрические явления в тонких пленках. М.: Мир, 1972. (Chopra K. Electric phenomena in thin films. M.: Mir, 1972.)

20. Косевич В.М., Палатник Л.С. О возможных механизмах образования вакуумных конденсатов // ДАН СССР. 1964. 158. 1314. (Kosevich V.M., Palatnik L.S. Probable mechanisms of formation of vacuum condensates // Proc. of the Science Academy of the USSR. 1964. 158. 1314.)

21. Комник Ю.Ф. Характерные температуры конденсации тонких пленок // ФТТ. 1964. 6. 2897. (Komnik Yu.F. Representative temperatures of condensation of thin films // Solid state physics. 1964. 6. 2897.)

22. Гладких Н.Т. Фазовый размерный эффект в конденсированных пленках. Автореф. дисс. ... докт. техн. наук. Харьков. 1975 (Харьковский ун-т им. А.М.Горького). (Gladkikh N.T. Phase dimensional effects in condensed films. Synopsis of doctorate thesis. 1975 (The A.M. Gorky University in Kharkov).

23. Гладких Н.Т., Ларин В.И., Набока М.Н. Фазовые переходы жидкость- кристалл в тонких пленках. Нитевидные кристаллы и тонкие пленки. Ч.2. Воронеж. Изд-во ВПИ, 1975. 75. (Gladkikh N.T., Larin V.I., Naboka M.N. Phase transitions liquid-crystal in thin films . Wire-type crystals and thin films Part 2. Voronezh. Publishing house of Voronezh Polytechnic Institute, 1975. 75.)

24. Гладких Н.Т., Северин В.М. Влияние условий препарирования на образование жидкой фазы при вакуумной конденсации // Кристаллография. 1974. 19. 414. (Gladkikh N.T., Severin V.M. Effect of preparation conditions on liquid phase formation during vacuum condensation // Crystallography. 1974. 19. 414.)

25. Палатник Л.С., Гладких Н.Т., Набока М.Н. О второй (нижней) граничной температуре конденсации In, Sn, Pb, и Bi // ФТТ. 1962. 4. 1. С. 202−206. (Palatnik L.S., Gladkikh N.T., Naboka M.N. Second (lower) limit temperature of condensation of In, Sn, Pb, and Bi // Solid state physics. 1962. 4. 1. P. 202–206.)

26. Палатник Л.С., Гладких Н.Т. Об эффекте микрогетерогенной конденсации металлов в вакууме // ДАН СССР. 1961. 140. 3. С. 567–570. (Palatnik L.S., Gladkikh N.T. The effect of micro heterogeneous condensation of metals in vacuum // Proc. of the science academy of the USSR. 1961. 140. 3. P. 567–570.)

27. О форме частиц металлических конденсатов на начальных стадиях роста / В.М. Косевич, Л.С. Палатник, С.И. Шевченко, В.А. Антонова // ФТТ. 1964. 6. 3240. (Concerning forms of metallic condensate particles at the early stages of their growth / V.M. Kosevich, L.S. Palatnik, S.I. SHevchenko, V.A. Antonova // Solid State Physics.. 1964. 6. 3240.)

28. Структурные переходы в вакуумных конденсатах меди / Г.В. Федоров, Л.С. Палатник, Я.С. Павляк, В.И. Евтушенко // УФЖ. 1967. 12. 1980. (Phase transconformation in vacuum condensates of copper / G.V. Fedorov, L.S.Palatnik, IA.S. Pavliak, V.I. Evtushenko // The Ukrainian Journal of Physics. 1967. 12. 1980.)

29. Трусов Л.И. Холмянский В.А. Островковые металлические пленки. М.: Металлургия, 1973. (Trusov L.I. Kholmianskii V.A. Island type metallic films. M.: Metallurgy, 1973.)

30. Северденко Д.П., Точицкий А.И. Структура тонких металлических пленок. Минск: Наука и техника, 1968. (Severdenko D.P., Tochitckii A.I Structure of thin metallic films. Minsk: Science and engineering, 1968.)

31. Ройх И.Л., Колтунова Л.Н. Защитные вакуумные покрытия на стали. М.: Машиностроение, 1971. (Roikh I.L., Koltunova L.N. Protective vacuum coatings on steel. M.:Mashinostroyenie, 1971.)

32. Мовчан Б.А., Демчишин А.В. // ФММ. 1969. 28. 4. 653. (Movchan B.A., Demchishin A.V. // Physics and metallography. 1969. 28. 4. 653.)

33. Демчишин А.В., Мовчан Б.А. // ФиХОМ. 1967. 1. С. 44−50. (Demchishin A.V., Movchan B.A. // Physics and Chemistry of treatment of metals. 1967. 1. P. 44–50.)

34. Тонкая структура и фазовый состав конденсационных покрытий NiCrAlY / Ю.Р. Немировский, М.С. Хадыев, В.П. Кузнецов, В.П. Лесников // Защита металлов. 2000. 36. 3. С. 310−314. (Thin structure and phase composition of condensation coatings NiCrAlY / I.R.Nemirovskii, M.S. Khadyev, V.P. Kuznetcov, V.P. Lesnikov // Metal protection. 2000. 36. 3. P. 310–314.)

35. Улановский Я.Б. Исследование закономерностей формирования структуры вакуумных конденсатов сплавов на основе титана и разработка процесса получения титановой фольги. Дис. ... докт. техн. наук. Москва, 1991. (Ulanovskiy I.B. The study of character of formation of of vacuum titanium based condensate structures and the deign of titanium foil production process. Doctoral Thesis. Moscow, 1991.)

36. Улановский Я.Б., Дубник Г.И. Металловедение и новая технология легких и жаропрочных сплавов. М.: ВИЛС. 1982. С. 200−202. (Ulanovskiy I.B. Dubnik G.I. Physical metallurgy and innovation technique of production of light ant high-temperature alloys. M.: VILS (All-Union Institute Of Light Alloys). 1982. P. 200−202.)

37. Колачев Б.А., Ливанов В.А., Елагин В.И. Металловедение и термическая обработка цветных металлов. М.: Металлургия, 1981. (Kolachev B.A., Livanov V.A., Elagin V.I. Physical metallurgy and heat treatment of nonferrous metals. M.: Metallurgy, 1981.)

38. Герт Л.М., Артемов В.И., Исалипов Р.Х. // ФиХОМ. 1976. 42. 5. С. 1100–1107. (Gert L.M., Artemov V.I., Isalipov R.KH. // Physics and Chemistry of treatment of metals. 1976. 42. 5. P. 1100–1107.)

39. Shevakin J.U., Kharitonova L.D., Ostrovskaya L.M. // Thin Solid Films, 1972. 62. P. 337–346. (Shevakin J.U., Kharitonova L.D., Ostrovskaya L.M. // Thin solid films, 1972. 62. P. 337–346.)

40. Бабад-Захряпин А.А., Кузнецов Г.Д. Текстурованные высокотемпературные покрытия. М.: Атомиздат, 1980. (Babad-Zakhriapin A.A., Kuznetcov G.D. Textured high temperature coatings. M.: Atomizdat 1980.)

41. Dixit K.R. Investigation of the orientations in thin evaporated metallic films by the method of electron difraction // Phil. Mag. 1933. 16. 1049.

42. Харитонова Л.Д., Смирнова И.И., Масловский В.А. Исследование текстур конденсатов титана // Депонир. рукопись. Гипроцветметобработка. 1978. 242. 2251. (Kharitonova L.D., Smirnova I.I., Maslovskii V.A. The study of textures of titanium condensates // Deposited manuscript. GIPROTSVETMETOBRABOTKA. 1978. 242. 2251.)

43. Структура титановых покрытий при конденсации нестационарных вакуумных пучков / В.И. Пашков, А.В. Демчишин, Л.С. Васильева, З.А. Урелева // Пробл. спец. электрометаллургии. 1978. 9. С. 66–77. (Structure of titanium coatings obtained during condensation of non stationary vacuum bundles / V.I. Pashkov, A.V. Demchishin, L.S. Vasileva, Z.A. Ureleva // Problems of special electrometallurgy. 1978. 9. P. 66–77.)

44. Федякина В.С. Исследование процесса нанесения титановых покрытий на тонкую стальную полосу в вакууме применительно к непрерывным линиям. Дис. ... канд. техн. наук. Москва, 1973. (Fediakina V.S. The study of titanium coatings application on a thin steel strip in vacuum applicably to continuous lines. PhD thesis. Moscow, 1973.)

45. Тестурообразование в слоях, получаемых конденсацией из молекулярных пучков / Л.М. Герт, А.А. Бабад-Захряпин, В.И. Артемов, Р.Х. Жалилов // ФММ. 1976. 42. 350. (Formation of textures in layers obtained from molecular bundles through condensation technique / L.M. Gert, A.A. Babad-Zakhriapin, V.I. Artemov, R.KH. ZHalilov // Physics AND metallography. 1976. 42. 350.)

46. Палатник Л.С., Комник Ю.Ф. Текстура зарождения в конденсатах, образованных на аморфной подложке // Кристаллография. 1960. 5. 775. (Palatnik L.S., Komnik Yu.F. Nucleation structure in condensates formed on the amorphous substrate. Crystallography. 1960. 5. 775.)

47. Холлэнд. Нанесение тонких пленок. М.: Госэнергоиздат, 1963. (Holland. The application of thin films. M.: Gosenergoizdat, 1963.)

48. Данилин Б.С. Вакуумное нанесение тонких пленок. М.: Энергия, 1967. (Danilin B.S. Vacuum application of thin films. M.: Energy, 1967.)

49. Hibbs M.K., Sundgren J.E. Hentrell H.T. // Thin Solid Films. 1984. 116. 177

50. Horhg C.T., Vook R.W. // J. Vac. Sci. Techn. 1973. 10. 1. P. 160–163.

51. Улановский Я.Б., Иванов В.В., Жильцов Е.С. и др. // ТЛС. М.: ВИЛС. 1979. 2. С. 50–54. (Ulanovskiy I.B., Ivanov V.V., Zhiltcov E.S. et al // Production engineering of light alloys. M.: VILS (All-Union Institute Of Light Alloys). 1979. 2. P. 50–54.)

52. // Заводская лаборатория. 1960. 5. 625. (// Plant laboratory 1960. 5. 625.)

53. Патент Франции № 2111796. (Patent of France № 2111796.)

54. Патент США № 3181209. (USA patent № 3181209.)

55. Авт. свид. № 323469. (Author's certificate № 323469.)

56. Патент США № 3608615. (USA patent № 3608615)

57. Патент ФРГ № 1143077. (Patent of Federal Republic of Germany № 1143077.)

58. Aerospace Alloy Foils by Electron Beam Vapor Deposition, 1970.

59. Патент Бельгии № 632911. (Patent of Belgium № 632911.)

60. Патент РФ № 2036244. Способ изготовления тонкой бериллиевой фольги / Г.И. Волокита, Е.С. Карпов, И.И. Папиров, В.С. Шокуров. (Patent RF № 2036244. A method of production of thin beryllium foil production / G.I. Volokita, E.S. Karpov, I.I. Papirov, V.S. Shokurov.)

61. Патент РФ № 2098878. Способ изготовления катодной фольги и катодная фольга электролитического конденсатора / С.Н. Рязанцев, И.Н. Юркевич. (Patent RF № 2098878. A method of production of the cathode foil for e chemical capacitor / S.N. Riazantcev, I.N.Iurkevich.)

62. Юркевич И.Н., Кошелевский В.Ф., Мисожников Л.В., Гевал Ю.Н. Способ получения катодной фольги и катодная фольга электролитических конденсаторов. Патент РФ № 2313843. (Yurkevich I.N., Koshelevskii V.F., Misozhnikov L.V., Geval Yu.N. A method of production of the cathode foil and the cathode foil for e chemical capacitors. Patent RF № 2313843.)

63. Патент РФ № 2400851. Способ получения катодной фольги и катодная фольга электролитических конденсаторов / В.Ф. Кошелевский, И.Н. Юркевич, Л.В. Мисожников, Ю.Н. Гевал. (Patent RF № 2400851. A method of production of the cathode foil for e chemical capacitor / V.F. Koshelevskii, I.N. Yurkevich, L.V. Misozhnikov, Yu.N. Geval)

64. Улановский Я.Б., Ядин Э.В., Мовчан Б.А. // Тезисы докладов 4-ой НТК «Вакуумные покрытия – 87». ЛатИНТИ. 1987. С. 20–21. (Ulanovskiy I.B. Iadin E.V., Movchan B.A // The abstracts of the 4-th scientific conference «Vacuum coatings – 87», Latvian Institute of Scientific and engineering information. 1987. P. 20−21.)

65. Улановский Я.Б., Ядин Э.В., Мовчан Б.А. Первая отечественная опытнопромышленная установка УВ68Л для изготовления фольги вакуумным осаждением // ТЛС. 1990. 1. С. 46–49. (Ulanovskiy I.B. IADin E.V., Movchan B.A. The first home-grown experimental commercial-scale plant УВ68Л for manufacturing of foil through vacuum deposition technique // Production engineering of light alloys. 1990. 1. P. 46–49.)

66. Улановский Я.Б., Бушуев А.В. // Тезисы докладов 4-ой НТК «Вакуумные покрытия – 87», ЛатИНТИ. 1987. С. 18–19. (Ulanovskiy I.B., Bushuev A.V. // The abstracts of the 4-th scientific conference «Vacuum coatings – 87», Latvian Institute of Scientific and engineering information. 1987. P. 18−19.)

67. Улановский Я.Б., Ядин Э.В., Мовчан Б.А. Технологический процесс изготовления фольги вакуумным осаждением // ТЛС. 1991. 1. 15. (Ulanovskiy I.B., Iadin E.V., Movchan B.A. Production process of foil manufacturing through vacuum deposition. // Production engineering of light alloys. 1991. 1. 15.)

68. Hughes J.L. // Met. Eng. Quart. 1974. 2. 1–5.

69. Улановский Я.Б., Ядин Э.В., Самодуров И.М. Создание высокопроизводительного агрегата УВФ-2,0 для получения фольги из труднодеформируемых сплавов вакуумным осаждением // Вопросы авиационной науки и техники. ТЛС. 1991. 6. 36. (Ulanovskiy I.B., Iadin E.V., Samodurov I.M. Design of high-production unit УВФ-2,0 for production of foil from hard to deform alloys through vacuum deposition technique// Problems of aviation science and engineering. Production engineering of light alloys. 1991. 6. 36.)

70. Использование процессов испарения и конденсации в вакууме для получения тонкой фольги: Сб. «Рипорт». ВИМИ. 1975. 13. (The application of processes of vacuum vaporization and condensation for thin foil production: Collection of articles. «Report». VIMI. 1975. 13.)

71. Белов А.Ф., Улановский Я.Б. Металловедение и литье из легких сплавов. М.: Металлургия. 1977. С. 277–278. (Belov A.F., Ulanovskii I.B. Physical metallurgy and light alloy castings. M.: Metallurgy. 1977. P. 277–278.)

72. Белов А.Ф., Улановский Я.Б. Вопросы авиационной науки и техники // ТЛС. М.: ВИЛС. 1986. 8. С. 36–46. (Belov A.F., Ulanovskii I.B. Problems of aviation science and engineering // Production engineering of light alloys. M.: VILS (All-Union Institute Of Light Alloys). 1986. 8. P. 36–46.)

73. Улановский Я.Б., Ядин Э.В. и др. Применение в металлургии процесса испарения и конденсации в вакууме. М.: ВИЛС, ООНТИ, 1975. 143 с. (Ulanovskiy I.B., Iadin E.V. et al . The application of vacuum vaporization and condensation processes in metallurgy. M.: VILS (All-Union Institute Of Light Alloys), OONTI, 1975. 143 p.)

74. Шиллер З., Гайзиг У., Панцер З. Электронно-лучевая технология. М.: Энергия, 1980. 528 с. (Shiller Z., Gaizig U., Pantcer Z. Electron beam process engineering. M.:Energy, 1980. 528 p.)

75. Хокинг М., Васантасри В., Сидки П. Металлические и керамические покрытия: получение, свойства и применение. М.: Мир. 2000. 576 с. (Khoking M., Vasantasri V., Sidki P. Metall and ceramic coatings: production, properties and application. M.: Mir. 2000. 576 p.)

76. Reinhold E., Richter J., Seyfert U., Wenzel B.D. New Aspects of EB-PVD for Large Area Coating of Metal Strips // 43th Ann. Tech. Conf. Proc. Society of Vacuum Coaters, 2000. P. 153–160.

77. Reinhold E., Richter J., Gawer O., Zschieschang E. High Rate EB-PVD Processes for Optical Coating and Their Applicability for Long Time Deposition Cycles in Production Coaters // 42th Ann. Tech. Conf. Proc. Society of Vacuum Coaters. 1999. P. 273–279.

78. Roehrig M., Bright C., Evans D. Vacuum Heat Transfer Models for Web Substrates: Review of Theory and Experimental Heat Transfer Data // 43th Ann. Tech. Conf. Proc. Society of Vacuum Coaters, 2000. P. 335–341.

79. Nimmagada R., Bunshah R.F. Temperature and thickness distribution on substrate during high-rate physical vapor deposition of materials // J. Vac. Sci. Technol. 1971. 8. 6. P. 677–686.

80. Никитин М.М. Технология и оборудование вакуумного напыления. М.: Металлургия, 1992. 112 с. (Nikitin M.M. Process engineering and equipment for vacuum deposition. M.: Metallurgy, 1992. 112 p.)

81. Мельник В.И., Мельник И.В., Порицкий П.В. Численное моделирование технологического процесса нанесения тонких пленок в газоразрядных электроннолучевых испарителях // Прикладная физика. 2000. 2. С. 168–172. (Melnik V.I., Melnik I.V., Poritckii P.V. Numerical simulation of engineering process of thin films applying in gas discharge electron beam vaporizers // Applied Physics. 2000. 2. P. 168–172.)

82. Афанасьев И.В., Тимашов В.А., Щербицкий В.В. Диаграмма направленности парового потока при электронно-лучевом испарении армко-железа // Пробл. спец. электрометаллургии. 1985. 1. С. 41–45. (Afanasev I.V., Timashov V.A., Shcherbitckii V.V. Diagrams of steam flow directivity in the course of EB vaporization of armko-iron. // Problems of special electric metallurgy. 1985. 1. P. 41–45.)

83. Зеберин А.Г., Пипкевич Г.Я. Исследование тепло- и массообмена в процессе осаждения металлических покрытий испарением и конденсацией в вакууме. В кн.: Металлизация в вакууме. Рига: Авотс. 1983. С. 34–43. (Zeberin A.G., Pipkevich G.IA. The study of heat and mass transfer in the course of metallic coatings vacuum deposition and condensation. In the book: Vacuum metallization . Riga: Avots. 1983. P. 34–43.)

84. Улановский Я.Б., Соловейчик В.Р. О пространственном распределении парового потока при высокоскоростном испарении // ДАН СССР. 1990. 315. 3. С. 613–616. (Ulanovskiy I.B. Soloveichik V.R. Concerning space dissipation of vapor flow during high-intensive vaporization // Proc. Of the Science Academy of the USSR. 1990. 315. 3. p. 613–616.)

85. Улановский Я.Б., Крупенников С.А., Левицкий И.А. Математическое моделирование массопереноса при высокоскоростном электронно-лучевом испарении на движущуюся ленту-подложку // Изв. вузов. Цветная металлургия. 2003. А. С. 63–69. (Ulanovskiy I.B. Krupennikov S.A., Levitckii I.A. Mathematical simulation of heat transfer under conditions of high-speed EB vaporization to the travelling strip-substrate // VILS (All-Union News of Higher Educational Institutions. Nonferrous Metallurgy. 2003. A. P. 63–69.)

86. Улановский Я.Б., Крупенников С.А., Левицкий И.А. Математическое моделирование теплопереноса при высокоскоростном электронно-лучевом испарении на движущуюся ленту-подложку // Изв. вузов. Цветная металлургия. 2003. Б. С. 59–65. (Ulanovskiy I.B. Krupennikov S.A., Levitckii I.A.Mathematical simulation of heat transfer under conditions of high-speed EB vaporization to the travelling strip-substrate // News of Higher Educational Institutions. Nonferrous Metallurgy. 2003. B. P. 59–65.)

87. Улановский Я.Б., Крупенников С.А., Левицкий И.А. Теоретические аспекты тепло- и массопереноса при высокоскоростном электронно-лучевом испарении и конденсации в вакууме: В сб. Перспективные технологии легких и специальных сплавов. М.: Физматлит. 2006. С. 255–267. (Ulanovskiy I.B., Krupennikov S.A., Levitckii I.A.. Theoretical aspects of heat and mass transfer under conditions of high-speed EB vaporization and condensation in vacuum: In the collection of scientific works . Promising production techniques of light and special alloys. M.: Fizmatlit. 2006. P. 255–267.)

88. Зигель Р., Хауэлл Дж. Теплообмен излучением. М.: Мир, 1975. 840 с. (Zigel R., Khauell G.Radiation heat transfere. M.: Mir, 1975. 840 p.)

89. Knudsen M. The Kinetic Theory of Gases. N.-Y.: McGraw-Hill Book Comp., 1938. 26.

90. Кикоин А.К., Кикоин И.К. Молекулярная физика. М.: Наука, 1976. 480 с. (Kikoin A.K., Kikoin I.K. Molecular physics. M. Nauka, 1976. 480 p.)

91. Смитлз К. Дж. Металлы: Справ. М.: Металлургия, 1980. 447. (Smithles K. Jh. Metals: guidbook. M.: Metallurgy, 1980. 447.)

92. Дэшман С. Научные основы вакуумной техники. М.: Мир, 1964. 715 с. (Deshman S. Scientific essentials of vacuum process technique. M.: Mir, 1964. 715 p.)

93. Арутюнов В.А., Бухмиров В.В., Крупенников С.А. Математическое моделирование тепловой работы промышленных печей. М.: Металлургия, 1990. 239 с. (Arutunov V.A., Bukhmirov V.V., Krupennikov S.A.Mathematical simulation of thermal operation of industrial furnaces. M.: Metallurgy, 1990. 239 p.)

94. Шуп Т. Решение инженерных задач на ЭВМ: Практ. руководство. М.: Мир, 1982. 238 с. (Shup T. Solution of engineering problems on computer, Guidebook. M.: Mir, 1982. 238 p.)

95. Самарский А.А. Теория разностных схем. М.: Наука, 1989. 616 с. (Samarskii A.A. Theory of difference schemes. M.: Nauka, 1989. 616 p.)

96. Годунов С.К., Рябенький В.С. Разностные схемы. М.: Наука, 1977. 439 с. (Godunov S.K., Riabenkii V.S. Difference schemes. M.: Nauka, 1977. 439 p.)

97. Физические величины: Справ. / Под ред. И.С. Григорьева и Е.С. Мейлихова. М.: Энергоатомиздат, 1991. 1323 с. (Physical values: Guidbook / Under the editorship of I.S. Grigoreva and E.S. Meilikhova. M.: Energoatomizdat, 1991. 1323 p.)

98. Zinsmeister G. // Vakuum-Technik. 1964. 8. P. 233–240.

99. Santala T., Adams C.M. // J. Vac. Sci. and Technol. 1970. 7. 6. P. 22–29.

100. Poster J.S., Pfeiler W.H. // J. Vac. Sci. and Technol. 1972. 9. 6. P. 1379–1384.

101. Бадиленко Г.Ф. // Пробл. спец. электрометаллургии. 1975. 2. С. 62–66. (Badilenko G.F.// Problems of special electric metallurgy. 1975. 2. P. 62–66.)

102. Бадиленко Г.Ф. и др. // Пробл. спец. электрометаллургии. 1986. 3. С. 43–46. (Badilenko G.F.et al // Problems of special electric metallurgy. 1986. 3. P. 43–46.)

103. Бадиленко Г.Ф. и др. // Пробл. спец. электрометаллургии. 1987. 1. С. 40–44. (Badilenko G.F.et al // Problems of special electric metallurgy. 1987. 1. p. 40–44.)

104. Nimmagadda R. et al . // J. Vac. Sci. Techn. 1972. 9. 6. P. 1406–1412.

105. Клебанов Ю.Д. и др. // ФиХОМ. 1977. 3. С. 50–54. (Klebanov U.D. et al // Physics and Chemistry of treatment of metals. 1977. 3. P. 50–54.)

106. Клебанов Ю.Д. // ФиХОМ. 1978. 4. С. 64–69. (Klebanov U.D. // Physics and Chemistry of treatment of metals. 1978. 4. P. 64–69.)

107. Dale E.B. // J. Appi. Phys. 1971. 42. 10. P. 3617–3702.

108. Улановский Я.Б. // ДАН СССР. 1990. 312. 5. С. 1126–1128. (Ulanovskiy I.B. // Proc. of the Science Academy of the USSR. 1990. 312. 5. P. 1126–1128.)

109. Улановский Я.Б., Жильцов Е.G., Егорова Г.И. // Тезисы II Межреспубликанской конференции «Вакуумная металлизация в народном хозяйстве». Рига. ЛатИН ТИ, 1977. 32. (Ulanovskiy I.B. Zhiltcov E.G., Egorova G.I. // The abstracts of the II-nd scientific Inter-republic conference «Vacuum metallurgy in national economy». Riga. Latvian Institute of Scientific and engineering information. 1977. 32.)

110. Улановский Я.Б. и др. Авт. свид. № 1238419 от 15.02.86. (Ulanovskiy I.B. et al Author's certificate № 1238419 dated 15.02.86.)

111. Жуховицкий А А., Шварцман Л А. Физическая химия. М.: Металлургия, 1968. (Zhukhovitckii A.A., Shvartzman L.A. Physical chemistry. M.: Metallurgy, 1968.)

112. Улановский Я.Б., Соловейчик В.Р., Соловейчик М.Р. // ТЛС. 1994. 1–2. 25. (Ulanovskiy I.B. Soloveichik V.R., Soloveichik M.R. // Production engineering of light alloys. 1994. 1–2. 25.)

113. Нестерова И.Н., Этингант А.А., Гашинин А.В. // ФиХОМ. 1984. 2. 73. (Nesterova I.N., Etingant A.A., Gashinin A.V. // Physics and Chemistry of treatment of metals. 1984. 2. 73.)

114. Улановский Я.Б., Соловейчик В.Р. // ЖФХ. 65. 2243. (Ulanovskiy I.B. Soloveichik V.R. //Journal of Physical Chemistry. 65. 2243.)

115. Улановский Я.Б. и др. // Тезисы II Межреспубликанской конференции «Вакуумная металлизация в народном хозяйстве». Рига. ЛатИНТИ. 1977. С. 90–91. (Ulanovskiy I.B.et al // The abstracts of the II-nd scientific Inter-republic conference «Vaccum metallurgy in national economy». Riga. Latvian Institute of Scientific and engineering information. 1977. p. 90–91.)

116. Баталин Г.И., Белобородова Е.А., Казимиров В.П. Термодинамика и строение жидких сплавов на основе алюминия. М.: Металлургия, 1983. 158. (Batalin G.I., Beloborodova E.A., Kazimirov V.P. Thermodynamics and structure of liquid aluminium. M.: Metallurgy, 1983. 158.)

117. Kenn J. et al // The X Int. Conf, on Vacuum Metallurgy, Beijing, China, June, 1990 (Abstracts). 41.

118. Константцов Ю.А., Папиров И.И., Канчерин А.С. // Физ. и хим. обработка материалов. 1978. 1. 143. (Konstantcov Yu.A., Papirov I.I., Kancherin A.S. // Physical and chemical processing of materials1978. 1. 143.)

119. Патент США № 3.729.046, 1973. (USA patent № 3.729.046, 1973.)

120. Глазунов С.Г., Моисеев В.Н. Конструкционные титановые сплавы. М.: Металлургия, 1974. (Glazunov S.G., Moiseev V.N. S. Structural titanium alloys), M.: Metallurgy, 1974.)

121. Патент Великобритании № 990692. (Great Britain Patent № 990692.)

122. Braski D.N. // Neuch. Inst. and Meth. 1972. 102. 1972. 102. 3. P. 553–565.

123. Патент Франции № 2152624. (Patent of France № 2152624.)

124. Рашевиц Д.Т., Федякина В.С., Вовси А.И. и др. // Труды III Международной конференции по титану. М.: ВИЛС. 1977. 3. 565. (Rashevitc D.T., Fediakina V.S., Vovsi A.I. et al // Proceedings of the III-d International Conference on Titanium. M.: VILS (All-Union Institute Of Light Alloys). 1977. 3. 565.)

125. Улановский Я.Б., Жильцов Е.С, Журавель А.П. // ФиХОМ. 1981. 3. 69. (Ulanovskiy I.B., Zhiltcov E.S., Zhuravel A.P. // Physics and Chemistry of treatment of metals. 1981. 3. 69.)

126. Дэшман С. Научные основы вакуумной техники. М.: Мир, 1964. (Deshman S. Scientific essentials of vacuum engineering. M.: Mir, 1964.)

127. Уикс К.Е., Блок Ф.Е., Термодинамические свойства 65 элементов их окислов, галогенидов, карбидов и нитридов. М.: Металлургия, 1965. (Uiks K.E., Blok F.E. Thermodynamic properties of 65 elements and their oxides, halogenides, carbides and nitrides, M.: Metallurgy, 1965.)

128. Палатник Л.С., Фукс М.Я., Черемской П.Г. // ДАН СССР. Кристаллография. 1972. 203. 5. 1058. (Palatnik L.S., Fuks M.IA., Cheremskoi P.G. // Proc. Of the Science Academy of the USSR. Crystallography 1972. 203. 5. 1058.)

129. Улановский Я.Б., Дубник Г.И., Садков В.В. и др. // Вопросы авиационной науки и техники // ТЛС. М.: ВИЛС. 1989. 1. 14. (Ulanovskiy I.B. Dubnik G.I., Sadkov V.V. et al // Process engineering problems of light alloys. M.: VILS (All-Union Institute Of Light Alloys). 1989. 1. 14.)

130. Фукс М.Я., Палатник Л. С. и др. // ФТТ. 1971. 13. 6. (Fuks M.I., Palatnik L. S. et al // Solid State Physics. 1971. 13. 6.)

131. Островская Л.М., Серебренникова О.С., Соллертинская Е.С // Научные труды института ГИПРОЦМО. 1978. 55. С. 17–19. (Ostrovskaia L.M., Serebrennikova O.S., Sollertinskaia E.S. // Research papers of GIPROTCMO. 1978. 55. P. 1719.)

132. Харитонова Л.Д., Островская Л.М. и др. // Научные труды института ГИПРОЦМО. 1978. 55. С. 20–23. (Kharitonova L.D., Ostrovskaia L.M. et al // Collection of GIPROTCMO institute studies. 1978. 55. P. 2023.)

133. Куров Г.А., Маркарян А.Б., Жильков Э.А. Сб. научных трудов по проблемам микроэлектроники (физ.-мат. серия), 1974. XVIII. С. 101–104. (Kurov G.A., Markarian A.B., Zhilkov E.A. Collection of proceedings on microelectronics (phys.-math, series), 1974. XVIII. P. 101–104.)

134. Куров Г.А., Маркарян А.Б., Жильков Э.Я. Микроэлектроника. Т. 2. 1973. С. 145–153. (Kurov G.A., Markarian A.B., Zhilkov E.I. Microelectronics. T. 2. 1973. P. 145–153.)

135. Виткин А.И., Суровцева В.С., Тычинин А.И. // Защита металлов. 1972. 6. 729. (Vitkin A.I., Surovtceva B.C., Tychinin A.I. // Metal protection. 1972. 6. 729.)

136. Создание машин и исследование процессов получения вакуумных конденсационных покрытий // Труды ВНИИМЕТМАШ. 1977. 51. (Design machines and study of vacuum condensation coating pocess) // Proceedings of VNIIMETMASH. 1977. 51.)

137. Куров Г.А., Жильков Э.А. и др. // ДАН СССР. 1974. 203. 5. С. 1058–1061. (Kurov G.A., Zhilkov E.A. et al // Proc. of the Science Academy of the USSR. 1974. 203. 5. P. 1058–1061.)

138. Ройх И.Л., Федосов С.Н., Вискалова И.М, Терезман Е.Ф. // ФиХОМ. 1974. 5. С. 41–45. (Roikh I.L., Fedosov S.N., Viskalova I.M, Terezman E.F. // Physics and Chemistry of treatment of metals. 1974. 5. P. 41–45.)

139. Meyers R.G., Morgan R.P. Trans. Vac. Met. Conf., N.Y. 1966. Boston, Amer. Vac. Soc. 1967. P. 271–288.

140. Hewig L.E., Murray M.V. // Metal Finish. 1969. 67. 11. p. 44–46.

141. Ройх И.Л., Коваленко В.Б., Колтунова Л.Н. // Заводская лаборатория. 1971. С. 314–315. (Roikh I.L., Kovalenko V.B., Koltunova L.N. // Plant laboratory. 1971. 3. P. 314–315.)

142. Lloi Dzh.R., Nakakhara S. // Thin Solid Films, 1982. 93. P. 281–286.

143. Bunshah R.F., Webster R.T. // J. Vac. Sci. Technol. 1971. 8. 6. P. 887–890.

144. Аннотации докладов IV Всесоюзного совещания по применению ускорителей заряженных частиц в народном хозяйстве. Ленинград. НИИЭФА. 1982. 170. (Annotation of Proceedings of the IV-th All-Union conference on using the charge particle accelerators in National economy. Leningrad. NIIEFA. 1982. 170.)

145. Эсле В. Технология электровакуумных материалов. М.: Госэнергоиздат, 1962. 1. 631. (Esle V. Process Engineering of vacuum electronics materials. M.: Gosenergoizdat, 1962. 1. 631.)

146. Улановский Я.Б., Данилкин В.А. // ТЛС. 1971. 4. 95. (Ulanovskiy I.B., Danilkin V.A. // Production engineering of light alloys. 1971. 4. 95.)

147. Грег С., Синг К. Адсорбция, удельная поверхность, пористость. М.: Мир, 1970. (Greg S., Sing K. Adsorption, specific surface. M.: Mir, 1970.)

148. Темкин М. И. // ЖФХ. 1955. 29. 1610. (Temkin M. I. // Journal of physical chemistry. 1955. 29. 1610.)

149. Рот А. Вакуумные уплотнения, М.: Энергия, 1971. 29. (Rot A. Vacuum seals, M.: Energy, 1971. 29.)

150. Несис Е.И. Кипение жидкостей. М.: Наука, 1973. (Nesis E.I. Boiling of liquids, M. Nauka, 1973.)

151. Карлов Н.В. и др. // Письма в ЖЭТР. 1974. 19. 2. 111. (Karlov N.V. et al // The letters to Journal of experimental and theoretical physics 1974. 19. 2. 111.)

152. Рыкалин Н.Н., Ушов А.А., Зуев И.В. // ФиХОМ. 1979. 1. С. 3–11. (Rykalin N.N., Ushov A.A., Zuev I.V. // Physics and Chemistry of treatment of metals. 1979. 1. P. 3–11.)

153. Winkler O., Bakish R. Vac. Metallurgy-Amsterdam. Elsevies Pull. Comp., 1971.

154. Шиллер З. и др. Электронно-лучевая технология: Пер. с нем. Энергия, 1980. 528. (Shiller Z. et al Electon beam technique: Translated from German. Energy, 1980. 528.)

155. Bunshah R.P. Physical Vapour Deposition of Metals, Alloys and Ceramics, in New Trends in Materials Processing. American Society for Metals. 1974.

156. Тимошенко С. П. Сопротивление материалов. М.: Наука, 1965. (Timoshenko S. P. Performance of Construction Materials. M.: Nauka, 1965.)

157. Улановский Я.Б., Бушуев А.В. // ТЛС. М.: ВИЛС. 1988. 3. С. 41–46. (Ulanovskiy I.B., Bushuev A.V. // Production engineering of light alloys. M.: VILS (All-Union Institute Of Light Alloys). 1988. 3. p. 41–46.)

158. Пипко А.И., Плисковский В.Я., Пенчко Е.А. Конструирование и расчет вакуумных систем. М.: Энергия, 1970. (Pipko A.I., Pliskovskii V.I., Penchko E.A. Design and calculation of vacuum systems. M.: Energy, 1970)

159. Соловейчик В.Р., Улановский Я.Б., Соловейчик М.Р. К теории газопроницаемости многослойных экранов из фольги с регламентированной сквозной пористостью // ТЛС. 1994. 5–6. 121. (Soloveichik V.R., Ulanovskiy I.B. Soloveichik M.R. Concerning gas penetration of multi-layer foil screens with specified porosity // Production engineering of light alloys. 1994. 5–6. 121.)

160. Ландау Л.Д., Лившиц Е.М. Статистическая физика. М., 1964. (Landau L.D., Livshitc E.M. Statistical Physics. M., 1964.)

161. Берд Г. Молекулярная газовая динамика. М.: Мир, 1981. (Berd G. Molecular gas dynamics. M.: Mir, 1981.)

162. Балеску Р. Равновесная и неравновесная статистическая механика. М.: Мир, 1978. (Balesku R. Equilibrium and non-equilibrium statistical mechanics, M.: Mir, 1978.)

163. Теория образования текстур в металлах и сплавах. / Я.Д. Вишняков, А.А. Бобареко, С.А. Владимиров, И.В. Эгиз. М.: Наука, 1979. (A theory of formation of textures in metals and alloys. / I.D. Vishnyakov, A.A. Bobareko, S.A. Vladimirov, I.V. Egiz. M.: Nauka, 1979.)

164. Цвиккер У. Титан и его сплавы. М.: Металлургия, 1979. (Tsvikker U. Titanium and its alloys. M.: Metallurgy, 1979.)

165. Попова Л.Е., Попов А.А. Диаграммы превращения аустенита в сталях и бета-раствора в сплавах титана. Справочник. М.: Металлургия, 1991. 502. (Popova L.E., Popov A.A. Diagram of austenitic transformation in steels and beta solutions in titanium alloys. Guide. M.: Metallurgy, 1991. 502.)

166. Hochied B., Klima R., Beavvais C., Papin M. // Met. Sci. Rev. Metall, 1970. 67. 9. P. 583–590.

167. Лясоцкая В.С., Лясоцкий И.В., Мещеряков В.Н. и др. // Изв. вузов. Цветная металлургия. 1986. 2. С. 86–93. (Liasotckaia V.S., Liasotckii I.V., Meshcheriakov V.N. et al // News of Higher Educational Institutions. Nonferrous metallurgy. 1986. 2. P. 86–93.)

168. Вигдорович В.Н., Попов В.И. // Изв. АН СССР. Металлы. 1977. 5. С. 115–120. (Vigdorovich V.N., Popov V.I. // News of the Science Academy of the USSR. Metals. 1977. 5. P. 115–120.)

169. Улановский Я.Б., Дубник Г.И. Сб. Процессы обработки легких и жаропрочных сплавов. М.: Наука, 1981. С. 234–240. (Ulanovskiy I.B. Dubnik G.I. Processes of treatment of light and high-temperature alloys. M.: Nauka, 1981. P. 234–240.)

170. Улановский Я.Б., Жильцов Е.С., Журавель А.П. и др. // ФММ. 1981. 52. 1. С. 217–220. (Ulanovskiy I.B. Zhiltcov E.S., Zhuravel A.P. et al // Physics and metallography. 1981. 52. 1. P. 217–220.)

171. Горелик С.С. Рекристаллизация металлов и сплавов. М.: Металлургия, 1967. (Gorelik S.S. Recrystallization of metals and alloys. M.: Metallurgy, 1967)

172. Grovenor G.R.M., Hentrell H.T.G., Smith D.A. The Development of Grain Structure During Growth of Metallic Films // Acta Met. 1984. 32. 5. p. 773–781.

173. Горелик С.С., Расторгуев Л.Н., Скаков Ю.А. Рентгенографический и электронно-оптический анализ. М.: Металлургия, 1970. (Gorelik S.S., Rastorguev L.N., Skakov Yu.A. X-ray and optoelectronic analysis. M.: Metallurgy, 1970.)

174. Молчанова Е.К. Атлас диаграмм состояния титановых сплавов. М.: Машиностроение, 1964. (Molchanova E.K. Atlas of phase equilibrium diagrams of titanium alloys M.: Mashinostroyenie, 1964.)

175. Улановский Я.Б., Журавель А.П. // ДАН СССР. 179. 244. 3. С. 599–601. (Ulanovskiy I.B. Zhuravel A.P. // Proc. of the Science Academy of the Ussr. 179. 244. 3. P. 599–601.)

176. Улановский Я.Б., Дубник Г.И., Бушуев А.В. // ТЛС. 1981. 5. 72. (Ulanovskiy I.B., Dubnik G.I., Bushuev A.V. // Production engineering of light alloys. 1981. 5. 72.)

177. Улановский Я.Б., Дубник Г.И., Овечкин Б.И. и др. // Тезисы докладов Всесоюзного совещания по применению вакуума в черной и цветной металлургии. М.: ИМЕТ, 1979. 142. (Ulanovskiy I.B. Dubnik G.I., Ovechkin B.I. et al // Abstracts of reports of All union scientific Conference on vacuum application in ferrous and non ferrous metallurgy. M.: Institute of metallurgy and Physical metallurgy (IMET), 1979. 142.)

178. Улановский Я.Б., Дубник Г.И., Скаков Ю.А. // Тезисы докладов IV Всесоюзной конференции по текстурам и рекристаллизации в металлах и сплавах. Горький. ГНИ, 1983. 296. (Ulanovskiy I.B., Dubnik G.I., Skakov Yu.A. // Abstracts of the IV scientific All Union Conference on textures and recrystallization in metals and alloys. Gorkiy. Gni, 1983. 296.)

179. Улановский Я.Б., Егорова Г.И. // Тезисы докладов «Вакуумная металлизация в народном хозяйстве». Лат ИНТИ, Рига, 1977. С. 66–67. (Ulanovskiy I.B., Egorova G.I. // Abstracts of scientific conference «Vacuum metallization in national economy». Latvian Institute of Scientific and Engineering information, Riga, 1977. P. 66–67.)

180. Улановский Я.Б., Дубник Г.И. // Тезисы докладов 4-й НТК «Вакуумные покрытия – 87». ЛатИНТИ, 1987. С. 20–21. (Ulanovskiy I.B., Dubnik G.I. // Proc. Of the 4-th scientific Scientific-Engineerig Conference «Vacuum coatings – 87». Latvian Institute of Scientific and Engineering information, 1987. P. 20–21.)

181. Авт. свид. № 965023 от 07.06.82. / О.Ф. Демидов, Т.П. Романова, Я.Б. Улановский, А.В. Бущуев, Г.И. Дубник. (Author's certificate № 965023 dated 07.06.82. / O.F. Demidov, T.P. Romanova, I.B. Ulanovskii, A.V. Bushchuev, G.I. Dubnik.)

182. Улановский Я.Б., Скаков Ю.А., Дубник Г.И. // Изв. вузов. Черная металлургия. 1985. 9. 112. (Ulanovskiy I.B. Skakov Yu.A., Dubnik G.I. // News of Higher Educational Institutions. Ferrous metallurgy. 1985. 9. 112.)

183. Улановский Я.Б., Дубник Г.И., Захарова А.А. и др. // Тезисы доклада II совещания по тепловой микроскопии. М.: ИМАШ АН СССР, 1986. 165. (Ulanovskiy I.B., Dubnik G.I., Zakharova A.A. et al // Proc of the II-nd Conference on thermal microscopy. M.: Engineering Science Institute of the Science Academy of the USSR − IMMASH, 1986. 165.)

184. Улановский Я.Б., Дубник Г.И., Захарова А.А. и др. // Вопросы авиационной науки и техники. ТЛС. 1987. 1. 31. (Ulanovskiy I.B., Dubnik G.I., Zakharova A.A. et al // Problems of aviation science and engineering. Production engineering of light alloys. 1987. 1. 31.)

185. Палатник Л.С., Федоренко А.И. // ФММ. 1966. 22. 6. С. 936–938. (Palatnik L.S., Fedorenko A.I. // Physics and metallography. 1966. 22. 6. P. 936−938.)

186. Косевич В.М., Палатник Л.С. // ФММ. 1968. 25. 1. 62. (Kosevich V.M., Palatnik L.S. // Physics and metallography. 1968. 25. 1. 62.)

187. Попов В.И. // ФиХОМ. 1975. 1. С. 51–53. (Popov V.I. // Physics and Chemistry of treatment of metals. 1975. 1. P. 51−53.)

188. Костржицкий А.И., Гусарева О.Ф. // Металлы. 1987. 1. С. 169–172. (Kostrzhitckii A.I., Gusareva O.F. // Metals. 1987. 1. P. 169−172.)

189. Панов Ю.И., Прокопчук С.И. Металловедение прецизионных сплавов на основе цветных металлов: Сб. научных трудов. М.: Металлургия, 1984. 87. (Panov Yu.I., Prokopchuk S.I. Physical metallurgy of precision non-ferrous metals alloys. Collection. M.: Metallurgy, 1984. 87.)

190. Никгонов М.Б., Пешков В.В., Родионов В.Н. // Сварочное производство. 1986. 3. С. 37–39. (Nikgonov M.B., Peshkov V.V., Rodionov V.N. // Welding engineering. 1986. 3. P. 37−39.)

191. Damodare D. // J. Mater. Sci. 1982. 17. 9. P. 2713−2617.

192. Бабук В.В., Иващенко С.А., Моисеенко С.И. Машиностроение. Минск, 1983. С. 88–90. (Babuk V.V., Ivashchenko S.A., Moiseenko S.I. Mashinostroyenie. Minsk, 1983. P. 88−90.)

193. Колачев Б.А., Горшков Ю.В., Шевченко В.В. // МиТОМ. 1972. 5. С. 6–10. (Kolachev B.A., Gorshkov Yu.V., Shevchenko V.V. // Metal science and heat treatment of metals 1972. 5. P. 6−10.)

194. Борисов Е.А., Шашенкова И.И., Глебова Р.Д. // МиТОМ. 1972. 5. С. 10–13. (Borisov E.A., SHashenkova I.I., Glebova R.D. // Metal science and heat treatment of metals 1972. 5. P. 10−13.)

195. Улановский Я.Б., Дубник Г.И. // ТЛС. 1980. 6. С. 48–52. (Ulanovskiy I.B., Dubnik G.I. // Production engineering of light alloys. 1980. 6. P. 48−52.)

196. Глазунов С.Г., Моисеев В.Н. Конструкционные титановые сплавы. М.: Металлургия, 1974. (Glazunov S.G., Moiseev V.N. Structural titanium alloys. M.: Metallurgy, 1974.)

197. Горшков Ю.В., Улановский Я.Б., Садков В.В. и др. // ТЛС. 1988. 12. 57. (Gorshkov I.V., Ulanovskiy I.B., Sadkov V.V. et al // Production engineering of light alloys. 1988. 12. 57.)

198. Авт. свид. №.1151056. А.Ф. Белов, Я.Б. Улановский, О.Н. Санков, Ю.В. Горшков, В.В. Садков, Л.И. Корселадзе, А.В. Бушуев. (Author's certificate №.1151056. A.F. Belov, I.B. Ulanovskiy, O.N. Sankov, Yu.B. Gorshkov, V.V. Sadkov, L.I. Korseladze, A.V. Bushuev.)

199. Авт. свид. № 1173770. Ю.В. Горшков, Я.Б. Улановский, О.Н. Санков, А.В. Бушуев. (Author's certificate № 1173770. Yu.V. Gorshkov, I.B. Ulanovskiy, O.N. Sankov, A.V. Bushuev.)

200. Авт. свид. № 1221983 от 1.12.1985. А.В. Бушуев, Ю.В. Горшков, Л.И. Корселадзе, О.П. Санков, Н.А. Семавин, Я.Б. Улановский. (Author's certificate № 1221983 dated 1.12.1985. A.V. Bushuev, Yu.V. Gorshkov, L.I. Korseladze, O.P. Sankov, H.A. Semavin, I.B. Ulanovskiy.)

201. Авт. свид. № 1311323 от 15.01.87. Я.Б. Улановский, А.В. Бушуев, О.Н. Санков. (Author's certificate № 1311323 dated 15.01.87. I.B. Ulanovskiy, A.V. Bushuev, O.N. Sankov.)

202. Авт. свид. № 1097008 от 8.02.1984. Ю.В. Горшков, Я.Б. Улановский, О.Н. Санков, А.В. Бушуев. (Author's certificate № 1097008 dated 8.02.1984. Yu.V. Gorshkov, I.B. Ulanovskiy, O.N. Sankov, A.V. Bushuev.)

203. Улановский Я.Б., Санков О.Н. , Бущуев А.В. // ТЛС. М.: ВИЛС. 1988. 5. 67. (Ulanovskiy I.B. Sankov O.N., Bushchuev A.V. // Production engineering of light alloys. M.: VILS 1988. 5. 67.)

204. Авт. свид. № 824683. Я.Б. Улановский, А.П. Журавель. (Author's certificate № 824683. I.B. Ulanovskiy, A.P. Zhuravel.)

205. Авт. свид. № 618970. Я.Б. Улановский, О.Т. Рашевиц, Э.В. Ядин, А.И. Вовси. (Author's certificate № 618970. I.B. Ulanovskiy, O.T. Rashevitc, E.V. Iadin, A.I. Vovsi.)

206. Авт. свид. № 1067854. Я.Б. Улановский, Г.И. Дубник, В.М. Платонов, Ю.И. Хрычев. (Author's certificate № 1067854. I.B. Ulanovskiy, G.I. Dubnik, V.M. Platonov, Yu.I. Khrychev.)

207. Авт. свид. № 1667405. Я.Б. Улановский, Г.И. Дубник и др. (Author's certificate № 1667405. I.B. Ulanovskiy, G.I. Dubnik et al.)

Ulanovskiy Iakov B.

THEORY AND PRACTICE OF MAKING FOILS BY VACUUM DEPOSITION

Computer design *A.S. Antsiferova*

Подписано в печать 23.12.15	Бумага офсетная	
Формат 60 × 90 $^{1}/_{16}$	Печать офсетная	Уч.-изд. л. 14,5
	Тираж 500 экз.	Заказ 4884

National University Of Science And Technology ‘MISIS’,
4, Leninsky Prospect, Moscow, Russia, 119049

Izdatelskiy Dom ‘MISIS’,
4, Leninsky Prospect, Moscow, Russia, 119049
Tel. +7 (495) 638-45-22

Отпечатано в типографии Издательского Дома МИСиС
119049, Москва, Ленинский пр-т, 4
Тел. (499) 236-76-17, тел./факс (499) 236-76-35